



Li, Guoshuai (2020) Experimental studies on shock wave interactions with flexible surfaces and development of flow diagnostic tools. PhD thesis.

<https://theses.gla.ac.uk/81703/>

Copyright and moral rights for this work are retained by the author

A copy can be downloaded for personal non-commercial research or study, without prior permission or charge

This work cannot be reproduced or quoted extensively from without first obtaining permission in writing from the author

The content must not be changed in any way or sold commercially in any format or medium without the formal permission of the author

When referring to this work, full bibliographic details including the author, title, awarding institution and date of the thesis must be given



**EXPERIMENTAL STUDIES ON SHOCK WAVE INTERACTIONS
WITH FLEXIBLE SURFACES AND DEVELOPMENT OF FLOW
DIAGNOSTIC TOOLS**

Submitted in fulfilment of the requirements for the degree of

Doctor of Philosophy

Guoshuai Li

School of Engineering

College of Science and Engineering

University of Glasgow

February 2020

I. Author's Declaration

I declare that, except where explicit reference is made to the contribution of others, this dissertation is the result of my own work and has not been submitted for any other degree at the University of Glasgow or any other institution.

Signature: _____

Printed name: Guoshuai Li

II. Abstract

Nowadays, light-weight composite materials have increasingly used for high-speed flight vehicles to improve their performance and efficiency. At supersonic speed, sonic fatigue, panel flutter, severe instabilities, and even catastrophic structural failure would occur due to the shock wave impingement on several flexible components of a given structural system either internally or externally. Therefore, investigation on shock wave interaction with flexible surfaces is crucial for the safety and performance of high-speed flight vehicles. This work aims to investigate the mechanism of shock wave interaction with flexible surfaces with and without the presence of the boundary layer. The first part involves the shock wave generated by supersonic starting jets interaction with flexible surfaces and the other one focuses on shock wave and boundary layer interaction (SBLI) over flexible surfaces.

A novel miniature and cost-effective shock tube driven by detonation transmission tubing was designed and manufactured to simulate the supersonic starting jet and investigate the interaction of a supersonic starting jet with flexible surfaces. To investigate the characterization of this novel type shock tube, the pressure-time measurement in the driven section and the time-resolved shadowgraph were performed. The result shows that the flow structure from the open end of the shock tube driven by detonation transmission tubing agrees with that of conventional compressed-gas driven shock tubes. Moreover, this novel type of shock tube has good repeatability of less than 3% with a Mach number range of 1.29-1.58 when the weight of the NONEL explosive mixture varies from 3.6mg to 12.6mg.

An unsteady background oriented schlieren (BOS) measurement system and a sprayable Polymer-Ceramic unsteady pressure sensitive paint (PC-PSP) system were developed. The preliminary BOS result in a supersonic wind tunnel shows that the sensitivity of the BOS system is good enough to visualize weak density variations caused by expansion waves, boundary layer, and weak oblique shocks. Additionally, compared with the commercial PC-PSP from Innovative Scientific Solutions Incorporated (ISSI), the in-house developed unsteady PSP system has higher pressure sensitivity, lower temperature sensitivity, and photo-degradation rate.

To identify the shock movement, distortion and unsteadiness during the processes of the supersonic starting jet impingement and shock wave boundary layer interaction (SBLI) over flexible surfaces, an image processing scheme involving background subtraction in the frequency domain, filtering, resampling, edge detection, adaptive threshold, contour detection, feature extraction, and fitting was proposed and applied to process shadowgraph and schlieren sequences automatically. A large shadowgraph data set characterized by low signal to noise ratio (SNR) and small spatial resolution (312×260 -pixel), was used to validate the proposed scheme. The result proves that the aforementioned image processing scheme can detect, track, localize, and fit shock waves in a subpixel accuracy.

The mechanism of the interaction between the initial shock wave from a supersonic starting jet and flexible surfaces was investigated based on a square shock tube driven by detonation transmitting tube. Compared with that of the solid plate case, flexible surfaces can delay the shock reflection process because of the flexible panel deformation generated by the pressure difference between the top and the bottom. The delay time is around $8\mu\text{s}$ in the case of 0.1mm thick flexible surface, whereas it declines to around $4\mu\text{s}$ in the case of 0.3mm thick flexible surface because of the lower flexibility and deformation magnitude. However, interestingly, the propagation velocity of the reflected shock wave is basically the same for the solid plate and flexible panels, which means the flexible surface doesn't reduce the strength of the reflection wave, although it delays its propagation. Also, there is not an apparent difference in the velocity of the reflected shock wave in the case of different incident shock Mach numbers when M_s varying from 1.22 to 1.54. These experimental results from this study are useful for validating numerical codes that are used for understanding fluid-structure interaction processes.

III. Acknowledgements

My deepest gratitude goes to my supervisors Professor Konstantinos Kontis and Professor Zhaolin Fan for all the guidance and encouragement they have offered me throughout my studies. Thanks to all the things they have taught me, without which I would not be where I am today.

I would like to thank CARDC for funding this research. Special acknowledgments also go to my leaders and colleagues from the High Speed Institute of CARDC for all their help and support during my PhD.

My special thanks to my close friends and colleagues Dr. Takahiro Ukai, Dr. Hossein Zare-Behtash, Dr. Sriram Rengarajan Chitra, Dr. Kin Hing Lo, and Dr. Craig White for all their technical help and guidance. Many thanks to other PhDs in my research group, Mr. Andrew Russell, Mr. Kosuke Fujiwara, Mr. Michael Wojewodka, Miss Sarah Fitzpatrick, Miss Francesca Gnani, Mr. Thomas Andreou Mr. Shaun Skinner, Mr. Andrew Cusick, Mr. Hassam Guevara Jelid, Mr. Muhammed Burak Agir, Mr. Senthil Kumar, Mr. Fan Jiang and Mr. Ziqu Cao for helping me and being with me in the long hours I spent in the labs but more importantly for all the laughs we had.

I especially acknowledge Dr. Richard Green for providing access of the commercial PSP system from ISSI, Professor Lucas for offering the high-speed camera, Professor Antony Kelly for lending the SiPM photodetector, Professor Andrew Glidle for allowing me to use the spraying lab of the biomedical engineering division, Dr. Weizhen Li and Dr. Yingkai Lv for offering optical fibre lines.

The author would also like to thank Professor Qiang Zhou and Professor Yasuhiro Egami for their advice in the fast pressure sensitive paint development and Dr. Stryczniewicz Wit for his help and discussions in background oriented schlieren technique.

Thanks also go to all the technical and administrative staffs at the James Watt school of engineering of the University of Glasgow. I especially acknowledge the help and support of technicians Dr. Neil Owen, Dr. Alistair Macfarlane, and Dr. Thomas Dickson for their

assistance in the design and manufacturing of the rig parts and for their continuous support during the experiment.

Thank you to everyone who at some point has provided any means of support during my PhD. I am forever in all your debt. I wish you all success.

Last, but definitely not the least, I wish to express my love and gratitude to my parents, wife, and my little charming son who always encourage and support me, and believe in me no matter what I decided to do. All I have done was to make them proud.

IV. Contents

I. Author's Declaration.....	iii
II. Abstract.....	v
III. Acknowledgements	viii
IV. Contents	ix
V. List of tables.....	xiii
VI. List of figures	xv
VII. Nomenclature.....	xxvii
VIII. List of publications.....	xxxiii
Chapter 1 Introduction.....	1
1.1 Aims and objectives	5
1.2 Thesis structure	6
Chapter 2 Literature review	9
2.1 Shock waves	9
2.1.1 Fundamental theory	9
2.1.2 Shock reflection.....	13
2.1.3 Shock diffraction	15
2.1.4 Shock focusing	16
2.2 Supersonic starting jets and their impingement	16
2.2.1 Free supersonic starting jets	17
2.2.2 Supersonic starting jet impingement	19
2.3 Shock wave boundary layer interaction over flexible surfaces.....	25
2.4 Conclusions	36
Chapter 3 Experimental apparatus and methodology	39
3.1 Flow production apparatus	39

3.1.1 Shock tube.....	39
3.1.2 Supersonic wind tunnel.....	43
3.2 Flow analysis techniques	45
3.2.1 Pressure measurement.....	45
3.2.2 Schlieren and shadowgraph photography	47
3.2.3 Background oriented schlieren (BOS).....	50
3.2.4 Unsteady pressure sensitive paint (PSP).....	57
Chapter 4 Design of a novel shock tube driven by detonation transmission tubing ...	65
4.1 Overview of the experimental facility	65
4.2 Design details.....	66
4.3 Properties of the shock tube.....	71
4.3.1 Mach number range	72
4.3.2 Repeatability	76
4.3.3 Running time.....	79
4.3.4 Flow structure from the open end	82
4.4 Conclusions.....	98
Chapter 5 Development of BOS and unsteady PSP systems	99
5.1 Development of background oriented schlieren system	99
5.1.1 Background pattern.....	99
5.1.2 Image acquisition system.....	101
5.1.3 Image post-processing	102
5.1.4 Validation case of the BOS system.....	105
5.2 Development of unsteady PSP system	107
5.2.1 Paint formulation	107
5.2.2 Preparation system.....	108
5.2.3 Illumination.....	109

5.2.4	Image acquisition	110
5.2.5	Synchronization and control.....	111
5.2.6	Static calibration.....	111
5.2.7	Dynamic calibration	113
5.2.8	Validation case of unsteady PSP system.....	114
5.3	Conclusions	119
Chapter 6	Image processing techniques for shock wave detection and tracking.....	120
6.1	Image processing algorithms.....	124
6.1.1	Background subtraction.....	124
6.1.2	Image filter	134
6.1.3	Image resampling	142
6.1.4	Edge detection.....	143
6.1.5	Adaptive threshold	147
6.1.6	Contour detection and feature extraction	149
6.2	Software development for shock wave detection and tracking.....	152
6.2.1	Image processing procedure.....	153
6.2.2	Software graphical interface.....	154
6.3	Conclusions	155
Chapter 7	Impingement of a supersonic staring jet on flexible surfaces	157
7.1	Impingement of a supersonic staring jet on a solid surface	159
7.1.1	Shock reflection and distortion	159
7.1.2	Shock and vortex loop interaction.....	163
7.2	Effects of the surface thickness	166
7.3	Effects of Mach number.....	170
7.4	Conclusions	174
Chapter 8	Conclusions and future work.....	177

8.1 Conclusions.....	177
8.1.1 Design of novel shock tubes driven by detonation transmission tubing.....	177
8.1.2 Development of BOS and PSP systems.....	178
8.1.3 Software development for shock wave detection and tracking	179
8.1.4 Impingement of a supersonic staring jet on flexible surfaces.....	180
8.2 Future work and recommendations.....	181
8.2.1 Shock wave/boundary layer interaction over flexible surfaces	181
8.2.2 Enhancement of current BOS and PSP systems	183
8.2.3 Pressure loading and panel structure response measurements during supersonic staring jet impingement	183
Bibliography.....	185
Appendices	213
Appendix A Design of shock tube	215
A.1 Design of the axisymmetric shock tube.....	216
A.2 Design of the square shock tube	218
A.3 Design of the shock tube for PSP dynamic calibration	219
Appendix B Design of flexible panels in supersonic wind tunnel.....	223
Appendix C Design of Pitot rake.....	233
Appendix D Interfaces of the software for shock wave detection and tracking	235
Appendix E Program code examples of the software for shock wave detection.....	239
E.1 Background image subtraction in frequency domain.....	239
E.2 Contour detection and extraction	240

V. List of tables

Table 4.1 Shock Mach number M_s of the square shock tube in different NOENL tube lengths	74
Table 5.1 Comparison of properties between in-house developed PC-PSP and a commercial one from ISSI	119
Table 6.1 Thresholding types and operations	127
Table 7.1 Velocities of incident shock and reflected shock for different NOENL tube lengths in the case of 0.1mm thick alloy aluminium flexible surface and $D=30\text{mm}$	174

VI. List of figures

Figure 1.1 Aircraft with hybrid metal-composite construction [1]	1
Figure 2.1 Shock waves on X-15 flight vehicle [43]	10
Figure 2.2 Supersonic flow over a concave corner	10
Figure 2.3 Strong and weak shock waves	11
Figure 2.4 Oblique shock waves of a hypersonic plane featuring a scramjet propulsion system [46]	11
Figure 2.5 Schematic of a detached bow shock	12
Figure 2.6 Schematic of differences between: (a) a stationary; and (b) moving normal shock [42].....	13
Figure 2.7 Different types of shock wave reflection [57]	14
Figure 2.8 Schematic of a regular reflection wave configuration–RR [56].....	14
Figure 2.9 Schematic of a Mach reflection wave configuration–MR [56]	15
Figure 2.10 Flow feature of diffraction around a sharp wedge at (a) $M = 1.31$; (b) $M = 1.59$ [65]	15
Figure 2.11 Shock focusing due to turning of a supersonic aircraft to illustrate wave fronts, rays, caustics, and arête [66]	16
Figure 2.12 Ideally expanded (left), overexpanded (centre), and underexpanded (right) jets [42]	17
Figure 2.13 Stages of the starting jet [83]	18
Figure 2.14 Flow configuration showing the development of the Kelvin–Helmholtz vortices [83] (The vorticity magnitude is shown in a black and white colour scale).....	19
Figure 2.15 Illustration (left view) of laboratory test launch of missile with highlighted pressure sensors and qualitative illustration of the pressure-time results (right view) [87].	20
Figure 2.16 Illustration of missile launch tests from helicopter: (a)locations of pressure sensors; (b) qualitative illustration of the pressure-time results [87].....	20
Figure 2.17 Blast shock wave impact prediction on crew module for liquid rocket explosion on launch pad:(a) Rocket 3D model; (b) Pressure contours of air blast at different time after stage-3 explosion [95].....	21

Figure 2.18 Comparison between schlieren representations obtained from computations(left) and experiments (right) on blast wave interaction with a three-level building [102]	22
Figure 2.19 A schematic of one possible configuration of steady state flow for an impinging underexpanded jet, with accompanying schlieren image of the jet at impingement distance $z/d = 4$ and nozzle pressure ratio $\text{NPR} = 3.2$ [108].....	23
Figure 2.20 Acoustic phenomena from supersonic impinging jet [5]	24
Figure 2.21 Schlieren images for the case of the perforated plate at a shock Mach number of 1.61 (a) 1.45ms; (b) 1.50ms; and (c) 1.55ms [110]	25
Figure 2.22 Canonical configurations employed for fundamental studies of SBLI [111] ..	26
Figure 2.23 Schematic of the two-dimensional SBLI over deforming surface [36]	26
Figure 2.24 RC-19 modified test section, denoting flexible panel, shock generator, optical access and details of early “bonded” thin-panel arrangement [40]	27
Figure 2.25 3D DIC pattern applied across the machined panel surface and the tunnel/specimen frame. Note there are 153 facets identified in (a) across the random pattern, while (b) shows the machined panel prior to test and prepared for measurement using DIC [40]	28
Figure 2.26 Single point displacement spectral response and operational deflected shapes with SBLI ($x/L \approx 1/4$). Vertical markings on the principal axis denote the measured panel frequencies before installation into the RC-19 tunnel ($U_\infty = 490 \text{ m/s}$, $q_\infty = 123 \text{ kPa}$) [40]	28
Figure 2.27 Panel center displacement power spectra and corresponding full-field PSP images for different shock impingement conditions ($M_\infty = 2.0$, $q_\infty = 123 \text{ kPa}$) [40]	29
Figure 2.28 Sketch of the experiment on elastic panel flutter in a supersonic wind tunnel (left) and the picture of the model installed into the wind tunnel (right) [115].....	30
Figure 2.29 Experimental setup of supersonic panel flutter due to SBLI without shock impingement: (a) design of the flexible panel and clamping pieces; (b) 3D DIC and laser vibrometer setup [130].....	31
Figure 2.30 Typical experimental results of supersonic panel flutter due to SBLI without shock impingement: (a) Schlieren image; (b) comparison of power spectral density between DIC and vibrometer for 0.2 mm- thick panel clamped on all sides at $M=2.0$. Pwelch denotes the power spectral density (PSD) estimate of the input deformation signal using Welch's overlapped segment averaging estimator. [130].....	31

Figure 2.31 Sonic fatigue: (a) Geometric (hard-spring) nonlinear response typical of acoustic fatigue [131]; (b) Ceramic matrix composite panel failure (172 dB) [132], and (c) C-130 aluminium aircraft panel failure (160 dB) due only to acoustic/dynamic resonant fatigue.....	32
Figure 2.32 Experimental setup for investigating the interaction of a flexible panel with an oblique shock in the supersonic wind tunnel of Imperial College (ICL) , dimensions in mm, Width=150 mm [38]	33
Figure 2.33 Oil flow images together with detailed schematic diagrams with positions of flow features marked. The origin is indicated by the red dotted lines and lies on $x = 109$ mm with reference to Figure 2.32. [38]	34
Figure 2.34 Schematic of the model with compliant material insert shown in blue [37]	35
Figure 2.35 Comparison of top-view surface streak line images with rubber surface on top and rigid model on bottom, Mach 2.5 for compression ramp angles of (a) 16° , (b) 20° , and (c) 24° [37]	35
Figure 3.1 Shock tube experiment and wave diagram [153]	40
Figure 3.2 A low-duty-cycle diaphragmless shock tube schematic [159]	43
Figure 3.3 CAD assembly of the designed wind tunnel in University of Glasgow [164] ...	44
Figure 3.4 Optical windows of the wind tunnel [164]	44
Figure 3.5 LabVIEW program for pressure data acquisition: (a) front panel; (b) block diagram.....	46
Figure 3.6 Calibration curve of Kulite XTE-190M pressure transducer	47
Figure 3.7 Schematic of working principle of schlieren photography [168]	47
Figure 3.8 Schlieren and shadowgraph techniques applied to an airfoil flow at Mach 0.76 and 8° attack angle: (a) shadowgraph; (b) schlieren [168]	49
Figure 3.9 BOS imaging configuration [169]	50
Figure 3.10 BOS focusing position and image blur [169]	52
Figure 3.11 BOS system of AEDC 16T propulsion wind tunnel (looking downstream) [171]	53
Figure 3.12 Randomized dot pattern (top) applied to starboard wall (bottom) of NASA National Transonic Facility for capsule wake RBOS test [172]	54
Figure 3.13 3D BOS setup of ONERA's S1MA wind tunnel [173].....	54
Figure 3.14 NASA air-to-air BOS setup: (a) aircraft positioning; (b) cabin setup [174]	55

Figure 3.15 NASA air-to-air BOS system for a supersonic jet flying over the Mojave Desert: (a) natural background; (b) fly image; (c) result by cross-correlation, dy ; (d) result by optical flow, dy [174].....	55
Figure 3.16 Working principle of ground-to-air BOS system using celestial objects [181]	56
Figure 3.17 Flow structure of a supersonic jet from ground-to-air BOS system using celestial objects [181]	56
Figure 3.18 Schematic of PSP system: (a) steady PSP; (b) unsteady polymer-ceramic PSP [188].....	57
Figure 3.19 Unsteady pressure sensitive paint applied to generic launch vehicle model in the 11- by 11-foot Transonic Wind Tunnel at Ames Research Center [189, 190].....	58
Figure 3.20 Fast PSP results from AEDC 16T test showing the amplitude of the pressure fluctuations at the first two Rossiter frequencies [191]	58
Figure 3.21 Unsteady pressure-sensitive paint covers the blade tips of a helicopter being tested in a wind tunnel at NASA's Langley Research Center in Virginia [192].....	59
Figure 3.22 Map of pressure coefficients on a rocket fairing model in unsteady transonic flow: the left image shows an instant of the PSP data demonstrating the shock/boundary layer interaction and the right plots show the pressure coefficients at three locations as a function of time [198, 205].....	59
Figure 3.23 PSP with porous material as a binder: (a) schematic illustrations; (b) scanning electron micrographs [214].....	60
Figure 3.24 Typical experimental setup of shock tube for response time calibration of PSP [193].....	62
Figure 3.25 Acoustic tube for response time calibration of PSP [237]	63
Figure 4.1 Working principle of the shock tube driven by detonation transmission tubing [162].....	68
Figure 4.2 Assembly of the circular cross-section shock tube [162].....	70
Figure 4.3 Assembly of the square cross-section shock tube	71
Figure 4.4 Schematic of the experimental setup.....	72
Figure 4.5 Pressure-time history of Kulite pressure transducer in the driven section of square shock tube (Nonel tube length $L=200\text{mm}$): (a) timescale of 6ms; (b) timescale of 150ms.....	73

Figure 4.6 Shadowgraph images from the open end of the circular shock tube using different lenses (a) shadowgraph image for flow structure visualization; (b) shadowgraph image for shock Mach number calculation	75
Figure 4.7 Repeatability of pressure-time history in the driven section of square shock tube ($L = 200$ mm)	77
Figure 4.8 Repeatability of shock wave locations from the open end of the circular shock tube ($L = 300$ mm)	78
Figure 4.9 Framing shadowgraph images showing flow structure evolution from the open end of the circular shock tube at $L = 500$ mm: (a) $\Delta t=16\mu s$; (b) $\Delta t=80\mu s$; (c) $\Delta t=144\mu s$; (d) $\Delta t=208\mu s$; (e) $\Delta t=272\mu s$; (f) $\Delta t=336\mu s$; (g) $\Delta t=400\mu s$; (h) $\Delta t=464\mu s$; (i) $\Delta t=528\mu s$; (j) $\Delta t=544\mu s$; (k) $\Delta t=560\mu s$; (l) $\Delta t=576\mu s$	80
Figure 4.10 Pressure-time histories of the square shock tube for different driven section lengths (NONEL tube length $L=300$ mm)	81
Figure 4.11 Pressure-time histories of the square shock tube for NONEL tube lengths (driven section length $L_D=280$ mm)	81
Figure 4.12 Flow structure from the open end of the circular shock tube (NONEL tube length $L = 600$ mm, $\Delta t=184\mu s$)	83
Figure 4.13 Framing shadowgraph images showing flow structure evolution from the open end of the circular shock tube at NONEL tube length $L=300$ mm: (a) $\Delta t=4\mu s$; (b) $\Delta t=24\mu s$; (c) $\Delta t=44\mu s$; (d) $\Delta t=64\mu s$; (e) $\Delta t=84\mu s$; (f) $\Delta t=104\mu s$; (g) $\Delta t=124\mu s$; (h) $\Delta t=144\mu s$; (i) $\Delta t=164\mu s$; (j) $\Delta t=184\mu s$; (k) $\Delta t=204\mu s$; (l) $\Delta t=224\mu s$	85
Figure 4.14 Framing shadowgraph images showing flow structure evolution from the open end of the circular shock tube at NONEL tube length $L=400$ mm: (a) $\Delta t=4\mu s$; (b) $\Delta t=24\mu s$; (c) $\Delta t=44\mu s$; (d) $\Delta t=64\mu s$; (e) $\Delta t=84\mu s$; (f) $\Delta t=104\mu s$; (g) $\Delta t=124\mu s$; (h) $\Delta t=144\mu s$; (i) $\Delta t=164\mu s$; (j) $\Delta t=184\mu s$; (k) $\Delta t=204\mu s$; (l) $\Delta t=224\mu s$	86
Figure 4.15 Framing shadowgraph images showing flow structure evolution from the open end of the circular shock tube at NONEL tube length $L=500$ mm: (a) $\Delta t=4\mu s$; (b) $\Delta t=24\mu s$; (c) $\Delta t=44\mu s$; (d) $\Delta t=64\mu s$; (e) $\Delta t=84\mu s$; (f) $\Delta t=104\mu s$; (g) $\Delta t=124\mu s$; (h) $\Delta t=144\mu s$; (i) $\Delta t=164\mu s$; (j) $\Delta t=184\mu s$; (k) $\Delta t=204\mu s$; (l) $\Delta t=224\mu s$	87
Figure 4.16 Framing shadowgraph images showing flow structure evolution from the open end of the circular shock tube at NONEL tube length $L=600$ mm: (a) $\Delta t=4\mu s$; (b) $\Delta t=24\mu s$;	

(c) $\Delta t=44\mu s$; (d) $\Delta t=64\mu s$; (e) $\Delta t=84\mu s$; (f) $\Delta t=104\mu s$; (g) $\Delta t=124\mu s$; (h) $\Delta t=144\mu s$; (i) $\Delta t=164\mu s$; (j) $\Delta t=184\mu s$; (k) $\Delta t=204\mu s$; (l) $\Delta t=224\mu s$	88
Figure 4.17 Image intensity profiles along the axis of symmetry of the circular shock tube, NONEL tube length $L=300$ mm, $\Delta t=136\mu s$	89
Figure 4.18 Intensity profiles along the axis of symmetry of the circular shock tube at NONEL tube length $L=600$ mm: (a) $\Delta t=136\mu s$; (b) $\Delta t=184\mu s$	89
Figure 4.19 Framing shadowgraph images showing flow structure evolution from the open end of the square shock tube at $L=200$ mm: (a) $\Delta t=34\mu s$; (b) $\Delta t=48\mu s$; (c) $\Delta t=62\mu s$; (d) $\Delta t=76\mu s$; (e) $\Delta t=90\mu s$; (f) $\Delta t=104\mu s$; (g) $\Delta t=118\mu s$; (h) $\Delta t=132\mu s$; (i) $\Delta t=146\mu s$; (j) $\Delta t=160\mu s$; (k) $\Delta t=174\mu s$; (l) $\Delta t=188\mu s$	93
Figure 4.20 Framing shadowgraph images showing flow structure evolution from the open end of the square shock tube at $L=300$ mm: (a) $\Delta t=4\mu s$; (b) $\Delta t=48\mu s$; (c) $\Delta t=62\mu s$; (d) $\Delta t=76\mu s$; (e) $\Delta t=90\mu s$; (f) $\Delta t=104\mu s$; (g) $\Delta t=118\mu s$; (h) $\Delta t=132\mu s$; (i) $\Delta t=146\mu s$; (j) $\Delta t=160\mu s$; (k) $\Delta t=174\mu s$; (l) $\Delta t=188\mu s$	94
Figure 4.21 Framing schlieren images showing motion of the vortex loop from the open end of the square shock tube at $L=300$ mm: (a) $\Delta t=24\mu s$; (b) $\Delta t=40\mu s$; (c) $\Delta t=56\mu s$; (d) $\Delta t=72\mu s$; (e) $\Delta t=88\mu s$; (f) $\Delta t=104\mu s$; (g) $\Delta t=120\mu s$; (h) $\Delta t=136\mu s$; (i) $\Delta t=152\mu s$; (j) $\Delta t=168\mu s$; (k) $\Delta t=184\mu s$; (l) $\Delta t=200\mu s$	95
Figure 4.22 Framing shadowgraph images showing flow structure evolution from the open end of the square shock tube at $L=400$ mm: (a) $\Delta t=4\mu s$; (b) $\Delta t=48\mu s$; (c) $\Delta t=62\mu s$; (d) $\Delta t=76\mu s$; (e) $\Delta t=90\mu s$; (f) $\Delta t=104\mu s$; (g) $\Delta t=118\mu s$; (h) $\Delta t=132\mu s$; (i) $\Delta t=146\mu s$; (j) $\Delta t=160\mu s$; (k) $\Delta t=174\mu s$; (l) $\Delta t=188\mu s$	96
Figure 4.23 Framing shadowgraph images showing flow structure evolution from the open end of the square shock tube at $L=500$ mm: (a) $\Delta t=76\mu s$; (b) $\Delta t=90\mu s$; (c) $\Delta t=104\mu s$; (d) $\Delta t=118\mu s$; (e) $\Delta t=132\mu s$; (f) $\Delta t=146\mu s$; (g) $\Delta t=160\mu s$; (h) $\Delta t=174\mu s$; (i) $\Delta t=188\mu s$; (j) $\Delta t=202\mu s$; (k) $\Delta t=216\mu s$; (l) $\Delta t=230\mu s$	97
Figure 5.1 Graphic interface for generating BOS random dot background pattern	100
Figure 5.2 PIVlab software for BOS image post-processing	102
Figure 5.3 Overview of the workflow and the implemented features of PIVlab [290]....	104
Figure 5.4 Schematic of BOS experimental setup in the indraft supersonic wind tunnel of University of Glasgow	105

Figure 5.5 BOS results of the pitot tube test in the case of free stream Mach number $M=2.0$: (a) raw BOS image; (b) displacement distribution in pixels; (c) horizontal displacement in pixels; (d) vertical displacement in pixels	106
Figure 5.6 Flow structure obtained from BOS displacement distribution	107
Figure 5.7 PSP static calibration system in University of Glasgow [165]	112
Figure 5.8 Schematic of dynamic calibration setup for unsteady PSP	114
Figure 5.9 Stern-Volmer plot of in-house developed PC-PSP.....	115
Figure 5.10 Interface for curve fitting of Stern-Volmer equation.....	115
Figure 5.11 Stern–Volmer curves of PtTFPP-based PC-PSP in different temperatures....	116
Figure 5.12 Temperature sensitivity of in-house developed PC-PSP	117
Figure 5.13 Photo-degradation rate of in-house developed PC-PSP	118
Figure 6.1 A shock wave detection method by combining Canny’s edge detection and Rankine-Hugoniot relations for CFD simulation of a hypersonic flow over blunt body: (a) mesh; (b) pressure distribution; (c) schematic drawing; (d) detection result [326]	122
Figure 6.2 Software development for pattern recognition in high speed schlieren visualization at the high enthalpy shock tunnel Göttingen: (a) original image; (b) gradient image with detected circle as cylinder shape; (c) partial shock wave fitting; (d) stagnation point line intersecting circle centre and shock shape [331]	123
Figure 6.3 Shock detection for a three-dimensional waverider installed in AEDC Tunnel 9 with a nominal free stream Mach number of 8: (a) original schlieren image; (b) shock contour extracted after applying a bilateral filter [320, 334]	124
Figure 6.4 Background image subtraction in frequency domain for a shadowgraph image of the jet flow from a circular shock tube: (a) background image; (b) test image; (c) background image in frequency domain; (d) test image in frequency domain; (e) background subtracted image in frequency domain; (f) background subtracted image in spatial domain	125
Figure 6.5 Restore the test model and the region out of measurement by global thresholding operation for a shadowgraph image from the open end of a circular shock tube: (a) background image; (b) test image; (c) background subtracted image; (d) extraction of the test model and the region out of measurement by global thresholding operation (thresholding type: Threshold Binary, threshold value: thresh=93); (e)	

background subtracted image after restoration of the test model and the region out of measurement; (f) pseudo colour image of frame (e)	128
Figure 6.6 Restore the test model and the region out of measurement by global thresholding operation for a shadowgraph image from the open end of a square shock tube: (a) background image; (b) test image; (c) background subtracted image; (d) extraction of the test model and the region out of measurement by global thresholding operation (thresholding type: Threshold Binary, threshold value: thresh=54); (e) background subtracted image after restoration of the test model and the region out of measurement; (f) pseudo colour image of image (e)	129
Figure 6.7 Image segmentation for separating the test model and the region out of measurement from the shadowgraph images through Otsu automatic thresholding algorithm.....	132
Figure 6.8 Schematic of triangle thresholding algorithm [337]	133
Figure 6.9 Image segmentation for separating the test model and the region out of measurement from shadowgraph images through Triangle automatic thresholding algorithm.....	134
Figure 6.10 Mean filter: (a) original shadowgraph image after background subtraction; (b) image after 3×3 mean filter; (c) image after 5×5 mean filter; (d) image after 7×7 mean filter.....	136
Figure 6.11 Gaussian filter: (a) original shadowgraph image after background subtraction; (b) image after 3×3 Gaussian filter; (c) image after 5×5 Gaussian filter; (d) image after 7×7 Gaussian filter	137
Figure 6.12 Median filter: (a) original shadowgraph image after background subtraction; (b) image after 3×3 Median filter; (c) image after 5×5 Median filter; (d) image after 7×7 Median filter	138
Figure 6.13 Bilateral filter: (a) original shadowgraph image after background subtraction; (b) image after 3×3 bilateral filter; (c) image after 5×5 bilateral filter; (d) image after 3×3 median filter and 3×3 bilateral filter	139
Figure 6.14 Sobel filter: (a) original shadowgraph image after background subtraction; (b)image after Sobel filter in x direction; (c) image after Sobel filter in y direction; (d) image after 3×3 median filter and Sobel filter in y direction.....	141

Figure 6.15 Laplacian filter: (a) original shadowgraph image after background subtraction; (b)image after Laplacian filter; (c) image after 3×3 Gaussian filter and Laplacian filter..	142
Figure 6.16 Image resampling: (a) original shadowgraph image with a 312×260 -pixel resolution; (b) image after 3×3 median filter and 3×3 Gaussian filter; (c) shadowgraph image after upsampling (624×520 -pixel resolution) followed by 3×3 median filter and 3×3 Gaussian filter	143
Figure 6.17 Schematic of hysteresis thresholding.....	146
Figure 6.18 Edge detection through modified Canny algorithm: (a) original shadowgraph image; (b) edge detection result	147
Figure 6.19 Edge detection through adaptive threshold algorithm: (a) original shadowgraph image; (b) adaptive threshold image; (c) edge detection result	148
Figure 6.20 Contour detection through different algorithms: (a) original shadowgraph image; (b) contour detection by modified Canny edge detection; (c) contour detection by adaptive threshold; (d) contour detection by performing adaptive threshold and modified Canny edge detection in sequence	150
Figure 6.21 shock wave extraction and fitting: (a) shock wave extraction from the contour image; (b) shock wave fitting.....	151
Figure 6.22 Software main interface.....	155
Figure 7.1 Schematic of the flexible surface design and experimental setup	158
Figure 7.2 Shock reflection at $M_s \sim 1.28$, NONEL tube length $L=200\text{mm}$, the distance between shock tube end and solid plate $D=55\text{mm}$: (a) $\Delta t=0$; (b) $\Delta t=4\mu\text{s}$; (c) $\Delta t=8\mu\text{s}$	160
Figure 7.3 Shock reflection at $M_s \sim 1.37$, NONEL tube length $L=300\text{mm}$, the distance between shock tube end and solid plate $D=55\text{mm}$: (a) $\Delta t=0$; (b) $\Delta t=4\mu\text{s}$; (c) $\Delta t=8\mu\text{s}$	160
Figure 7.4 Shock reflection at $M_s \sim 1.46$, NONEL tube length $L=400\text{mm}$, the distance between shock tube end and solid plate $D=55\text{mm}$: (a) $\Delta t=0$; (b) $\Delta t=4\mu\text{s}$; (c) $\Delta t=8\mu\text{s}$	160
Figure 7.5 Shock reflection at $M_s \sim 1.53$, NONEL tube length $L=500\text{mm}$, the distance between shock tube end and solid plate $D=55\text{mm}$: (a) $\Delta t=0$; (b) $\Delta t=4\mu\text{s}$; (c) $\Delta t=8\mu\text{s}$	161
Figure 7.6 Trace line for calculating reflected shock velocity.....	162
Figure 7.7 Time evolution of reflected shock wave at $M_s \sim 1.53$, NONEL tube length $L=500\text{mm}$, the distance between shock tube end and solid plate $D=30\text{mm}$	162
Figure 7.8 Distortion of the reflected shock wave at $M_s \sim 1.53$, NONEL tube length $L=500\text{mm}$, $\Delta t=8\mu\text{s}$ and the distance between shock tube end and solid plate $D=55\text{mm}$...163	

Figure 7.9 Framing shadowgraph images demonstrating reflected shock and vortex loop interaction at $M_s \sim 1.37$, NONEL tube length $L=300\text{mm}$, the distance between shock tube end and solid plate $D=55\text{mm}$: (a) $\Delta t=0$; (b) $\Delta t=58\mu\text{s}$; (c) $\Delta t=72\mu\text{s}$; (d) $\Delta t=86\mu\text{s}$; (e) $\Delta t=100\mu\text{s}$; (f) $\Delta t=114\mu\text{s}$; (g) $\Delta t=120\mu\text{s}$; (h) $\Delta t=128\mu\text{s}$; (i) $\Delta t=142\mu\text{s}$; (j) $\Delta t=156\mu\text{s}$; (k) $\Delta t=170\mu\text{s}$; (l) $\Delta t=184\mu\text{s}$	165
Figure 7.10 Shock reflection on a 0.1mm-thick alloy aluminium surface in the case of $M_s \sim 1.37$, NONEL tube length $L=300\text{mm}$, the distance between shock tube end and solid plate $D=55\text{mm}$: (a) $\Delta t=0$; (b) $\Delta t=2\mu\text{s}$; (c) $\Delta t=4\mu\text{s}$; (d) $\Delta t=6\mu\text{s}$; (e) $\Delta t=8\mu\text{s}$; (f) $\Delta t=10\mu\text{s}$; (g) $\Delta t=12\mu\text{s}$; (h) $\Delta t=14\mu\text{s}$; (i) $\Delta t=16\mu\text{s}$; (j) $\Delta t=18\mu\text{s}$; (k) $\Delta t=20\mu\text{s}$; (l) $\Delta t=22\mu\text{s}$	166
Figure 7.11 Shock reflection on a 0.3mm-thick alloy aluminium surface in the case of $M_s \sim 1.37$, NONEL tube length $L=300\text{mm}$, the distance between shock tube end and solid plate $D=55\text{mm}$: (a) $\Delta t=0$; (b) $\Delta t=2\mu\text{s}$; (c) $\Delta t=4\mu\text{s}$; (d) $\Delta t=6\mu\text{s}$; (e) $\Delta t=8\mu\text{s}$; (f) $\Delta t=10\mu\text{s}$; (g) $\Delta t=12\mu\text{s}$; (h) $\Delta t=14\mu\text{s}$; (i) $\Delta t=16\mu\text{s}$; (j) $\Delta t=18\mu\text{s}$; (k) $\Delta t=20\mu\text{s}$; (l) $\Delta t=22\mu\text{s}$	167
Figure 7.12 Comparison of time evolution between of the reflected shock wave locations between the solid plate and 0.1mm thick flexible surface at $M_s \sim 1.53$, NONEL tube length $L=500\text{mm}$ and the distance between shock tube end and surfaces $D=30\text{mm}$	169
Figure 7.13 Shock detection and fit for calculating reflected shock velocity in the case of $M_s \sim 1.27$, NONEL tube length $L=200\text{mm}$ and distance between shock tube end and the surface $D=30\text{mm}$: (a) original shadowgraph image; (b) shock contour detection and extraction; (c) shock contour fitting	170
Figure 7.14 Shock reflection on a 0.3mm-thick alloy aluminium surface in the case of $M_s \sim 1.27$, NONEL tube length $L=200\text{mm}$, the distance between shock tube end and the surface $D=55\text{mm}$: (a) $\Delta t=0$; (b) $\Delta t=2\mu\text{s}$; (c) $\Delta t=4\mu\text{s}$; (d) $\Delta t=6\mu\text{s}$; (e) $\Delta t=8\mu\text{s}$; (f) $\Delta t=10\mu\text{s}$; (g) $\Delta t=12\mu\text{s}$; (h) $\Delta t=14\mu\text{s}$; (i) $\Delta t=16\mu\text{s}$; (j) $\Delta t=18\mu\text{s}$; (k) $\Delta t=20\mu\text{s}$; (l) $\Delta t=22\mu\text{s}$	171
Figure 7.15 Shock reflection on a 0.3mm-thick alloy aluminium surface in the case of $M_s \sim 1.46$, NONEL tube length $L=400\text{mm}$, the distance between shock tube end and the surface $D=55\text{mm}$: (a) $\Delta t=0$; (b) $\Delta t=2\mu\text{s}$; (c) $\Delta t=4\mu\text{s}$; (d) $\Delta t=6\mu\text{s}$; (e) $\Delta t=8\mu\text{s}$; (f) $\Delta t=10\mu\text{s}$; (g) $\Delta t=12\mu\text{s}$; (h) $\Delta t=14\mu\text{s}$; (i) $\Delta t=16\mu\text{s}$; (j) $\Delta t=18\mu\text{s}$; (k) $\Delta t=20\mu\text{s}$; (l) $\Delta t=22\mu\text{s}$	172
Figure 7.16 Shock reflection on a 0.3mm-thick alloy aluminium surface in the case of $M_s \sim 1.53$, NONEL tube length $L=500\text{mm}$, the distance between shock tube end and the surface $D=55\text{mm}$: (a) $\Delta t=0$; (b) $\Delta t=2\mu\text{s}$; (c) $\Delta t=4\mu\text{s}$; (d) $\Delta t=6\mu\text{s}$; (e) $\Delta t=8\mu\text{s}$; (f) $\Delta t=10\mu\text{s}$; (g) $\Delta t=12\mu\text{s}$; (h) $\Delta t=14\mu\text{s}$; (i) $\Delta t=16\mu\text{s}$; (j) $\Delta t=18\mu\text{s}$; (k) $\Delta t=20\mu\text{s}$; (l) $\Delta t=22\mu\text{s}$	173

Figure 8.1 Schematic of wind tunnel test setup for oblique shock and boundary layer interaction over a flexible surface	182
Figure 8.2 Support unit for flexible panels	182
Figure A.1 Design and dimensions of the driven section of the axisymmetric shock tube	216
Figure A.2 Design and dimensions of NONEL tube holder of the axisymmetric shock tube	217
Figure A.3 Design and dimensions of NONEL tube holder of the square shock tube	218
Figure A.4 Design and dimensions of the driven section of the square shock tube	218
Figure A.5 Assembly of the square shock tube for PSP dynamic calibration. (The red part is the NONEL tube holder, the blue part is the driven section with two optical windows on its two sides and the orange part at the end of the driven section was designed for mounting Kulite pressure transducer).	219
Figure A.6 Design and dimensions of the driven section of the shock tube for PSP dynamic calibration.....	220
Figure A.7 Design and dimensions of shock tube end for mounting Kulite pressure transducer	221
Figure B.1 Assembly of flexible panel support unit in the supersonic wind tunnel (The red part is the bottom support connecting with wind tunnel, the yellow part is the flexible panel support, the small grey part underneath the bottom support is a connector to adjust the height of the flexible panel, the green part with a step is the upstream connector and the right rosybrown part is the downstream connector).....	224
Figure B.2 Design and dimensions of the bottom support.....	225
Figure B.3 Design and dimensions of the flexible panel support	226
Figure B.4 Design and dimensions of the connector for flexible panel support and bottom support.....	227
Figure B.5 Design and dimensions of the downstream connector.....	228
Figure B.6 Design and dimensions of the upstream connector.....	229
Figure B.7 Design and dimensions of the solid panel.....	230
Figure B.8 Design and dimensions of the shock wave generator	231
Figure C.1 Geometry of the Pitot rake (all dimensions in mm).....	233

Figure C.2 Schematic of Pitot rake installation in the supersonic wind tunnel with pressure taps locations.	234
Figure D.1 The graphical interface for image filter setting	236
Figure D.2 The graphical interface for background image subtraction	236
Figure D.3 The graphical interface for restoring the test model and the region out of measurement	237
Figure D.4 The graphical interface for edge detection	237

VII. Nomenclature

Latin symbols

a	The speed of sound [m/s]
d	Diameter [mm]
E	Optical thickness [mm]
f	Focal length of the lens [mm]
G	Image gradient
h	Height [mm]
I	Irradiance
K	Filter kernel
L	Length [mm]
L_D	Length of the driven section [mm]
L_h	Length of the tuber holder [mm]
M	Mach number
M_s	Shock wave Mach number
n	Refractive index
P	Pressure [P_a]
T	Temperature [o], threshold value
T_H	High threshold value
T_L	Low threshold value
t	Time [s]
u	Velocity [m/s]
WA	Weighted average value
w	Class probabilities

Greek symbols

β	Oblique shock wave angle [$^{\circ}$]
γ	Gas specific heat capacity ratio
ε	Deflection angle [$^{\circ}$]
θ	Turning angle [$^{\circ}$]
μ	Class mean
ρ	Gas density [kg/m^3]

Subscripts

1	Pre-shock conditions
2	Post-shock conditions
d	Driven section
H	High
h	Tube holder
L	Low
m	Mean
max	Maximum value
min	Minimum value
ref	Reference condition
s	Shock wave
x	x axis direction
y	y axis direction

Acronyms

SBLI	Shock wave boundary layer interaction
PSP	Pressure sensitive paint
TSP	Temperature sensitive paint
DIC	Digital image correlation
BOS	Background oriented schlieren
PIV	Particle image velocimetry
LDA	Laser doppler vibrometer
SPL	Sound pressure level
OASPL	Overall sound pressure level
RR	Regular reflection
IR	Irregular reflection
MR	Mach reflection
vNR	Von Neumann reflection
VTOL	Vertical take-off and landing
STOL	Short take-off and landing
CFD	Computational fluid dynamics
FSI	Fluid and structure interaction
LCO	Limit cycle oscillation
DLR	German aerospace center
AFRL	Air force research laboratory
HSCT	High speed civil transport
RLV	Reusable launch vehicle
HTT	High temperature tunnel
JSF	Joint strike fighter

OML	Outer mold line
UCAV	Unmanned combat aerial vehicle
TPS	Thermal protection system
SSTO	Single stage to orbit vehicle
CAD	Computer-aided design
NI	National instruments
LabVIEW	Laboratory instrument engineering workbench
TDM	Technical data management
TDMS	Technical data management system
NASA	National aeronautics and space administration
TLC	Thin-layer chromatography
AA-PSP	Anodised aluminium pressure sensitive paint
PC-PSP	Polymer-ceramic pressure sensitive paint
PMT	Photomultiplier tube
NONEL	Non-electric
ID	Inner diameter
OD	Outer diameter
ROI	Region of interest
CLAHE	Contrast limited adaptive histogram equalization
DCC	Direct cross-correlation
DFT	Discrete Fourier transformation
FFT	Fast Fourier transformation
RTV	Room temperature vulcanizing silicon rubber
ISSI	Innovative scientific solutions incorporation
LED	Light-emitting diodes

CCD	Charge-coupled device
TTL	Transistor-transistor logic
PSG	Pulse sequence generator
AEDC	Arnold engineering development center
SAIL	Stanford artificial intelligence laboratory
SNR	Signal-noise ratio

VIII. List of publications

Journal Papers:

1. G. Li, M. Burak Agir, K. Kontis, T. Ukai, and S. Rengarajan, "Image Processing Techniques for Shock Wave Detection and Tracking in High Speed Schlieren and Shadowgraph Systems," *Journal of Physics: Conference Series*, vol. 1215, p. 012021, 2019.
2. G. Li, T. Ukai, and K. Kontis, "Characterization of a novel open-ended shock tube facility based on detonation transmission tubing," *Aerospace Science and Technology*, vol. 94, p. 105388, 2019.
3. G. Li, T. Ukai, K. Kontis, and Zhaolin Fan, " Experimental Investigation of Supersonic Starting Jet Impingement on Flexible Surfaces", *Experimental Thermal and Fluid Science*, 2020. (submitted)
4. G. Li, K. Kontis, and Zhaolin Fan, "Automatic Shock Detection, Extraction and Fitting in High Speed Schlieren and Shadowgraph Visualization", *AIAA Journal*, 2020. (accepted)

Conference Papers:

1. G. Li, K. Kontis, M. B. Agir. Software Development for Shock Wave Detection and Tracking in High Speed Schlieren System. *The 1st International Symposium on Advances in Aerodynamics*, 2018.
2. G. Li, J. Wu, K. Kontis, S. Wit, Z. Fan. Development of Unsteady Background-oriented Schlieren System in an Indraft Supersonic Wind Tunnel. *The 4th International Conference on Aeronautical, Aerospace and Mechanical Engineering*, 2021. (submitted)

Chapter 1

Introduction

Light-weight composite materials have increasingly used for high-speed flight vehicles for improving their performance and efficiency. At supersonic speed, sonic fatigue, panel flutter, severe instabilities, and even catastrophic structural failure would occur due to the shock wave impingement on several flexible components of a given structural system either internally or externally. Therefore, fluid and structure interaction (FSI) is crucial for the safety and performance of high-speed flight vehicles.

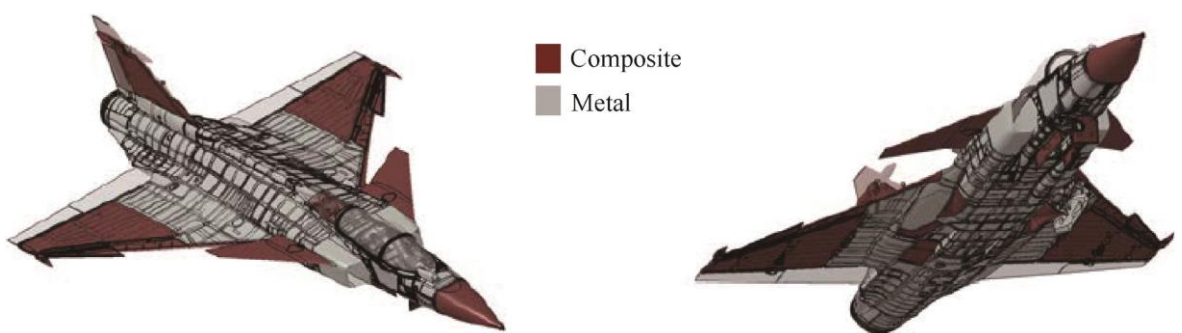


Figure 1.1 Aircraft with hybrid metal-composite construction [1]

The first part of this research involves the shock wave generated by supersonic starting jets

interaction with flexible surfaces. The initial shock wave generated by the supersonic starting jet during the rocket or missile launching induces high pressure loading on the surroundings, just like a sonic boom from a supersonic cruising flight. The turbulent continuous or starting jet impingement on plates produces significant pressure fluctuations, which in turn can cause vibration or flutter of the plates. A lot of experimental and computational studies regarding supersonic continuous and starting jet interaction with a variety of surfaces such as the rigid perpendicular plate, inclined plate, and perforated surface have been performed last decades. Despite the simplest geometry, it still is challengeable, particularly for developing turbulence models, to simulate the flow structure of supersonic jet impingement on a perpendicular solid plate [2]. The supersonic impinging jet is a highly resonant flow field that is governed by a well-known aeroacoustics feedback loop [3-5]. Instability waves in the jet shear layer are initiated by this feedback loop that develops into large-scale vortices when they propagate downstream [6-8]. Due to the influence of the large-scale vortices on the rigid plate, pressure fluctuations and acoustic waves are generated, propagating upstream [9-12]. These upstream propagated waves arrive at the nozzle exit and produce the instability waves, closing the feedback loop [13, 14]. Non-vertical supersonic jet impingement with different nozzle-to-plate distances and different impingement angles has been previously investigated both numerically [15-19] and experimentally [20, 21]. Solving the three-dimensional Navier–Stokes equations based on a modified weighted compact nonlinear scheme, Nonomura et al. [22] investigated the influences of nozzle-to-plate distance and jet temperature on the acoustic field of ideally expanded supersonic jet impingement on an inclined plate. Analyzing results of the octave-banded sound pressure level (SPL) and overall sound pressure level (OASPL) in the symmetry plane, Nonomura et al. [22] studied at least three types of possible noise sources: (i) Mach wave radiation associated with supersonically convected large-scale turbulent flow structures (similar to free jets), (ii) acoustic waves produced in the impingement area and (iii) Mach waves produced in the shear layer of the supersonic wall jet downstream of the impingement area. They also proposed that the investigation of the second mechanism of noise generation is crucial because conventional empirical methods [23, 24] for estimating rocket-plume acoustics do not take these waves into account. Skews [25] has examined the shock wave and perforated plate interaction experimentally at different conditions of shock wave strength, incidence angle and blockage ratio, concluding that the secondary waves induced by the reflections from the medium

Chapter 1 Introduction

internal surfaces make the shock wave releasing from the back edge of the perforated plates stronger. Torrens and Wrobel [26] provided a model for the situation that shock waves transmit from the porous plate edge into the surrounding medium based on the other model by Levy et al. [27]. The initial model proposed by Levy et al. described the shock wave and solid porous foam interaction in the case of placing a perforated medium at the back edge of a shock tube [27]. However, few results have been obtained for supersonic continuous and starting jet interaction with flexible surfaces. One of the major objectives of this research is to investigate the flow structure and interaction mechanism of supersonic starting jet impingement on flexible surfaces based on a miniature and cost-effective shock tube.

The other important occasion for fluid-structure interaction in modern high-speed aircraft design is shock wave boundary layer interaction (SBLI) over flexible surfaces. At supersonic speed, we can expect a number of shock wave impingements on several flexible components of a given structural system either internally or externally. Thereafter, the deformation of the flexible panels causes shock movement except for the natural unsteadiness of the impinged shock. The shock wave impingement location movement in turn results in the flexible panels to further deform which once again moves the shock. This loop of shock wave movements and subsequent deformations results in shock oscillations over flexible surfaces. SBLI with an impinging shock wave or just the presence of a supersonic flow can trigger self-exciting vibrations of flexible skin panels of the high-speed flight vehicles. Such panel flutter consisting of the periodic deformation of a flexible panel generally has high amplitude and can induce fatigue damage of the skin panels. Furthermore, for supersonic civilian and military aircrafts, sonic fatigue has long been a crucial issue remaining to be solved. Also, it has been long known that the fluid-structure interactions in helicopters can result in safety concerns, degradation of structural integrity, aerodynamic, and flight handling [28]. Often shock waves over the airfoil can terminate the supersonic flows. Under specific flow conditions, self-sustained shock oscillations known as buffeting occur due to the shock wave interaction with the boundary layer and downstream separation flow over the airfoil [29]. Furthermore, the aeroelastic instabilities combined with the dynamic SBLI also occur in the transonic flight. The dynamic response of a flexible panel under an oblique shock impingement has been studied by S. Spottswood et al. [30]. For the first time ever, the full-field dynamic displacement response of flexible panels was measured by the high-speed

digital image correlation (DIC) technique. The dynamic shock wave and flexible surface interaction with the presence of the boundary layer in turn might trigger an aeroelastic flutter or limit cycle oscillation (LCO) [31-33]. More recent works also demonstrated that such behaviour is also observed with a forced prescribed motion, when the frequency of the prescribed motions is close to shock-buffet frequency and amplitude is greater than a threshold value [34] and the nature of the incoming boundary layer has no impact on the nature of the limit cycle oscillation, as observed by Hartmann et al. [35].

However, on the other hand, extensive recent studies have suggested that at specific conditions, flexible panels show potentials to be used as a passive flow control method to provide positive effects.

Brouwer et al. [36] studied the impact of panel deformation on SBLI in supersonic flows to reduce the separation size caused by the steady and unsteady deformations. Although the study was not intended with a flow control objective, the authors did demonstrate considerable modification on the separation size from a deformed plate compared to a rigid flat plate. A similar finding was also obtained by Pham et al. [37] by employing a flexible material instead of the solid panel. More recently, Tan et al. [38] conducted experiments to study the influence of curvature and shock impingement location on the separation size. Visbal [39] numerically examined the oblique shock and flexible panel interaction process. In the presence of flow separation, aeroelastic oscillations of the flexible panel were proven to decrease the separation length compared to the rigid surface.

To investigate the fluid-structure interaction mechanism of SBLI over flexible surfaces experimentally, a variety of advanced full-field flow diagnostic techniques such as three-dimensional digital image correlation (3D DIC) for deformation measurement, particle image velocimetry (PIV) for spatial velocity, pressure-sensitive paint (PSP) for surface pressure, temperature-sensitive paint (TSP) for surface temperature and oil flow for streaklines are needed. Recently, with the increased interest in validating numerical simulations, experimental results are required for both the structure and the flow. Great efforts have been done in these directions recently by Spottsworth et al. [40], who measured thin panel response to SBLI using 3D DIC, laser Doppler vibrometer, and pressure sensitive paint. For similar applications, optical measurement techniques have also been used by Jinks

et al. [41] where PIV and schlieren were applied for studying the flow structure under the thin panel movement. In this work, a time-resolved background oriented schlieren (BOS) system and a sprayable Polymer-Ceramic PSP system were developed preliminarily. Based on these advanced measurement techniques, the influence of the strength, location of the impinging shock and the aspect ratio, thickness, clamping conditions of the flexible panel on flow properties such as the unsteady pressure loading, the static pressure recovery and the separation region size can be investigated systematically.

1.1 Aims and objectives

The main objectives of this research are:

- Design a miniature and cost-effective shock tube to simulate the supersonic starting jet and investigate the interaction of the supersonic starting jet with flexible surfaces.
- Identify the flow structure and behaviours of the transmitting shock wave from the supersonic starting jet during the process of shock impingement on flexible surfaces.
- Examine the influence of the strength, location of the impingement shock and the aspect ratio, thickness, clamping conditions of the flexible panel on flow properties such as unsteady pressure loading, static pressure recovery, and size of the separation region systematically.
- Visualise the flow field associated supersonic starting jet impingement and SBLI over flexible surfaces using a time-resolved conventional schlieren system or background oriented schlieren (BOS) system.
- Develop an image processing software based on advanced computer vision techniques for automatic shock wave detection, tracking, and feature extraction to identify the shock movement, distortion, and unsteadiness.
- Establish a sprayable Polymer-Ceramic PSP system to quantify the full-field, unsteady surface pressure loading caused by supersonic starting jet impingement and SBLI over flexible surfaces.

1.2 Thesis structure

The thesis is divided into the following sections:

Chapter 2 presents the topic of shock waves from the fundamentals of compressible flow and studies conducted on unsteady shock wave impingements, oblique shock, and their interactions with surfaces.

Chapter 3 provides a description of the experimental techniques and apparatus used in the current investigation.

Chapter 4 proposes and demonstrates a novel concept to design the shock tube using a type of commercially available and cost-effective detonation transmission tubing. More specifically, two different shock tubes with a circular and square cross-section respectively were manufactured to simulate different engineering applications. Overpressure measurement in the driven section of the shock tubes was performed using a dynamic Kulite pressure transducer and time-resolved shadowgraph tests were conducted to study the properties and capabilities of the shock tubes.

Chapter 5 provides the basic description of the setup and image processing tools of the in-house developed BOS and PSP systems.

Chapter 6 includes details of the software developed for shock wave detection and tracking in the time-resolved schlieren and shadowgraph techniques. The primary process involves background image subtraction, object area restoration, enhancement, adaptive threshold, contour detection, and feature extraction. To validate the image processing algorithms proposed, an experiment associated with shock wave impinging on a solid surface was conducted.

Chapter 7 discusses the mechanism of the interaction between the initial shock wave from a supersonic starting jet and flexible surfaces. The square shock tube driven by the detonation transmitting tube proposed in Chapter 4 was used to simulate the supersonic starting jet, and the software in Chapter 6 was adopted to detect, extract and fit shock waves visualized in a

Chapter 1 Introduction

high-speed shadowgraph system.

Chapter 2

Literature review

This chapter introduces the topic of shock waves from the fundamentals of compressible flow and presents a review of analytical, experimental, and numerical investigations conducted on shock waves, unsteady shock wave impingements, oblique shocks, and their interactions with various surfaces.

2.1 Shock waves

2.1.1 Fundamental theory

As shown in Figure 2.1, when an object travels at supersonic speed, the flow is unaware of the presence of the fast-moving object ahead of time and can only negotiate its presence by compressing. Therefore, shock waves essentially are a discontinuity that forms in order for the flow to meet some downstream conditions [42-45]. The propagation speed of shock waves is higher than the local speed of sound in the medium. The general types of shock waves and their corresponding properties are briefly introduced as follows:

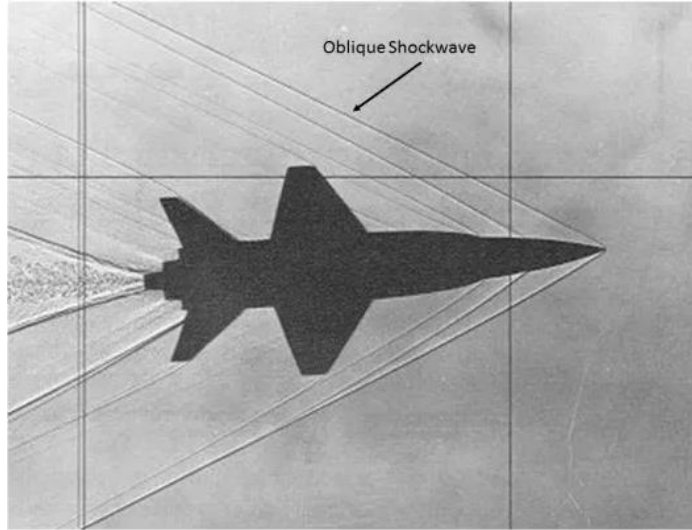


Figure 2.1 Shock waves on X-15 flight vehicle [43]

Oblique shock

The shock wave which is still attached to the body and deviates at some arbitrary angle from the flow direction is termed oblique shock. Figure 2.2 illustrates the supersonic flow over a concave corner. The supersonic flow at M_1 reaches an upturned corner which has a turning angle θ . There will be a sudden compressive process and a large pressure gradient as the supersonic flow approaches the corner. An oblique shock wave forms by the compressive process, emerging from the apex of the concave corner. The oblique shock wave angle is β and the downstream Mach number changes to M_2 .

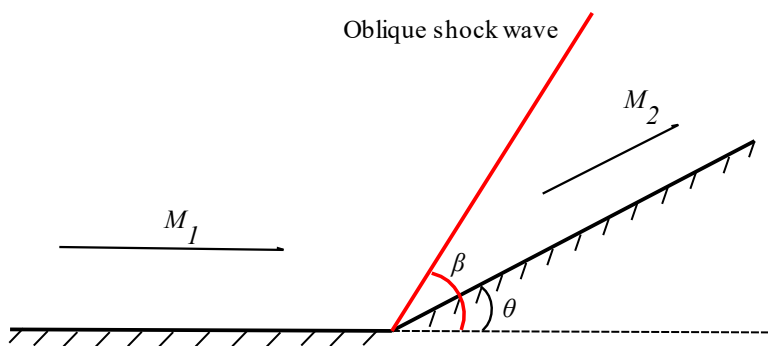


Figure 2.2 Supersonic flow over a concave corner

It is worth noting that, for a specific upstream Mach number M_1 and deflection angle θ , there

are two possible downstream flow conditions, one produced by a weak shock and the other by a strong shock (Figure 2.3). The wave angle β and the entropy increase is lower in the case of weak shock waves. In the weak shock case, the downstream Mach number is supersonic, whereas the downstream Mach number is subsonic in the strong shock case. Whether the weak or strong shock solution occurs is determined by the downstream pressure. If the downstream pressure is forced to increase (by mechanical means or a blockage), a strong shock occurs.

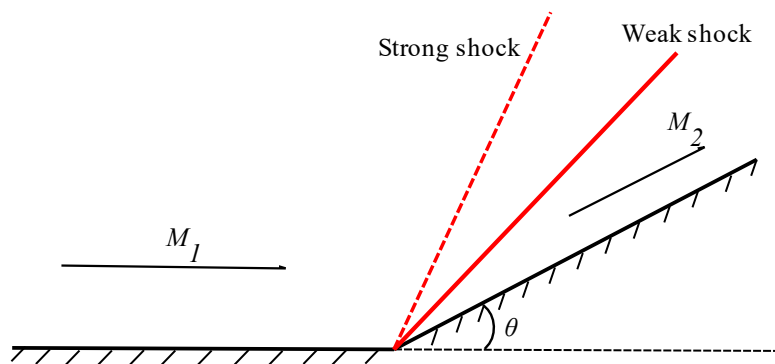


Figure 2.3 Strong and weak shock waves

The oblique shock wave is a common aerodynamic phenomenon in supersonic flow, and if controlled effectively, a number of potential applications can be achieved [47-52], such as weakening wave drag and sonic boom of the supersonic vehicle, optimizing shock waves of the supersonic inlet in off-design conditions, reducing pressure loss, controlling shock waves of the wave rider, changing shock wave symmetry to achieve flight control and inducing shock waves in the aero-engine nozzle to achieve thrust vector control.

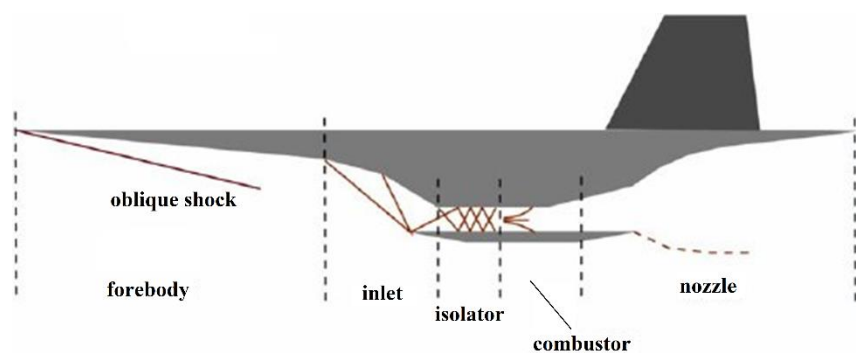


Figure 2.4 Oblique shock waves of a hypersonic plane featuring a scramjet propulsion system [46]

Bow shock

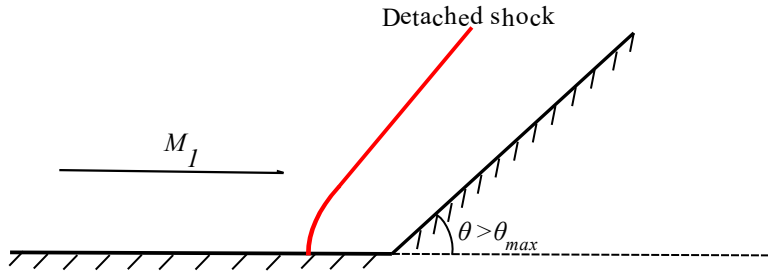


Figure 2.5 Schematic of a detached bow shock

For a given upstream Mach number, M_1 , there is a maximum flow deflection angle θ_{max} that an oblique shock can accommodate. As shown in Figure 2.5, if the required flow deflection θ is larger than the maximum flow deflection angle θ_{max} , then the oblique shock assumptions break down, and a curved bow shock forms ahead of the body. This bow shock is detached from the body and is curved in shape.

Bow shocks often occur around blunt bodies [53-55], because of the high deflection angle that the body imposes to the flow around it. The thermodynamic transformation across a bow shock is non-isentropic and the flow velocity is decreased from supersonic velocity upstream to subsonic velocity downstream. The bow shock significantly increases the drag in a vehicle travelling at a supersonic speed.

Normal shock

Normal shock is a simpler case of the bow shock. Two more assumptions need to be postulated in the case of normal shock: that the flow across the shock wave is adiabatic and non-isentropic. Similarly, the flow velocity across a normal shock is decreased from supersonic to subsonic, leading to an increase of the static pressure, density, and temperature.

Unsteady/moving shock

The above shock waves are steady. The term ‘steady’ means that the flow is moving in the opposite direction with the same velocity magnitude as the wave velocity, giving the

impression that the shock wave is actually stationary [42]. When the velocity of the upstream flow is zero and the shock wave propagates freely in space such as balloon bursting, shock tube, and shock wave from the explosion, this type of shock wave is termed an unsteady shock wave [56]. Because the flow field is a function of both time and distance, the motion is defined as unsteady or moving. The fundamental difference between a steady and a moving shock is that the total enthalpy is constant in a normal steady shock wave which is not seen for an unsteady shock wave.

It is worth noting that all aforementioned types of shock waves obey the usual laws of fluid mechanics, including conservation of mass, momentum, energy, and the law of thermodynamics. The equations governing the velocity, momentum, energy, and density across shock waves can be found in previous studies and textbooks [42, 44, 45], which are not listed in this dissertation.

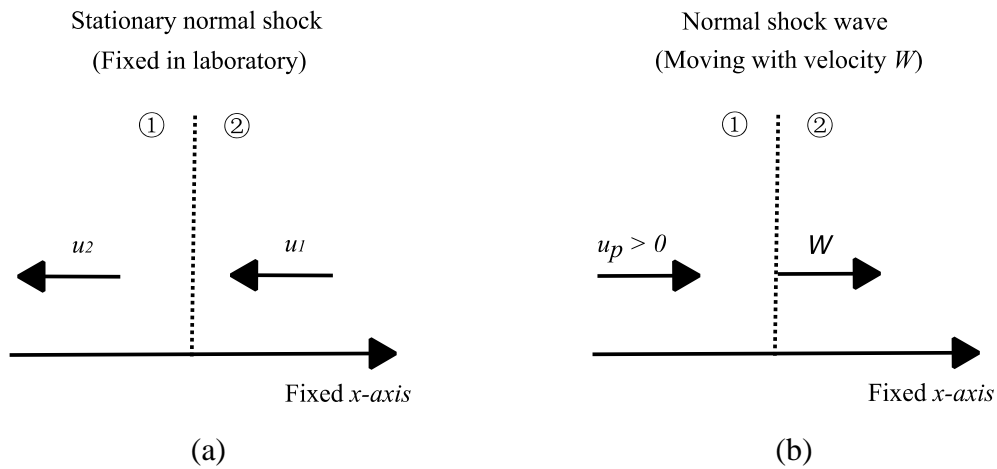


Figure 2.6 Schematic of differences between: (a) a stationary; and (b) moving normal shock [42]

2.1.2 Shock reflection

When shock waves impinge on an obstacle, they are reflected back from it. Ernst Mach was the first scientist to notice and report the shock reflection phenomenon. His ingenious experimental investigation was surveyed by Reichenbach [58] and re-conducted by Krehl and van der Geest [59]. Shock reflections can broadly be divided into two different categories: irregular reflection (IR) and regular reflection (RR). There are many different types of irregular reflection. Figure 2.7 shows the tree of possible reflections and their

abbreviations.

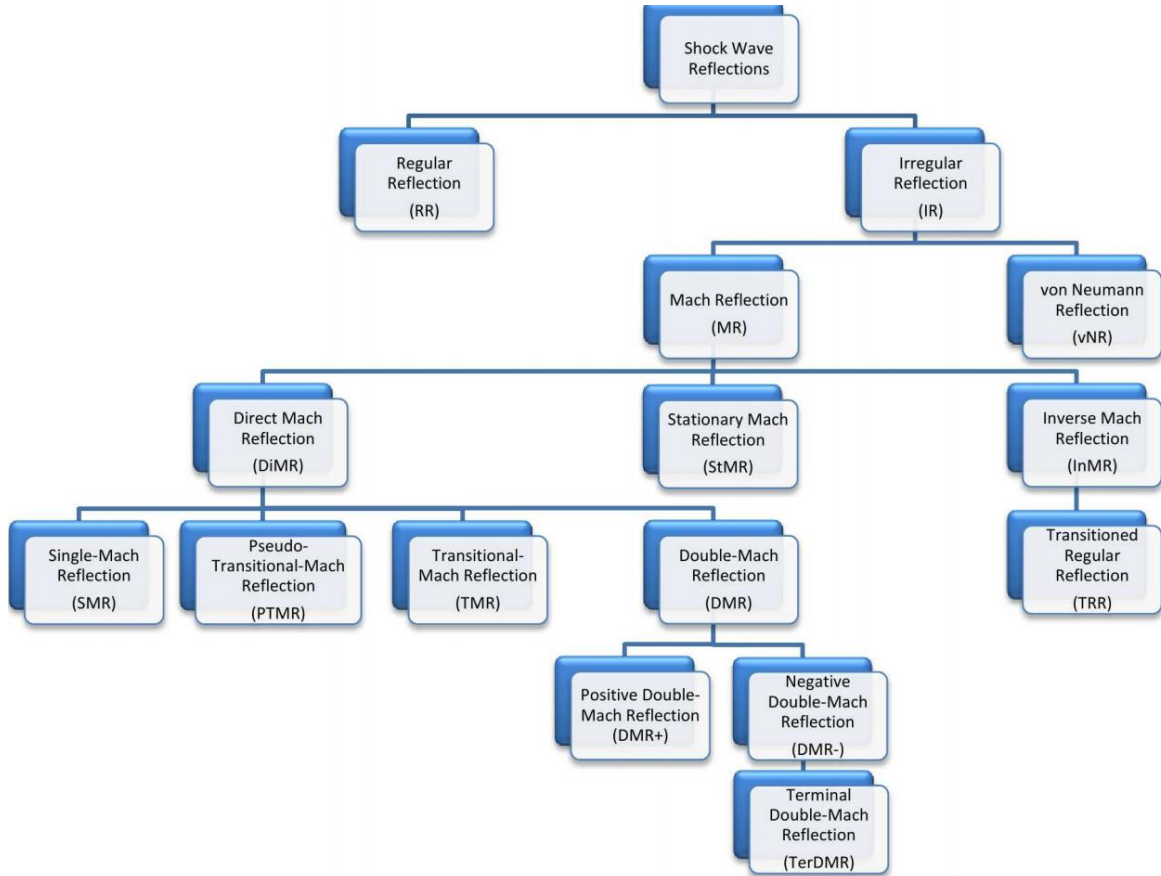


Figure 2.7 Different types of shock wave reflection [57]

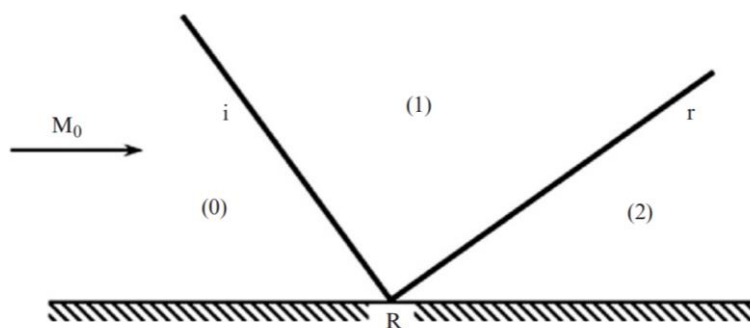


Figure 2.8 Schematic of a regular reflection wave configuration–RR [56]

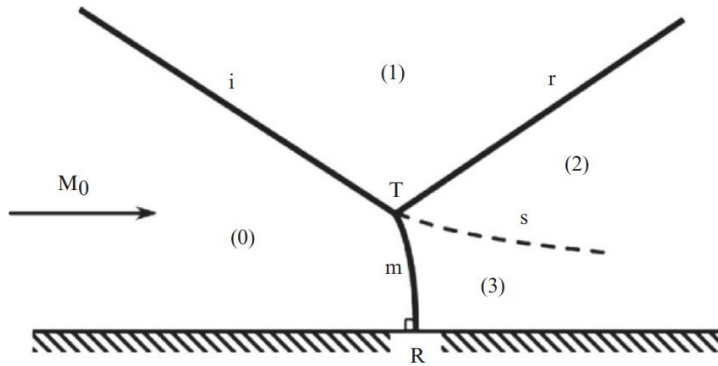


Figure 2.9 Schematic of a Mach reflection wave configuration–MR [56]

As shown in Figure 2.8, regular reflection configuration consists of the incident shock wave i and the reflected shock wave r . These two shock waves intersect at the reflection point R . The irregular reflection can be divided, in general, into two categories: Mach reflection (MR) and von Neumann reflection (vNR). As illustrated in Figure 2.9, the MR wave configuration consists of three shock waves that intersect at a single point called the triple point T , which is located above the reflecting surface.

2.1.3 Shock diffraction

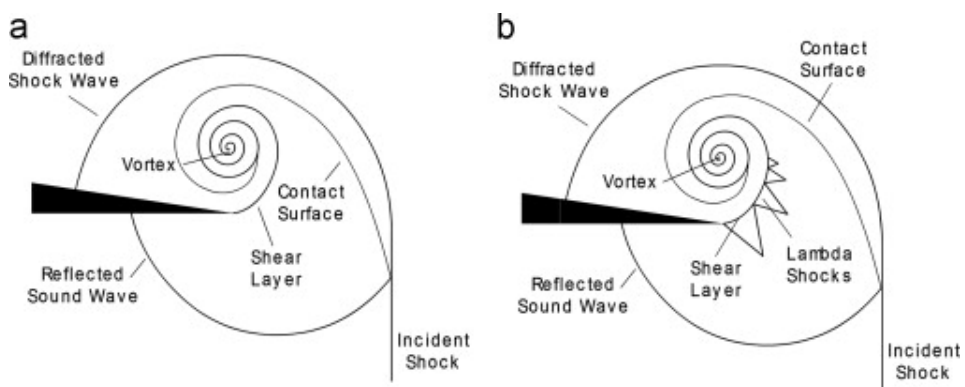


Figure 2.10 Flow feature of diffraction around a sharp wedge at (a) $M = 1.31$; (b) $M = 1.59$ [65]

When the normal path of a shock wave is impeded by some obstacle, the shock wave diffraction phenomenon occurs [60-63]. Figure 2.10 illustrates the flow feature of shock diffraction around a sharp wedge [65]. In the case of Mach number is 1.31, the region bounded by the planar incident shock wave consisting in the curved diffracted shock and the

reflected expansion shock was called the perturbed region by Skews et al. [64] and remains subsonic for an incident Mach number less than 2.068. In the case of $M = 1.59$, the incoming flow becomes locally supersonic in the vicinity of the corner and leads to the development of the typical lambda shock structure on the shear layer.

2.1.4 Shock focusing

Shock wave focusing happens when a shock wave propagates through a nonuniform or moving media and reflects from curved surfaces or through reflections with other shock waves [66]. The extremely high pressure and temperature focal region resulted from shock focusing can be either beneficial or detrimental. The shape of the shock wave is fundamentally altered when it emerges from the focal region. The shock wave focusing phenomenon can generate extreme conditions in fluids within micro or even nanosecond timescale and is of great interest because of its connection to a great variety of phenomena in nature, technology, and medicine [66].

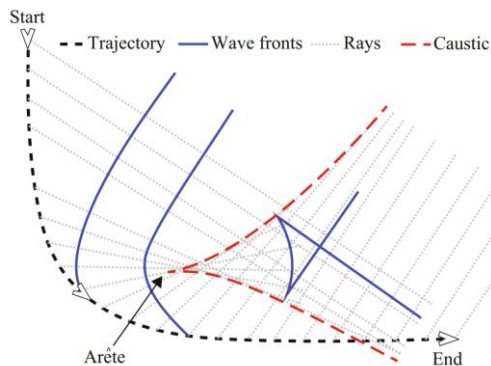


Figure 2.11 Shock focusing due to turning of a supersonic aircraft to illustrate wave fronts, rays, caustics, and arête [66]

2.2 Supersonic starting jets and their impingement

An improved understanding of the physical mechanisms governing supersonic jets, their impingement, and associated noise generation mechanisms is of great interest for aeronautical and astronautical applications including supersonic transport, rocket propulsion,

projectile launch, mixing augmentation, enhanced combustor performance and thrust vector control [67-71]. As shown in Figure 2.12, the supersonic jet flow structure from a nozzle is governed by the ratio between the exit pressure of the jet p_e and the local atmosphere pressure p_b . There are three types of supersonic jets based on this pressure ratio: ideally expanded, overexpanded, and underexpanded. If the ideal isentropic value for the design exit Mach number is reached, a normal shock is generated at the nozzle exit. In the case of $p_e < p_b$, the supersonic jet is overexpanded and a series of compression waves forms outside the nozzle to reach equilibrium in the flow. Oppositely, when $p_e > p_b$, an underexpanded supersonic jet is generated, which is capable of additional expansion. The equilibrium is reached by a set of expansion waves that attach to the nozzle exit [42].

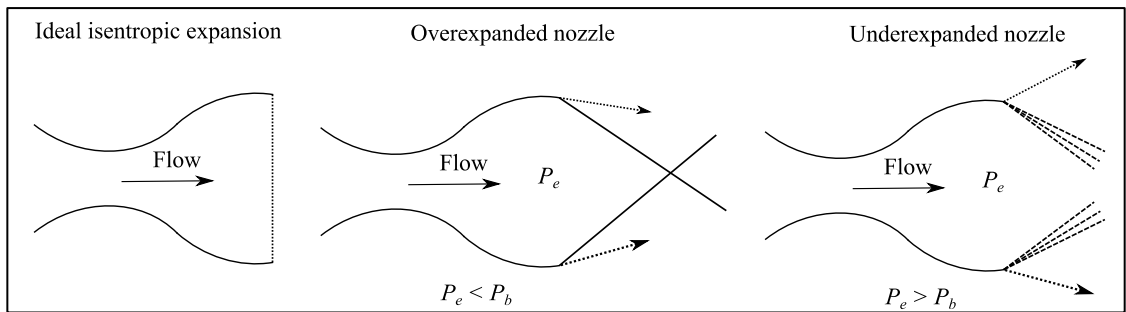


Figure 2.12 Ideally expanded (left), overexpanded (centre), and underexpanded (right) jets [42]

Also, the nozzle geometry can significantly influence the major flow structure of a supersonic jet [72]. As an efficient approach of passive flow control, non-circular jets, such as elliptical, rectangular, square, and triangular jets, have been extensively studied to control the flow mixing and entrainment rate [73-78]. Zare-Behtash et al. [67, 79] investigated the flow properties of non-circular vortex loops from square, elliptic, and exotic nozzle geometries and demonstrated that the circulation of circular vortex ring is higher than that of non-circular vortex loops. According to the numerical simulation of Zhang et al. [80], counter-rotating stream-wise vortices at the corners of the nozzle exit are generated by a square vortex loop, and mixing is accelerated in the vortex core.

2.2.1 Free supersonic starting jets

Supersonic jets have been investigated intensively in the literature both in the continuous

and pulsed cases. This dissertation concentrates on the starting phase of a supersonic jet. A continuously blowing jet can be produced in this phase if it is ejected from an infinite reservoir. By contrast, when the jet is ejected from an extremely short reservoir compared to the nozzle diameter, this phase only can lead to a single vortex ring with no jet at all. Pulsed jets [81] and synthetic (zero mass flux) jets [82] are similar to the situation of the starting jet.

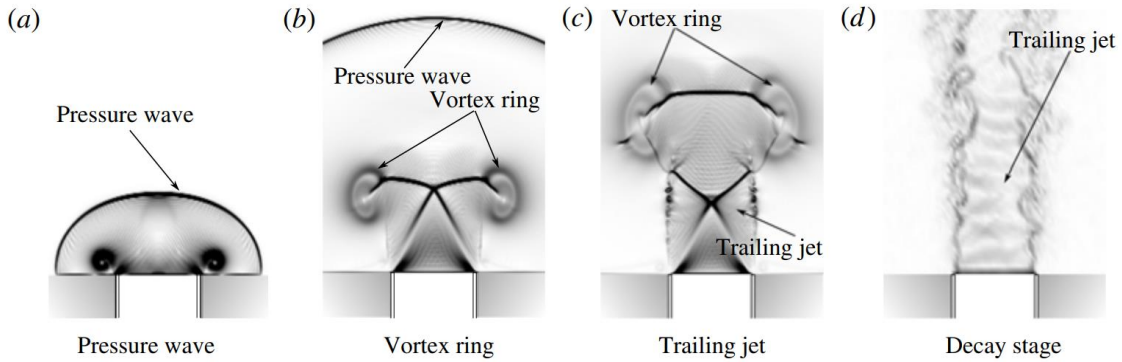


Figure 2.13 Stages of the starting jet [83]

As shown in the Figure 2.13, in the supersonic starting jet with a circular nozzle, an initial shock wave forms just after the high pressure and temperature gas is released from the nozzle exit [83]. The shock wave has a half-spherical shape and propagates into the unbounded chamber with the speed of sound if it is a pressure wave or faster if it is a blast shock wave [84].

Behind the initials shock wave, a vortex ring is always produced because of the large velocity gradients between the high-speed jet flow and the surrounding gas. The size of the vortex ring grows until it reaches a critical size ($1.08D$ proposed by Didden [85] and D is the nozzle exit diameter) and then the vortex ring begins propagating in the axial direction. Shortly after the formation of the vortex ring, it separates from the trailing jet, detached from the rest of the flow. This separation process is called ‘pinch-off’ and is ideally defined as the lack of vorticity between the vortex ring and the trailing jet [83].

As shown in Figure 2.14, the pinch-off process is driven by the Kelvin–Helmholtz instabilities from the shear layer in the trailing jet [86]. When the successive Kelvin–Helmholtz vortices in the shear layer are produced, they start rotating and drawing in

vorticity from upstream and downstream of the vortex in the shear layer, which results in a vorticity distribution along the shear layer with concentrated regions of large vorticity separated by regions of relatively low vorticity. These spaces between vortices are the possible points where the pinch-off process takes place [83].

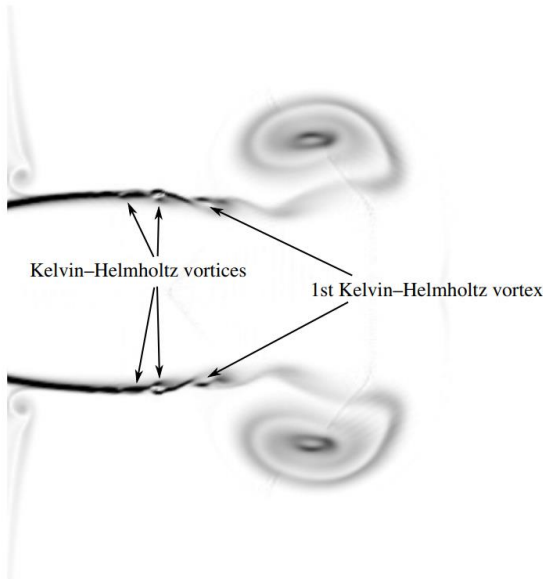


Figure 2.14 Flow configuration showing the development of the Kelvin–Helmholtz vortices [83]
(The vorticity magnitude is shown in a black and white colour scale)

If a trailing jet is generated, the jet would interact with the vortex ring in the case of a large Reynolds number. This shock–shear layer–vortex ring interaction is one of the loudest noise sources of the supersonic starting jet [83].

2.2.2 Supersonic starting jet impingement

Applications

Supersonic starting jet impingement can be found during a rocket launch, the initial stage of a launch abort, multi-stage rocket separation, jet-engine exhaust impingement for short take-off and landing (STOL), and powered vertical take-off and landing (VTOL) aircraft.

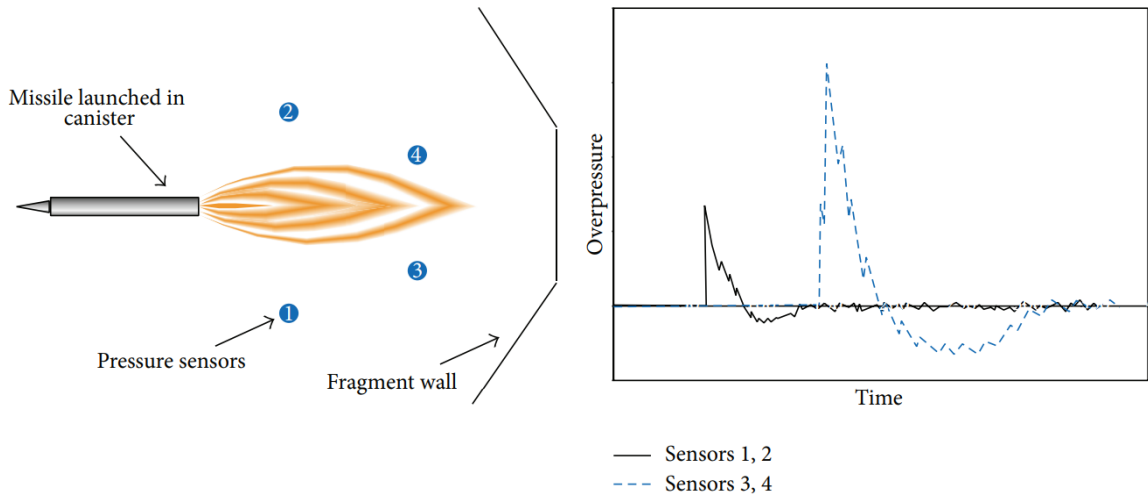


Figure 2.15 Illustration (left view) of laboratory test launch of missile with highlighted pressure sensors and qualitative illustration of the pressure-time results (right view) [87]

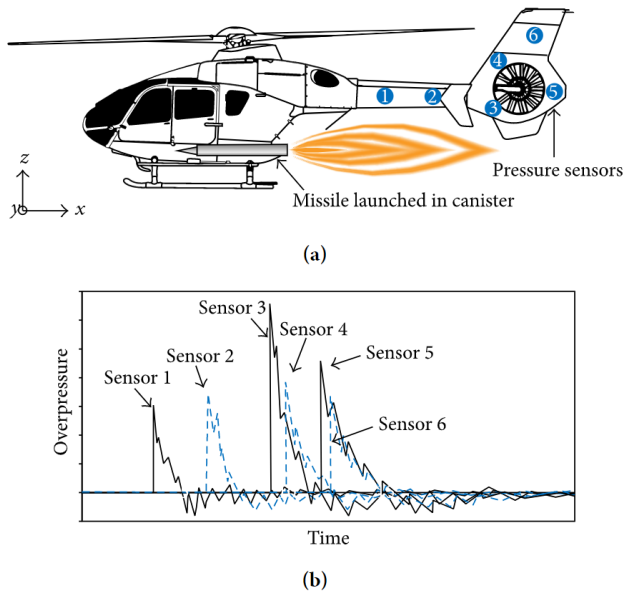


Figure 2.16 Illustration of missile launch tests from helicopter: (a) locations of pressure sensors; (b) qualitative illustration of the pressure-time results [87]

The supersonic starting jet during a space rocket or military missile launch produces an initial shock wave releasing from the nozzle exit, leading to high pressure loading on surroundings like a sonic boom. The structural loading should be assured that it does not exceed the design limits of the surrounding structures. As shown in Figure 2.15 and Figure 2.16, Extensive experimental studies have been performed on the supersonic jet interaction

with aircraft structure. Computational fluid dynamics (CFD) is the other efficient approach to investigate this problem [88]. Kidd and Cloke [89] numerically simulated the development of the shock wave generated during the launch of a missile from a helicopter. Similarly, Lee et al. [90] reported several CFD models to study the missile launch focusing on the missile movement. Extensive CFD investigations of the exhaust plume during rocket launch were also conducted by Gusman et al. [91], Alexeenko et al. [92], Ebrahimi et al. [93], and Vitkin et al. [94]. The complexity of the flow structure produced by the supersonic jets is challenging for numerical simulations.

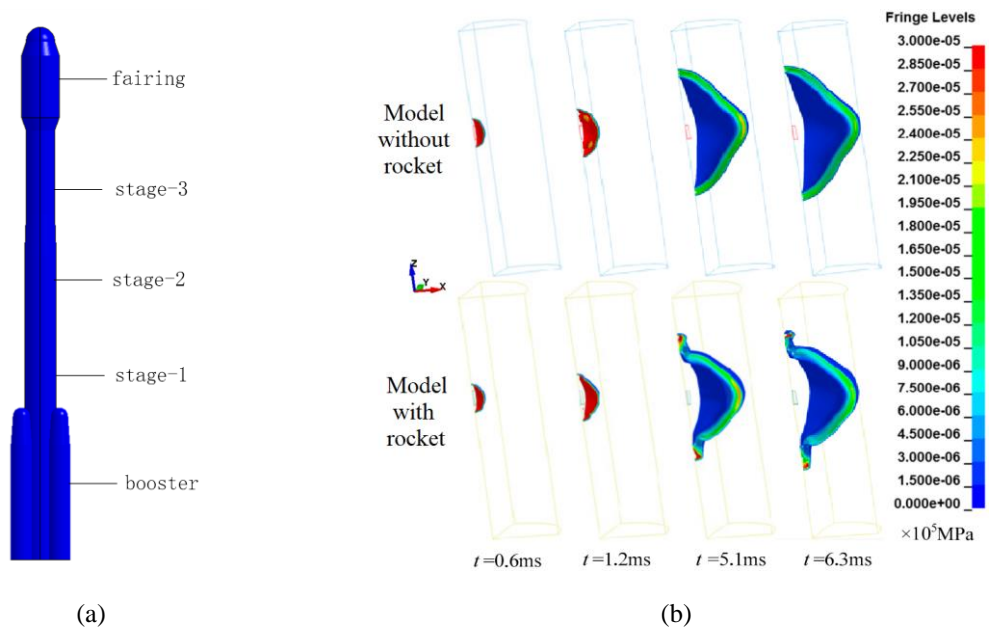


Figure 2.17 Blast shock wave impact prediction on crew module for liquid rocket explosion on launch pad:(a) Rocket 3D model; (b) Pressure contours of air blast at different time after stage-3 explosion [95]

Heimbs, et al. [87] proposed an empirical method to calculate the shock wave loading during the missile launch from a military aircraft, which then is used in numerical simulations. Based on a series of experiments, a mathematic model was proposed to predict the unsteady overpressure.

The supersonic jet impingement is also a key issue in the manned space mission. Seven astronauts on board lost their lives during the launch of the space shuttle Challenger in 1986 [96]. Much more attention was paid on risks that can threaten the launch safety after the

Challenger disaster. The hazards of blast wave generated during the process of liquid propellant explosion had been reviewed by Fletcher et al. [97]. The pressure loading induced by the blast wave can be determined by empirical formulas for simple geometries. Numerical tools such as LS-DYNA have been used for a complicated model with rocket [98]. Bo et al. [99] numerically investigated the blast peak overpressure using AUTODYN software. The blast wave attenuation law was also discussed in their study. Similarly, Ke and Jingpeng et al. studied the blast wave hazards from the rocket explosion on launch pad based on the accident consequence analysis software PHAST [100, 101]. Although CFD has been proven an effective tool to study supersonic starting jet impingement, experimental investigations are still necessary to validate simulation models and study the complex flow situations which is difficult to be simulated by CFD tools.

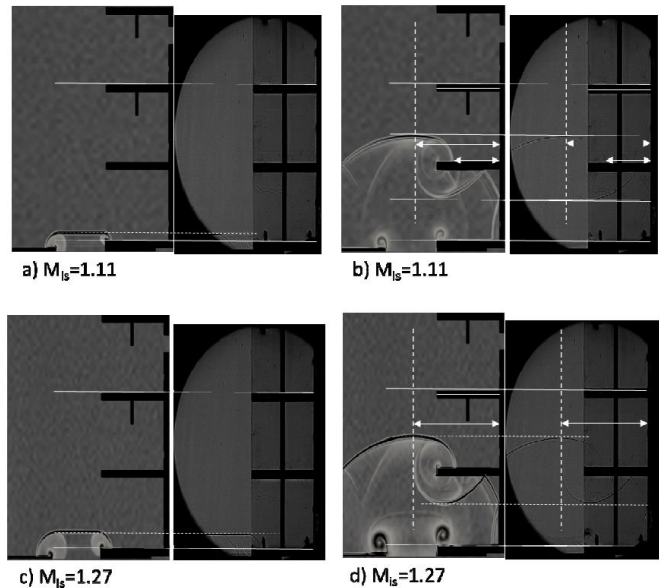


Figure 2.18 Comparison between schlieren representations obtained from computations(left) and experiments (right) on blast wave interaction with a three-level building [102]

Shock waves discussed above are strong ones. In fact, weak shock waves are also quite harmful when they hit a body after multiple reflections from existing walls and corners. An experimental and numerical investigation regarding weak blast wave interaction with a three levels building had been performed by Massoni, et al. [102] based on a conventional shock tube and numerical tools. The result showed that blast wave damages were higher for people standing near a wall, or near corners. Furthermore, the overpressure behind the reflected

blast wave from a room corner was significantly higher than that experienced in the open atmosphere. Therefore, the flow characteristics of strong or weak shock interaction with various geometries are quite different. It is important to investigate the mechanism of the shock wave from the supersonic starting jet interaction with different geometries.

It is worth noting that the shock tube has been proven an effective facility to simulate the supersonic jet [103] and the shock loading [104-107]. Therefore, shock tube was chosen as the experimental tool to generate supersonic jets in this research.

Perpendicular flat plate

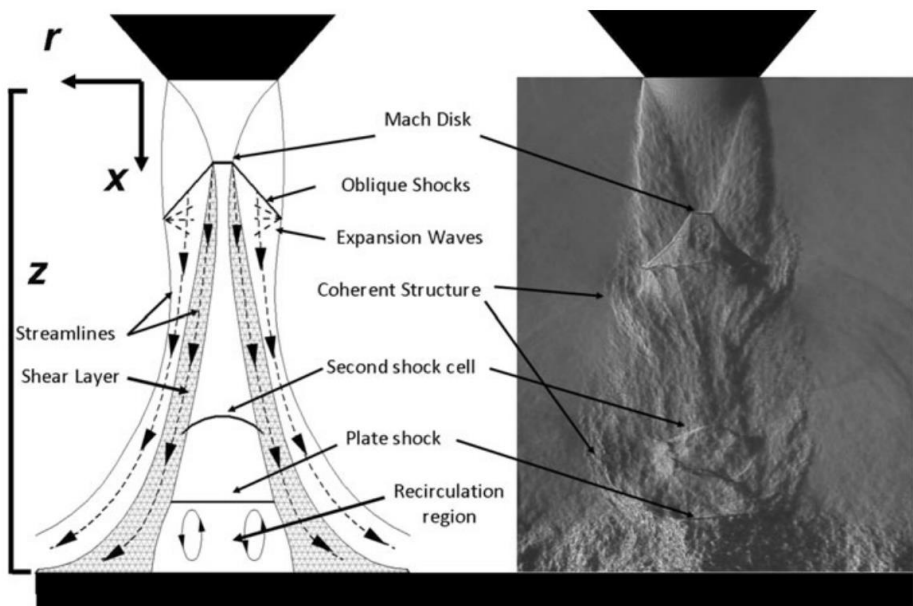
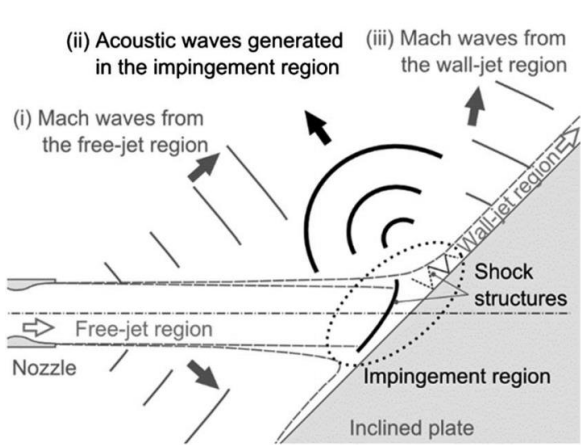


Figure 2.19 A schematic of one possible configuration of steady state flow for an impinging underexpanded jet, with accompanying schlieren image of the jet at impingement distance $z/d = 4$ and nozzle pressure ratio $\text{NPR} = 3.2$ [108]

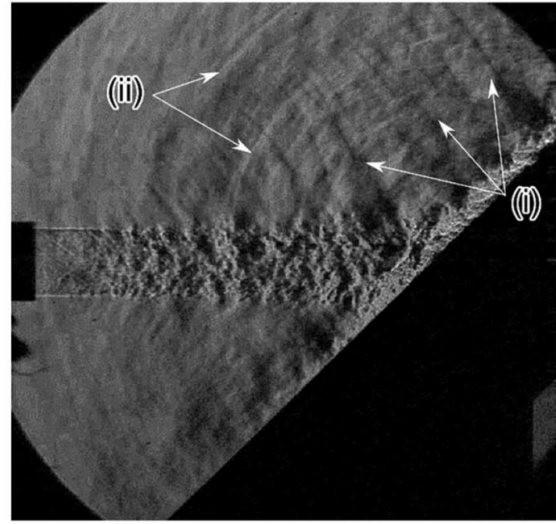
Supersonic jet impingement on perpendicular solid plates is of practical interest because of its presence in various applications. The flow characteristics of supersonic jet impingement on a perpendicular solid plate, despite the geometrical simplicity, are very complex and have posed challenges to CFD simulations, especially for turbulence modelling [2, 3, 109]. The supersonic jet impingement generates significant pressure fluctuations, which in turn results in vibrations of the plate. The pressure fluctuation depends on several characteristics of the

jet such as the nozzle pressure ratio, nozzle-to-plate spacing, properties and size of the plate and the nozzle geometry itself.

Inclined plate



a) Schematic



b) Schlieren image [19]: Mach waves from the free-jet region (point i), and acoustic waves generated in the impingement region (point ii)

Figure 2.20 Acoustic phenomena from supersonic impinging jet [5]

Non-vertical jet impingement of a supersonic jet with different nozzle-to-plate distances and different impingement angles has been previously studied both numerically [15-19] and experimentally [20, 21]. Solving the three-dimensional Navier–Stokes equations with a modified weighted compact nonlinear scheme, Nonomura et al. [22] studied the influences of nozzle-to-plate distance and jet temperature on the acoustic field of ideally expanded supersonic jets impinging on an inclined plate. Analyzing distributions of the overall sound pressure level (OASPL) and octave-banded sound pressure level (SPL) in the symmetry plane, Nonomura et al. [22] observed at least three types of possible noise sources.

Perforated surface

As discussed above, the attenuation of initial shock strength from a supersonic starting jet, has been the subject of research in the last decades. Perforated plates have been proven an effective way of mitigating blast waves. Skews [25] has experimentally investigated the

shock wave interaction with a porous plate at different conditions of shock wave strength, incident angles and blockage ratios. The experiment result shows that the secondary waves induced by the reflections from the medium internal surfaces increase the strength of the shock wave from the back edge of the porous plates. Kontis, et al [110] examined the flow structure during the shock wave and vortex ring from a shock tube open end interact with (i) a solid, and (ii) a porous wall. The result showed that, as the shock wave propagates through the porous plate, a portion of the shock wave is reflected from the plate internal surfaces and induces a series of compression waves when it leaves the front edge of the porous wall. After the shock wave passed through the porous plate, its strength reduced and the pressure fluctuation became stronger with increasing distance downstream of the porous wall.

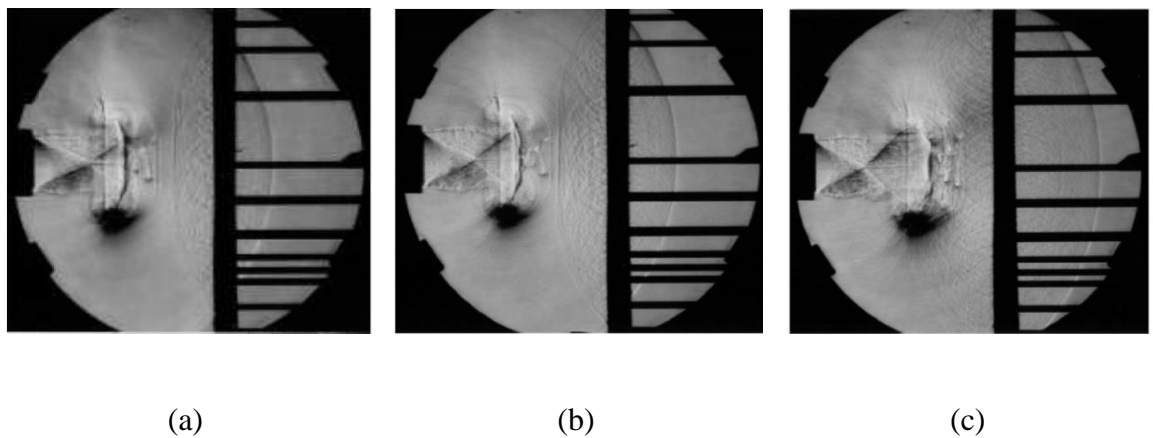


Figure 2.21 Schlieren images for the case of the perforated plate at a shock Mach number of 1.61
(a) 1.45ms; (b) 1.50ms; and (c) 1.55ms [110]

However, few studies have been conducted for supersonic jet interaction with flexible plates. One of the major objectives of this research is to investigate the flow structure and interaction mechanism of supersonic starting jet impingement on flexible surfaces.

2.3 Shock wave boundary layer interaction over flexible surfaces

Shock wave boundary layer interaction

Shock wave and boundary layer interaction (SBLI) existed in various practical situations such as transonic aerofoils, high-speed inlets, nozzles at off-design conditions and

supersonic control flaps can be very harmful and need to be factored into design trade-offs [112]. For external flows, SBLI can cause loss of control authority, increase the thermomechanical loading, and induce an adverse structural response. In internal flows, SBLI can increase pressure losses, and in extreme cases could lead to unstart. From a fundamental fluid dynamics perspective, such interactions produce a diverse range of phenomena such as flow separations, vortical structures, turbulence amplification, and structure flutter.

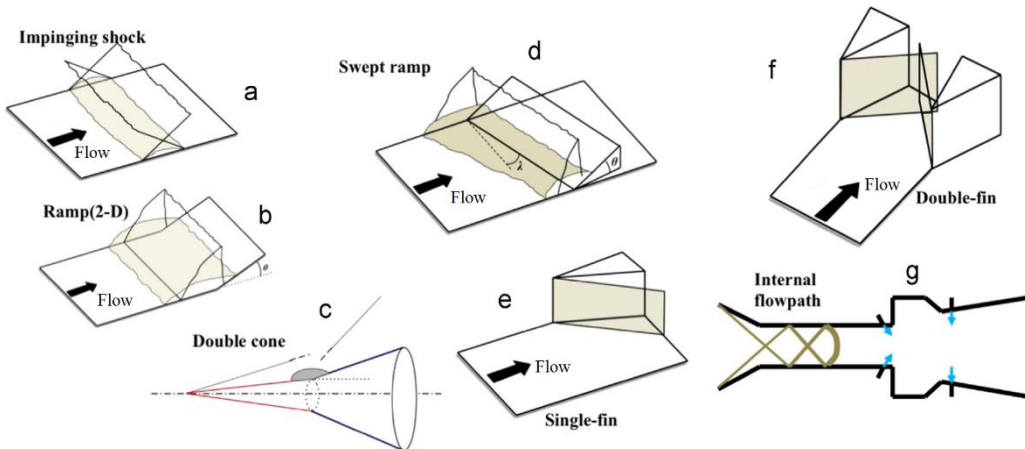


Figure 2.22 Canonical configurations employed for fundamental studies of SBLI [111]

The importance of SBLI is reflected in the emphasis they have received. Efforts from NASA, European, Australian, and Japanese programs have focused on varied aspects of SBLI and have greatly contributed to fundamental and applied advances over the last decade [113].

Fluid and structure interaction

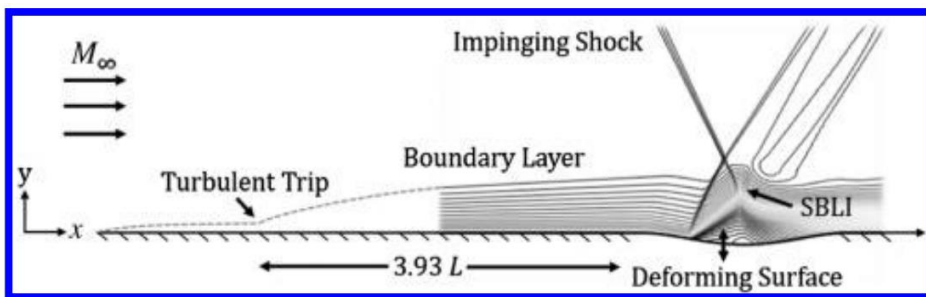


Figure 2.23 Schematic of the two-dimensional SBLI over deforming surface [36]

The fluid and structure interaction (FSI) is an important topic for all modern aircraft designs. At supersonic speed, the fluid and structure interaction under SBLI can lead to severe instabilities and catastrophic structural failure of thin walled structures of an aircraft.

Spottswood, et al. [40] conducted an experimental study to measure the response of an aircraft-like structure induced by the shock and turbulent boundary-layer interaction. Similar experiments had also been previously conducted by Coe [114], Maestrello [115], and in DLR [116-118]. The experiments were conducted in the AFRL Research Cell 19 (RC-19) wind tunnel [119]. A $305 \times 152 \times 12.7$ mm alloy steel plate with a 0.635mm thick pocket was manufactured as the compliant panel. A variety of techniques were used: a Polytec OFV-552 laser doppler vibrometer (LDV) and digital image correlation (DIC) for the structure deformation measurement, pressure sensitive paint (PSP) for surface pressure measurement, thermocouples and temperature sensitive paint (TSP) for surface temperature measurement and foil strain gauges [40]. One of the major objectives of this research is to develop advanced flow diagnostic tools to investigate shock wave and flexible surface interaction with the presence of the boundary layer.

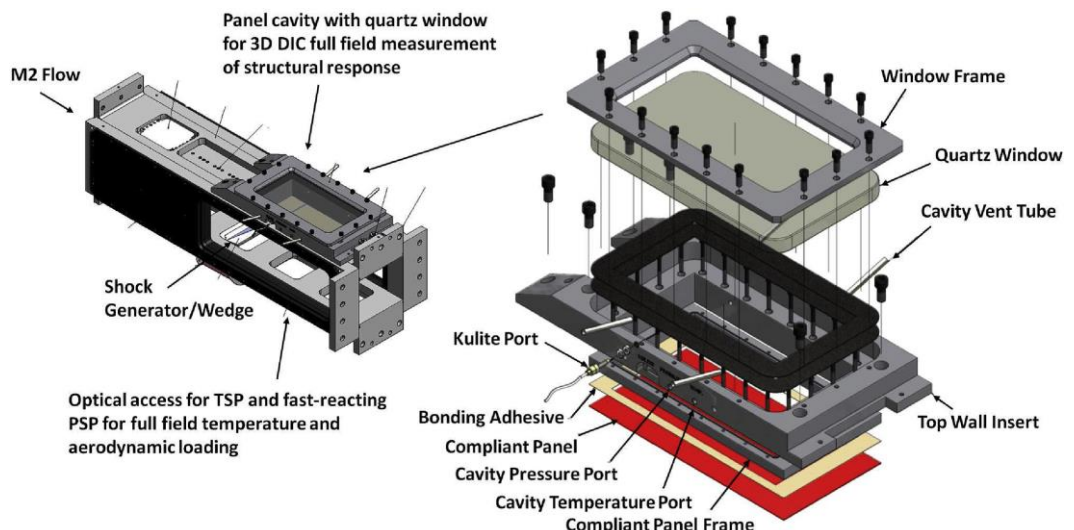


Figure 2.24 RC-19 modified test section, denoting flexible panel, shock generator, optical access and details of early “bonded” thin-panel arrangement [40]

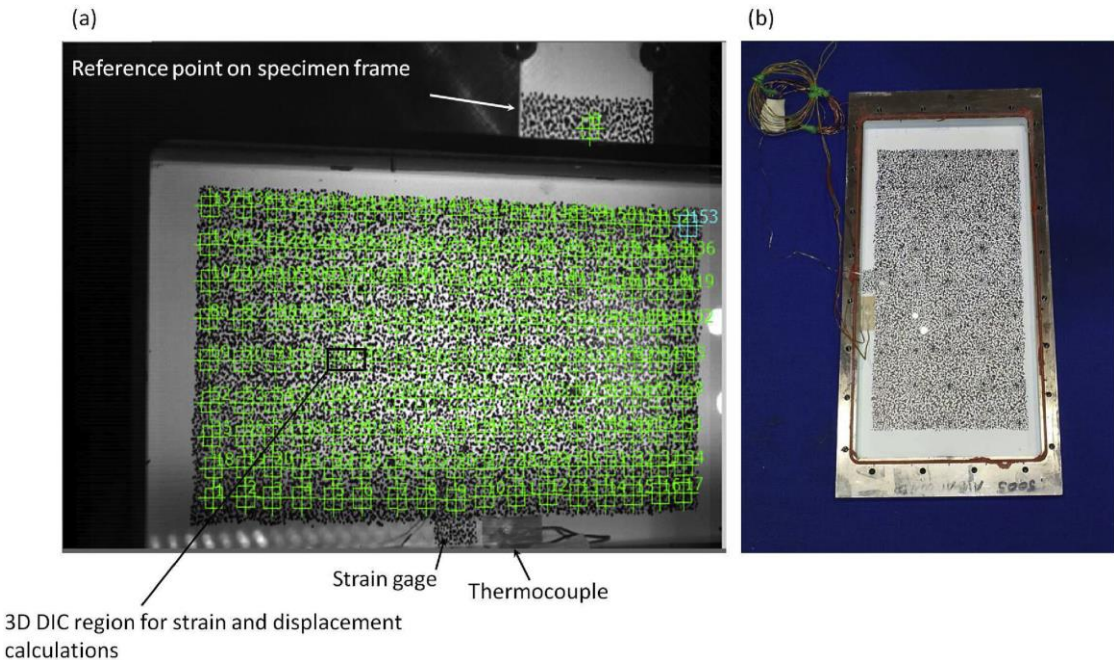


Figure 2.25 3D DIC pattern applied across the machined panel surface and the tunnel/specimen frame. Note there are 153 facets identified in (a) across the random pattern, while (b) shows the machined panel prior to test and prepared for measurement using DIC [40]

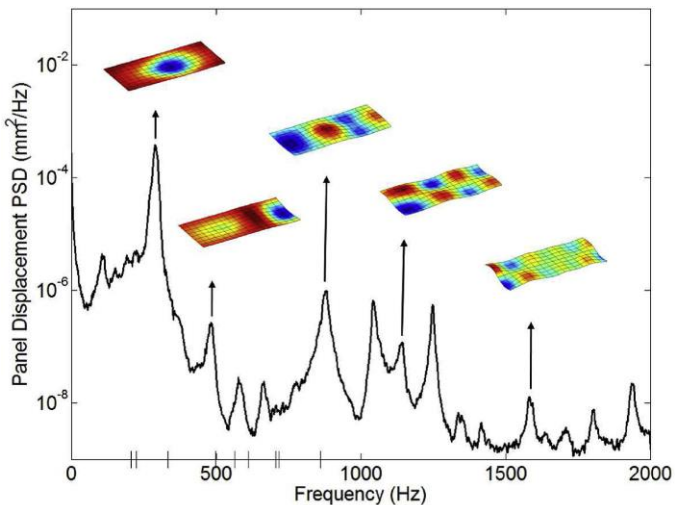


Figure 2.26 Single point displacement spectral response and operational deflected shapes with SBLI ($x/L \approx 1/4$). Vertical markings on the principal axis denote the measured panel frequencies before installation into the RC-19 tunnel ($U_\infty = 490$ m/s, $q_\infty = 123$ kPa) [40]

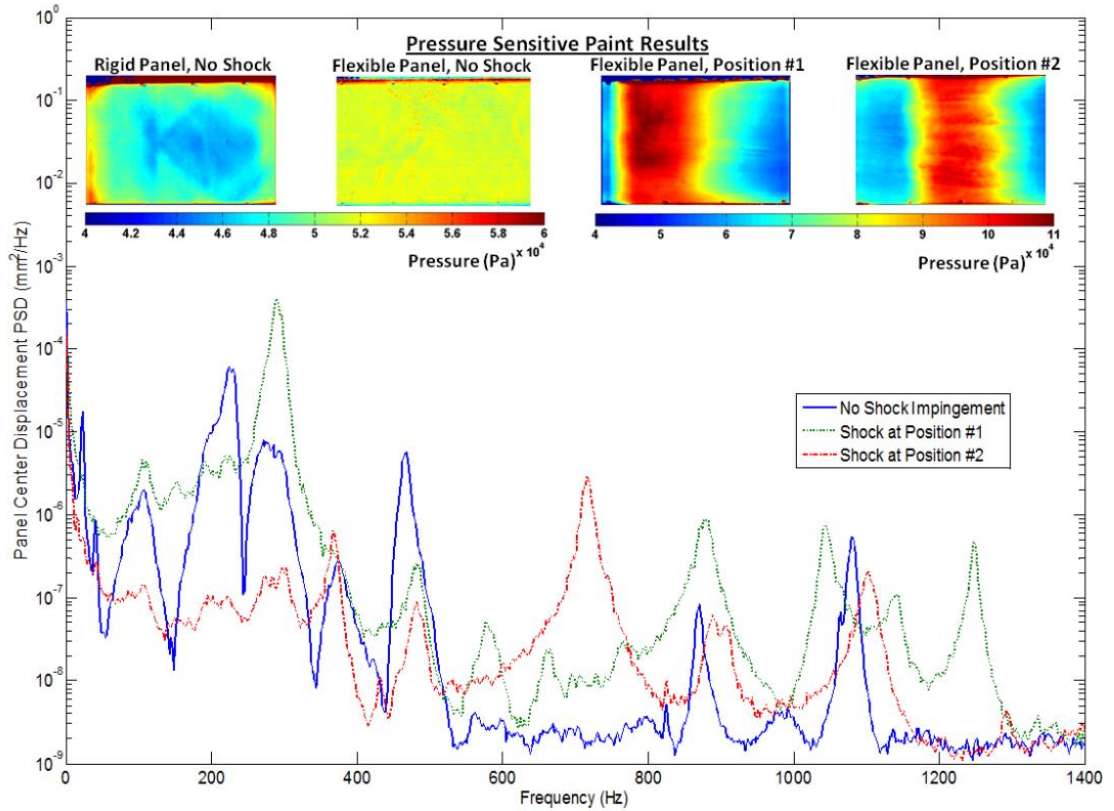


Figure 2.27 Panel center displacement power spectra and corresponding full-field PSP images for different shock impingement conditions ($M_\infty = 2.0$, $q_\infty = 123\text{kPa}$) [40]

Supersonic panel flutter

Panel flutter is a phenomenon of self-exciting vibrations of skin panels of high-speed flight vehicles [120]. Such vibrations usually have high amplitude and can cause fatigue damage of the panels, transferring energy from the flow to the structure [121]. Panel flutter can be triggered by the presence of an impinging shock wave or by just the presence of supersonic flow [122]. With the resurgent interest in high-speed flight vehicles such as the High-Speed Civil Transport (HSCT), the X-33 Advanced Technology Demonstrator, the Reusable Launch Vehicle (RLV), the Joint Strike Fighter (JSF), and the X-38 Spacecraft using a lifting-body concept, panel flutter analysis is becoming increasingly important [123].

First studies of supersonic panel flutter were conducted to describe failures that happened on flight vehicles like the X-15 experimental aircraft [124]. The overview of supersonic

flutter can be found in Dowell's review paper [28] and more extensively in his book [125]. Most of the experimental results regarding the supersonic panel flutter reported in the literature are quite dated and primarily focus on structural responses. Dowell and Voss [126] and Kappus et al. [127] used strain gauges to determine the panel deflection, in combination with pressure measurements to investigate the flutter of a panel clamped on all sides. These techniques are utilized even in some of the few recent papers about this topic in transonic speed [128]. On the other hand, with the development of computational power, more advanced numerical simulations are also performed, including structural non-linearities [129]. With the increased interest in validating CFD simulations, experimental results are needed both for the structure and for the flow. Great efforts have been done recently by Spottswood et al. [40], who measured the thin panel response to the shock wave and boundary layer interaction using three-dimensional digital image correlation (DIC), laser doppler vibrometer (LDV) and pressure sensitive paint (PSP). Similarly, PIV and Schlieren are applied by Jinks et al. for studying thin panel movement [41].

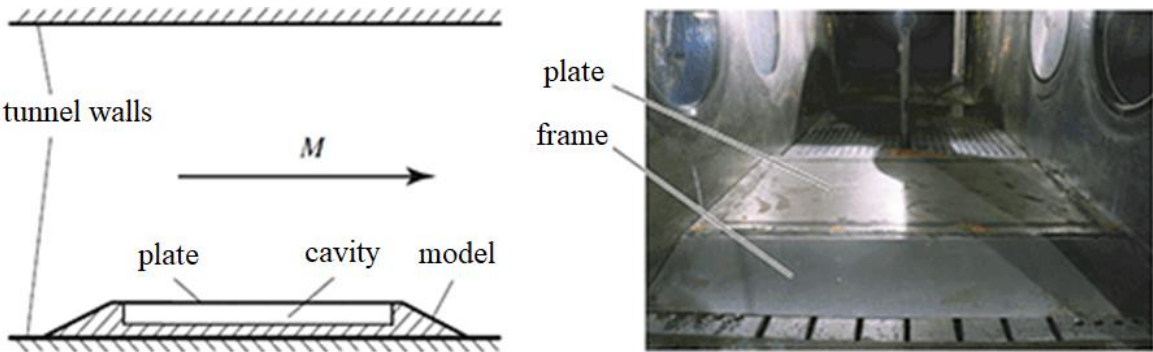


Figure 2.28 Sketch of the experiment on elastic panel flutter in a supersonic wind tunnel (left) and the picture of the model installed into the wind tunnel (right) [115]

As shown in Figure 2.29, D'Aguanno, et al [130] investigated the feasibility of studying supersonic panel flutter using digital image correlation (DIC) and validated the results with a laser doppler vibrometer. The experiment was carried out in a supersonic wind tunnel at a Mach number of 2, using two 100×100 mm panels with different thicknesses and clamping conditions (made in Al7075-T6). The DIC results demonstrated periodic oscillations of the flexible panel at 776 Hz in perfect agreement with the laser vibrometer. Additionally,

synchronized Schlieren and DIC measurements studied simultaneously the behaviour of the structure and of the flow.

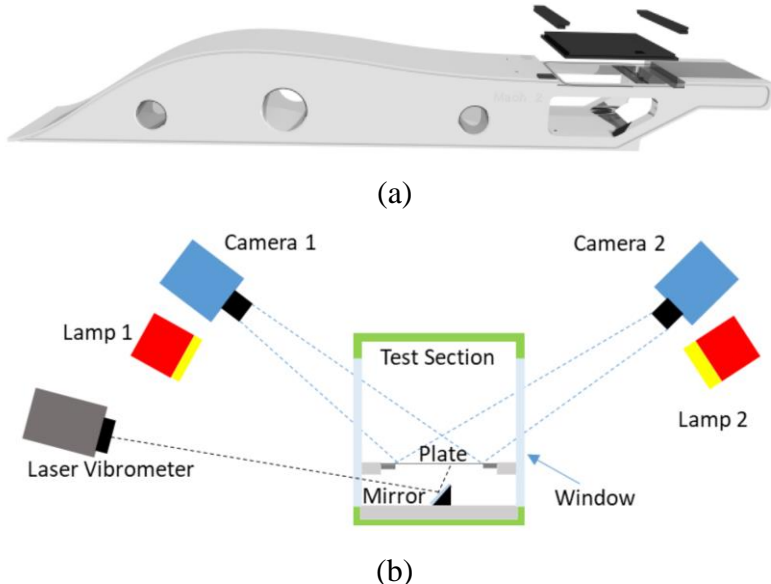


Figure 2.29 Experimental setup of supersonic panel flutter due to SBLI without shock impingement: (a) design of the flexible panel and clamping pieces; (b) 3D DIC and laser vibrometer setup [130]

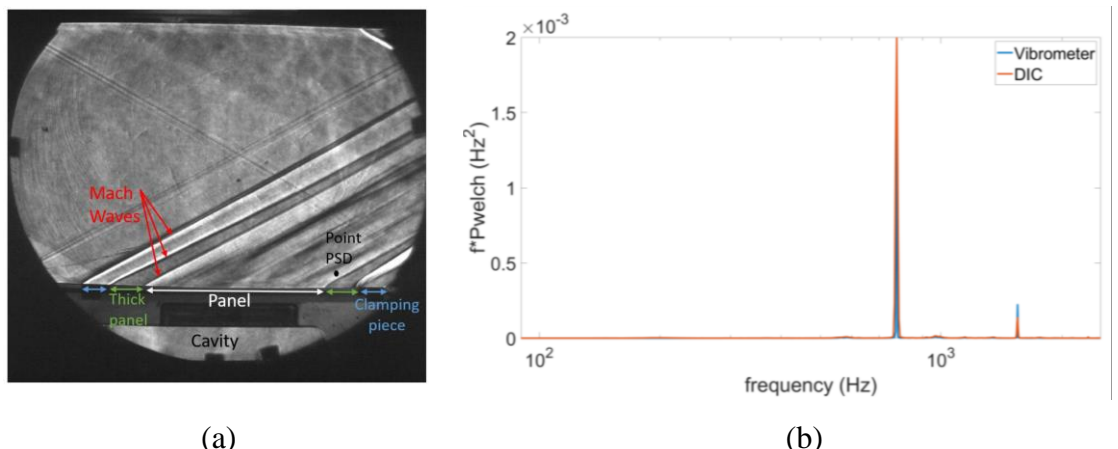


Figure 2.30 Typical experimental results of supersonic panel flutter due to SBLI without shock impingement: (a) Schlieren image; (b) comparison of power spectral density between DIC and vibrometer for 0.2 mm-thick panel clamped on all sides at $M=2.0$. Welch denotes the power spectral density (PSD) estimate of the input deformation signal using Welch's overlapped segment averaging estimator. [130]

Sonic fatigue

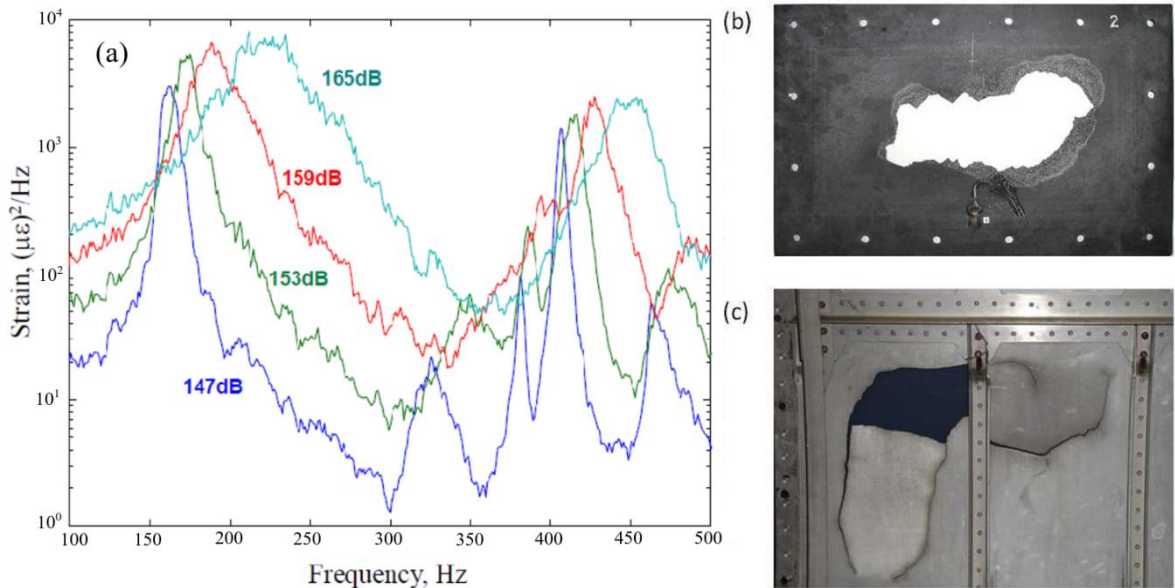


Figure 2.31 Sonic fatigue: (a) Geometric (hard-spring) nonlinear response typical of acoustic fatigue [131]; (b) Ceramic matrix composite panel failure (172 dB) [132], and (c) C-130 aluminium aircraft panel failure (160 dB) due only to acoustic/dynamic resonant fatigue

Sonic fatigue induced by the shock wave interaction with boundary layer has long been, an essential issue for the design of modern civilian and military aircrafts [133]. Figure 2.31 (a) shows the nonlinear structural response of constrained aircraft OML panels, while Figure 2.31 (b-c) demonstrates typical types of structural failure. Increasing the bending stiffness of the fatigue-prone area usually results in the high-cycle fatigue issue elsewhere. The optimal method probably is to damp or remove the offending dynamic loading. Liguore and Beier [134] reported sonic fatigue properties and then detailed the data of a flight test of the F-15 aircraft. It is more complex for structures that are exposed to severe thermal gradients, combined with the unsteady dynamic pressure loading induced by shock and boundary layer interaction [135]. The addition of the thermal effect can result in time-dependent material behaviour [136].

During the dynamic process of the shock wave and boundary layer interaction, it was found that the frequency of the shock motion is much lower than the boundary layer characteristic frequency [137, 138]. Sonic fatigue can be induced by the resonance of the aircraft panel

driven by the low frequency shock motion [139]. A single-stage-to-orbit (SSTO) vehicle configuration was adopted by Blevins et al. [140] as the basis for investigating appropriate loading distribution. During the flight test of the X-33, Kontinos and Palmer [141] tried insulated metallic thermal-protection system (TPS) panels. Also, Glass, and Hunt performed an experimental research using the same method in NASA's High Temperature Tunnel (HTT) [142, 143]. Culler and McNamara [144] also conducted impressive experimental studies and demonstrated that the hot-structure response is highly sensitive to boundary conditions.

Flow control

As discussed above, the dynamic shock wave and boundary layer interaction over flexible surfaces can lead to severe instabilities and catastrophic structural failure of an aircraft. However, acting as a passive flow control method, the aeroelastic oscillations of the flexible panel can also provide a positive impact, such as reducing the length of the flow separation. Visbal [39] and Brouwer et al. [36] numerically investigated the oblique shock and flexible panel interaction process. Their studies demonstrate that a flexible panel can reduce flow separation size and improve the characteristics of a supersonic transport aircraft [145-147].

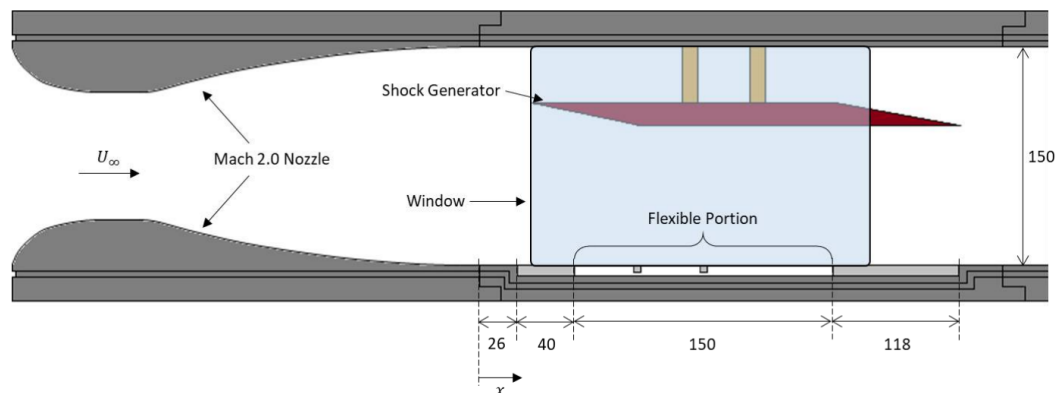


Figure 2.32 Experimental setup for investigating the interaction of a flexible panel with an oblique shock in the supersonic wind tunnel of Imperial College (ICL), dimensions in mm, Width=150 mm [38]

Tan, et al. conducted an experimental investigation on the shock wave and boundary layer interaction over a flexible panel to explore whether a positive effect can be obtained by

flexible surfaces or not [38]. Their results demonstrated that the initial shock becomes stronger and the region of flow re-acceleration is larger when increasing the curvature of the flexible panel. In addition, upstream shock motion increases the static pressure after the shock wave and reduces the overall strength of the SBLI. Also, the separation region size could be reduced by an increasing curvature. They also suggested that an optimal relative position of the flexible may exist to achieve a best effect on increasing static pressure recovery and reduced the size of flow separation.

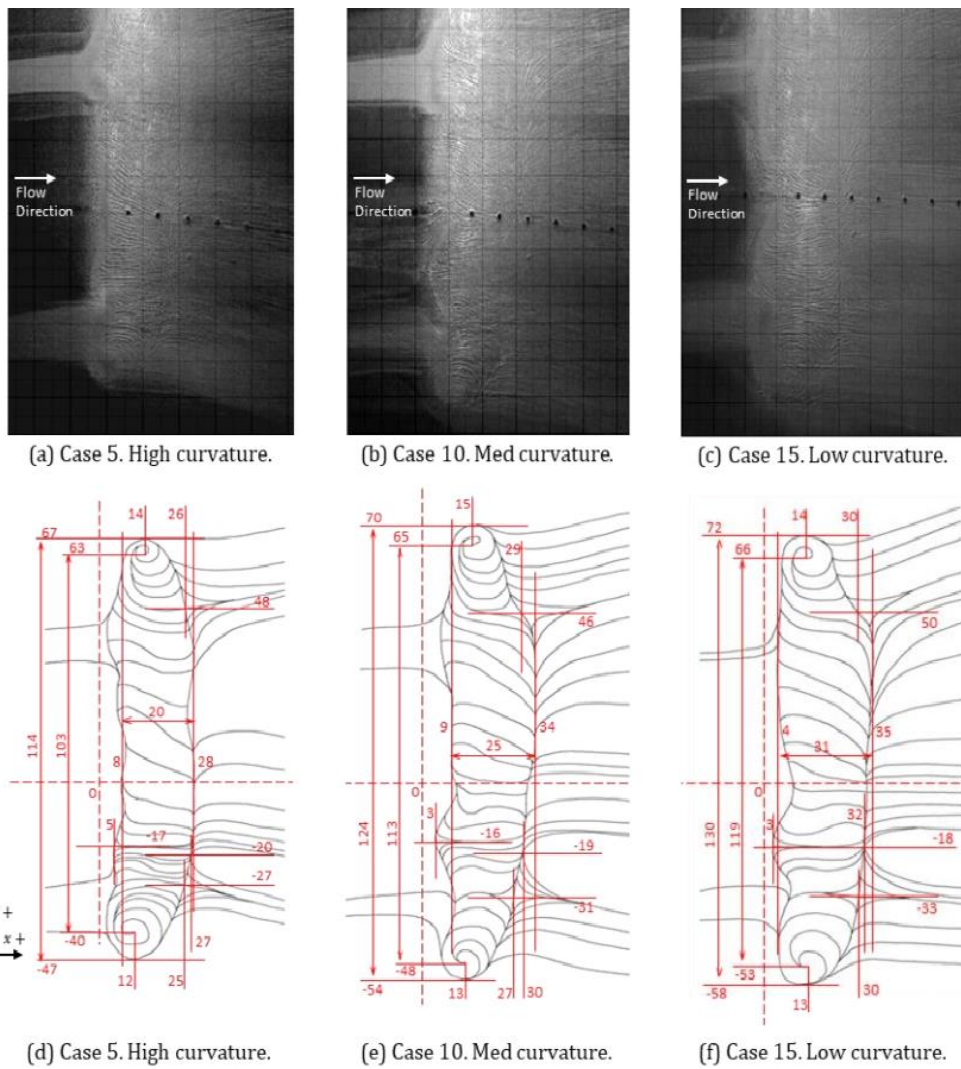


Figure 2.33 Oil flow images together with detailed schematic diagrams with positions of flow features marked. The origin is indicated by the red dotted lines and lies on $x = 109$ mm with reference to Figure 2.32. [38]

The possibility of using flexible panels to mitigate the unsteady pressure loading and the size

of flow separation during the process of shock wave and boundary layer interaction was explored by Pham et al. [37]. They experimentally studied the unsteady shock wave oscillating over a rubber flexible surface in different compression ramp angles. Their result showed that the soft rubber surface delays the flow separation by an average of 25% compared to rigid surfaces. Meanwhile, the mean pressure profiles only present less than 5% difference between the rigid and the flexible surface, suggesting the presence of the rubber surface did not change considerably the mean lift and drag forces. However, the energy content of shock wave oscillations reduced significantly in the intermittent region over the flexible rubber surface.

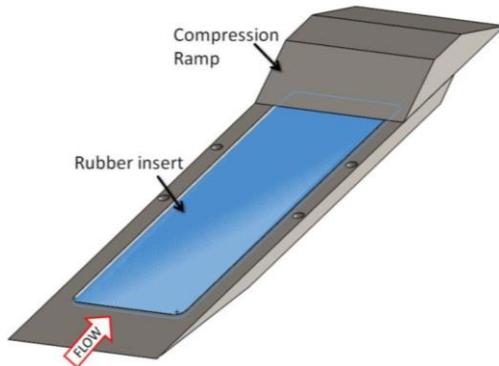


Figure 2.34 Schematic of the model with compliant material insert shown in blue [37]

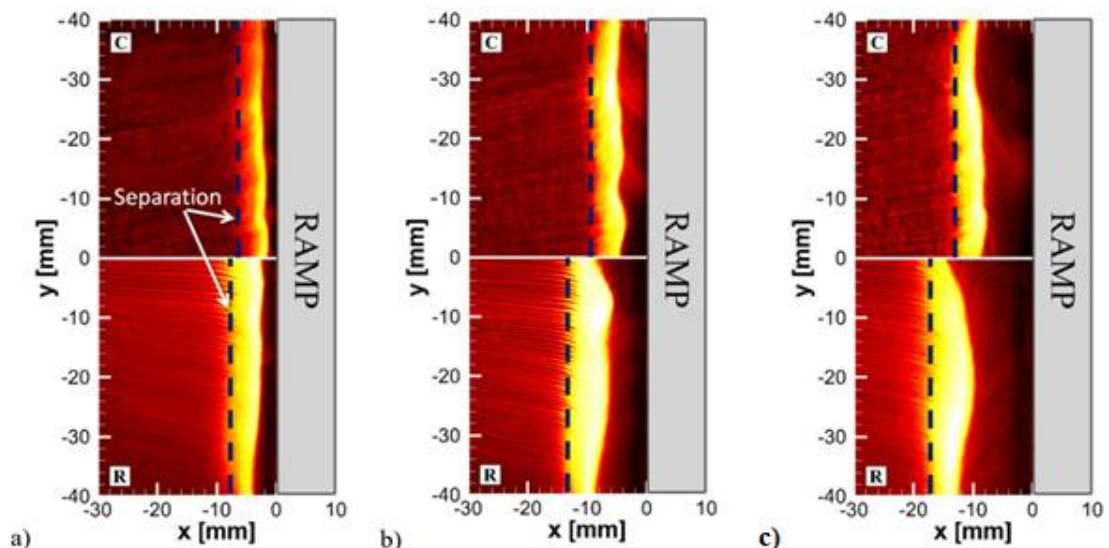


Figure 2.35 Comparison of top-view surface streak line images with rubber surface on top and rigid model on bottom, Mach 2.5 for compression ramp angles of (a) 16° , (b) 20° , and (c) 24° [37]

It can be seen from the above literature review that the shock wave boundary layer interaction over flexible surfaces can have negative and positive effects on the performance of high-speed flight vehicles. In this work, based on advanced measurement techniques, the mechanism of the shock wave and flexible surface interaction with the presence of the boundary layer is aimed to be investigated in depth, including the influence of the strength, location of the impinging shock and the aspect ratio, thickness, clamping conditions of the flexible panel on flow properties such as the unsteady pressure loading, the static pressure recovery and the separation region size.

2.4 Conclusions

Light-weight composite materials have increasingly used for high-speed flight vehicles for improving their performance and efficiency. At supersonic speed, sonic fatigue, panel flutter, severe instabilities, and even catastrophic structural failure would occur due to the shock wave impingement on several flexible components of a given structural system either internally or externally.

The initial shock wave generated by the supersonic starting jet during the rocket or missile launching induces high pressure loading on the surroundings, just like a sonic boom from a supersonic cruising flight. The turbulent continuous or starting jet impingement on plates produces significant pressure fluctuations, which in turn can cause vibration or flutter of the plates. The experimental and computational studies regarding supersonic continuous and starting jet interaction with a variety of surfaces such as the rigid perpendicular plate, inclined plate, and perforated surface are reviewed in this Chapter. However, few studies have been conducted for supersonic jet interaction with flexible plates. One of the major objectives of this research is to investigate the flow structure and interaction mechanism of supersonic starting jet impingement on flexible surfaces.

The fluid and structure interaction under SBLI can lead to panel flutter, sonic fatigue, and severe instabilities of thin walled structures of an aircraft. On the other hand, the aeroelastic panel oscillations were found to reduce the separation region compared to a rigid surface, showing potential for use as a passive flow control device. Previous studies regarding this

Chapter 2 Literature review

problem are reviewed. In this work, the mechanism of the shock wave and boundary layer interaction over flexible surfaces is aimed to be investigated in depth, based on advanced measurement techniques.

Chapter 3

Experimental apparatus and methodology

This section presents the physics and theories of the equipment used in the test campaign. The fundamental physics of the shock tube and supersonic wind tunnel is presented first, followed by the theories concerning advanced flow diagnostic tools.

3.1 Flow production apparatus

3.1.1 Shock tube

The working principle, operation, and equations of the shock tube can be found in previous studies and textbooks [148-152]. In this dissertation, Only the fundamental theory of the shock tube relevant to the current research is briefly introduced. The conventional shock tube is generally a duct divided into two sections as shown schematically in Figure 3.1. The first part accommodating high pressure gas (P_4) is the driver section and the low-pressure test gas (P_1) is contained by the other part, the driven section. The two sections are separated by a diaphragm or a fast-acting valve.

The typical flow structure and wave propagation diagram are illustrated in Figure 3.1. Once the diaphragm suddenly ruptures or the fast-acting valve opens, a shock wave is produced and propagates into the driven section. On the other hand, an expansion wave is produced,

propagating into the driver section. The diver and driven gases are separated by a contact surface behind the shock wave.

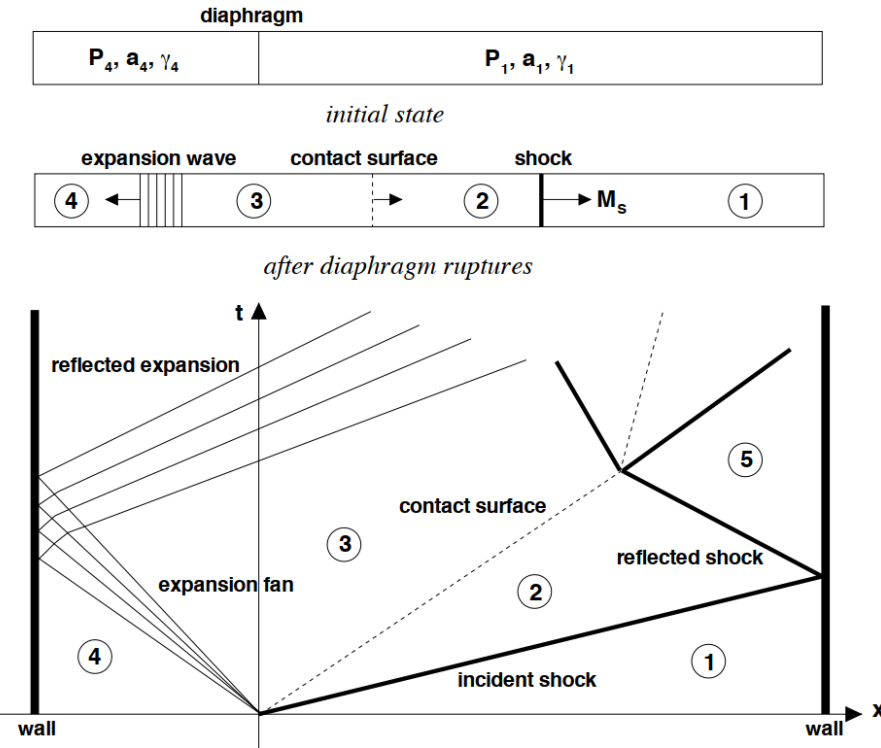


Figure 3.1 Shock tube experiment and wave diagram [153]

For a perfect gas, the pressure and temperature are suddenly increased across the shock wave front and the following equation can be derived from the one-dimensional conservation equations of mass, momentum, and energy [153]:

$$\frac{\rho_1}{\rho_2} = \frac{u_1}{u_2} = \frac{(\gamma+1)M_s^2}{2+(\gamma-1)M_s^2} \quad (3.1)$$

Where M_s is the shock wave Mach number, ρ and u are the gas density and velocity respectively. Index 1 refers to pre-shock conditions and 2 refers to post-shock conditions. γ is the gas specific heat capacity ratio.

The pressure and temperature relations across the shock wave are given in the following two equations [153]:

$$\frac{P_2}{P_1} = 1 + \frac{2\gamma}{(\gamma+1)}(M_s^2 - 1) \quad (3.2)$$

$$\frac{T_2}{T_1} = 1 + \frac{2(\gamma-1)}{(\gamma+1)^2} \frac{\gamma M_s^2 + 1}{M_s^2} (M_s^2 - 1) \quad (3.3)$$

Theoretically, the flow pressure and velocity crossing the contact surface stay the same. So, $u_3 = u_2$ and $P_3 = P_2$. Additionally, the flow across the rarefaction wave is isentropic and the following equation can be obtained using the isentropic flow relation:

$$\frac{P_3}{P_4} = \left(\frac{a_3}{a_4}\right)^{\frac{2\gamma}{\gamma-1}} \quad (3.4)$$

As illustrated in Figure 3.1 the rarefaction wave propagates toward the end-wall of the driver section in the first place and is reflected backwards when it reaches the end-wall. Along the

Mach waves composing the rarefaction wave, the relation $u + \frac{2}{\gamma-1}a = const$ can be held

and state 3 to state 4 can be related by the following equation [153]:

$$u_4 + \frac{2}{\gamma-1}a_4 = u_3 + \frac{2}{\gamma-1}a_3 \quad (3.5)$$

Based on equations 3.1-3.5, a relation between the initial pressure ratio and the shock wave Mach number M_s can be derived:

$$\frac{P_4}{P_1} = \frac{1 + \frac{2\gamma}{\gamma+1}(M_s^2 - 1)}{\left[1 - \frac{\gamma-1}{\gamma+1} \frac{a_1}{a_4} \left(M_s - \frac{1}{M_s}\right)\right]^{\frac{2\gamma}{\gamma-1}}} \quad (3.6)$$

For the above equations, it was assumed that the same gas is used in the driver and the driven section. On some occasions, different types of gases with different γ values are adopted in the driver section and driven section to get a higher shock Mach number.

$$\frac{P_4}{P_1} = \frac{1 + \frac{2\gamma_1}{\gamma_1 + 1} (M_s^2 - 1)}{\left[1 - \frac{\gamma_4 - 1}{\gamma_4 + 1} \frac{a_1}{a_4} \left(M_s - \frac{1}{M_s} \right) \right]^{\frac{2\gamma_4}{\gamma_4 - 1}}} \quad (3.7)$$

Equation 3.7 [153] gives the relation between the initial pressure ratio and shock wave Mach number M_s in the case that different types of ideal gases are used in the driver section and driven section. It can be seen from Equation 3.7 that, to achieve the highest M_s , the initial pressure ratio P_4/P_1 must be as high as possible. Specifically, when $\frac{P_4}{P_1} \rightarrow \infty$, $M_s \rightarrow \frac{\gamma_1 + 1}{\gamma_4 - 1} \frac{a_4}{a_1}$. Therefore, for a given driven gas, a higher shock Mach number can be obtained by using a light and hot driver gas.

A variety of shock tubes have been used on studies regarding shock and blast wave phenomena worldwide during the past century. Also, shock tubes are being used as a tool to simulate impulses generated by explosions. Because it is difficult to produce an actual explosion outdoor to study the impact of the blast wave overpressure on structures, animals, and other surroundings, shock tube facilities have been utilized to perform laboratory blast testing and develop strategies for mitigating explosion destruction [154-157].

It is worth noting that, in recent years, there has been substantial progress made with regard to developing novel types of shock tubes that are less expensive and easier to operate. Downey, et al. [158] designed a diaphragmless shock tube facility using a novel rapid opening valve which efficiently replacing the function of a bursting diaphragm. The opening time of its design is in the region of 0.5 ms. A similar diaphragmless design concept was proposed at the National Aerothermochemistry Laboratory at Texas A&M University by Taylor [159], employing a shock wave generating mechanism that consists of a rotating door and locking cam-shaft system. Janardhanraj and Jagadeesh [160] proposed a novel concept to generate miniature shock waves using an in situ oxyhydrogen generator. Kai et al. [161] presented a novel shock tube involving laser-induced micro shock waves (LIMS) in a square glass capillary. Shock waves at the scale of several micrometres or even hundreds of

nanometres can be generated by this method.

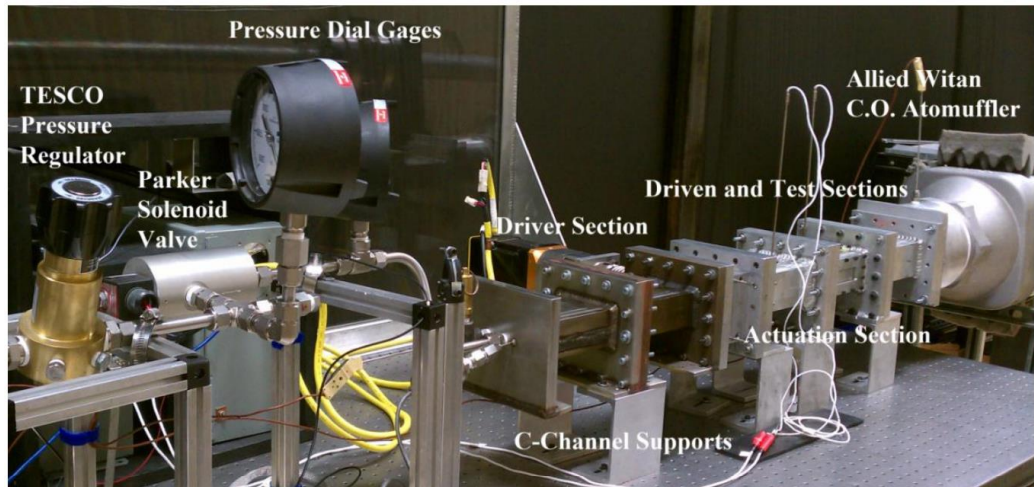


Figure 3.2 A low-duty-cycle diaphragmless shock tube schematic [159]

In this research, a novel concept to design the shock tube using detonation transmission tubing has been proposed and demonstrated [162]. More details regarding the design of the shock tube are given in Chapter 4.

3.1.2 Supersonic wind tunnel

The wind tunnel is a fundamental facility to investigate the aerodynamic properties of flight vehicles. Since the first wind tunnel established in the 1920s, a large amount of valuable experimental data has been collected to replicate various flight conditions and analyse the behaviour of different types of flows.

Wind tunnels are firstly classified into low-speed, transonic, and supersonic wind tunnels based on the flow velocity in the test section[163]. An in-draft supersonic wind tunnel [164] in University of Glasgow was used to conduct the investigation on shock wave and boundary layer interaction over flexible surfaces in this research. As shown in the CAD assembly (Figure 3.3), the wind tunnel has a test section area of $101.60\text{ mm} \times 54.42\text{ mm}$ and 742.95 mm long. There are two nozzles for Mach 2.0 and 4.0 designed based on the Method of Characteristics [165]. The in-draft supersonic wind tunnel mainly consists of following components [164]: (1) drier, (2) settling chamber with honeycomb and mesh screens, (3)

Laval nozzle, (4) test section, (5) diffuser, (6) isolation valve, (7) vacuum chamber and (8) a vacuum pump. With the existing 34 m^3 vacuum tank, the running time of the indraft supersonic tunnel is up to 10s.

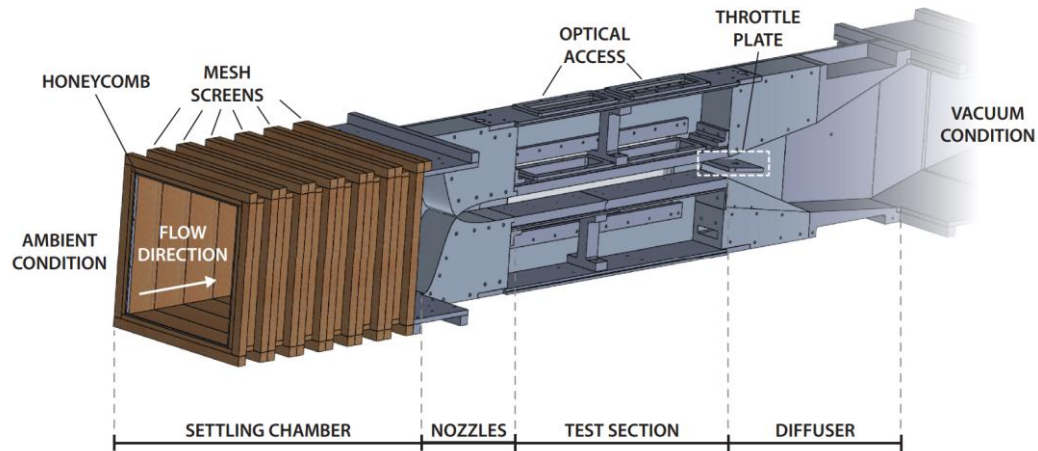


Figure 3.3 CAD assembly of the designed wind tunnel in University of Glasgow [164]



Figure 3.4 Optical windows of the wind tunnel [164]

As shown in Figure 3.4, to perform optical flow diagnostic techniques such as schlieren, PIV, DIC, and PSP, there is optical access on the two side walls and the upper wall.

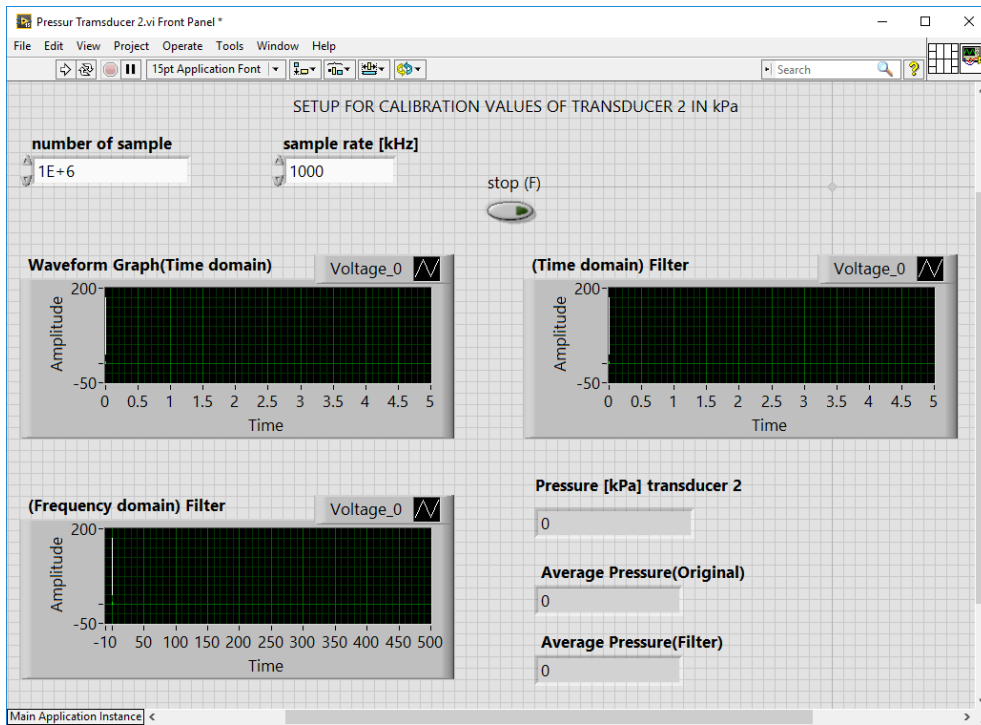
3.2 Flow analysis techniques

3.2.1 Pressure measurement

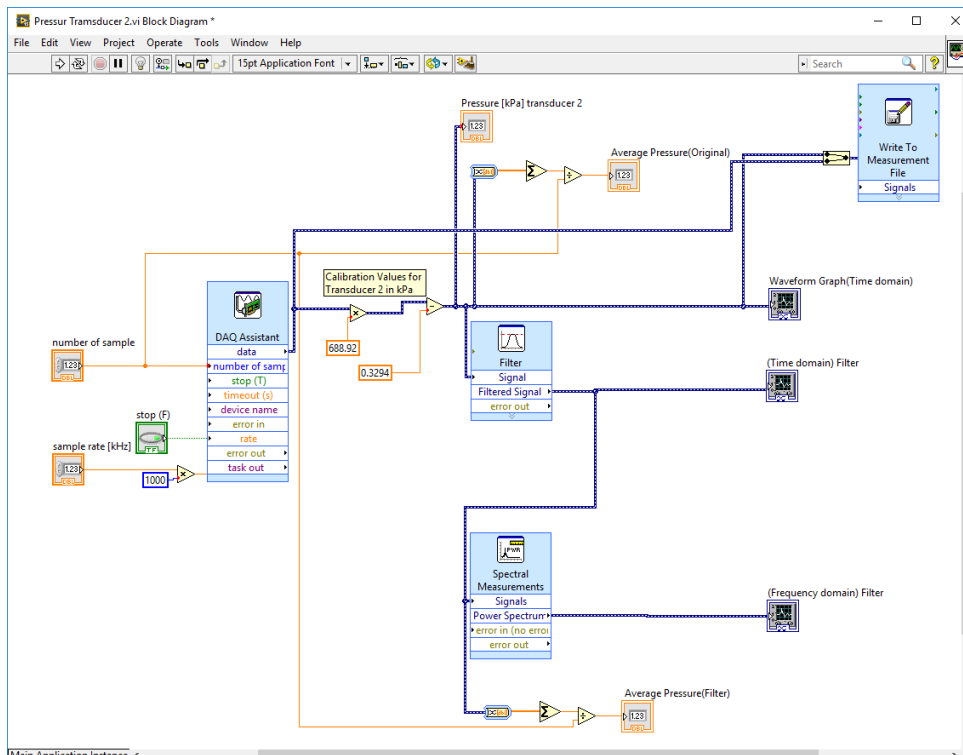
Pressure transducers (Kulite Semiconductor Products, Inc., model: XTE-190M, natural frequency: 175 kHz) were used to conduct the unsteady pressure measurement. The pressure variation was recorded using a data acquisition from National Instruments (model: NI-9178) driven by LabVIEW. NI 9264 was used as the voltage output module, which is a 25 kS/s/ch Simultaneous, ± 10 V, 16-Channel C Series Voltage Output Module. NI 9223 was used as the voltage input module. It is a ± 10 V, 1 MS/s, 16-Bit, Simultaneous Input, 4-Channel C Series Voltage Input Module. The NI-9223 can sample at the maximum sample rate per channel while the module next to it samples at a much slower rate, which is ideal for mixed-measurement test systems. To get high-precision results, the sampling rate of 1 MHz was chosen in this research.

Figure 3.5 shows the front panel and block diagram of the LabVIEW program developed for the real-time data acquisition, processing, and displaying of the unsteady pressure results. Specifically, a moving average (smoothing width is 14) algorithm was employed for the data filter and TDMS was adopted as the file format. DIAdem was selected as the software tool for the post-processing of large pressure data sets. It is a single software tool to quickly locate, load, visualize, analyze, and report measurement data collected during data acquisition and/or generated during simulations. Scripts in DIAdem is a very useful function module to automate repetitive data post-processing tasks and transform measurement data into valuable insights.

Based on the above acquisition and post-processing system, the Kulite XTE-190M pressure transducer was calibrated. The GE Druck DPI 610 portable pressure calibrator was used to provide high-precision calibrating pressures. It is worth mentioning that the density of data points towards the lower-pressure region of the calibration was increased to improve accuracy. The calibration curve of Kulite XTE-190M pressure transducer is given in Figure 3.6 with very good linearity.



(a)



(b)

Figure 3.5 LabVIEW program for pressure data acquisition: (a) front panel; (b) block diagram

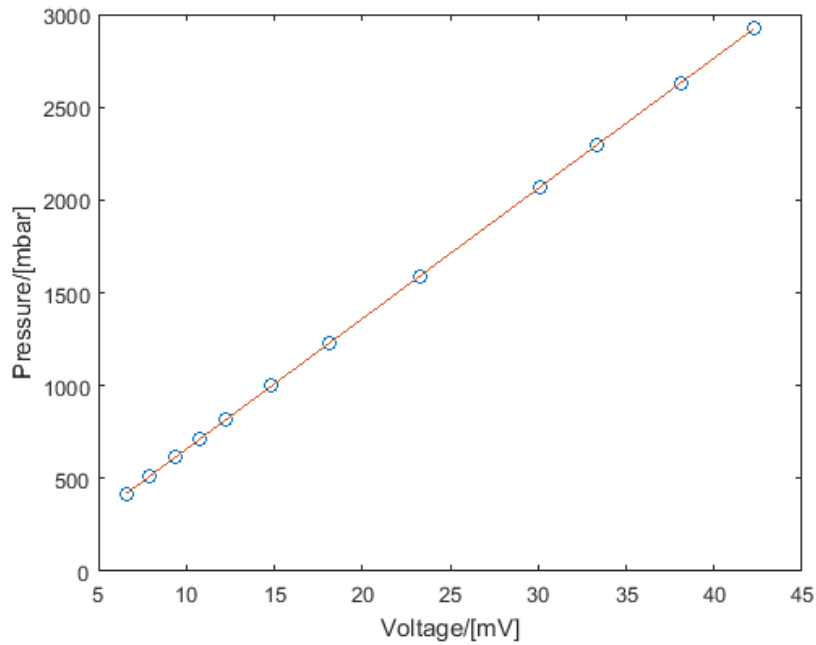


Figure 3.6 Calibration curve of Kulite XTE-190M pressure transducer

3.2.2 Schlieren and shadowgraph photography

Schlieren and shadowgraph were initially introduced by Robert Hooke in the 17th century [166, 167]. Currently, they have become standard laboratory tools for visualizing flow structures of various types of flows base on the flow density gradient.

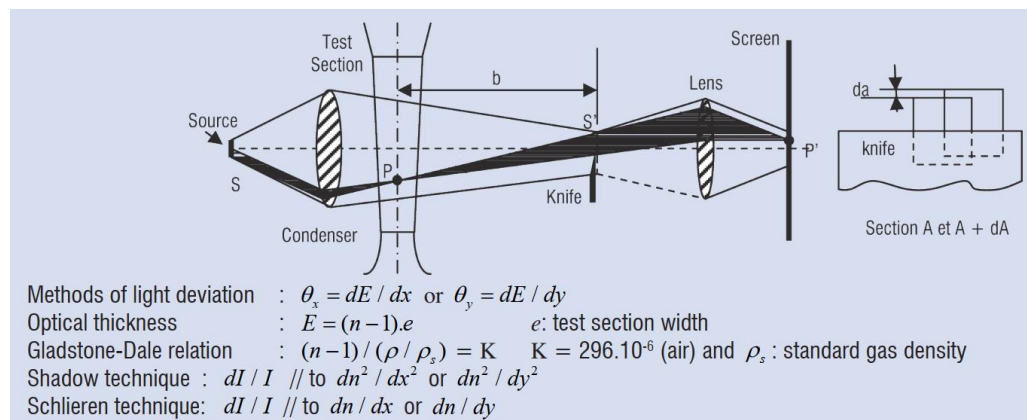


Figure 3.7 Schematic of working principle of schlieren photography [168]

As illustrated in Figure 3.7, the fundamental working principle of schlieren photography involves deflecting some of the light rays and intercepting with a knife [166, 168]. In a schlieren measurement system, an image S' that is cut with a knife is produced from a source S by a condenser. A lens between the image S' and the screen provides an image of the flow field in the test section. The knife intercepts some of the light rays passing through S and the other part converges on the screen (see Figure 3.7). If the flow is two-dimensional, the refractive index n , the gas thickness e , and the optical thickness E are independent of the axis z that is perpendicular to the flow. The Malus theorem [168] proves that the deviations θ_x or θ_y generated by the flow in the test section are equal to $\delta E/\delta x$ and $\delta E/\delta y$ respectively. If the intensity of the source S is not changed, the irradiance I is proportional to the light blocked by the knife. If there is not any density gradient in the test section, section A stays the same. In contrast, section A changes if the light beams are deflected. If b refers to the distance between the test section and the knife and h is the height of section A , the following equation can be derived [168]:

$$\frac{dI}{I} = \frac{dA}{A} = \frac{b}{h} \theta_x = \frac{b}{h} \frac{dE}{dx} \quad (3.8)$$

It can be seen from Equation 3.8 that schlieren photography presents the first derivative of the density for two-dimensional flow.

In the shadow technique, the knife in Figure 3.7 will be removed. The relative irradiance variation is used to determine the contrast on the screen [168]:

$$\frac{dI}{I} = -b \frac{dE^2}{dx^2} \quad (3.9)$$

It can be seen from Equation 3.9 that shadowgraph photography indicates the second derivative of the flow density.

A typical example of the shadow and schlieren results showing the flow structure around an airfoil at a transonic speed [168] is given in Figure 3.8. It can be seen from Figure 3.8 that the schlieren result reveals finer flow details such as the shock wave structure and the flow

separation.

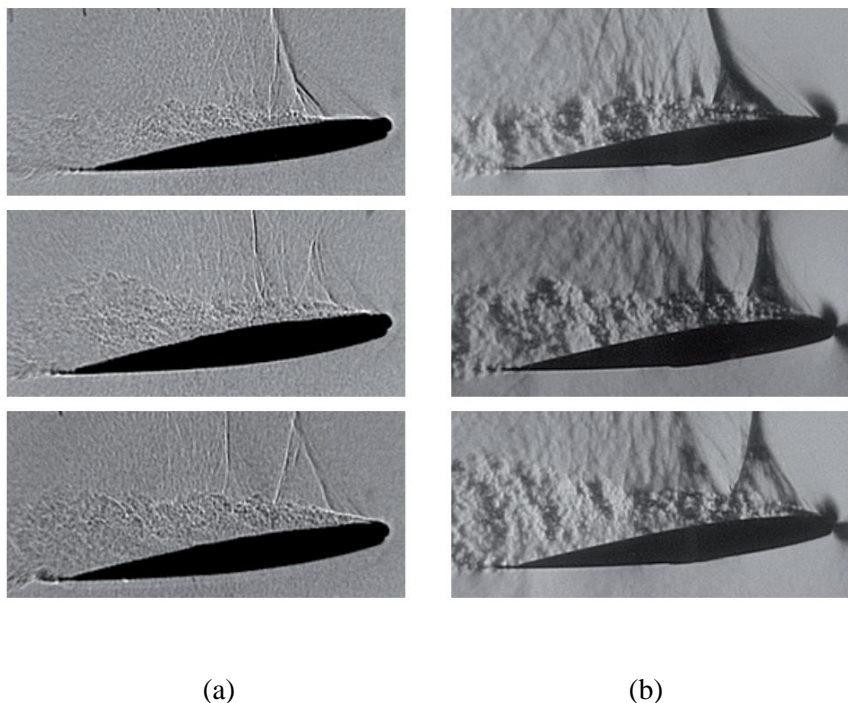


Figure 3.8 Schlieren and shadowgraph techniques applied to an airfoil flow at Mach 0.76 and 8° attack angle: (a) shadowgraph; (b) schlieren [168]

In this research, a high-speed shadowgraph system with a standard Z-type optical arrangement (see Figure 4.5) was used to visualize the supersonic flow, which includes a 450–1000W continuous Xe-Hg arc lamp (Newport, model: 66921), two 203.3 mm diameter parabolic mirrors with a focal length of 1829 mm, and a fast camera (Shimadzu Hyper Vision HPV-1 High-Speed Video Camera). At recording speeds in the range 30 to 1 million fps, the HPV-1 produces high-definition images at a resolution of 312×260 - up to 80,000 pixels per image. With storage capabilities built directly into the camera's imaging chip, 100 monochrome shots can be saved in BMP, TIF or AVI formats. To synchronize the high-speed camera, the pressure rising signal in the supersonic flow was employed to trigger the camera. A signal conditioner for converting the rising voltage output of the pressure transducer into a 5V TTL signal was specially designed.

Generally, schlieren and shadowgraph were thought to be mere qualitative visualization methods lacking quantitative power. In order to process a large number of the high-speed

schlieren and shadowgraph frames automatically, software for the automatic shock wave detection and tracking was developed in this dissertation based on MATLAB image processing toolbox. More details regarding the involved image processing procedure and algorithms are given in Chapter 6.

3.2.3 Background oriented schlieren (BOS)

The background-oriented schlieren technique was invented almost simultaneously in England and Germany at the end of the 20th century [167]. It is based on the Lorentz–Lorenz equation, which describes the relation between the fluid refractive index and its density. Compared with the aforementioned schlieren or shadowgraph techniques, the recording of the BOS method is simplified.

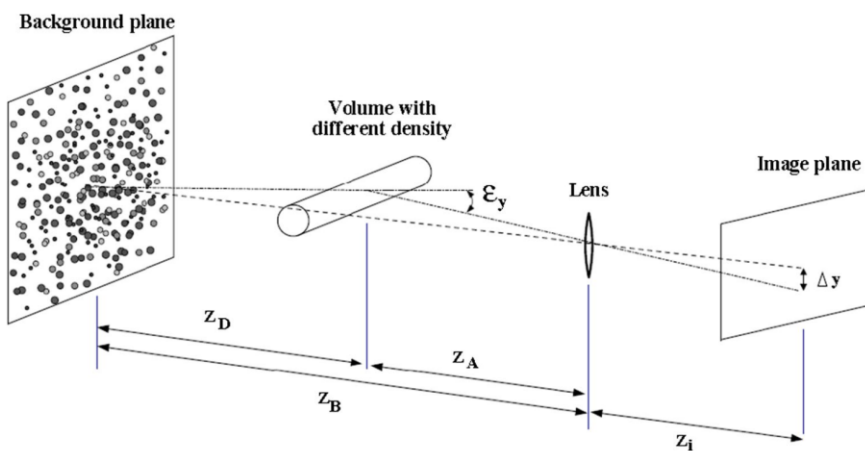


Figure 3.9 BOS imaging configuration [169]

The first step of a BOS recording is usually to generate a reference image by recording the background pattern without the flow in advance of the test. In the second step, the displaced test image of the background pattern under the flow will be captured. The image pair then is evaluated by image correlation methods. Image correlation and optical flow algorithms commonly used in PIV can directly be applied to compute the displacement distribution of the background patterns in BOS. Figure 3.9 demonstrates the typical BOS imaging configuration.

In the case of small deflection angles ($\varepsilon_y \approx \tan \varepsilon_y$), the image displacement Δy can be calculated by the following equation [170]:

$$\Delta y = Z_D M \varepsilon_y \quad (3.10)$$

Where $M = Z_i/Z_B$ is the magnification factor of the background, Z_D is the distance from the measured flow field to the dot pattern, Z_i refers to the distance from the dot pattern to the image plane and Z_B refers to the distance between the dot pattern and the target object. The deflection angle ε_y is determined by the following formula [169]:

$$\varepsilon_y = \frac{1}{n_0} \int \frac{\partial_n}{\partial_y} d_z \quad (3.11)$$

Thus, the displacement of the background pattern Δy can be rewritten as:

$$\Delta y = f \left(\frac{Z_D}{Z_D + Z_A - f} \right) \varepsilon_y \quad (3.12)$$

where Z_A is the distance between the measured flow field to the lens, f refers to the focal length of the lens. It can be seen from Equation 3.12 that increasing Z_D or decreasing Z_A can enhance the overall sensitivity of the BOS system with a larger displacement Δy . To calculate the image displacement distribution accurately, the background pattern has to be imaged with good contrast. If the BOS imaging system is focused on the dot pattern, the following equation should be satisfied [169]:

$$\frac{1}{f} = \frac{1}{Z_i} + \frac{1}{Z_B} \quad (3.13)$$

Ideally, the BOS imaging system also detects sharp density gradients at Z_i :

$$\frac{1}{f} = \frac{1}{Z_i} + \frac{1}{Z_B} \quad (3.14)$$

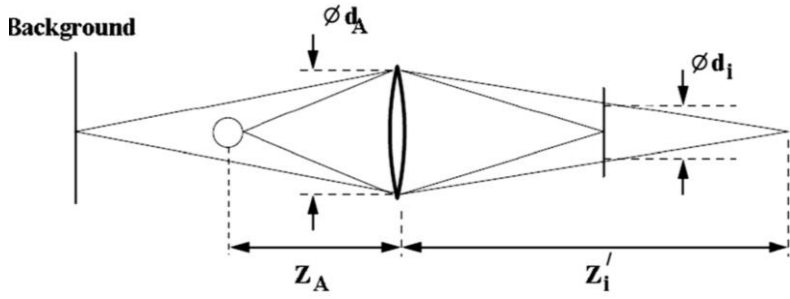


Figure 3.10 BOS focusing position and image blur [169]

This focusing problem of the BOS system is illustrated in Figure 3.10. Since the system is usually focused on the background to obtain a good correlation result, the contrast of the test model and flow field becomes limited. The geometric blur d_i (Figure 3.10) of a point at Z_A can be defined as the following formula [169]:

$$d_i = d_A \left[1 - \frac{1}{f} M' (Z_A - f) \right] \quad (3.15)$$

Where d_A is the aperture diameter and $M' = Z'_i / Z_A$ is the magnification of the density gradient imaging. Furthermore, the capability of detecting small-scale displacements in the background pattern is limited by diffraction. The following equation [169] can be derived to determine the diffraction limited minimum image diameter d_d :

$$d_d = 2.44 f / d_A (M + 1) \lambda \quad (3.16)$$

where λ is the light wavelength. The overall image blur d_Σ can be determined by the following Equation [169]:

$$d_\Sigma = \sqrt{d_d^2 + d_i^2} \quad (3.17)$$

There has to be a trade-off to optimize the image sharpness in BOS system [169]: increasing the aperture diameters d_A reduces the diffraction (Eq. 3.16), but produces a larger geometric blur d_i (Eq. 3.15). For most of the BOS systems, the latter effect is stronger. Therefore, a

small aperture diameter d_A is typically applied for BOS image acquisition, which means stronger illumination should be provided. Because the image correlation process averages over interrogation windows, the interrogation window size should be considerably larger than the overall image blur d_Σ .

Based on the aforementioned fundamental principle, the background-oriented schlieren (BOS) technique has been widely used in various wind tunnel tests [171-176] and scientific researches [177-179] due to its simplicity, flexibility, and non-intrusive nature. Unlike traditional schlieren photography, the BOS technique can obtain a very large field of schlieren view without large, expensive, and precision optics [180-182]. It also can provide unique solutions to some problems, including the large fields-of-view just described, as applied to aircraft and outdoor explosions [183-185], and schlieren imaging inside the test sections of large industrial wind tunnels [172, 186]. For example, slotted or perforated transonic test sections [171], which can be as large as 5 m across, generally have no sufficient optical access for conventional schlieren or shadowgraph techniques. Furthermore, two novel BOS systems, air-air and ground-to-air, have been proposed by NASA to investigate the shock wave structures of supersonic jets interacting in flight tests [174, 181, 182, 186]. These techniques can be used to test the design of future supersonic transport.

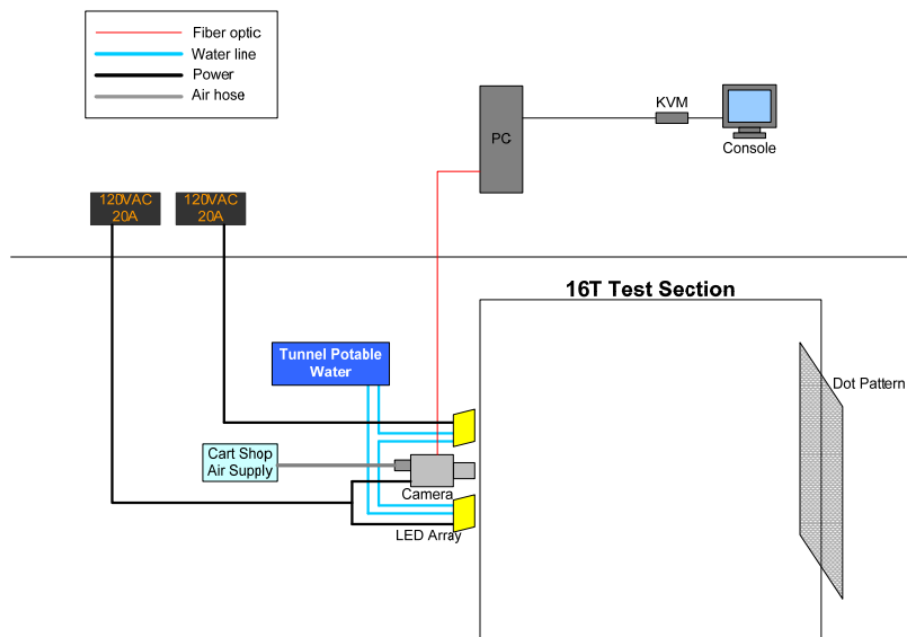


Figure 3.11 BOS system of AEDC 16T propulsion wind tunnel (looking downstream) [171]



Figure 3.12 Randomized dot pattern (top) applied to starboard wall (bottom) of NASA National Transonic Facility for capsule wake RBOS test [172]

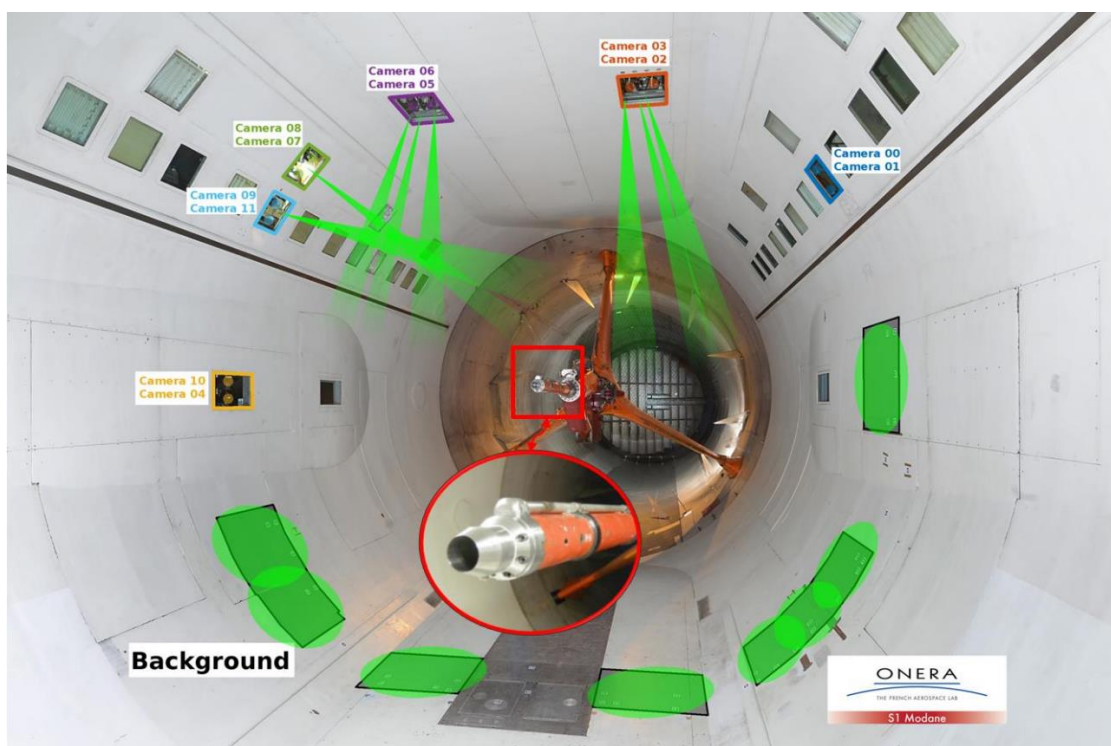


Figure 3.13 3D BOS setup of ONERA's S1MA wind tunnel [173]

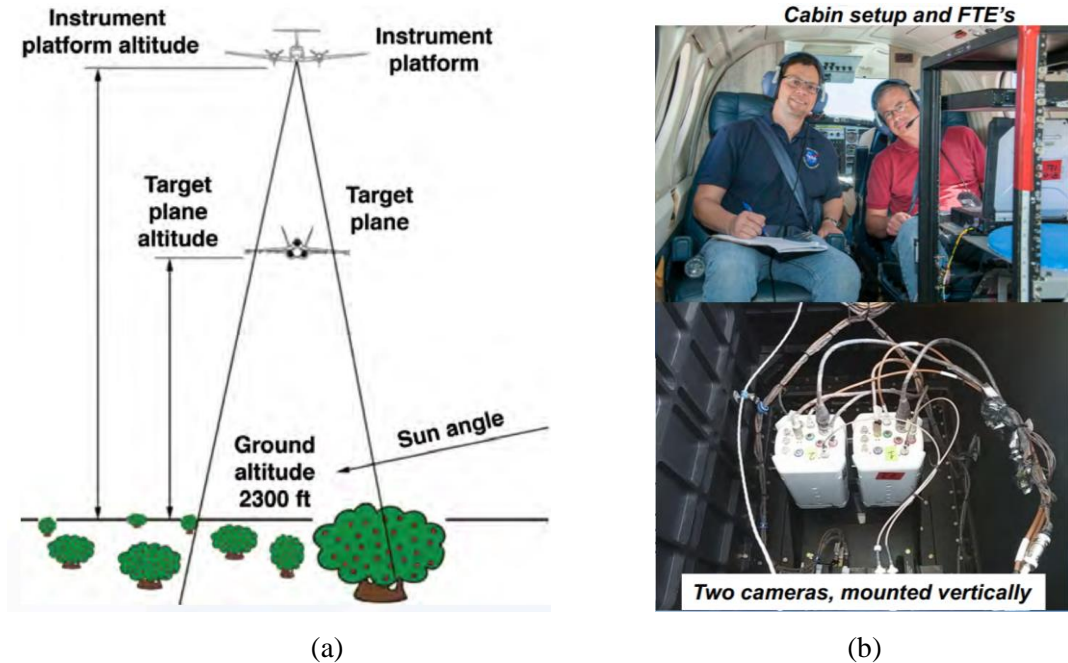


Figure 3.14 NASA air-to-air BOS setup: (a) aircraft positioning; (b) cabin setup [174]

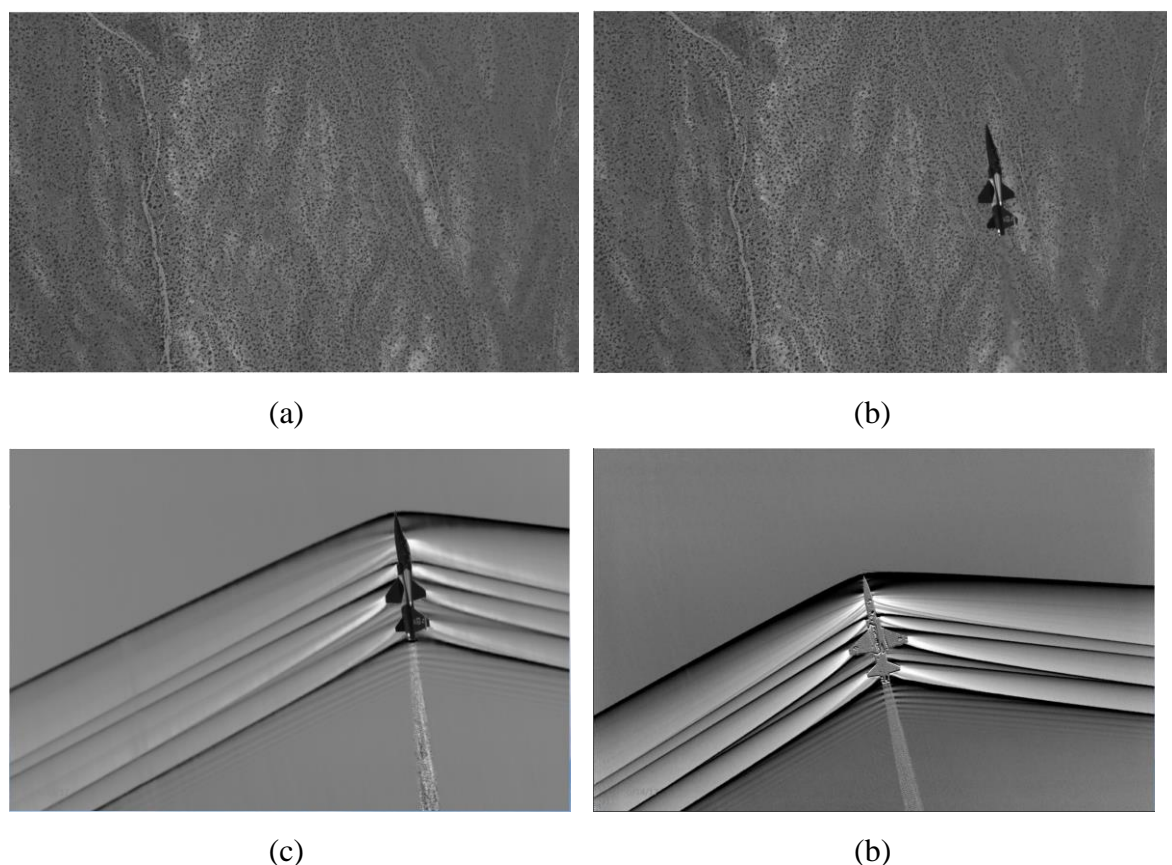


Figure 3.15 NASA air-to-air BOS system for a supersonic jet flying over the Mojave Desert: (a) natural background; (b) fly image; (c) result by cross-correlation, dy ; (d) result by optical flow, dy

[174]

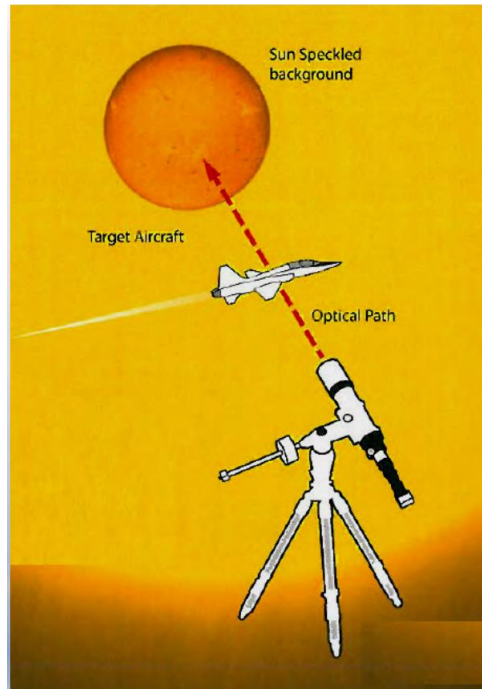


Figure 3.16 Working principle of ground-to-air BOS system using celestial objects [181]



Figure 3.17 Flow structure of a supersonic jet from ground-to-air BOS system using celestial objects [181]

In this dissertation, a BOS system was built up preliminarily in the indraft supersonic wind tunnel of the University of Glasgow (Section 3.1.2). More details regarding this BOS system are presented in Chapter 5.

3.2.4 Unsteady pressure sensitive paint (PSP)

Pressure-sensitive paint (PSP) is an optical measurement technique for global surface pressure measurements in wind tunnel testing. As shown in Figure 3.18, the working principle of PSP is the oxygen quenching of the luminescence molecules in the paint. Luminescence intensity emitted by the pressure sensitive paint decreases as the local air pressure increases because of the oxygen quenching. Then, the surface pressure of objects can be determined by the paint luminescence intensity detected by a camera. In the late 1980s and early 1990s, conventional steady pressure sensitive paints were first used to wind tunnels [187, 188]. The spatial resolution of the global surface pressure map provided by PSP is mainly limited by the spatial resolution of the photodetector, which is much higher than that of traditional pressure taps.

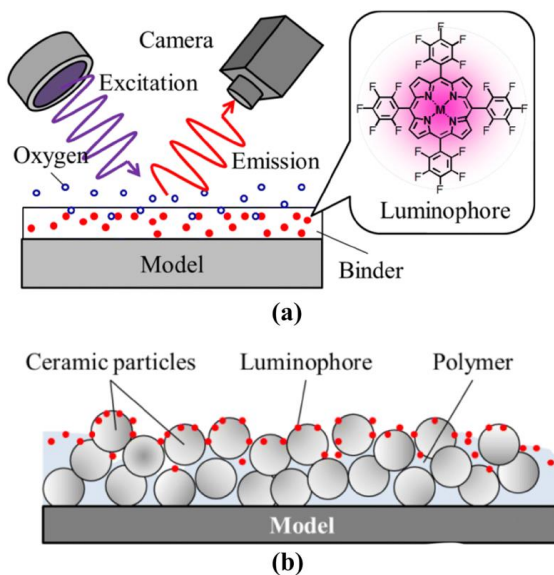


Figure 3.18 Schematic of PSP system: (a) steady PSP; (b) unsteady polymer-ceramic PSP [188]

Steady pressure sensitive paint generally consists of two components: the luminophore and a polymer binder for adhering the luminophore molecules to the model surface. The response time of steady pressure sensitive paints is largely determined by the gas diffusion rate of the polymer binder. Conventional, steady PSP formulations have a response time in the magnitude of seconds, however, a lot of aerodynamic phenomena are highly unsteady and

require a much faster PSP measurement system [189-202]. Also, facilities that have a short test time such as shock tunnels and shock tubes need a fast-responding pressure sensitive paint [203, 204]. Figures 3.19-3.21 present typical unsteady PSP systems and results from NASA wind tunnel facilities. In this research, an unsteady PSP system was developed to investigate the fluctuating pressure loading on the flexible surfaces due to the unsteady shock wave and boundary layer interactions.



Figure 3.19 Unsteady pressure sensitive paint applied to generic launch vehicle model in the 11- by 11-foot Transonic Wind Tunnel at Ames Research Center [189, 190]

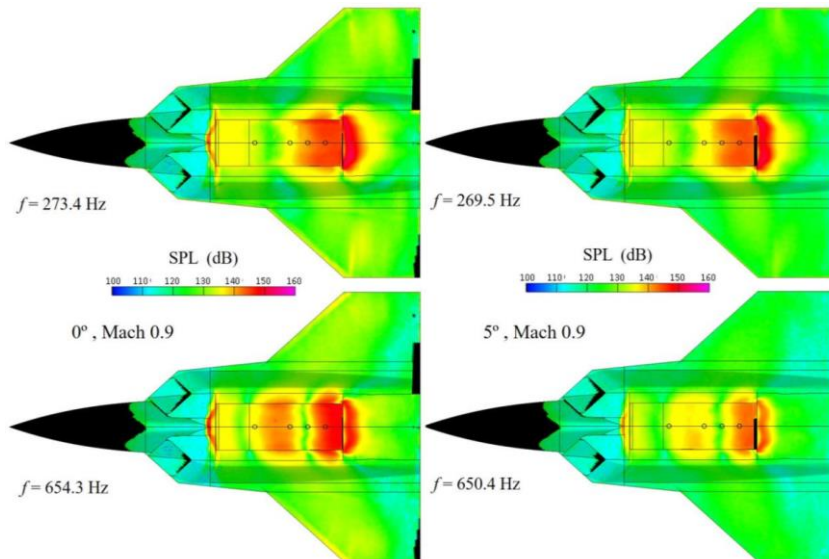


Figure 3.20 Fast PSP results from AEDC 16T test showing the amplitude of the pressure fluctuations at the first two Rossiter frequencies [191]

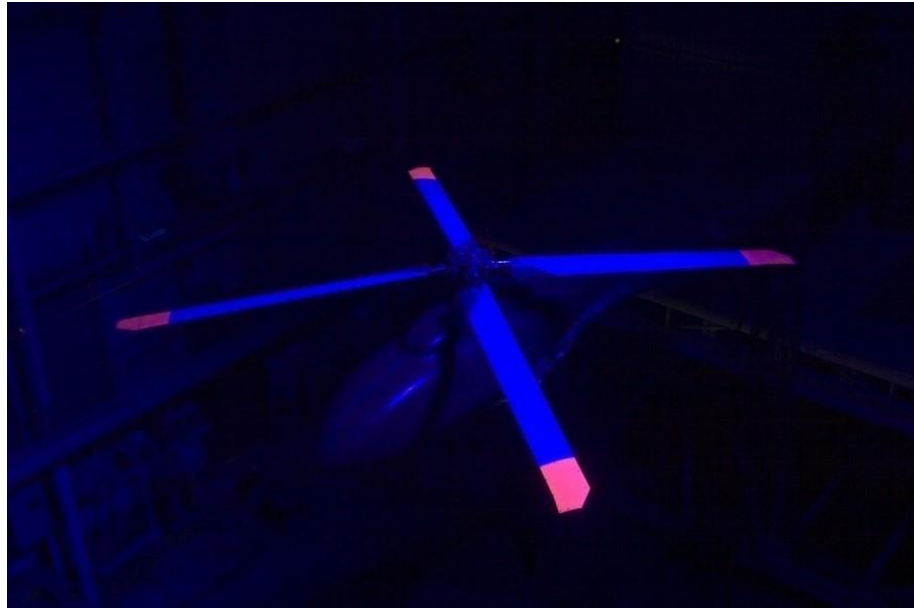


Figure 3.21 Unsteady pressure-sensitive paint covers the blade tips of a helicopter being tested in a wind tunnel at NASA's Langley Research Center in Virginia [192]

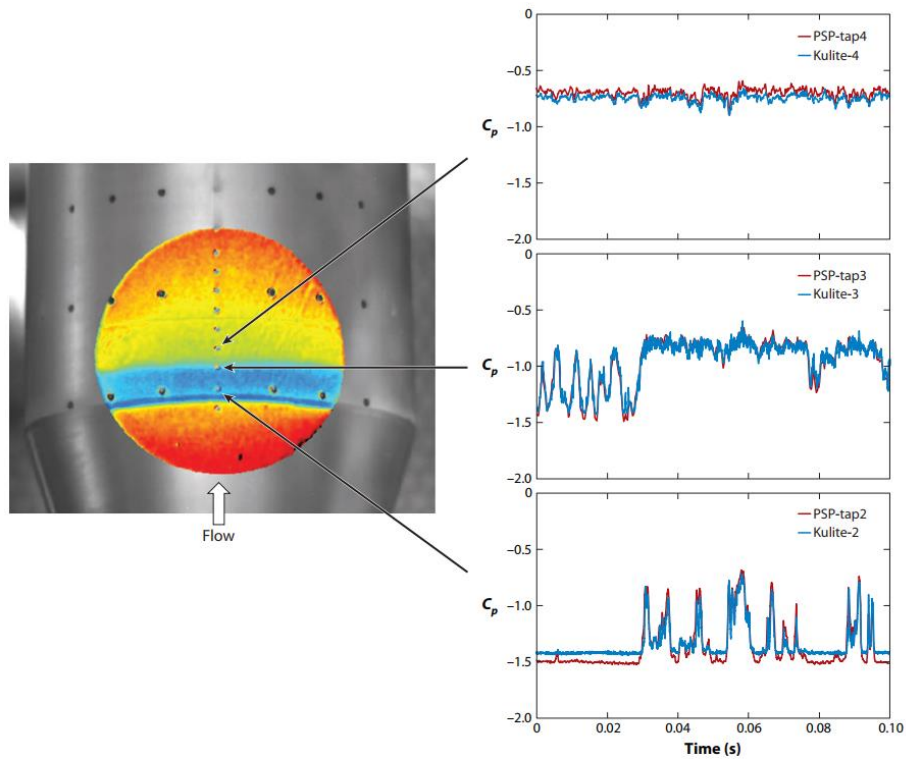


Figure 3.22 Map of pressure coefficients on a rocket fairing model in unsteady transonic flow: the left image shows an instant of the PSP data demonstrating the shock/boundary layer interaction and the right plots show the pressure coefficients at three locations as a function of time [198, 205]

The paint is the core of the unsteady PSP measurement system. Great efforts have been made to improve the timescale of gas diffusion for unsteady PSP formulations. As discussed above, the characteristics of the polymer binder determine the gas diffusion rate of the paint, but the lifetime of the pressure sensitive paint luminophore becomes equally crucial [206, 207], which stands for the physical limit of the attainable temporal resolution of the pressure sensitive paint. Three types of pressure sensitive probes have been applied: pyrene, porphyrin and ruthenium complexes [188]. The binder commonly used for unsteady PSP can be divided into two categories: porous ones and polymer ones with high oxygen permeability. These two types of fast PSPs are summarized below:

Porous fast Pressure-Sensitive Paint

The schematic of the unsteady PSP utilizing a porous binder is shown in Figure 3.23. Luminophore can be directly applied to the large surface area of the porous materials. The oxygen molecules in the air directly quench luminescence. The response time of this type of unsteady PSP is of the order of 1 μ s. A great variety of materials have been selected as porous PSP binders, including a thin-layer chromatography (TLC) plate [208], hydrothermal coating [209], sol-gel [210], anodized aluminium (AA) [211, 212], anodized titanium, polymer/ceramic (PC) [213], and porous filter. PC-PSP is the most popular option due to its simplicity and applicability.

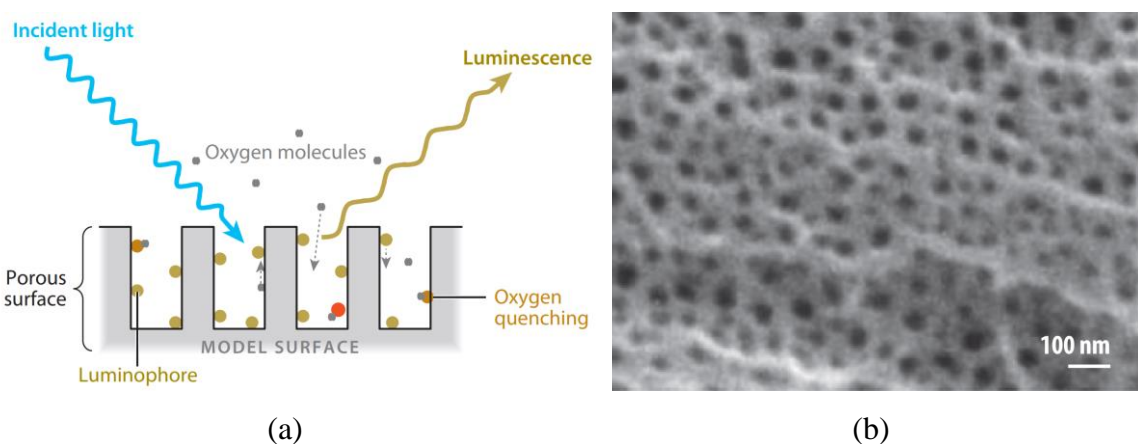


Figure 3.23 PSP with porous material as a binder: (a) schematic illustrations; (b) scanning electron micrographs [214]

TLC is commercially available and can be easily applied by dipping the test model into the

PSP luminophore solution. However, it only can be used for simple geometries because of its brittle nature [215-217]. For the AA-PSP, a thin aluminum oxide layer with 10- to 100-nm micropores is produced by an electrochemical anodization process [214] (see Figure 3.24). The preparation process of AA-PSP is relatively complicated and usually consists of the electrochemical anodization of the test model, the modification of the model surface using phosphoric acid, and dipping the model in the luminophore solution [193, 218]. The static properties of AA-PSP can be affected by the luminophore dipping process [219]. The lifetime of AA-PSPs with organic pressure sensitive luminophores is of the order of 1 ns [198].

Although TLC-PSP and AA-PSP have a very short lifetime, the requirements of test model material limit their extensive applications, leading to the motivation for developing the polymer/ceramic pressure-sensitive paint (PC-PSP) that can be sprayed onto any metal materials. Scroggin et al. initially proposed a PC-PSP formulation based on a tape casting procedure [213]. Gregory et al. improved the paint formulation and directly sprayed the paint onto the model surfaces [220]. Unsteady PC-PSP is also commercially available from Innovative Scientific Solutions, Inc. [221]. It is interesting to note that a novel paint formulation based on nanoscale ceramic particles was proposed by Kameda et al. [222], which is similar to PC-PSP, but no polymer binder is added.

Polymer-Based fast Pressure-Sensitive Paint

The other approach for developing porous unsteady PSP formulations is based on polymer binders that have very high oxygen permeability [223, 224]. For example, the gas permeability of Poly(TMSP) [poly(1-trimethylsilyl-1-propyne)] is around 10 to 50 times higher than polystyrene and silicone [224-227], which are two conventional polymers used in steady PSP. The temperature sensitivity is a major error source in the unsteady PSP measurement [188]. This problem can be solved by developing PSP formulations with small temperature sensitivity. Biluminophore PSP, in which pressure sensitive luminophore and temperature sensitive luminophore are mixed, has been developed to address this problem [228-230]. However, for most biluminophore PSPs, there is a problem of overlapped spectra of two types of luminophores [231], which limits the performances of the paints.

In this research, a novel PC-PSP formulation, in which the PtTFPP and mesoporous silica are selected as the luminophore and ceramic respectively, is proposed and demonstrated. The formulation and characteristics of this novel PC-PSP will be discussed in Chapter 5.

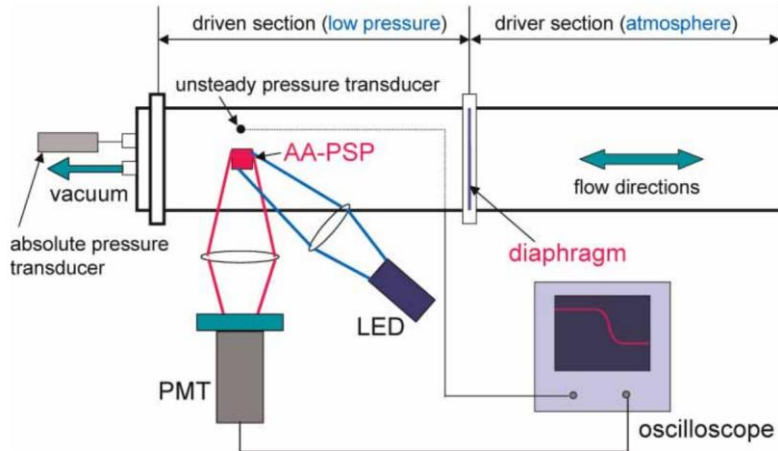


Figure 3.24 Typical experimental setup of shock tube for response time calibration of PSP [193]

After an unsteady PSP formulation is developed, dynamic calibration should be conducted to measure its response time. During the dynamic calibration, the PSP response is compared to the known standard pressure field produced by the calibration device and then the amplitude and phase delay of the PSP signal can be determined. Shock tube is the most popular dynamic calibration equipment [216, 232-234]. The shock wave generated in the shock tube provides a steep pressure variation. The luminescent intensity of the paint is usually detected via a photomultiplier tube (PMT). The response time of the unsteady PSP can be measured by shock tube accurately, however, frequency response characteristics including the phase and amplitude delay are not attainable. Fluidic oscillator is the other option for PSP dynamic calibration [235, 236]. The typical operating range of the oscillating jet is of the order of 1–10 kHz and the frequency increases with the supply pressure. The oscillation frequency is also influenced by the size of the oscillator. The acoustic standing wave tube [237-240] is also used recently in unsteady PSP dynamic calibrations. The amplitude and phase delay of the paint can be directly tested as a function of frequency. Mechanical shaker [241] is a similar method to provide pressure fluctuations for determining PSP dynamic properties.

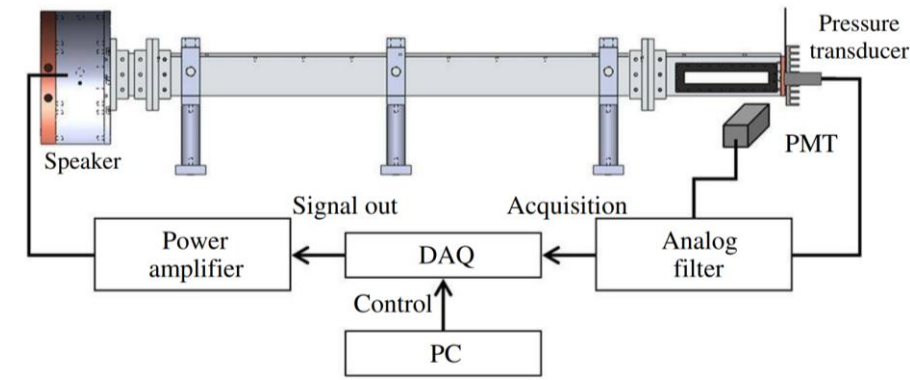


Figure 3.25 Acoustic tube for response time calibration of PSP [237]

In this work, a PSP dynamic calibration system is established preliminarily based on a novel type of shock tube driven by detonation transmission tubing. The experimental setup is detailed in Chapter 5.

Chapter 4

Design of a novel shock tube driven by detonation transmission tubing

4.1 Overview of the experimental facility

As discussed in Section 3.1.1, the shock tube has proven an exceptionally valuable facility for simulating blast waves and shock waves which can be directed and measured to study flow effects under laboratory conditions [242-244]. It also can be used to study aerodynamic flow in a wide range of temperatures and pressures that are difficult to obtain in other types of testing facilities [245-254]. Furthermore, it has been used in medicine, biology, and industry for various applications [154-156, 255-258].

Generally, a typical compressed-gas driven shock tube consists of two sections: one called the driver section and the other called the driven section. The driven section initially containing the test gas (low pressure chamber) is separated by a diaphragm or a fast-acting valve from the driver section (high pressure chamber). After the diaphragm ruptures, the driver gas expands into the low-pressure chamber, acting as a piston and generating a shock wave. However, conventional compressed-gas driven shock tubes are generally large in size and have a high cost of conducting tests and maintenance.

The present study proposes and demonstrates a novel concept to design the shock tube using a commercially available and cost-effective detonation transmission tubing [162]. Actually, detonation transmission tubing had been applied to generate micro-blast waves or small-scale explosion in previous studies [253, 259, 260]. Takahiro Ukai et al. had attempted to use the shock tube based on the detonation transmission tubing for the first time to investigate shock wave distortion in shock-square vortex loop interaction in the University of Glasgow [253]. However, detonation transmission tubing has not been taken as a real shock tube design concept yet and the properties and capabilities of this type of shock tube have not been studied so far. In this work, a novel type of shock tube driven by detonation transmission tubing was proposed. More specifically, two different shock tubes with a circular and square cross-section respectively were manufactured to simulate different engineering application occasions. Overpressure measurement in the driven section of the shock tubes is performed using a dynamic Kulite pressure transducer and time-resolved shadowgraph tests were conducted to study the properties and capabilities of the shock tube. For the shadowgraph image processing, an in-house developed software [261] based on MATLAB GUI and digital image processing techniques was used for shock wave detection and tracking.

4.2 Design details

Detonation transmission tubing is a safety explosive material widely used for detonator initiating and non-electric network igniting. It can be used in the blasting operation site where no explosion hazard of marsh-gas, coal-dust, or other inflammable mine dust exists. It has good or strong resistance to static electricity, stray current, high and low temperature, and oil corrosion, which makes it applicable in various environments. In this research, the non-electric (NONE) detonation transmission tubing system, a combination of NONE lead line and the blasting machine, is used to provide high pressure and temperature gas for shock tubes, acting as the driver section.

Figure 4.1 demonstrates the working principle of the shock tube driven by detonation transmission tubing. Unlike conventional compressed-gas driven shock tubes, the proposed shock tube is driven by detonation transmission tubing and there is no need for storage of

high pressure gases for shock wave generation. Detonation transmission tubing, also known as NONEL tube (M/s Dyno Nobel, Sweden), consists of an annular, small diameter, plastic tube (inner diameter: $ID = 1.3$ mm, outer diameter: $OD = 3$ mm) coated on the innermost wall with a reactive explosive compound, which, when ignited, propagates a low energy signal, similar to a dust explosion. The reaction travels at approximately 2,000 m/s along the length of the tubing with a minimal disturbance outside of the tube. The explosive mixture, about 18 mg/m, is predominantly high-melting explosive: HMX (~92 % by weight), along with traces of aluminium (~8% by weight). The detonation is initiated by an electronic blasting machine, DynoStart 2, with an output voltage of 2500 V. As shown in Figure 4.1, when the micro explosive is electrically triggered from one end of the polymer tube, the sudden expulsion of combustion gases which are in a state of high temperature and pressure act as compressed gases in the conventional shock tube, pushing the ambient air and eventually leading to the formation of a hemispherical blast wave. After releasing from NONEL tube end, the blast wave is diffracted and turns to a bigger spherical shape as it travels. G. Jagadeesh et. al [260] visualized the propagation of the blast wave from NONEL through schlieren photography. The result demonstrated the diffraction process of the blast wave from the NONEL tube end, in which the propagation of the blast wave varies along different azimuths. As soon as the blast wave impinges on the wall of the driven section, it becomes increasingly even. Eventually, the blast wave front forms an approximately flat plane except for a small deflection in the boundary layer next to the inner surface. In a similar way to the compressed-gas driven shock tubes, the shock wave gives to the air in the driven section a brutal acceleration accompanied by a jump of temperature, pressure and density and the air flow in the driven section is limited by a contact surface separating this flow from the driver combustion gas.

It is worth mentioning that the effect of viscosity results in the formation of a boundary layer on the shock tube inner wall, which interacts with the shock wave and has a significant impact on the flow development inside the shock tube. A lot of theoretical and experimental studies have been conducted regarding boundary layer development behind the incident shock for conventional compressed-gas driven shock tubes, demonstrating that such a shock-induced boundary layer is generally laminar in the first place and then transit to a turbulent one after a short distance [262-265].

It is also important to investigate the boundary layer condition inside shock tube facilities driven by detonation transmission tube. However, since the shock tube facilities established in this research don't have enough optical access, the flow pattern including the boundary layer development inside this novel type of shock tube is not capable of being visualized. Therefore, the growth of the boundary layer was not sketched in the schematic of the working principle of the shock tube driven by NONEL tube. Next, shock tubes with longer optical access or even fully made up of transparent glass will be designed to study the boundary layer development, whether the boundary transition occurs or not, and how the shock wave and boundary layer interaction influence the flow structure inside the shock tube driven by NONEL tube.

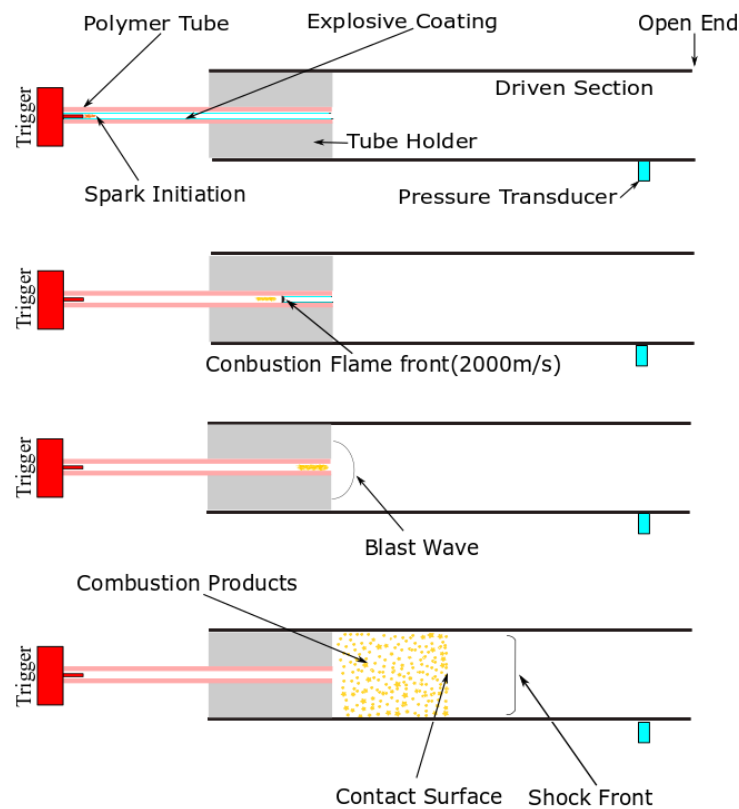


Figure 4.1 Working principle of the shock tube driven by detonation transmission tubing [162]

Several rules need to bear in mind for the design of shock tubes driven by NONEL tube: (i) A sufficient distance should be ensured between the NONEL tube end and the shock tube exit to form a planar shock wave inside the shock tube, which determines the minimum

length of the driven section. Besides, the driven section still needs to have proper sizes for mounting pressure transducer, thermometers, or optical windows for flow visualization if needed. (ii) There is a minimum ratio of the length of the NONEL tube to the diameter of the driven section. A minimum length of NONEL tube is needed to generate enough explosion energy, hence to produce sufficient high temperature and pressure gas for forming a shock wave. The explosive material coated on the inner wall of the NONEL tube can generate a shock front that propagates at a typical speed of 2000 m/s after ignited. G. Jagadeesh et. al [266] found that 1.6 mg of TNT is equivalent to 1 mg of HMX which is the primary component of NONEL explosive material and a minimum length of around 55mm is needed to reach a detonation velocity of 2000 m/s inside the tube. Therefore, the NONEL tube length must be larger than this value. (iii) The final shock wave Mach number is determined by the length of NONEL tube and sizes of the driven section. It is also crucial to limit the NONEL tube length, preventing the overpressure magnitude in the driven section exceeding the measuring range of pressure transducer or even the design load limit of the driven section.

Based on the aforementioned principles, two shock tube facilities driven by detonation transmission tubing were designed and manufactured. One is circular cross-sectional and the other is square. Sizes of the circular and square shock tubes designed in this work were preliminarily decided by empirical regulations for conventional compressed-gas driven shock tubes [110, 267, 268]. In the future, we aim to develop numerical tools to investigate the difference of the internal flow through a shock tube driven by NONEL and a conventional one. Based on these tools, how to determine the optimum shock tube diameter and length of the NONEL tube can be studied as well.

Figure 4.2 illustrates the assembly of the circular cross-section shock tube. More design details are given in Appendix A.1. To align the central axis of the flexible NONEL tube with that of the driven section, the NONEL tube was inserted into a stainless steel hypodermic tube holder ($ID = 3\text{ mm}$, $OD = 22\text{ mm}$, length $L_h = 140\text{ mm}$), followed by a circular cross-sectional driven section ($ID = 22\text{ mm}$, $OD = 25\text{ mm}$). More specifically, the NONEL tube was stably fixed during the detonation using a screw on the sidewall of the tube holder and a pressure transducer (Kulite Semiconductor Products, Inc., model: XTE-190M) was mounted 50mm from shock tube exit to record the pressure-time histories in the driven

section for estimating the shock Mach number M_s . In addition, two through holes were manufactured at two sides of the leading edge of the driven section, whereas two lines of blind thread holes were manufactured at two sides of the tube holder with a 50mm interval, which makes the relative position between these two components changeable.

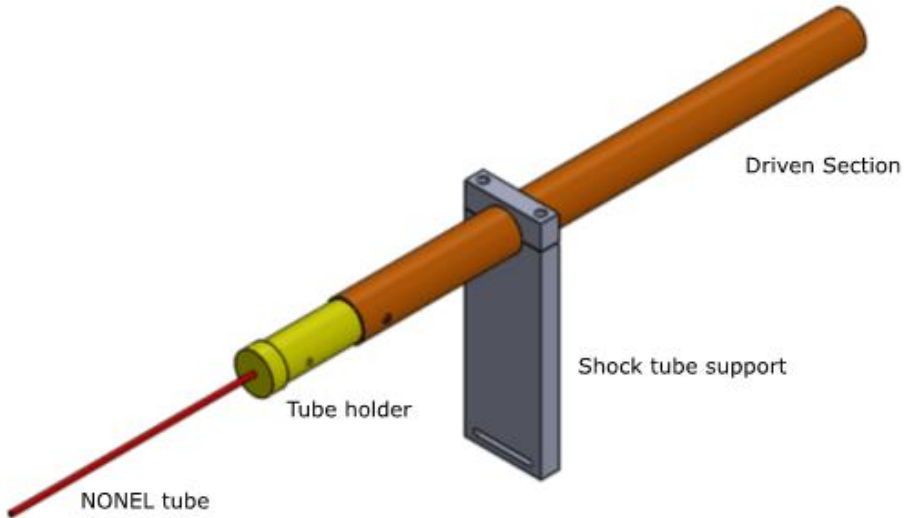


Figure 4.2 Assembly of the circular cross-section shock tube [162]

The circular shock tube is a very useful experimental facility to simulate compressible vortex rings [67, 245, 269-273] and axisymmetric supersonic jets, which have been applied in many practical applications, including jet and rocket propulsion, projectile launch, mixing augmentation, enhanced combustor performance and thrust vector control [67-71]. However, previous studies have demonstrated that the major flow structure of a jet is strongly related to the curvature of the nozzle geometry [72]. Actually, as an efficient method of passive flow control, non-circular jets, such as elliptical, rectangular, square, and triangular jets, have been extensively studied to enhance the mixing and entrainment rate [73-78]. Zare-Behtash et al. [67, 79] investigated the flow properties of non-circular vortex loops from square, elliptic, and exotic nozzle geometries. Zhang et al. [80] numerically investigated the flow characteristics of supersonic jets with different geometries and demonstrated that mixing can be accelerated by the counter-rotating stream-wise vortices generated by a square vortex loop. Therefore, the nozzle geometry has a significant impact on the flow properties from the nozzle exit.

Rectangular supersonic jets have been widely used in a great variety of applications including thrust vector control [75], jet noise suppression [274,275], combustion [276, 277] and lift augmentation. In order to investigate the blast wave and jet flow of rectangular supersonic jets, a square cross-section shock tube [253] was fabricated (see Appendix A.2) as well in this research. The square shock tube with side length $d = 22$ mm has a 200mm long driven section and a tube holder section for fixing the NONEL tube (see Figure 4.3). A flush-mounted pressure transducer was placed 50 mm from the driven section exit to measure the overpressure magnitude in the driven section.

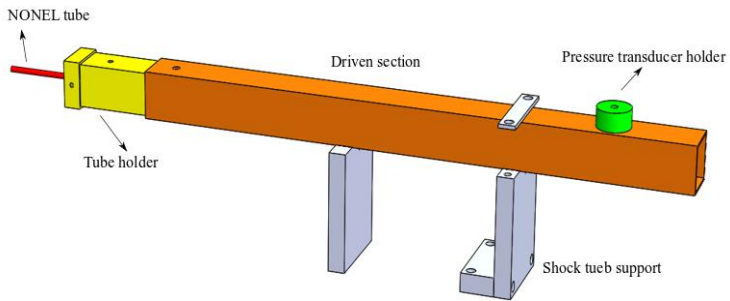


Figure 4.3 Assembly of the square cross-section shock tube

4.3 Properties of the shock tube

To investigate the capabilities and properties of the detonation transmission tubing driven shock tubes, pressure measurement for the overpressure magnitude in the driven section of the shock tube was performed to get the shock Mach number M_s . As discussed above, a pressure transducer (Kulite Semiconductor Products, Inc., model: XTE-190M, natural frequency: 175 kHz) was placed at 50 mm from the open end to record the pressure history in the driven section. The pressure variation was recorded by a NI-9223 module (National Instruments Corp., 1 MS/s, 16 bit, 4 channels) with a NI-9178 compact data acquisition system driven by LabVIEW. Furthermore, the sampling rate of 1 MHz is chosen to get high-precision results.

Additionally, the flow structure from the open end of the shock tube was visualized using the time-resolved shadowgraph system shown in Figure 4.4. To synchronize the high-speed camera, the pressure rising signal induced by the shock wave was employed to trigger the

camera (Figure 4.4). A signal conditioner for converting the rising voltage output of the pressure transducer into a 5V TTL signal was specially designed.

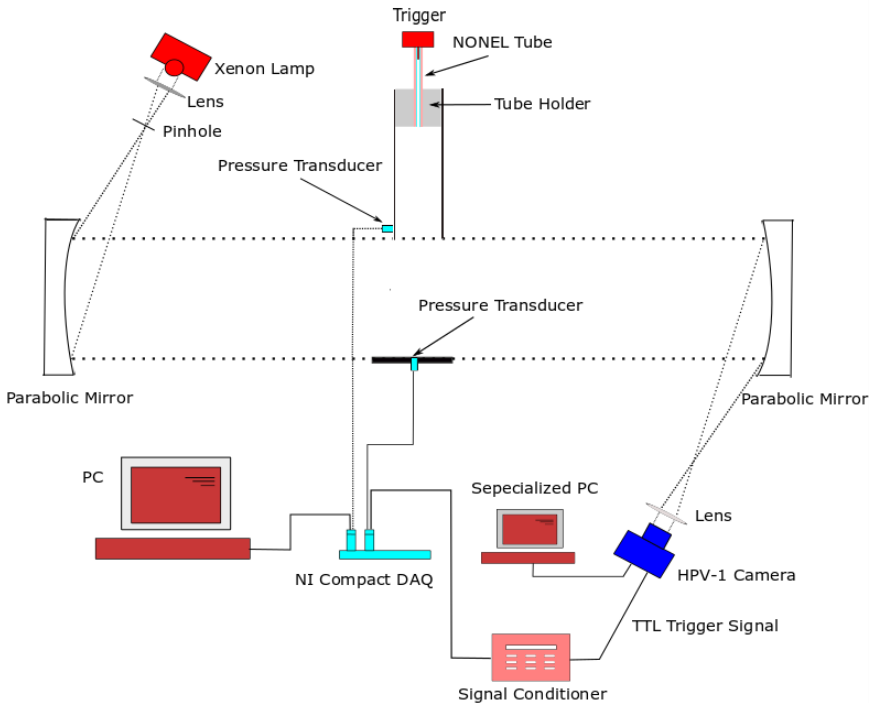
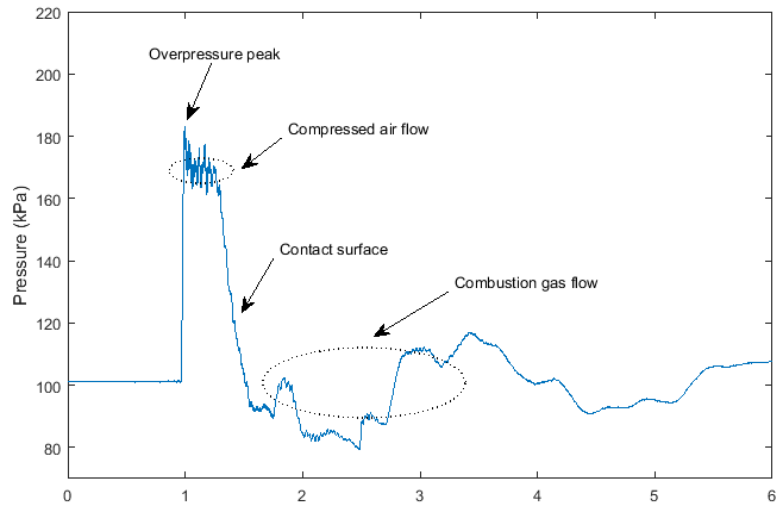


Figure 4.4 Schematic of the experimental setup

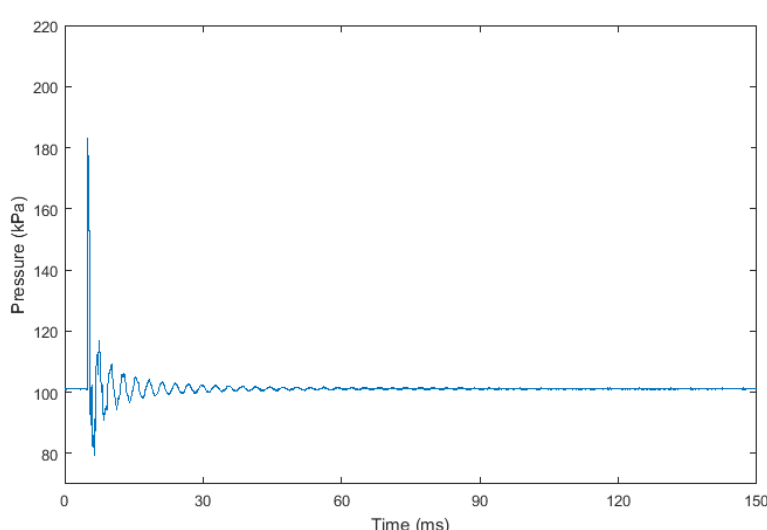
4.3.1 Mach number range

Figure 4.5 presents the pressure-time history measured by the Kulite pressure transducer in the driven section of the square shock tube. The timescale of Figure 4.5 (a) is 6ms, whereas a much larger timescale of 150ms is documented in Figure 4.5 (b). It is worth noting that the original pressure-time history contains high-frequency oscillations resulting from the high eigenfrequency of the Kulite pressure transducer. Figure 4.5 only showcases the data filtered by a moving average (smoothing width is 14). It can be seen from Figure 4.5 that a strong pressure increase from the ambient pressure to the peak pressure with a time scale of nanoseconds is generated due to the initial shock wave. When the shock wave arrives at the open end of the shock tube, a rarefaction wave is created, which travels back upstream. This rarefaction wave accelerates the out-flowing air and thereby causes the pressure to drop. After the contact surface separating the compressed air flow from the driver combustion gas passes the transducer, a sudden pressure decrease appears because of the relatively low

pressure in the combustion gas and rarefaction waves. The rarefaction waves accelerate the out-flowing combustion gas and thereby causes its pressure to drop even below the ambient pressure, whereas this low-pressure area then gives rise to the refilling process, which results in a pressure increase. This oscillation process lasts about 70ms and then the pressure in the driven section restores to the ambient condition. Overall, the pressure profile in the driven section of the shock tube is consistent with that of conventional compressed-air driven shock tubes [151].



(a)



(b)

Figure 4.5 Pressure-time history of Kulite pressure transducer in the driven section of square shock tube (Nonel tube length $L=200\text{mm}$): (a) timescale of 6ms; (b) timescale of 150ms

The shock Mach number M_s of the shock tube can be estimated by overpressure magnitude in its driven section based on the normal shock theories (see Section 3.1.1):

$$\frac{P_2}{P_1} = 1 + \frac{2\gamma}{(\gamma+1)}(M_s^2 - 1) \quad (4.1)$$

Where P_1 and P_2 are the static pressure, respectively, before and after the shock (the ambient pressure and the peak overpressure for this case), M_s is the shock wave Mach number, γ is the ratio of the specific heats of the gas. Meanwhile, the shock velocity also can be calculated by automatically detecting and tracking the initial shock wave from shadowgraph images. In this research, the shock wave velocity was calculated by detecting the shock locations of the first five shadowgraph images (250k frames per second) from the open end and the calculating process was conducted using in-house developed software (see Chapter 6), in which computer vision algorithms such as background subtraction in the frequency domain, adaptive threshold, and sub-pixel interpolation were utilized.

Table 4.1 Shock Mach number M_s of the square shock tube in different NOENL tube lengths

L (mm)	Explosive mixture(mg)	M_s by peak overpressure	M_s by shadowgraph
200	3.6	1.28	1.27
300	5.4	1.37	1.36
400	7.2	1.46	1.45
500	9.0	1.53	1.52
600	10.8	1.56	1.55
700	12.6	1.58	1.57

Table 4.1 showcases the shock Mach number M_s of the square shock tube calculated both by peak overpressure and shadowgraph images for NONEL tube length $L= 200$ to 700 mm. It can be seen from Table 4.1 that the shock Mach number calculated by peak overpressure in the driven section is basically consistent with that from shadowgraph images. However, M_s obtained through peak overpressure is higher than that from shadowgraph images on a whole,

which makes sense because the shock wave is dissipative after it emits from the open end of the shock tube. Moreover, it is apparent that the longer NONEL tube has higher denotation energy and generates a stronger shock wave with a higher velocity. However, the shock Mach number goes up nonlinearly versus the NONEL tube length. When the NONEL tube length is over 400 mm, the shock Mach number increases very slightly. Specifically, the shock Mach number range of this novel shock tube is around from 1.28 to 1.58 (NONEL tube length $L = 200\text{-}700$ mm). Further research can be conducted about the theoretical model correlating the strength of the shock wave with the energy of the NONEL tube or replacing the straight nozzle with other contours to increase the shock Mach number.

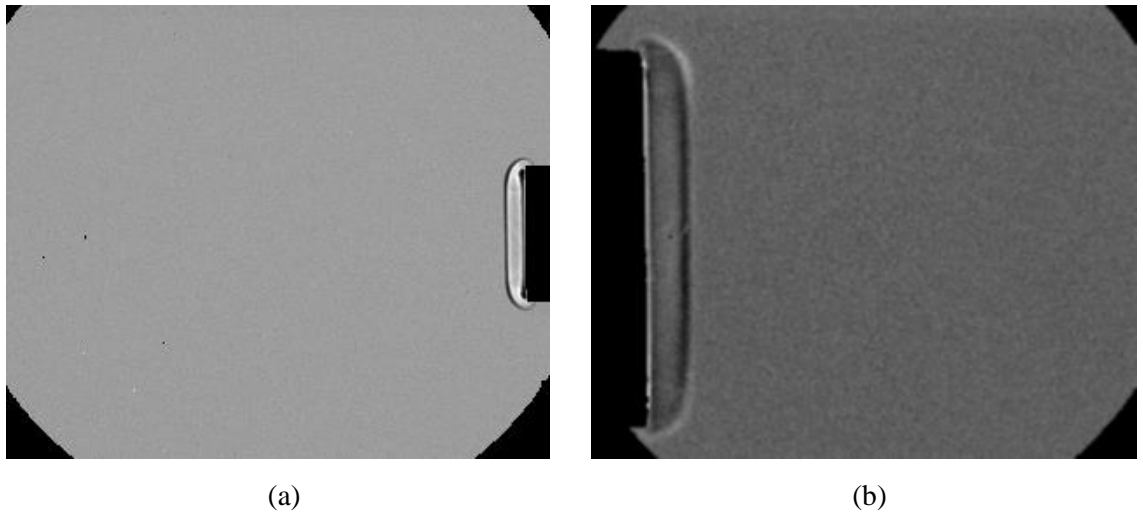


Figure 4.6 Shadowgraph images from the open end of the circular shock tube using different lenses
 (a) shadowgraph image for flow structure visualization; (b) shadowgraph image for shock Mach number calculation

It is worth noting that there are errors to some extent for both shock Mach number calculation methods. To estimate M_s by shadowgraph sequences, the accuracy is limited by the spatial resolution of the camera. Unfortunately, fast cameras used in high speed shadowgraph or schlieren are generally low in spatial resolution (only 312×260 -pixel resolution for the Shimazu fast camera used in this research) to pursue a better time resolution. In order to improve the shock Mach number calculation accuracy, lenses with different focal lengths were used for flow structure visualization and shock speed calculation respectively (see

Figure 4.6). Although only a shorter area from the open end of the shock tube was visualized for calculating the shock Mach number, there still is a ± 0.02 bias. As for the method that assesses the M_s by peak overpressure, the main error is coming from the moving average process. For the steady pressure measurement, the shot noise of the pressure measurement system can be eliminated effectively by moving average with a large smoothing width. However, it is difficult to make a trade-off between denoising and non-distortion for the strong unsteady pressure fluctuation signal. In this work, the sampling rate of Kulite pressure transducer was set to 1 MHz in order to get high-precision results as much as possible. However, the pressure on the side wall of the shock tube driven section goes up to its maximum value less than 1 μ s and then starts to decrease because of rarefaction waves very soon (see Figure 4.5(a)). Therefore, moving average results in a non-linear distortion to the original highly unsteady pressure signal. To sum up, all shock Mach numbers must be measured based on the same shadowgraph or overpressure magnitude measurement setup and evaluated using the same calculating parameters.

4.3.2 Repeatability

In different runs, there is deviation due to biases of the NONEL tube length, distribution inhomogeneity of the explosive material along the NONEL tube, or other operation errors. To validate the reliability of the shock tubes, the repeatability experiment of overpressure and shadowgraph was conducted using the same NONEL tube length and the same acquisition configuration including the time delay for the image capturing, exposure time, and frame rate. Specifically, the repeatability is represented by the relative standard deviation (RSD) [278] defined as the ratio of the standard deviation to the mean for a set of replication test results:

$$RSD = \sigma/x_m \quad (4.2)$$

where σ is the standard deviation of the overpressure magnitudes or shock wave locations from a set of replication tests, x_m denotes their corresponding arithmetic mean values. The

standard deviation is calculated by the equation as follows:

$$\sigma = \sqrt{\frac{1}{N} \sum_{i=1}^N (x_i - x_m)^2} \quad (4.3)$$

where x_i means the overpressure or the initial shock wave location of one sample run and N is the number of replication runs.

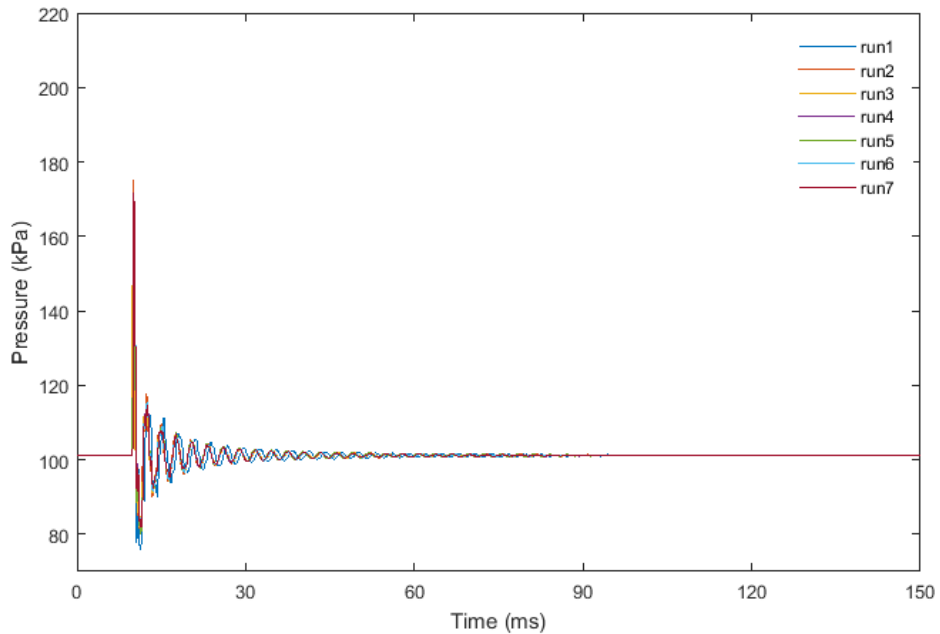


Figure 4.7 Repeatability of pressure-time history in the driven section of square shock tube ($L = 200$ mm)

Figure 4.7 presents pressure-time histories (NONEL tube length $L=200\text{mm}$) of 7 runs from the Kulite pressure transducer in the driven section of the square shock tube. The RSD of the peak overpressure magnitude induced by the primary shock wave is 1.64% in 7 runs. Therefore, the peak overpressure in the case of NONEL tube length $L=200\text{mm}$ is $178.89\text{kPa} \pm 1.64\%$. Because of the interaction of shock wave, boundary layer, and rarefaction waves, the flow inside the shock tube is quite unsteady. Therefore, only the repeatability analysis of the peak impulse overpressure magnitude induced by the primary shock wave was performed in this work.

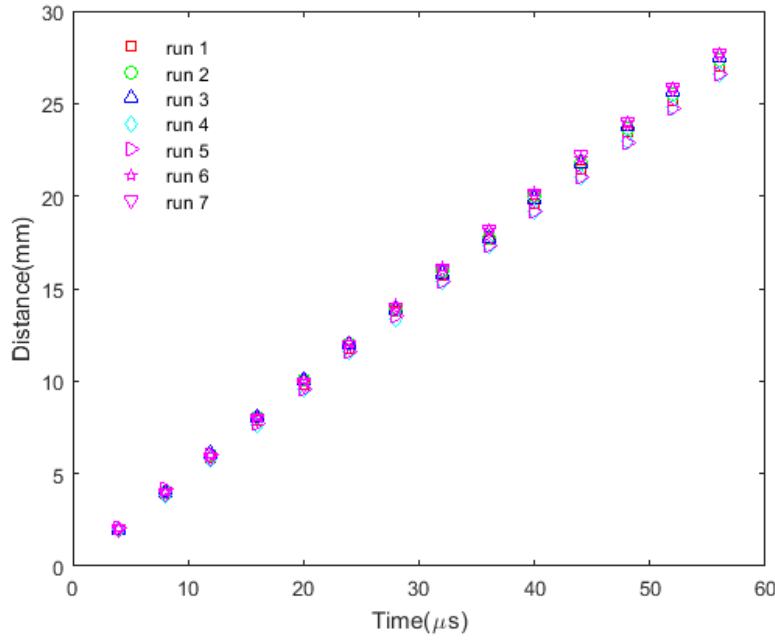


Figure 4.8 Repeatability of shock wave locations from the open end of the circular shock tube ($L = 300$ mm)

Figure 4.8 shows the instantaneous locations of the initial shock wave, detected from shadowgraph images of the circular shock tube (NONE tube length $L=300\text{mm}$) in 7 runs. It can be seen that initial shock wave locations for different runs qualitatively match very well when the elapsed time of shock wave out of the open end of the circular shock tube is less than $60\text{ }\mu\text{s}$. The repeatability of the shock wave location from the open end of the shock tube is calculated quantitatively by equations 4.2 and 4.3. The result shows that the relative standard deviation of the initial shock wave location in 13 different timing points of 7 runs varies from 1.86% to 2.82%.

It is worth mentioning that it is not reliable to estimate the shock tube Mach number M_s simply by the length of the NONE tube although good repeatability of less than 3% can be obtained for most of the cases. Occasionally, we still find some cases in which there is a larger difference in both overpressure magnitude and shadowgraph results compared with most of the cases in the same NONE tube lengths. The reason is probably the distribution inhomogeneity of the explosive material along the NONE tube. Therefore, the Mach number should be estimated each run through one of the two aforementioned methods.

4.3.3 Running time

Shock tubes can be developed in a wide range of sizes. The size and method of producing the shock wave determine the peak running time of the shock tube. For the conventional open end shock tubes driven by compressed air with a driven section in a magnitude of several meters [279], test times are a few milliseconds, mainly limited by the arrival of the contact surface.

Figure 4.9 depicts shadowgraph images from the open end of the circular shock tube in the case of NONEL tube length $L=500$ mm. It can be seen that the time duration before the contact surface arrives at the open end of the circular shock tube is roughly $528\mu\text{s}$, and then the combustion gases in a state of high temperature and pressure generated by the sudden expulsion of the NONEL tube comes out of the shock tube open end. It is worth mentioning that the reason why the brightness of shadowgraph sequences is different from frame to frame is the intensity variation of the light source and the very short exposure time ($4\mu\text{s}$), however, it doesn't influence the grayscale gradient of shadowgraph test images and the visualization of the flow structure.

Additionally, the running time of the shock tube is also can be obtained from the pressure-time history in the driven section. Figure 4.10 presents the pressure-time histories of the square shock tube for different driven section length L_D in the case of NONEL tube length $L=300$ mm. The length of the driven section is adjusted by changing the relative position between the tube holder and driven section (see Section 4.2). As given in Figure 4.10, the running time between the initial shock and contact surface in the case of driven section length $L_D=280$ mm and NONEL tube length $L=300$ mm is around $617\mu\text{s}$, however, there is a significant variation in the running time for different driven section length $L_D=280-330$ mm. The shock tube with a longer driven section has a longer running time. The running time differences between cases of $L_D=230$ mm and 280mm is $73\mu\text{s}$, while that of cases of $L_D=280$ mm and 330mm is $78 \mu\text{s}$. Although a significant running time difference has been found, the maximum overpressure magnitudes (Figure 4.10) due to the initial shock wave are basically the same for different driven section length $L_D=280-330$ mm in the case of NONEL tube length $L=300$ mm.

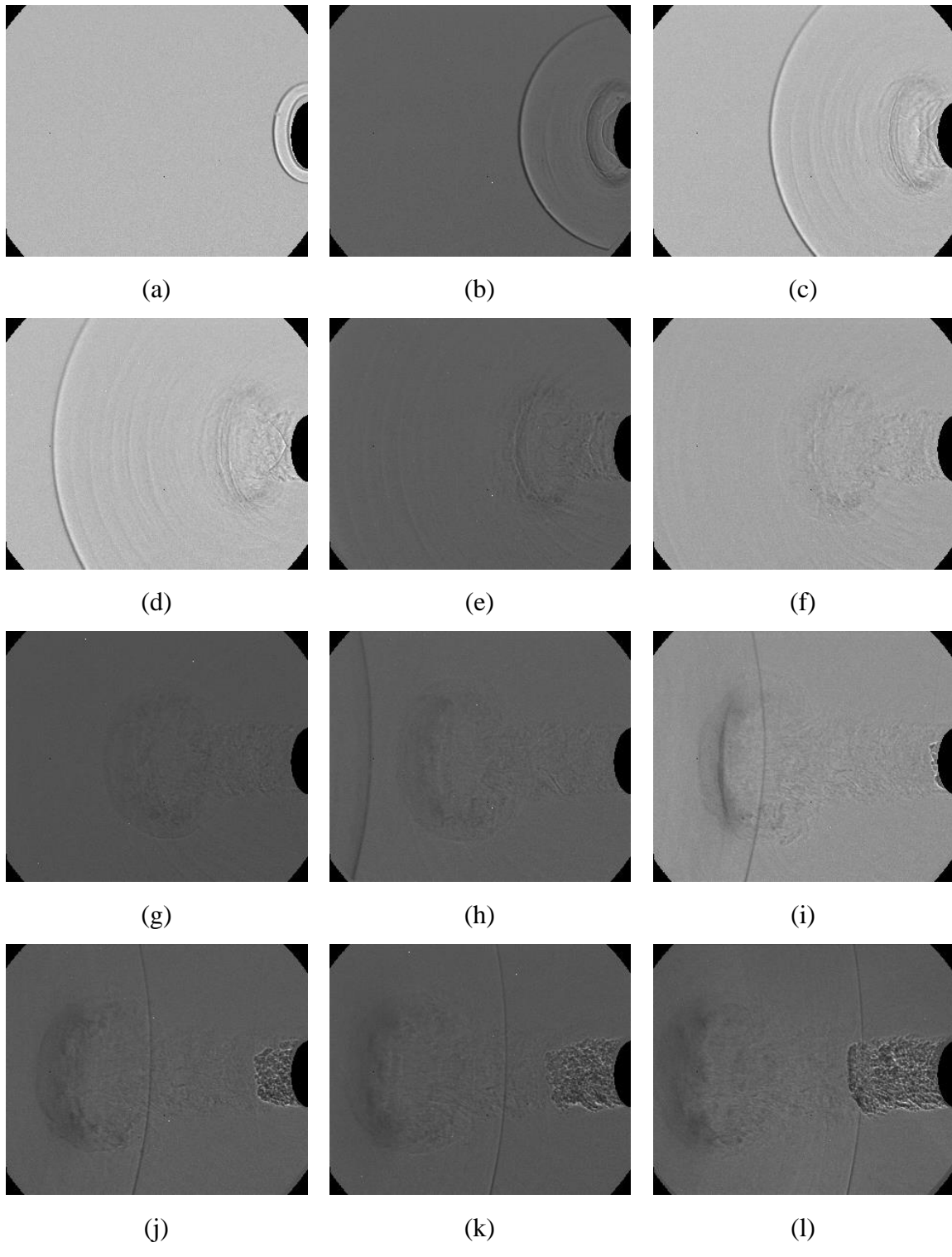


Figure 4.9 Framing shadowgraph images showing flow structure evolution from the open end of the circular shock tube at $L = 500$ mm: (a) $\Delta t = 16\mu s$; (b) $\Delta t = 80\mu s$; (c) $\Delta t = 144\mu s$; (d) $\Delta t = 208\mu s$; (e) $\Delta t = 272\mu s$; (f) $\Delta t = 336\mu s$; (g) $\Delta t = 400\mu s$; (h) $\Delta t = 464\mu s$; (i) $\Delta t = 528\mu s$; (j) $\Delta t = 544\mu s$; (k) $\Delta t = 560\mu s$; (l) $\Delta t = 576\mu s$

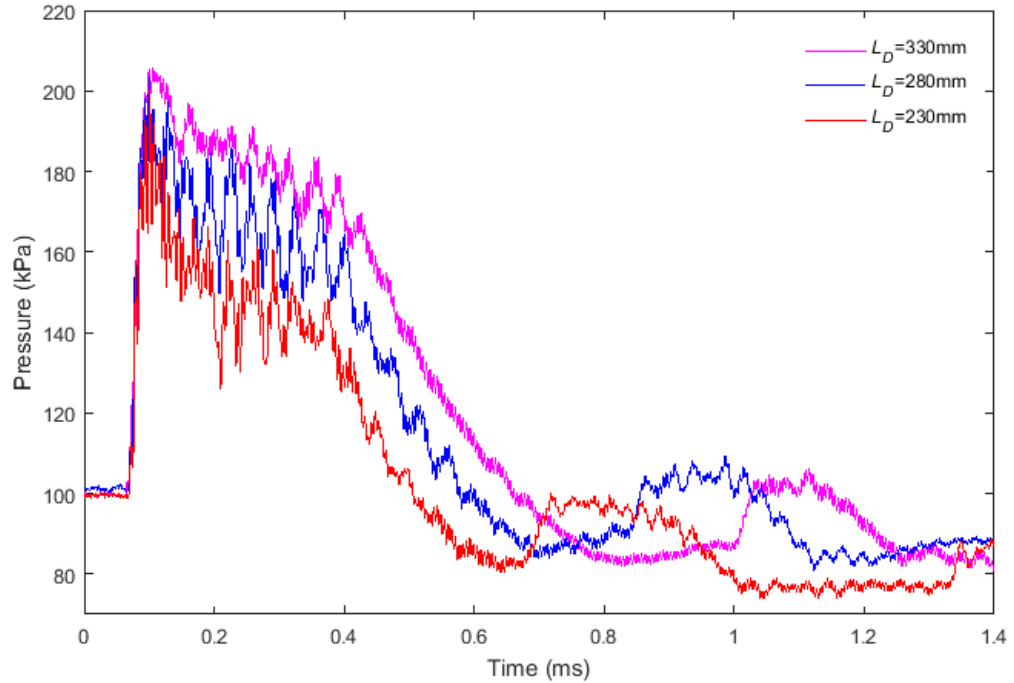


Figure 4.10 Pressure-time histories of the square shock tube for different driven section lengths
(NONEL tube length $L=300\text{mm}$)

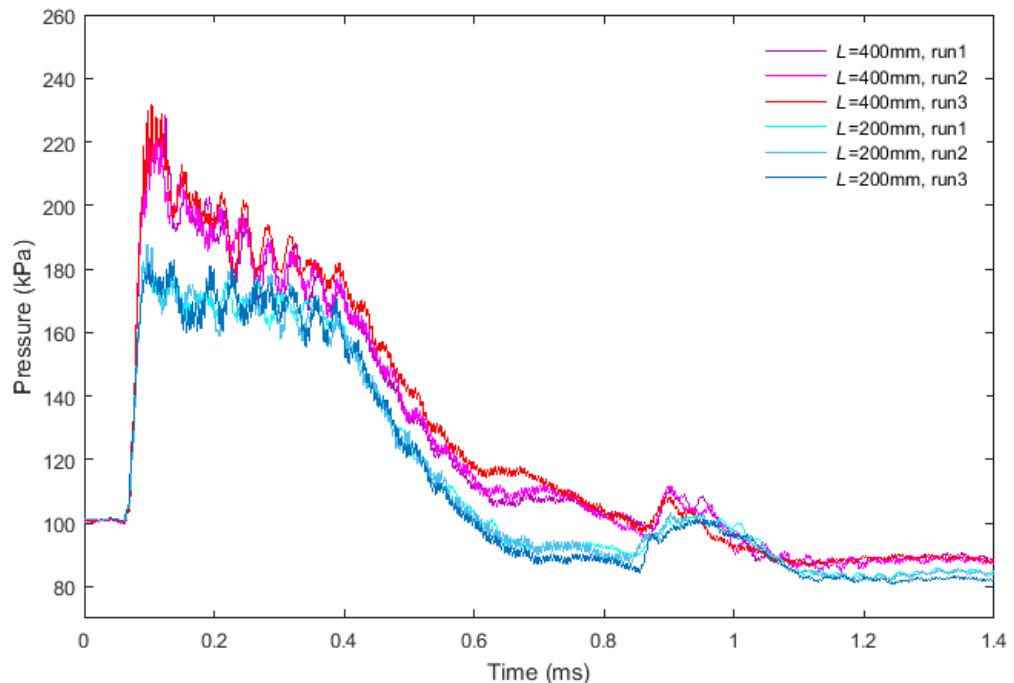


Figure 4.11 Pressure-time histories of the square shock tube for NONEL tube lengths (driven section length $L_D=280\text{mm}$)

Figure 4.11 demonstrates pressure-time histories of the square shock tube for different NONEL tube lengths. As shown in Figure 4.11, there is good repeatability both in maximum overpressure magnitude for calculating the shock Mach number and the phases of pressure-time histories. Compared with cases of NONEL tube length $L=200\text{mm}$ (shock Mach number $M_s=1.28$) and 400mm (shock Mach number $M_s=1.46$), the shock tube with higher explosion material and shock Mach number has a longer running time. The running time difference for cases of $M_s=1.28$ and $M_s=1.46$ is around $44\text{ }\mu\text{s}$.

All in all, the longer running time can be obtained by increasing the driven section length for a specific Mach number. Additionally, the running time is slightly longer in cases of higher Mach numbers. However, the running time of shock tubes driven by detonation transmission tubing is much shorter than that of conventional shock tubes due to its limited dimensions and explosion energy [279].

4.3.4 Flow structure from the open end

Circular shock tube:

Figure 4.12 demonstrates the primary flow structure from the open end of the circular shock tube in the case of NONEL tube length $L=600\text{ mm}$ and the elapsed time of the initial shock wave $\Delta t=184\text{ }\mu\text{s}$). As shown in Figure 4.12, the flow pattern from the open end of the circular shock tube driven by detonation transmission tubing consists of initial shock wave, secondary shock waves, vortex ring, embedded shock wave, and the oblique shock wave structure, which is consistent well with that of conventional compressed-gas driven shock tubes [10]. More detailed shadowgraph images showing the flow evolution emitting from the open end are given in Figures 4.13-4.16 (NONEL tube length $L = 300, 400, 500, 600\text{ mm}$ respectively). As shown in Figures 4.13-4.16, a planar shock wave emits from the shock tube open end in the first place. After emitting from the open end, the shock wave is diffracted and turns to a spherical shape as it travels. Because of rarefaction, the pressure behind the initial shock is reduced when it separates from the downstream jet head. If the pressure drops enough to a value below the atmospheric pressure, a secondary shock wave is generated. This secondary shock wave then separates from the jet head and the abovementioned process repeats, generating additional shock waves until the jet flow

becomes subsonic and no longer able to sustain the formation of secondary shock waves. The formation of secondary shock waves was also found in conventional open-ended shock tubes [257], explosive impulse [280], and volcanic eruptions [257, 281]. On the other hand, the air flow in the driven section behind the initial shock wave comes out and forms a shear layer between the high speed flow and ambient fluid. This shear layer is subsequently carried away from the edges of the shock tube exit and rolls up, generating a vortex ring. The initial shock wave becomes weak gradually because of its radial expansion and the subsequent pressure reduction communicates with the air flow in the shock tube via expansion waves. These expansion waves accelerate the flow in the tube until an oblique shock (Figures 4.13 (d)-4.16 (d)) starts to form near the shock tube exit, which also normally can be seen at the exit of a steady overexpanded jet. It should be noted that at this instant just after the oblique shock emergence, the flow field at the shock tube exit is influenced by not only the wall boundary layer, but also by the presence of the vortex ring. Once the oblique shock system is closed across the tube (Figure 4.13 (f), Figure 4.14 (f), Figure 4.15 (e), Figure 4.16 (f)), the flow at the tube exit can no longer be influenced by the downstream.

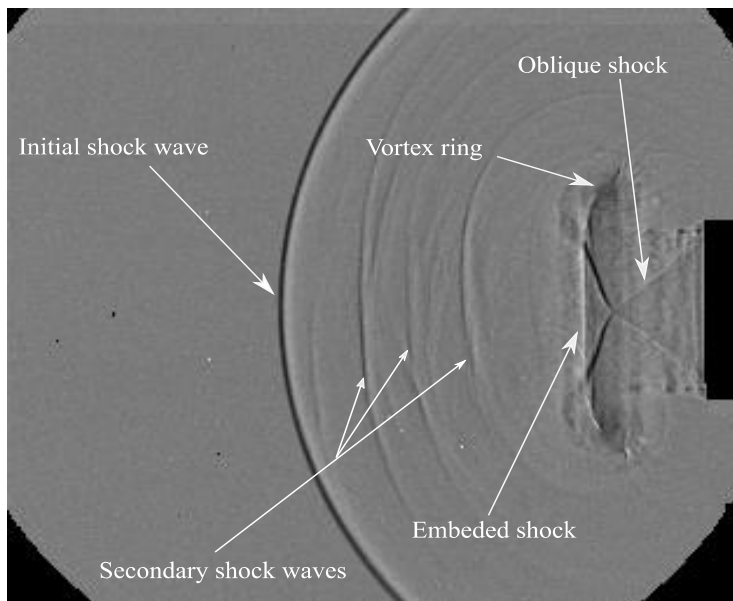


Figure 4.12 Flow structure from the open end of the circular shock tube (NONEL tube length $L = 600\text{mm}$, $\Delta t=184\ \mu\text{s}$)

For the vortex ring structure of the circular shock tube presented in Figures 4.13-4.16, it has two distinct flow regimes. The first one is illustrated in Figure 4.13, showing the flow field

produced in the case of $M_s \sim 1.37$. The propagation of the vortex ring is shock-free but probably with a supersonic area around the core of the vortex. The external flow is entrained during the vortex ring propagation, transitioning the vortex ring from initially laminar to turbulent with instabilities developing with time around the circumference of the core (Figures 4.13 (g)-(l)). Widnall et al. [282] have established the theoretical foundations for the development of instability waves on incompressible vortex rings. They showed that: (i) A given ring geometry results in only one unstable mode. (ii) The number of waves on the ring increases when the vortex core is reduced. In fact, $n \sim 2.7R/a$, where n is the number of waves around the ring, R is the vortex ring radius, and a is the core size. Based on this theoretical foundation, the size of the vortex ring can be estimated by the number of waves on the ring. At later times, the apparent core size of the ring is increased as the high wave number instabilities seem to have saturated their growth. The subsequent expansion of the core diameter reduces the number of waves on the ring. In the second flow regime (Figures 4.14-4.16), showing the flow field produced by $M_s \sim 1.46-1.58$, the vortex ring propagates with a rearward-facing shock in its recirculating region. The embedded shock wave is termed “rearward-facing” since the high-pressure region is upstream of the main flow. After the emergence of the oblique shock reflection (Figure 4.14 (g), Figure 4.15 (f), Figure 4.16 (f)), the rearward-facing shock embedded in the vortex ring starts to form. This rearward-facing embedded shock wave with the high pressure downstream and low pressure upstream appears because the induced flow velocity in the recirculating region of the ring becomes supersonic. Far downstream of the shock tube exit, the vortex ring has become highly turbulent and the shadowgraph image of the embedded shock is blurred (Figure 4.14-4.16 (h)-(l)); this particular shock wave disappears when the viscous forces of the flow are dominant, however, the propagation of the ring does not seem to slow down. Previous studies demonstrated that the threshold for the formation of the rearward-facing embedded shock wave in terms of $M_s \sim 1.43$ [149, 283], which is consistent with present experimental results. Additionally, far downstream of the open end of the shock tube, the vortex ring with its attendant shock leaves the oblique shock structure (Figure 4.14-4.16 (j)), and continues downstream leaving the oblique shock structure characteristic of an overexpanded jet attached to the tube exit. The oblique shock structure remains unchanged until the primary expansion wave reflected from the rear end of the tube eventually arrives at the shock tube exit.

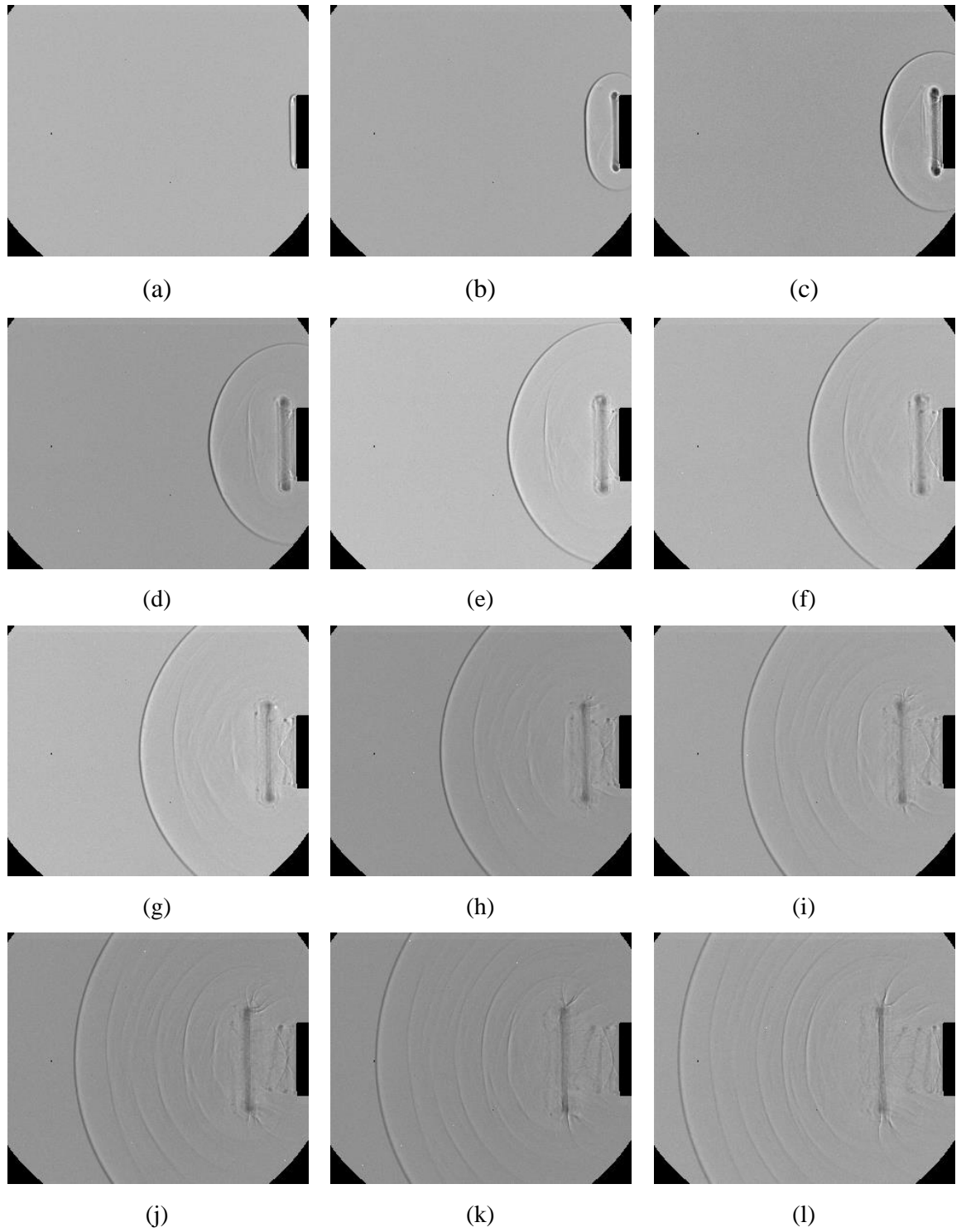


Figure 4.13 Framing shadowgraph images showing flow structure evolution from the open end of the circular shock tube at NONEL tube length $L=300$ mm: (a) $\Delta t=4\mu s$; (b) $\Delta t=24\mu s$; (c) $\Delta t=44\mu s$; (d) $\Delta t=64\mu s$; (e) $\Delta t=84\mu s$; (f) $\Delta t=104\mu s$; (g) $\Delta t=124\mu s$; (h) $\Delta t=144\mu s$; (i) $\Delta t=164\mu s$; (j) $\Delta t=184\mu s$; (k) $\Delta t=204\mu s$; (l) $\Delta t=224\mu s$

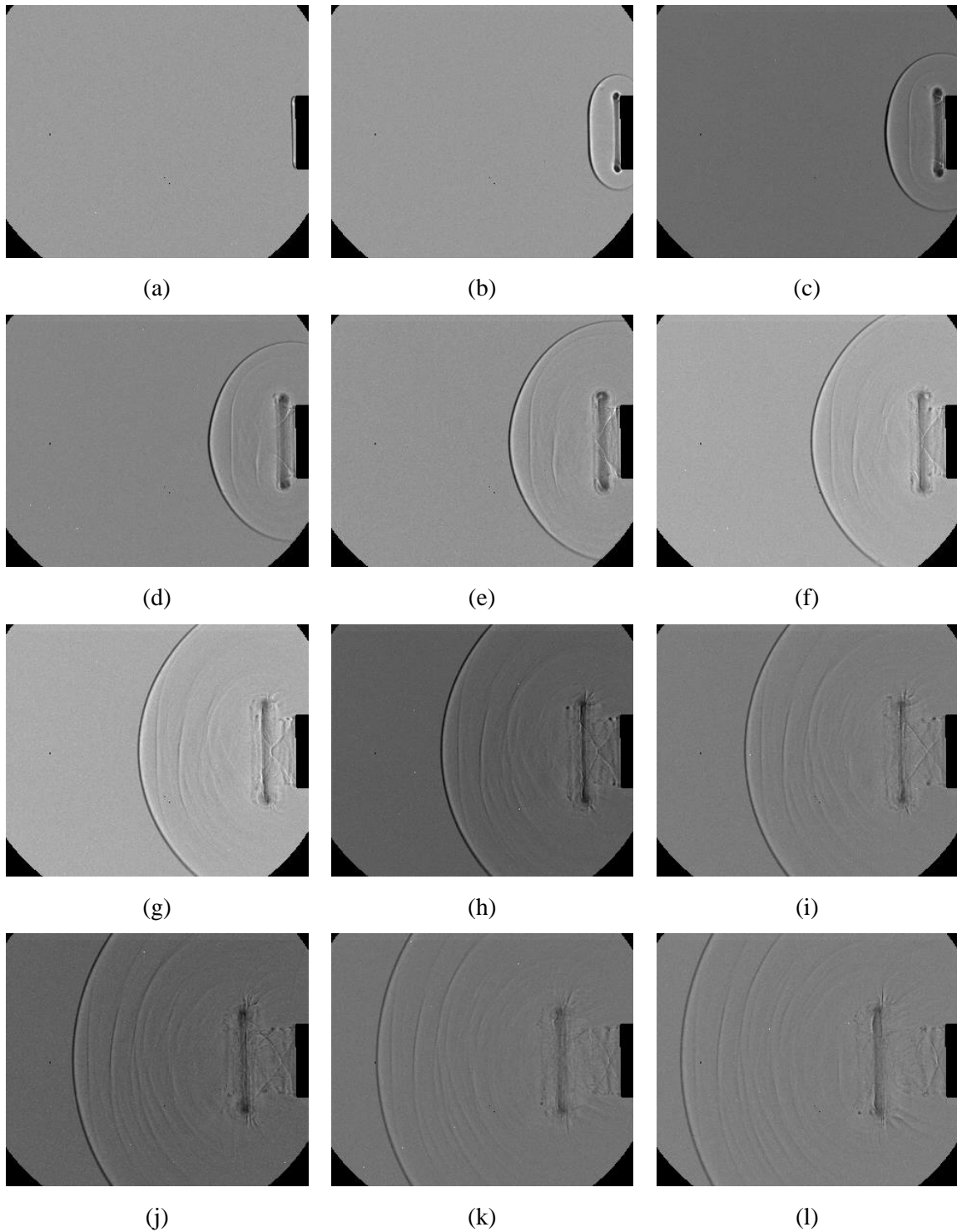


Figure 4.14 Framing shadowgraph images showing flow structure evolution from the open end of the circular shock tube at NONEL tube length $L=400$ mm: (a) $\Delta t=4\mu s$; (b) $\Delta t=24\mu s$; (c) $\Delta t=44\mu s$; (d) $\Delta t=64\mu s$; (e) $\Delta t=84\mu s$; (f) $\Delta t=104\mu s$; (g) $\Delta t=124\mu s$; (h) $\Delta t=144\mu s$; (i) $\Delta t=164\mu s$; (j) $\Delta t=184\mu s$; (k) $\Delta t=204\mu s$; (l) $\Delta t=224\mu s$

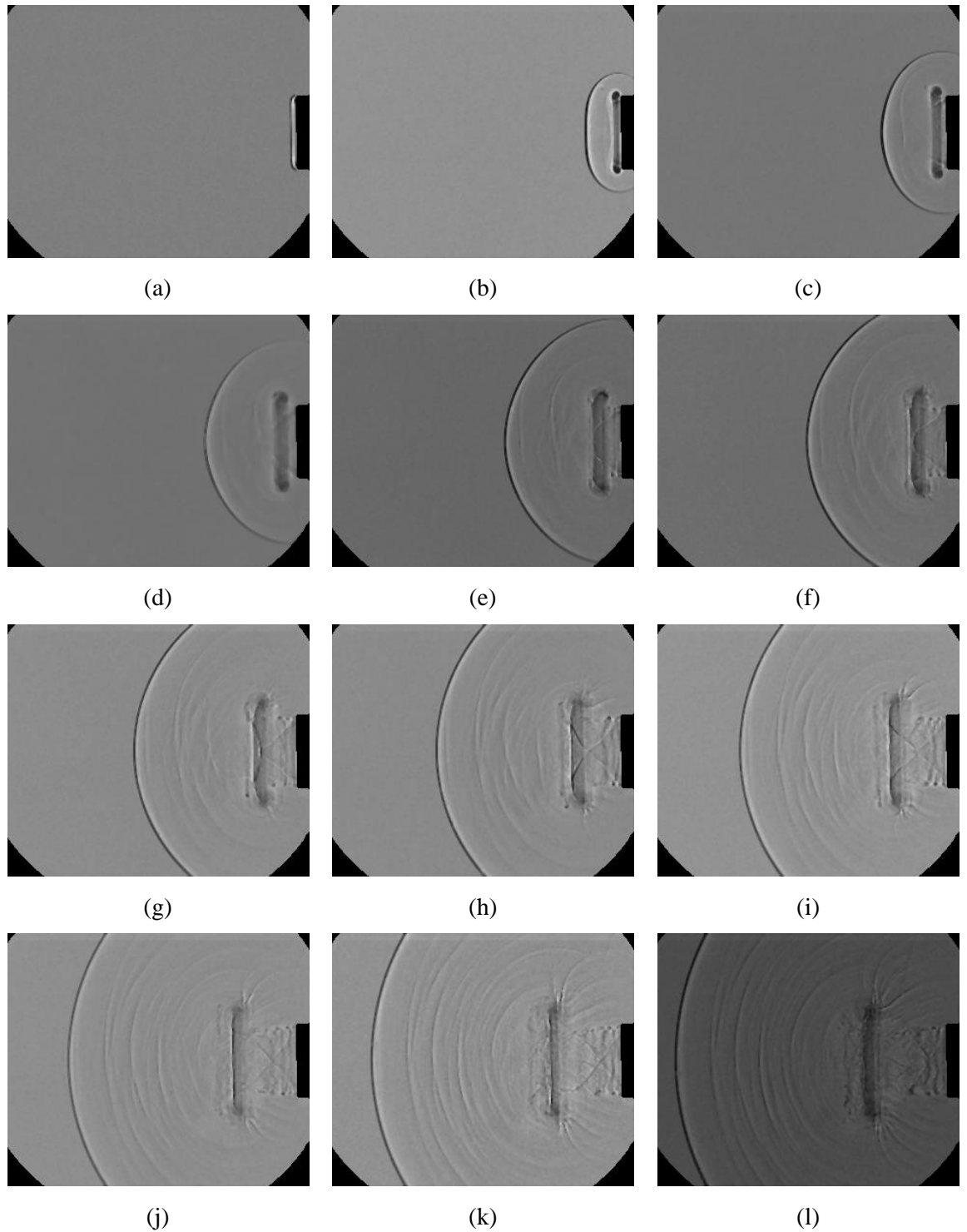


Figure 4.15 Framing shadowgraph images showing flow structure evolution from the open end of the circular shock tube at NONEL tube length $L=500$ mm: (a) $\Delta t=4\mu s$; (b) $\Delta t=24\mu s$; (c) $\Delta t=44\mu s$; (d) $\Delta t=64\mu s$; (e) $\Delta t=84\mu s$; (f) $\Delta t=104\mu s$; (g) $\Delta t=124\mu s$; (h) $\Delta t=144\mu s$; (i) $\Delta t=164\mu s$; (j) $\Delta t=184\mu s$; (k) $\Delta t=204\mu s$; (l) $\Delta t=224\mu s$

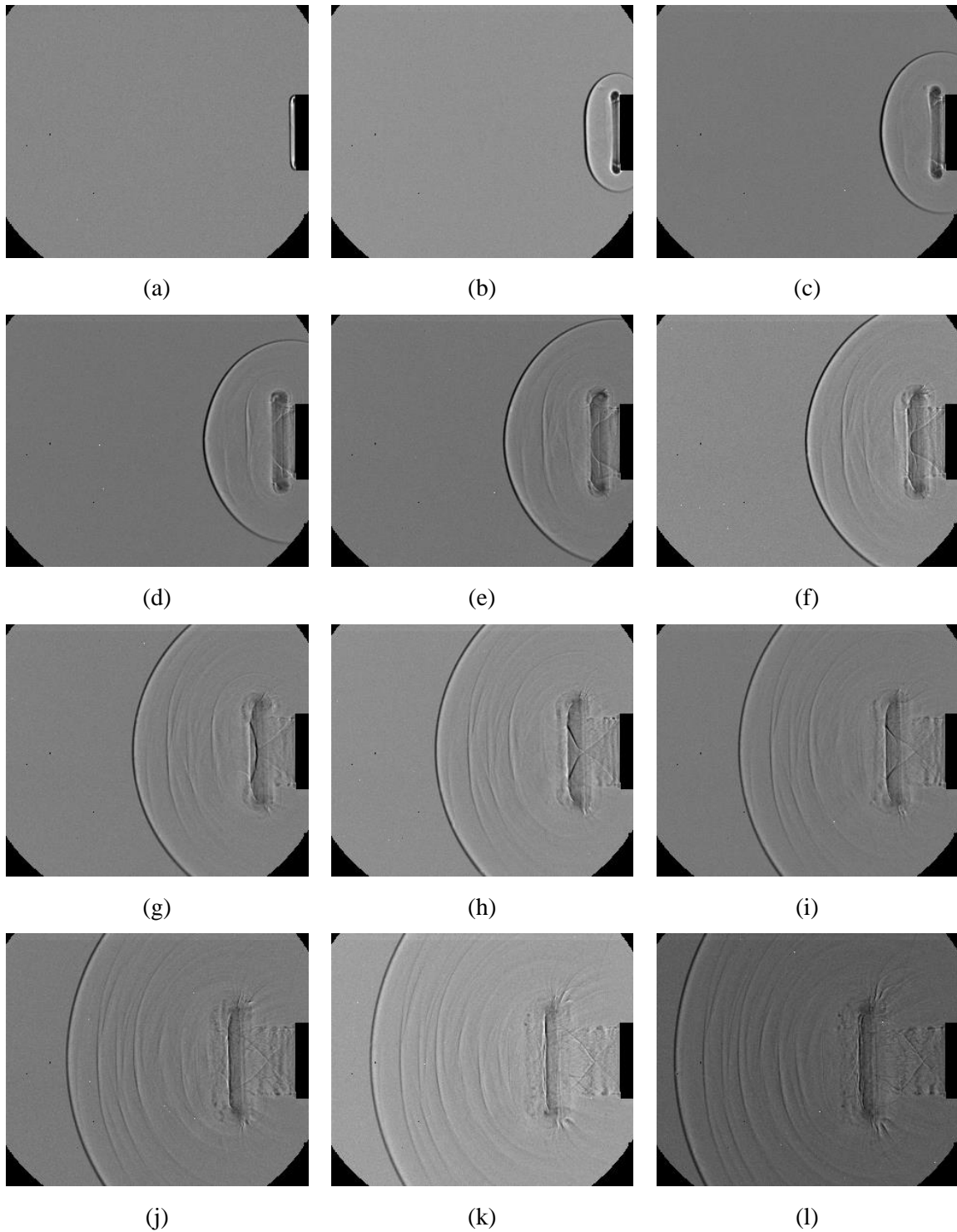


Figure 4.16 Framing shadowgraph images showing flow structure evolution from the open end of the circular shock tube at NONEL tube length $L=600$ mm: (a) $\Delta t=4\mu s$; (b) $\Delta t=24\mu s$; (c) $\Delta t=44\mu s$; (d) $\Delta t=64\mu s$; (e) $\Delta t=84\mu s$; (f) $\Delta t=104\mu s$; (g) $\Delta t=124\mu s$; (h) $\Delta t=144\mu s$; (i) $\Delta t=164\mu s$; (j) $\Delta t=184\mu s$; (k) $\Delta t=204\mu s$; (l) $\Delta t=224\mu s$

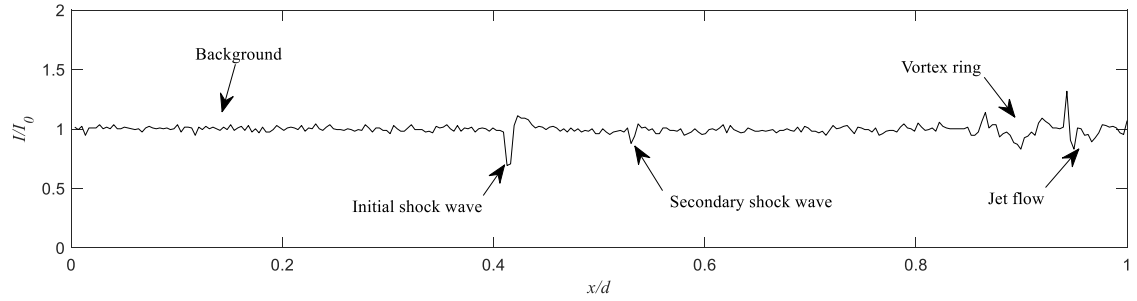
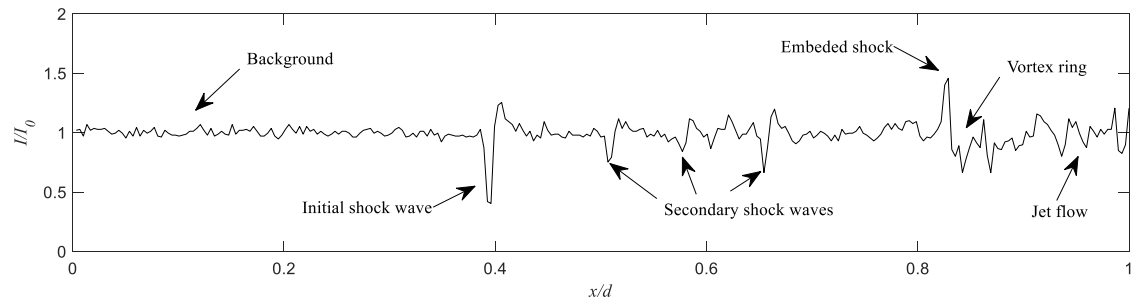
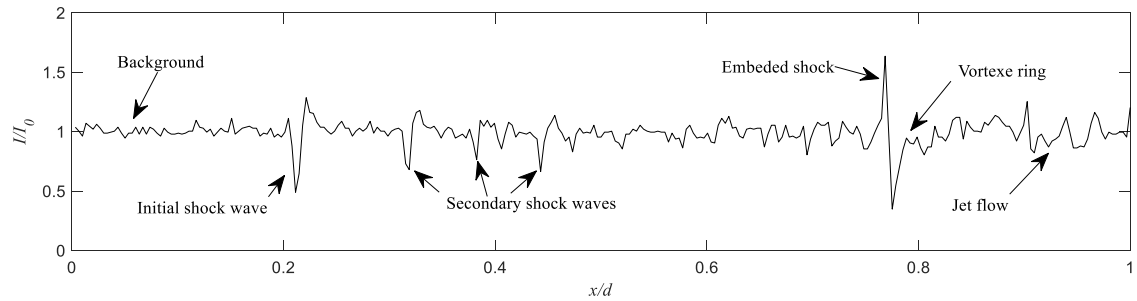


Figure 4.17 Image intensity profiles along the axis of symmetry of the circular shock tube,
NONEL tube length $L = 300$ mm, $\Delta t = 136 \mu\text{s}$



(a)



(b)

Figure 4.18 Intensity profiles along the axis of symmetry of the circular shock tube at NONEL tube length $L=600$ mm: (a) $\Delta t=136 \mu\text{s}$; (b) $\Delta t=184 \mu\text{s}$

In order to examine the evolution of the flow feature quantitatively, the intensity profiles of shadowgraph images along the axis of symmetry of the shock tube were obtained (Figures 4.17 and 4.18) using the in-house developed software [30]. The intensity of shadowgraph images was normalized by the image background brightness. The lateral axis x/d stands for

the normalized distance from the shock tube open end. As shown in Figure 4.17, the initial shock wave, secondary shock wave, vortex ring, and the oblique shock structure in the jet flow are detected in the intensity profile curve in the case of $L=300$ mm and $\Delta t=136$ μ s. However, there is not an obvious embedded shock wave in the vortex ring in this case. By contrast, a relatively strong embedded shock wave can be found for the case of $L=600$ mm, $\Delta t=136$ μ s (Figure 4.18 (a)). Meanwhile, it can be seen from Figure 4.17 and Figure 4.18 that the intensity of the initial shock wave for the case $L=600$ mm is higher than that of $L=300$ mm (the higher intensity gradient implies a steeper density gradient). In addition, the attenuation of the strength of initial shock wave with distance or elapsed time also can be found from Figure 4.18 (a) and Figure 4.18 (b). Comparing with Figure 4.17 and Figure 4.18 (a), the initial shock wave and vortex ring in the case of NONEL tube length $L=600$ mm move further far away from the open end than that of the $L=300$ mm, which means the velocities of the initial shock wave and the vortex ring are higher in the case of larger NONEL tube length. Moreover, shocklets between the initial shock and the vortex ring are more apparent and the jet flow after the vortex ring becomes more complicated for the longer NONEL tube length case. Figure 4.18 (b) presents the intensity profile of the shadowgraph image along the axis of symmetry of the shock tube at $L=600$ mm, $\Delta t = 184$ μ s. By measuring the distance of the initial shock wave in different shadowgraph images, the shock velocity can be determined.

Square shock tube:

For the flow coming out of the square shock tube, four primary physical processes [284, 285] are identified. The first one is the initial shock, which is planar when releasing from the square shock tube exit but evolves into a spherical shape rapidly. This shock diffraction process is similar to that of the above circular shock tube case, which affects the air flow behind it. The secondary flow structure is the secondary shock(s), which is also can be found in the case of an axisymmetric shock tube. Similarly, due to the rarefaction, the pressure behind the initial shock is reduced when it separates from the downstream jet head. If the pressure drops enough to a value below the atmospheric pressure, a secondary shock wave is generated. This secondary shock wave then separates from the jet head and the

abovementioned process repeats, generating additional shock waves until the jet flow becomes subsonic and no longer able to sustain the formation of secondary shock waves. The third process is the vortex loop distortion created by the shear layer originating from the tube exit. Although the generating mechanism of the vortex loop is similar to that of the vortex ring in the axisymmetric case, the vortex loop is much more unstable, appearing to be square and coplanar in the first place but converting to a twisted one rapidly. The vortex loop instability might be induced by the non-uniform vorticity produced from the secondary flow and the sharp corners. This instability can result in the earlier break-up of the primary vortex loop and the energy transformation from large-scale vortices to smaller ones. The fourth process is the so-called secondary oblique shock structure when NONEL tube length L is larger than 400mm, namely the Mach number of the initial shock wave exceeds 1.43 approximately. The oblique shock structure forms somewhere in the vortex loop core and then develops into a larger three-dimensional one very quickly. Also, the local supersonic flows return to subsonic ones because of this shock structure, which makes the vortex loop more unstable.

Figure 4.19 and Figure 4.20 depict shadowgraph sequences showing flow structure evolution from the open end of the square shock tube in the cases of NONEL tube length $L=200\text{mm}$ and 300mm respectively. As shown in Figures 4.19 and 4.20, only the first three major physical processes can be found when NONEL tube length L is smaller than 300mm, namely the initial shock Mach number is lower than 1.37 approximately. When the initial shock wave is released from the shock tube end, it has a square shape and the corners are rounded (Figure 4.20 (a)). The planar part of the initial shock becomes shorter and the corners are more rounded as time elapses, as seen in Figures 4.20 (b-e). The above shock diffraction process also makes the pressure and density distributions highly nonuniform. With the higher curvature, the remaining parts start moving downstream with increased velocity and become closer to the location of corners. Behind the initial shock wave, secondary shock waves due to rarefaction can be found in both cases of NONEL tube length $L=200\text{mm}$ and 300mm . Since the pressure behind the initial shock is reduced below the atmospheric pressure when

it separates from the downstream jet head, the secondary shock wave is generated. Also, the vortex loop motion is observed in Figures 4.19 and 4.20. Unlike the initial shock wave that converts into an axisymmetric shape from a planar one, the vortex loop is highly unstable and its configuration is always changing. To visualize the motion of the vortex loop more detailly, a schlieren test placing a knife edge on the focal point of the parabolic mirror was conducted with a smaller observation area. Figure 4.21 presents framing schlieren images showing the distortion of the vortex loop from the square shock tube exit in the case of NONEL tube length $L=300\text{mm}$. As shown in Figures 4.21 (b-g), the vortex loop near the mid-wall symmetric plane moves radially whereas the other part from the corners moves further downstream, which means the flow density close to the corners reduces rapidly when the flow is released from the shock tube exit. Therefore, the flow expansion near the side wall is weaker than that created around the corner. Compared with the vortex ring in the case of the circular shock tube, the vortex loop from the square shock tube exit is much more unstable with a much more complicated distortion and motion process. However, the fourth flow feature, the secondary oblique shock wave structure, was not observable in cases of NONEL tube length $L=200\text{mm}$ and 300mm due to the lower shock Mach number. The above observations agree with previous experimental and numerical results of conventional compressed-gas driven shock tubes reported by Zare-Behtash et al [67] and Jiang et al. [285].

Figure 4.22 and Figure 4.23 depict shadowgraph sequences showing flow structure evolution from the open end of the square shock tube in the cases of NONEL tube length $L=400\text{mm}$ and 500mm respectively. The major difference of the flow feature between NONEL tube length $L>400\text{mm}$ and abovementioned $L<400\text{mm}$ is the formation of the secondary oblique shock structure. The expansion of the flow is less intense in the mid-wall symmetric plane than that in the diagonal plane. As seen in Figure 4.22 (d) and Figure 4.23 (b), the local supersonic flow regions induced by the non-uniform expansion result in the formation of the secondary shock wave structure near the corners. These findings are consistent well with previous experimental and numerical results [67, 285] based on conventional compressed-gas driven shock tubes.

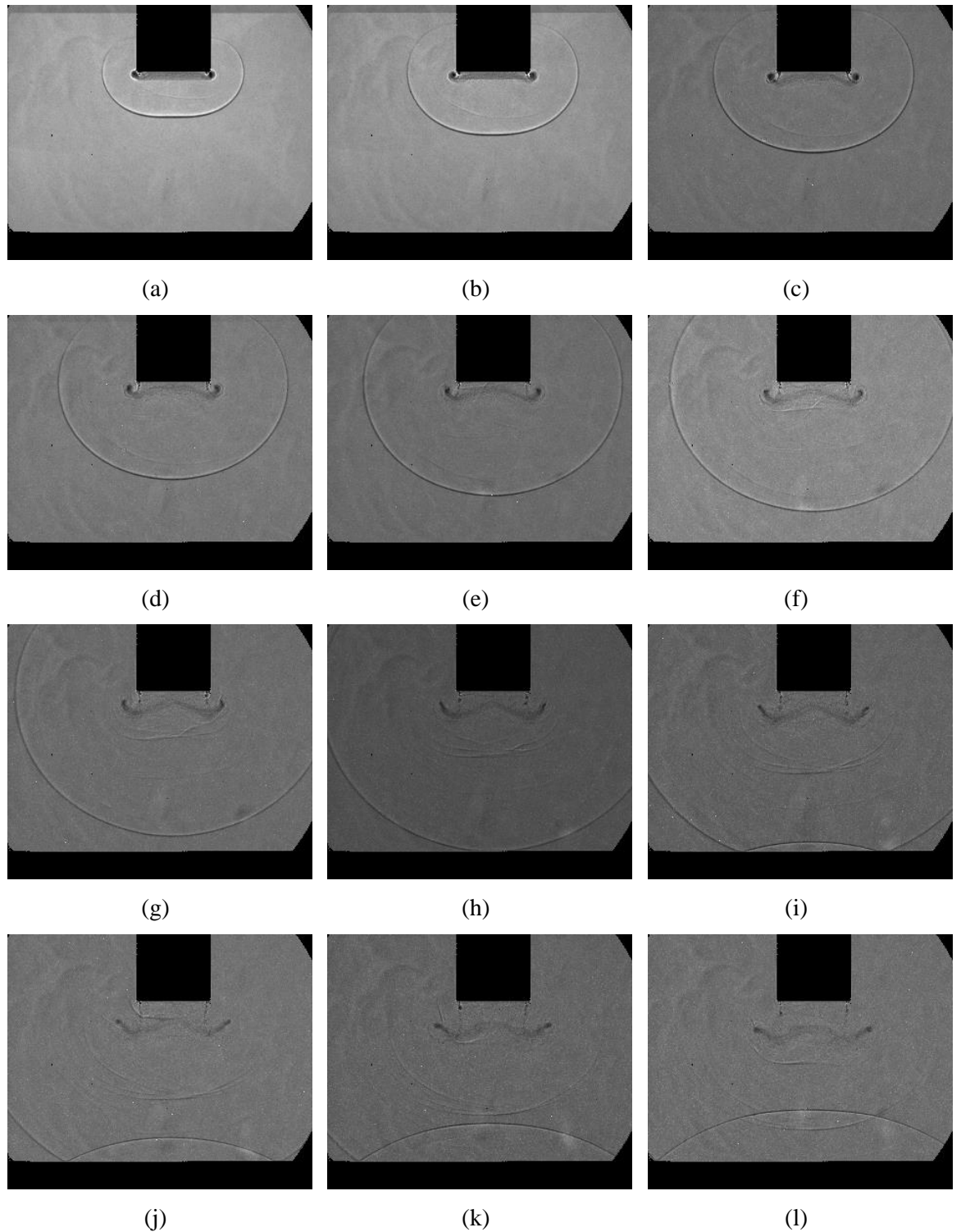


Figure 4.19 Framing shadowgraph images showing flow structure evolution from the open end of the square shock tube at $L=200\text{mm}$: (a) $\Delta t=34\mu\text{s}$; (b) $\Delta t=48\mu\text{s}$; (c) $\Delta t=62\mu\text{s}$; (d) $\Delta t=76\mu\text{s}$; (e) $\Delta t=90\mu\text{s}$; (f) $\Delta t=104\mu\text{s}$; (g) $\Delta t=118\mu\text{s}$; (h) $\Delta t=132\mu\text{s}$; (i) $\Delta t=146\mu\text{s}$; (j) $\Delta t=160\mu\text{s}$; (k) $\Delta t=174\mu\text{s}$; (l) $\Delta t=188\mu\text{s}$

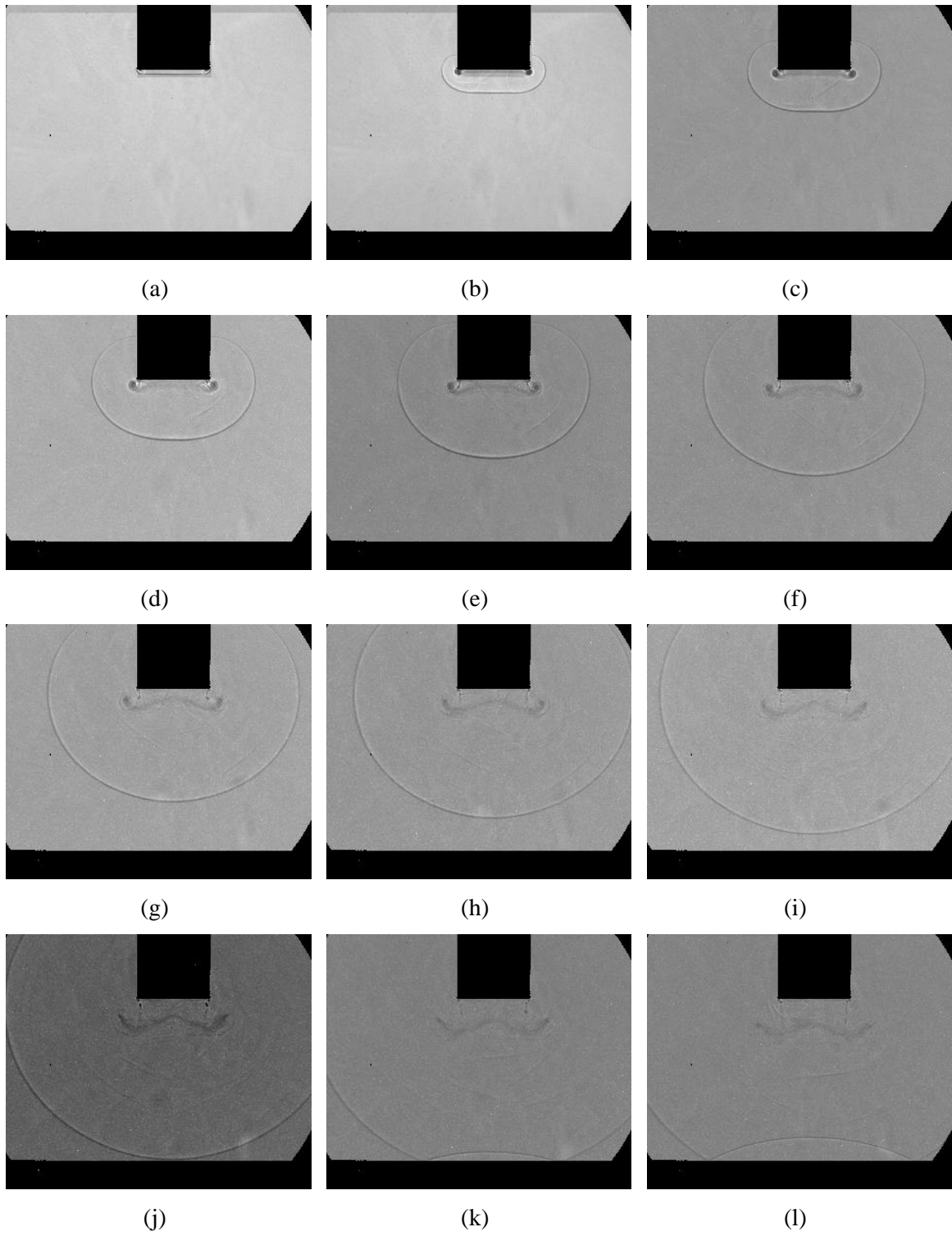


Figure 4.20 Framing shadowgraph images showing flow structure evolution from the open end of the square shock tube at $L=300\text{mm}$: (a) $\Delta t=4\mu\text{s}$; (b) $\Delta t=48\mu\text{s}$; (c) $\Delta t=62\mu\text{s}$; (d) $\Delta t=76\mu\text{s}$; (e) $\Delta t=90\mu\text{s}$; (f) $\Delta t=104\mu\text{s}$; (g) $\Delta t=118\mu\text{s}$; (h) $\Delta t=132\mu\text{s}$; (i) $\Delta t=146\mu\text{s}$; (j) $\Delta t=160\mu\text{s}$; (k) $\Delta t=174\mu\text{s}$; (l) $\Delta t=188\mu\text{s}$

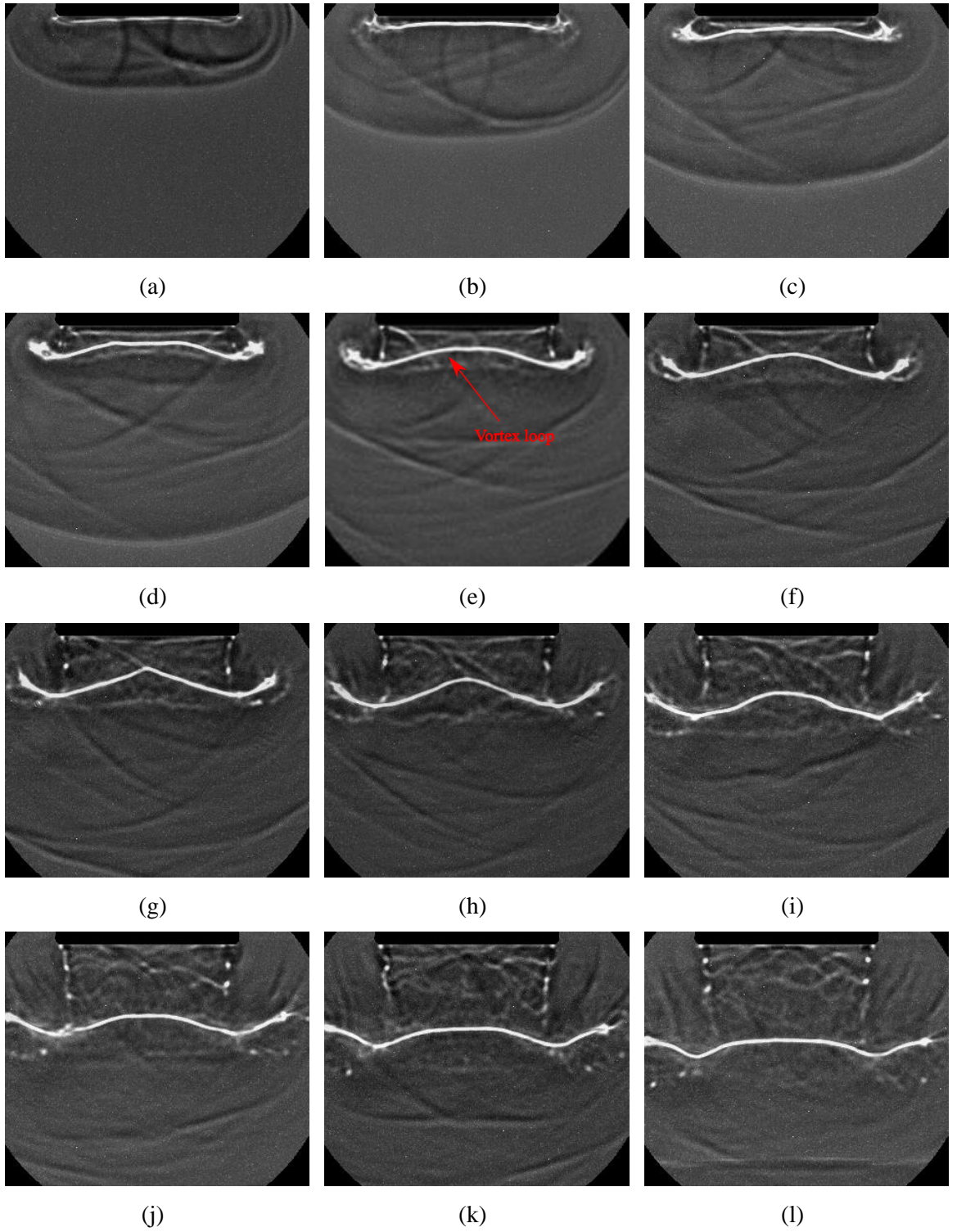


Figure 4.21 Framing schlieren images showing motion of the vortex loop from the open end of the square shock tube at $L=300\text{mm}$: (a) $\Delta t=24\mu s$; (b) $\Delta t=40\mu s$; (c) $\Delta t=56\mu s$; (d) $\Delta t=72\mu s$; (e) $\Delta t=88\mu s$; (f) $\Delta t=104\mu s$; (g) $\Delta t=120\mu s$; (h) $\Delta t=136\mu s$; (i) $\Delta t=152\mu s$; (j) $\Delta t=168\mu s$; (k) $\Delta t=184\mu s$; (l) $\Delta t=200\mu s$

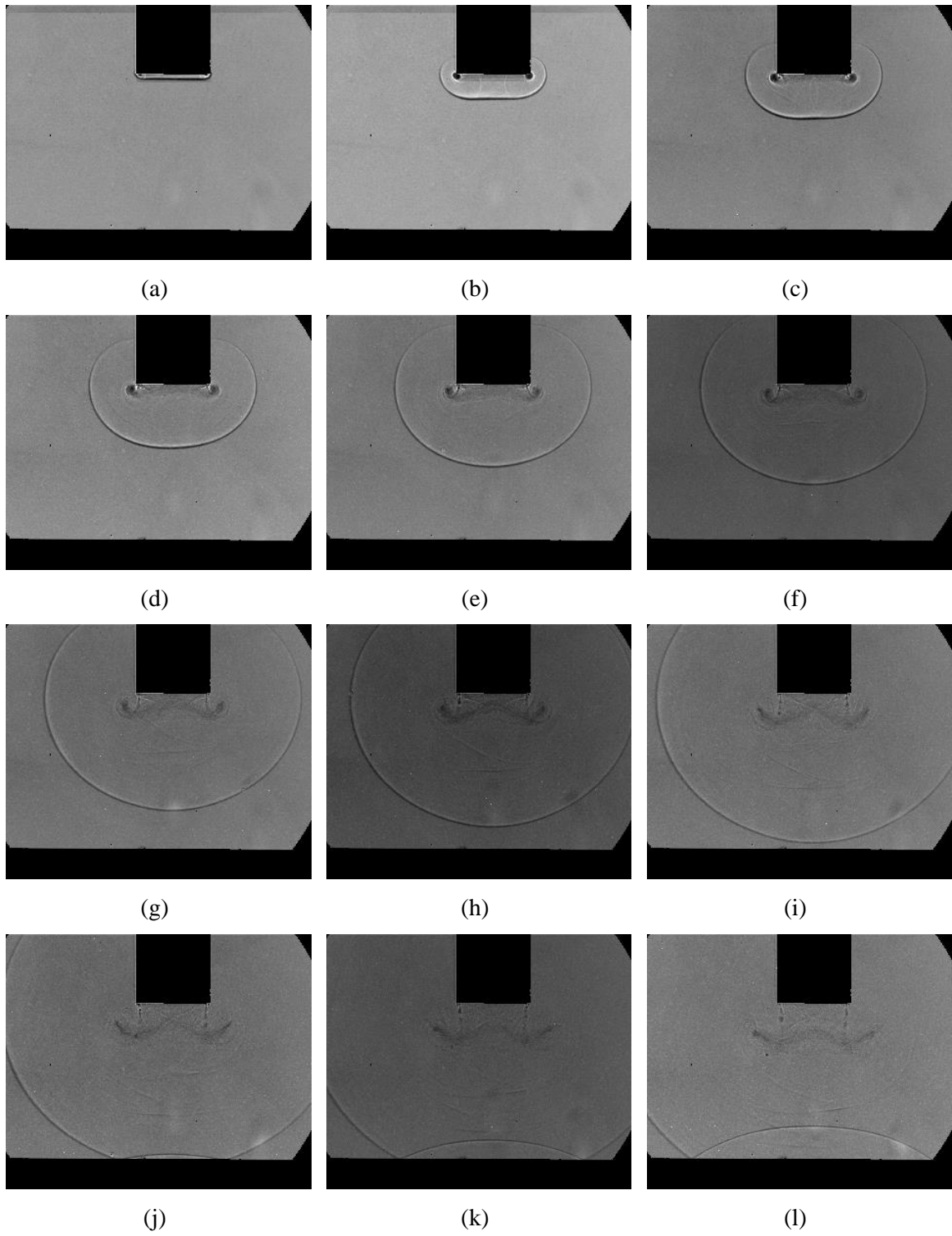


Figure 4.22 Framing shadowgraph images showing flow structure evolution from the open end of the square shock tube at $L=400\text{mm}$: (a) $\Delta t=4\mu\text{s}$; (b) $\Delta t=48\mu\text{s}$; (c) $\Delta t=62\mu\text{s}$; (d) $\Delta t=76\mu\text{s}$; (e) $\Delta t=90\mu\text{s}$; (f) $\Delta t=104\mu\text{s}$; (g) $\Delta t=118\mu\text{s}$; (h) $\Delta t=132\mu\text{s}$; (i) $\Delta t=146\mu\text{s}$; (j) $\Delta t=160\mu\text{s}$; (k) $\Delta t=174\mu\text{s}$; (l) $\Delta t=188\mu\text{s}$

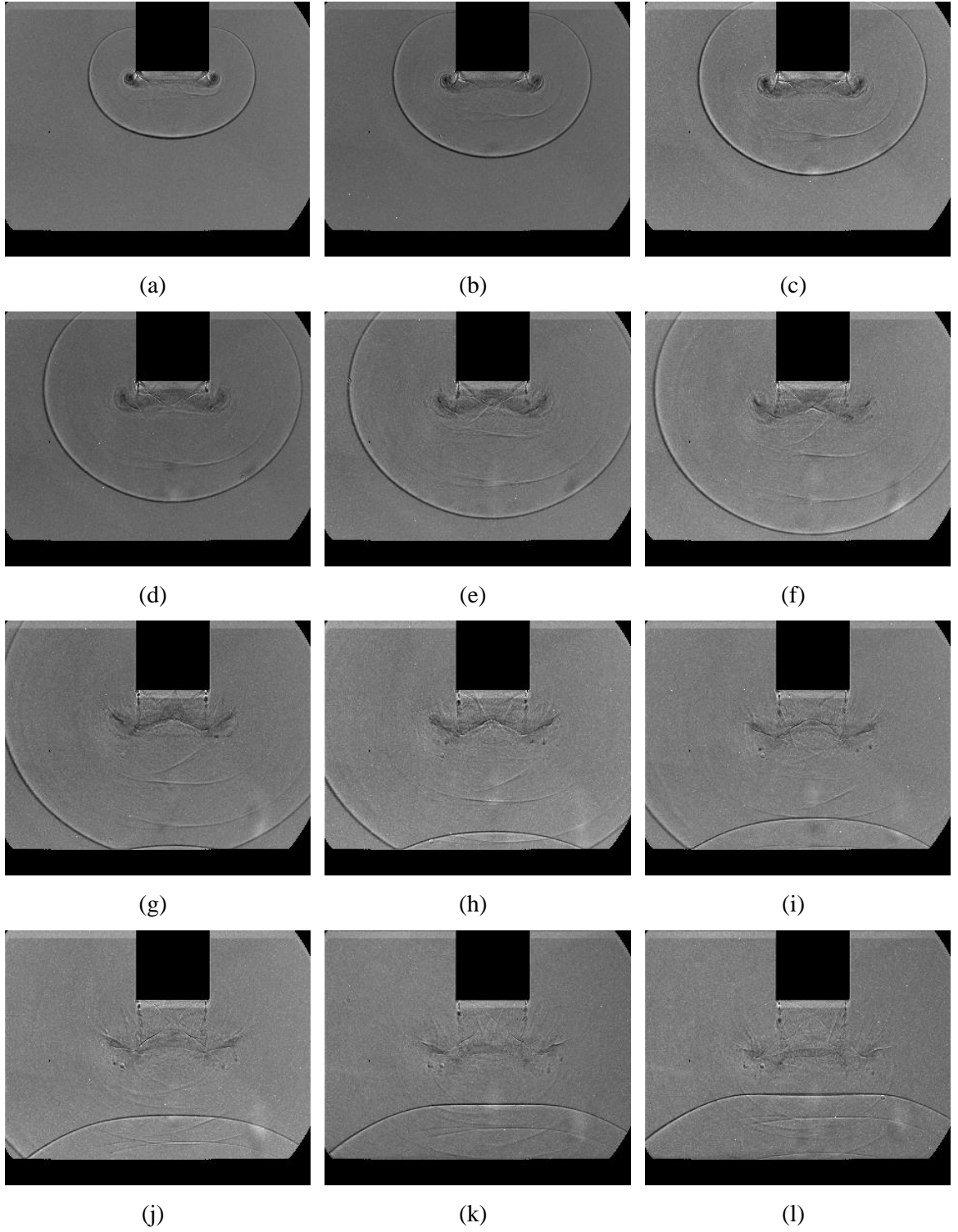


Figure 4.23 Framing shadowgraph images showing flow structure evolution from the open end of the square shock tube at $L=500\text{mm}$: (a) $\Delta t=76\mu\text{s}$; (b) $\Delta t=90\mu\text{s}$; (c) $\Delta t=104\mu\text{s}$; (d) $\Delta t=118\mu\text{s}$; (e) $\Delta t=132\mu\text{s}$; (f) $\Delta t=146\mu\text{s}$; (g) $\Delta t=160\mu\text{s}$; (h) $\Delta t=174\mu\text{s}$; (i) $\Delta t=188\mu\text{s}$; (j) $\Delta t=202\mu\text{s}$; (k) $\Delta t=216\mu\text{s}$; (l) $\Delta t=230\mu\text{s}$

4.4 Conclusions

A novel concept to design shock tubes driven by detonation transmission tubing in a reliable, repeatable, and safe manner for laboratory scale experiments is proposed and demonstrated in this work. Specifically, a circular open-ended shock tube with a straight driven section (inner diameter $ID = 22$ mm, driven section length $L_d = 330$ mm) was designed and manufactured. Also, a similar square shock tube was also fabricated to simulate square supersonic starting jets. To investigate the characterization of this novel type of shock tube, the pressure-time measurement in the driven section and the time-resolved shadowgraph test for the flow structure from the open end of the shock tubes were performed, which shows that the flow structure inside and out of the shock tubes driven by detonation transmission tubing is consistent with that of conventional compressed-gas driven shock tubes. Moreover, this novel type of shock tube has good repeatability of less than 3% with a Mach number range from 1.29 to 1.58 when the weight of the NONEL explosive mixture varies from 3.6mg to 12.6mg.

Compared with conventional compressed-gas shock tubes, the shock tube driven by detonation transmission tubing is smaller in size, more cost-effective, and much easier to operate. The flow structure from an open-ended shock tube driven by detonation transmission tubing is consistent with that of conventional ones. Therefore, it can be used in aerodynamics to investigate flows involving the shock wave, vortex loop, supersonic jets, and also applicable in medicine, biology, and other industries for various applications to replace conventional shock tubes. Investigations such as using different nozzle contours, the influence of the shock tube diameter or cross-section shape, and extending it into the close-ended shock tube will be performed further.

Chapter 5

Development of BOS and unsteady PSP systems

5.1 Development of background oriented schlieren system

Compared with conventional schlieren photography, the background-oriented schlieren (BOS) technique holds substantial potential as a practical qualitative visualization and complementary quantitative scientific research tool because of its simplicity, flexibility, and nonintrusive feature. The BOS technique can be divided into three major components: the background pattern, the image acquisition system, and the image post-processing tool. This section presents the BOS system developed in this research and the preliminary experimental results.

5.1.1 Background pattern

The design and manufacture of the background pattern is a significant variable for the resolution and overall capability of the BOS system and has been mostly qualitative in the past. Depending on the size and location of the background pattern, common methods for generating the BOS background pattern include splashing droplets of paint with a brush directly on a wind-tunnel wall [286], projecting laser speckles generated through ground

glass [287] and using computer-generated randomized monochromatic or coloured pixel segments [288, 289]. In this research, a MATLAB program was developed to generate and optimize the BOS random dot pattern through a user-controlled and fully customizable approach. Figure 5.1 shows the main interface of the MATLAB program for generating a BOS random dot background pattern. The number and diameter of dots along with the size of the background (A1-A4 paper) can be set through the program and then printed by a common ink-jet printer. The paper for printing can be conventional white copy paper sheets, white reflective film sheeting, or semi-transparent paper for increasing efficiency of the illumination.

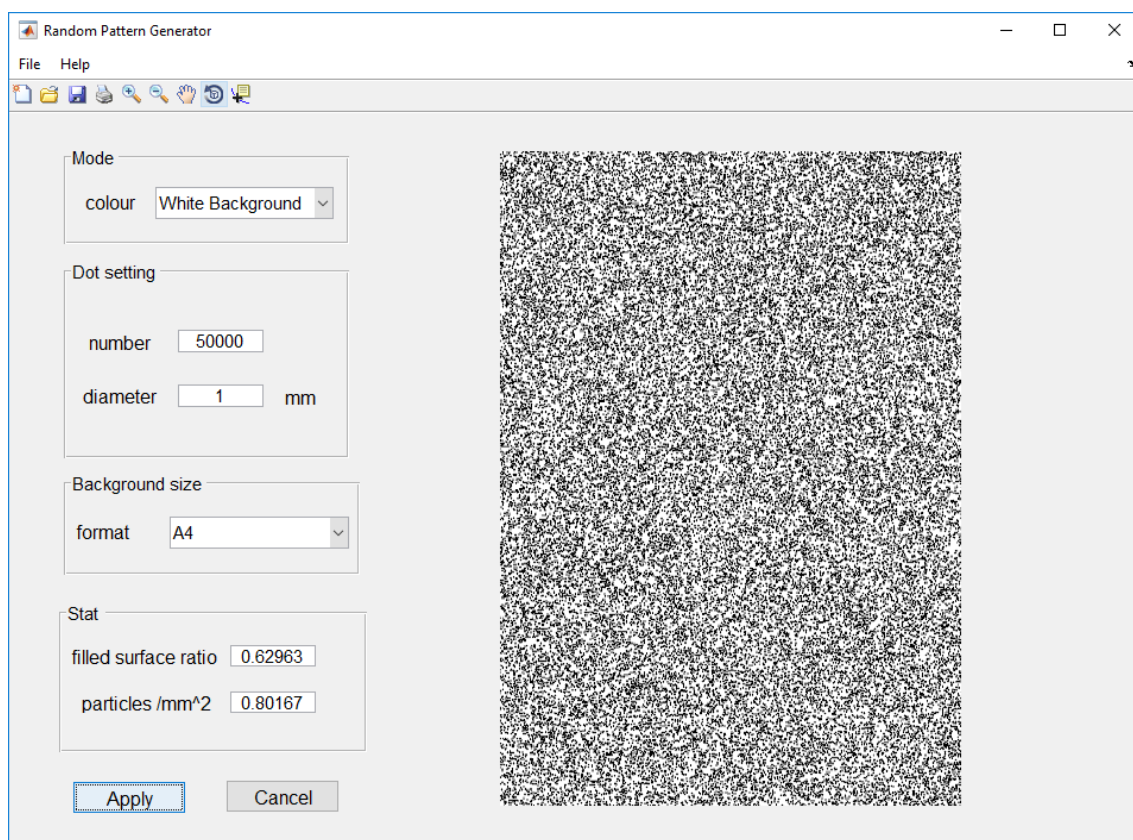


Figure 5.1 Graphic interface for generating BOS random dot background pattern

Generally, an individual random dot in a BOS image has an order of 3–5 pixels. In fact, 2-3 pixel images are better for the BOS accuracy, but frequently it is difficult to be reached due to the problem of diffraction at small apertures. The proper dot diameter of the background pattern depends on the camera spatial resolution and the experimental setup such as the focal

length of the lens f and the distance between the background and the camera Z_B . Therefore, several background patterns with different sizes and dot diameters need to be prepared for different occasions.

5.1.2 Image acquisition system

Unlike the traditional schlieren, the BOS setup can be performed without large, expensive, and precision optics [180-182]. For the BOS system developed in this work, only a background pattern printed by a common ink-jet printer, a light source, and a fast camera with a proper lens are needed.

The light source required for high-speed BOS must be small and bright, but otherwise is dependent mainly on the background pattern and the desired exposure time. Herein, a 450-1000W Xenon arc lamp from the Newport Corporation was used, which is also the main light source for high-speed shadowgraph and schlieren systems. By simply changing the socket adapter, you can interchange between different lamp types and wattages of the lamp. The continuous arc lamp used in this research offers the convenience of high-speed imaging without the need for flash synchronization. However, a synchronized flash lamp with greater illumination may be required in some applications.

Photron FASTCAM SA1.1 camera is selected as the time-resolved imaging device. Maintaining a square aspect ratio of 1024×1024 pixels for frame rates up to 5,400 fps, it is extremely useful when observing highly unsteady events such as shock wave propagation or distortion. With the benefit of a variable region of interest (ROI) to match the aspect ratio of the subject, the camera can capture images at a maximum frame rate of 675,000 fps and the capability of a sub-microsecond exposure can eliminate the shock motion blur.

5.1.3 Image post-processing

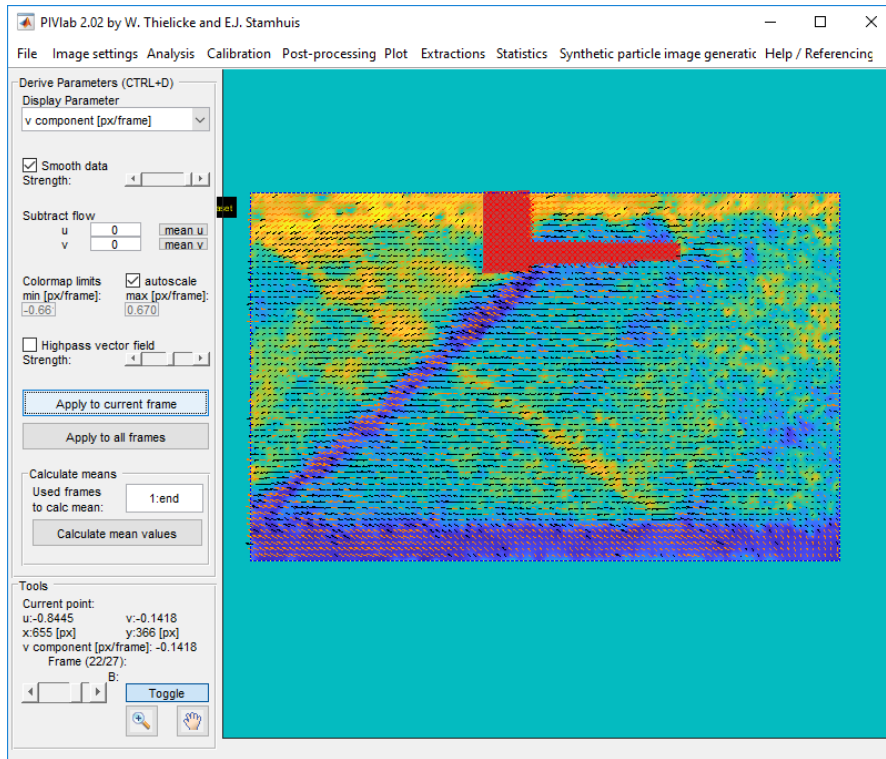


Figure 5.2 PIVlab software for BOS image post-processing

Raw BOS images are processed using an open source PIV software, PIVlab [290]. Detailed information regarding how to use this software can be found in its user manual [290]. In this dissertation, only the key image processing steps are briefly introduced:

(1) Setting a region of interest (ROI) and a mask

In most of the cases, the flow area is only a portion of the BOS image and an ROI setting is needed. To realize it, a mask is generally applied to exclude the test model in the image from subsequent analysis.

(2) Image pre-processing

It is a common approach to improve the BOS image quality before performing the actual image correlation [291, 292]. One of the most commonly used algorithms in PIVlab is contrast limited adaptive histogram equalization (CLAHE) [293]. The other effective

algorithm for pre-processing in PIVlab is the high-pass filter [294] that removes inhomogeneous lighting. It is assumed that the displacement of all dots within an interrogation is the same. In reality, brighter spots in the interrogation window contribute statistically more to the signal in the process of correlation to bias the non-uniform displacement. This problem can be solved by the intensity capping filter that sets a maximum limit of the greyscale intensity and replaces intensities of pixels higher than the threshold value by this limit value [292].

(3) Image correlation

The most key part in the BOS image processing is the cross-correlation algorithm that searches the dot pattern from the interrogation area A in an image back into the interrogation area B in the other image of an image pair, which can be performed by the discrete-cross correlation function [295]:

$$C(m, n) = \sum_i \sum_j A(i, j)B(i - m, j - n) \quad (5.1)$$

where A refers to the interrogation window from image A and B denotes the corresponding interrogation window from image B . The pixel location having the maximum intensity in the correlation matrix C provides the displacement of dot pattern from A to B [295].

The most straightforward method for calculating the correlation matrix C is the direct cross correlation (DCC) [296], or convolution filtering [297]. Correlation matrix C is calculated in the spatial domain for the DCC method and the two interrogation windows can have different sizes [297]. DCC has been demonstrated to obtain more accurate data than a standard discrete Fourier transform (DFT) algorithm [295]. However, the calculating efficiency of DCC is lower than that of the DFT method, particularly in the cases of large interrogation windows [291, 295, 298]. For the DFT algorithm, it employs interrogation windows of identical size, which increase the amount of background noise in the correlation matrix C [299]. This problem can be eliminated by performing multiple passes of the DFT [300]. The interrogation grid is refined within every pass [301] and a high spatial resolution and a better signal to noise ratio can be achieved in the final vector map. In real flows, the

BOS background pattern can be rotated or sheared [302-304]. In PIVlab, DFT approach with multiple passes is recommended for the image cross-correlation. The first pass obtains the displacement at the interrogation window centre. The original interrogation window *A* and the deformed interrogation window *B* are correlated in the next pass. After several passes, the displacement with high accuracy has been calculated.

(4) Post-processing

Post-processing is generally needed to achieve accurate displacement results [305]. The normalized median test [306] can be used to estimate the displacement fluctuation. After removing outliers, missing vectors can be replaced by interpolated data [305], which can be accomplished by the two-dimensional linear or spline interpolation [307]. Additionally, data smoothing can be conducted to reduce a certain amount of measurement noise. The smoothing algorithm implemented in PIVlab is an advanced penalized least squares method [308].

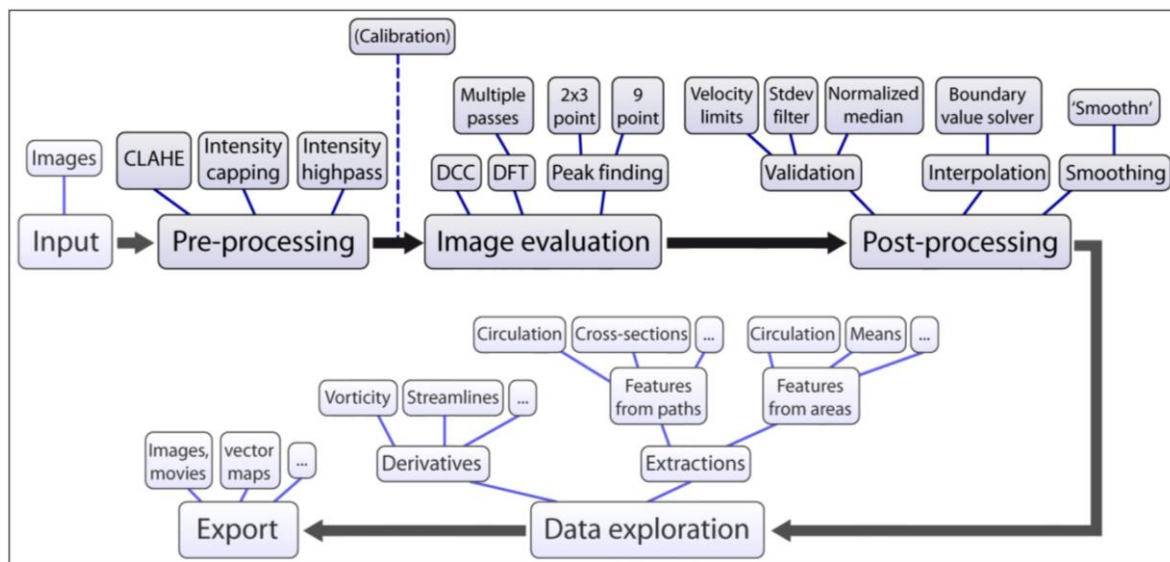


Figure 5.3 Overview of the workflow and the implemented features of PIVlab [290]

Figure 5.3 depicts the workflow and the implemented features of PIVlab software. To sum up, image processing techniques for BOS are similar to those in PIV. The main difference is that only the displacement induced by the density gradient is calculated in BOS and PIV needs to compute the velocity distribution based on the displacement result.

5.1.4 Validation case of the BOS system

To validate the aforementioned background oriented schlieren system, a pitot tube test in the supersonic wind tunnel (see Section 3.1.2) of the University of Glasgow was visualized using the BOS technique. Figure 5.4 shows the BOS experimental setup. A random-dot pattern was used as a background, where the diameter and the filled surface ratio was 1 mm and 63%, respectively. Reference (wind-off) images and test (wind-on) images were recorded with the same industrial video camera (Photron FASTCAM SA1.1 camera) for two-dimensional density measurements. Test images were recorded for one second at a framing rate of 1000 fps and an exposure time of 33 μ s. Background displacement caused by the flow around the pitot tube was determined by a cross-correlation analysis with PIVlab. In this experiment, the distances from the background to the centre of the wind tunnel, Z_D , and to the camera lens, Z_B , were 1000 mm and 1800mm respectively.

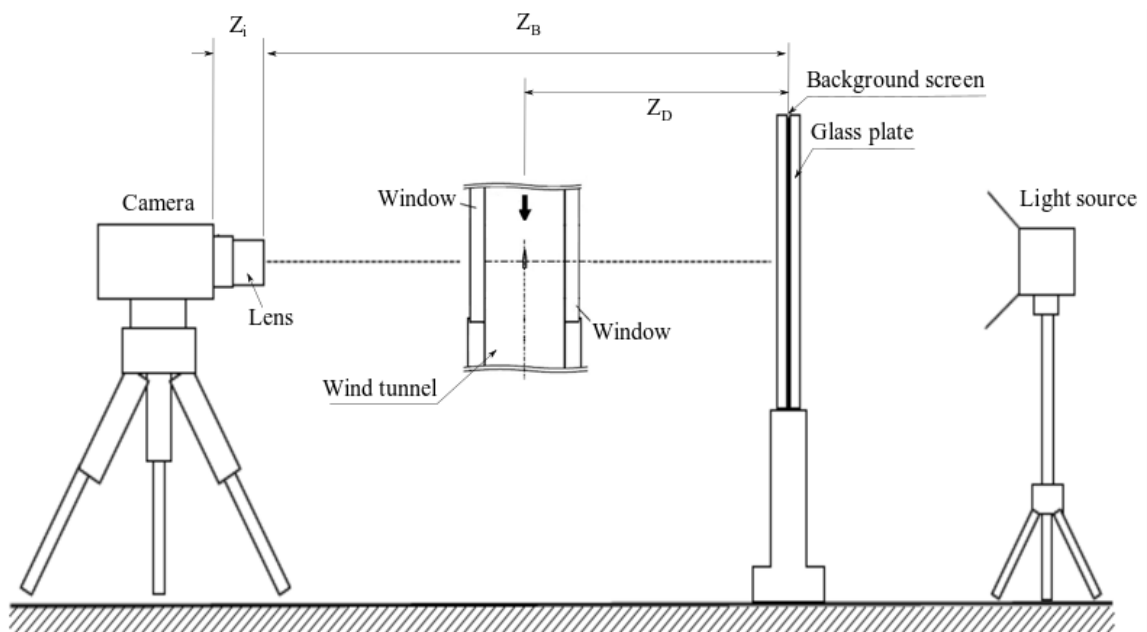


Figure 5.4 Schematic of BOS experimental setup in the indraft supersonic wind tunnel of the University of Glasgow

Figure 5.5 depicts displacement results from BOS in the case of $M=2.0$. The flow structure analysis based on the displacement/density distribution is given in Figure 5.6. As shown in Figure 5.5 and Figure 5.6, the sensitivity of the BOS system is good enough to visualize weak density variations caused by expansion waves, boundary layer, and weak oblique

shock generated by the small gap between the nozzle and test section upstream. It also presents the strong density gradient caused by the bow shock in the front of the hose tip of the pitot tube, normal shock ahead of the pitot tube root near the tunnel top wall, and the strong oblique shock system.

However, it also can be seen from Figure 5.5 and Figure 5.6 that shock waves visualized by the aforementioned BOS system are quite thick and blur. The reason for this is the long exposure time ($33\mu\text{s}$) and the high unsteadiness of the shock waves due to wind tunnel vibration and its inherent unsteady flow feature. Next, to improve the performance and capacity of the current BOS system, it will be optimized further including adding extra light sources to shorten the exposure time, testing new fast cameras with better spatial resolution, and optimizing the dot diameter and the filled ratio of the background pattern.

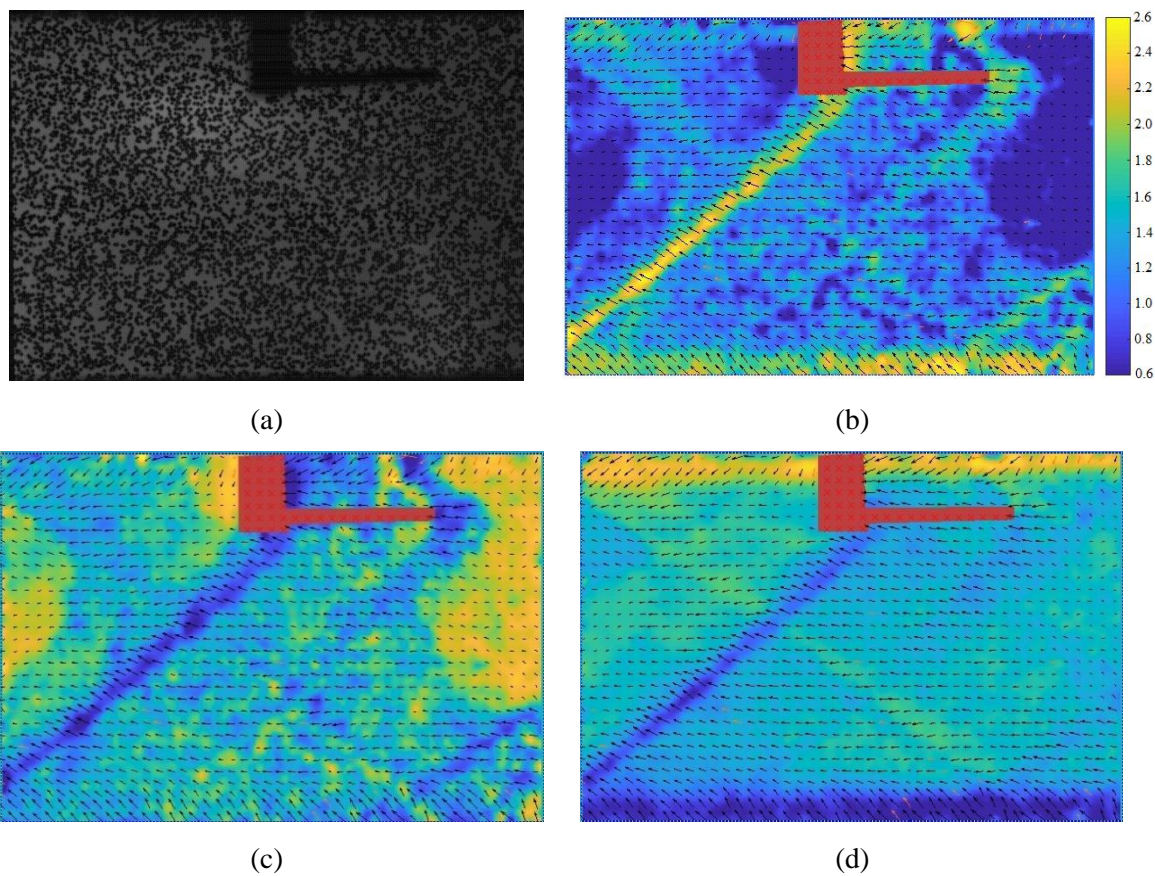


Figure 5.5 BOS results of the pitot tube test in the case of free stream Mach number $M=2.0$: (a) raw BOS image; (b) displacement distribution in pixels; (c) horizontal displacement in pixels; (d) vertical displacement in pixels

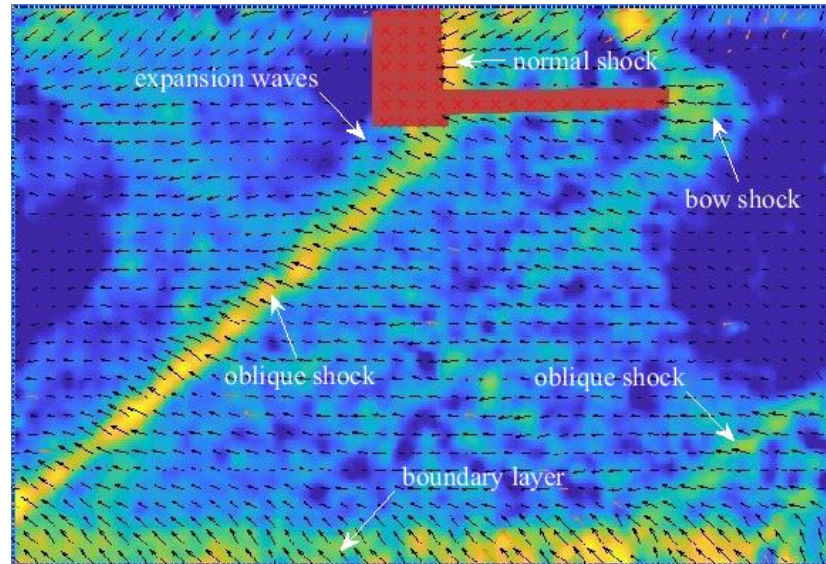


Figure 5.6 Flow structure obtained from BOS displacement distribution

5.2 Development of unsteady PSP system

In the University of Glasgow, there is a commercial steady PSP system from Innovative Scientific Solutions Inc. (ISSI). In this research, an unsteady polymer-ceramic pressure sensitive paint (PC-PSP) system based on a novel PtTFPP-based unsteady PSP formulation was built up on the basis of the commercial steady PSP system.

5.2.1 Paint formulation

The paint is the core of the unsteady PSP measurement system. In this work, a novel PC-PSP formulation was developed, which consists of a luminophore, porous particle, polymer, and solvent. Pt(II) meso-tetra(pentafluorophenyl)porphine (PtTFPP) from Santa Cruz Biotechnology, Inc. was selected as the pressure sensitive luminophore, which is ideally excited at 395nm. Mesostructured-silica (M-silica) purchased from Sigma-Aldrich and KE-441-T room temperature vulcanizing silicone rubber (RTV) from Shin-Etsu Chemical was chosen as incorporated particles and the polymer of the binder respectively. Toluene purchased from Sigma-Aldrich was used as a solvent.

The paint solution was well mixed using a stirrer and then sprayed onto sample surfaces

using a spray gun (HVLP 802342, DEVILBISS) with a nozzle diameter of 1.3 mm. The binder and luminophore solutions were often sprayed separately to improve the time response of PC-PSP in previous studies [309-311]. However, in this research, the luminophore and the binder of PC-PSP were mixed in the same solution and the PC-PSP coating could be finished by single spraying. The samples after spray then were cured in an oven for 8 hours before application.

5.2.2 Preparation system

The PC-PSP is prepared by the following steps:

(1) Clean the test model and calibration samples

Clean the test model and calibration coupons using acetone or alcohol on wipes. The adherence and properties of the paint can be affected by the oil and grease on the surfaces of the test model or calibration samples. To ensure the quality of the data obtained, it is important to clean them before spraying.

(2) Paint preparation

The PC-PSP formulation proposed in this research consists of four parts: the luminophore, porous particle, polymer, and solvent. The first step is to determine how much paint you wish to spray on the model and remove this volume from the solvent. For example, if you want to spray 100mL paint on the model you would remove 100mL toluene into an empty jar. Then, add a specific proportion of luminophore, porous particle, and polymer into the jar with solvent (3mg/10ml PtTFPP, 150mg/10ml M-silica, and 150mg/10ml RTV for this PSP formulation). A Sartorius CP225D laboratory balance with a high level of accuracy and precision (0.01-mg readability) was used to measure the weights of the luminophore, particle, and polymer. Once all the four parts are measured together in a jar, you can put a lid on and shake the jar very well. In this research, to enhance mixing, the paint in its container was put into a XUB digital ultrasonic bath from Grant Instruments filled with water for around 15 minutes.

(3) Spraying

In this work, a high volume low pressure (HVLP) spray gun from DEVILBISS with a nozzle diameter of 1.3 mm was employed without filtering or straining. If possible, a small amount of distilled water can be used to thin the paint. Set the gun pressure to 200 kPa and turn the siphon rate adjustment totally off. Open the siphon rate adjustment up until a light mist of paint is achieved from the nozzle of the spray gun. The distance of the spray gun from the model surface is generally approximately 30 cm. Over a bare metal surface, 7 to 9 light cross coats are usually applied (too many coats on the surface can result in flaking of the paint). The cross coat means working from left to right while moving down the model and then back up left to right. This constitutes one coat. The next coat is applied top to bottom or bottom to top in a similar manner.

(4) curing

After spraying, the paint needs to be cured to reach the glass transition of the polymer. The coated samples of PC-PSP were cured in an oven from SciQuip at 80°C for 8 hours after spraying. The SciQuip oven was designed to provide accurate temperature uniformity with no overshoot. There is a microprocessor inside the oven, which achieves precise environmental control and features the advantage of rapid recovery after door opening.

Once a model is painted and cured, place it out of room lighting or ambient lighting when not in use. Do not touch the surface once painted. If the model must be handled, use latex or nitrile gloves, careful not to scratch the painted surface. It is also worth noting that adequate ventilation or appropriate respiratory protection is needed during the spraying process. 3M-7500 reusable mask with A1 HgP3 organic vapour filter cartridges was used in this work. A ventilation system was also built up in the PTSP lab in the university of Glasgow.

5.2.3 Illumination

PtTFPP-based PC-PSP was excited by two 400-nm 4-inch air-cooled LEDs (LM4X-DMHP-400, Innovative Scientific Solutions Inc.). The LED light source provides uniform, stable and high-power illumination, for unsteady pressure sensitive paint measurements. This LED was actually designed for lifetime pressure and temperature sensitive paint acquisition systems. The rise and fall time is less than 500 ns. Because it is overdriven, the duty cycle is

limited to 5%, and its maximum pulse width is limited to 1 ms. Since the pressure fluctuation frequency of the shock wave and boundary layer interaction over flexible surfaces in this research is expected over 1kHz, and an exposure time of less 1ms is required. Therefore, this LED is also applicable to the intensity-based unsteady PC-PSP system.

Additionally, there are 4 kits of 2-inch air-cooled LEDs (LM2X-DMHP-400, Innovative Scientific Solutions Inc.) available. The 2-inch, air-cooled LEDs, as shown in, were designed for applications in smaller wind tunnels or test facilities where a model is relatively close. Although not as powerful as the aforementioned 4-inch air-cooled LEDs, they can be added when the illumination is not strong enough for highly unsteady or long-distance occasions. It is worth mentioning that two 460-nm LED arrays which were made up of 144 Bivar blue LEDs were built in-house for the potential Ru(dpp)₃-based unsteady pressure sensitive paint, which is ideally excited at 460nm. As this light source does not contain any temperature control or forced cooling, it will be left to settle to a running temperature at a fixed voltage before PSP data acquisition began. During this period of time, the PSP sample will be not exposed to the light to avoid excessive photodegradation.

5.2.4 Image acquisition

The luminescence from PC-PSP was captured by a 14-bit colour CCD camera (PSP-CCD-C, Innovative Scientific Solutions Inc.) with a 550-nm long pass filter (550FG05-50, Innovative Scientific Solutions Inc.) during the static calibration. In the case of potential binary unsteady PSP for eliminating the temperature sensitivity, a pressure-sensitive signal channel and a reference channel with different spectrum need to be acquired. Usage of a colour CCD allows binary pressure sensitive paint data (two separate spectral peaks) to be acquired at the same time. Unlike the conventional monochrome camera, in which optical filters in front of the camera lens are needed to detect light of a specific spectrum band, the filtering is applied on the chip using a standard Bayer filter for the colour camera. Therefore, all images are acquired through a single camera, which can minimize the image alignment errors and the stability of the illumination source will be a less significant issue. The major drawback of this approach is the loss of spatial resolution. In a colour chip, only ¼ of the pixels are sensitive to the signal channel (red pixels) on the standard Bayer filter. Despite the loss of spatial resolution, the colour camera approach produces excellent results at low

speed flows. For the unsteady PC-PSP wind tunnel test, a 12-bit monochrome Photron FASTCAM SA1.1 camera with a 1024×1024 -pixel spatial resolution will be adopted.

5.2.5 Synchronization and control

Since there is a rising time and falling time for the LED light source, the camera needs to start acquiring after the LEDs are open and become stable. Similarly, LED should be turned off after the exposure of the camera. The synchronization and timing strategy of light source and camera is performed by a pulse sequence generator (PSG-2, Innovative Scientific Solutions Inc.).

5.2.6 Static calibration

The relationship between the air pressure and the luminescence intensity of pressure sensitive paint is given by Stern-Volmer equation [188, 193]. Ideally, the Stern-Volmer coefficients are depended on pressure without temperature dependence. However, a more manageable polynomial form of the Stern-Volmer equation that takes the temperature sensitivity of the paint into account is commonly used:

$$\frac{I_{ref}}{I} = \chi_{ij} \sum_{i,j=0}^n \left(\frac{P}{P_{ref}} \right)^i T^j \quad (5.2)$$

where I refers to luminescence intensity from PSP, P is the pressure of the paint surface and T denotes temperature. The subscript “*ref*” refers to the reference condition of the prior calibration experiment. The constants χ_{ij} are Stern–Volmer coefficients. Generally speaking, the second-order approximation ($n=2$) is adequate to describe the nonlinear behaviour of pressure sensitive paint.

There are three common calibration methods to get the Stern–Volmer coefficients in Equation 5.2: prior calibration, in-situ calibration, and calibration of the model with paint directly in the test section of the pressurised wind tunnel. The prior calibration that is called also static calibration collects luminescent intensity data under different pressure and

temperature combinations, determining the Stern-Volmer coefficients prior to the wind tunnel test. Additionally, Klein et al. [312] demonstrated that the paint properties of calibration sample and the model in the wind tunnel test are different because of the paint thickness change and other factors. In an in-situ calibration, the pressure data from the pressure taps on the wind tunnel model is used to relate the luminescent intensity of PSPs [203, 313]. *k*-fit calibration method combines the static calibration and in-situ calibration [314]. This approach is especially effective when the pressure range of the pressure taps does not cover pressure range on the model surface [315].

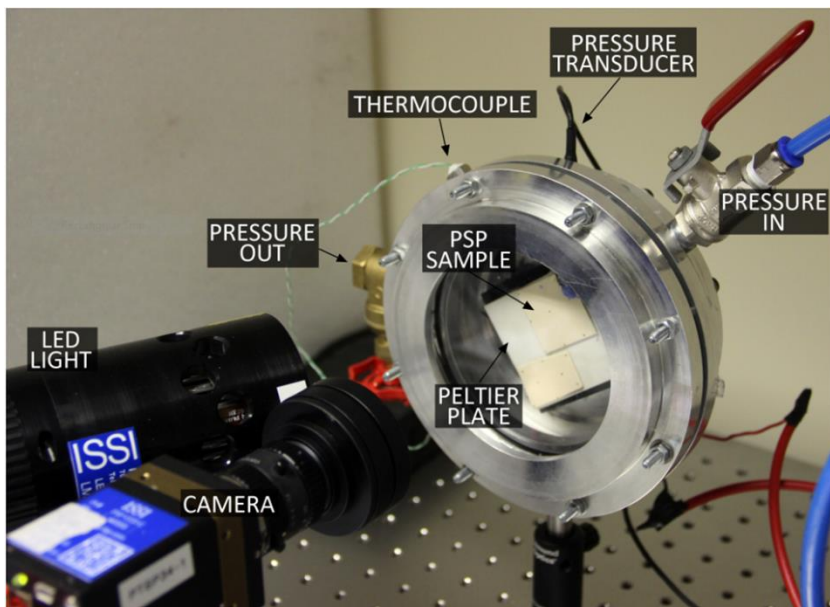


Figure 5.7 PSP static calibration system in University of Glasgow [165]

The experimental setup of the PSP static calibration system in the University of Glasgow is illustrated in Figure 5.7. The calibration chamber consists of a pressure vessel, a pressurising inlet, a valve to evacuate pressure, a Peltier thermoelectric plate, a pressure transducer and a temperature sensor [165]. The calibration sample was fixed on the Peltier plate by a thermal glue. The Peltier plate has a temperature difference of up to 74°C and the temperature was recorded with a thermocouple with an accuracy of $\pm 0.5^{\circ}\text{C}$. The pressure in the PSP static calibration chamber was measured with a Kulite pressure transducer.

400-nm LEDs from ISSI were chosen as the light source to excite the PSP calibration

samples. The PSP-CCD-C camera was placed normal to the optical window of the calibration chamber and the LEDs were mounted on its side. A 550-nm long-pass optical filter was used to separate light from the LEDs and the pressure sensitive paint.

Thirty “dark images” with the light sources switched off were captured ahead of the PSP calibration each test. For each pressure and temperature condition, only one test image with illumination was captured. The dark corrected test images were computed by subtracting the test image with the averaged dark images. This process aims to minimise background noise. These dark corrected test images were then processed by a MATLAB program and the data of 150×150 pixels of dark corrected test images were averaged to reduce the shot noise.

5.2.7 Dynamic calibration

To determine the response time of unsteady PSP, a dynamic calibration system was designed. The experimental setup for PSP dynamic calibration is illustrated in Figure 5.8. A square cross-sectional shock tube driven by NONEL tube has been designed, which has a test section with two optical windows allowing acquiring the luminescence intensity emitted from the PSP sample mounted on the end wall of the shock tube (see Appendix A.3). The pressure fluctuation on the end wall is monitored by a Kulite pressure transducer described in Section 3.2.1. LM4X-DMHP-400 LED from ISSI is adopted as the light source and the variation of the luminescence intensity from PC-PSP is expected to be observed by a photomultiplier tube (PMT) (H10721-20, Hamamatsu Photonics) with a 550nm long-pass filter. A digital storage oscilloscope (TDS2001C, Tektronix) will be used to monitor and display the voltage outputs of PMT and Kulite pressure transducer simultaneously. Afterwards, the response time of PSP can be determined by directly comparing the pressure step change curve measured by Kulite pressure transducer and the paint luminescent emission curve detected by PMT. Generally, the response time is represented by the time for a pressure-sensitive paint to reach 99% of its response to the pressure step change [188]. All equipment has been ready up to now and a debugging test for the whole PSP dynamic

calibration system will be conducted shortly.

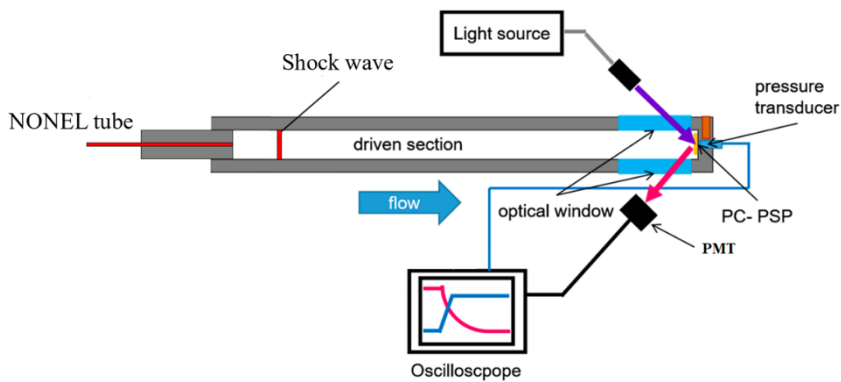


Figure 5.8 Schematic of dynamic calibration setup for unsteady PSP

5.2.8 Validation case of unsteady PSP system

To validate the aforementioned unsteady PSP system, 10ml PC-PSP solution was prepared, which consists of 3mg PtTFPP, 150mg M-silica, 150mg RTV, and 10ml toluene. After mixing the paint using an ultrasonic bath, the paint was sprayed onto aluminium calibration samples. Thereafter, the samples were cured in an oven at 80°C for 8 hours just after spraying.

The cured samples were calibrated in the static calibration system described in Section 5.2.6 with pressure varying from 10 to 200 kPa and temperature in a range of 10 to 50°C.

Pressure sensitivity

Figure 5.9 presents the Stern-Volmer plot of the PC-PSP sample cured at 80°C for 8 hours. The intensity ratios in each calibration point were calculated following the image processing procedure described in section 5.2.6. The second-order approximation ($n=2$) of Stern-Volmer equation (Equation 5.2) was employed to describe the behaviour of the "nonlinear" responding of PC-PSP. The Stern-Volmer coefficients were evaluated based on the curve fitting app of MATLAB (Figure 5.10). The function of the air pressure and the luminescence intensity of the PC-PSP sample cured at 80°C for 8 hours is:

Chapter 5 Development of BOS and unsteady PSP system

$$\frac{I_{ref}}{I} = \chi_{ij} \sum_{i,j=0}^2 \left(\frac{P}{P_{ref}} \right)^i T^j \quad (5.3)$$

Where $\chi_{00} = 0.1170$, $\chi_{10} = 0.1014$, $\chi_{20} = -0.00003$, $\chi_{01} = 0.0018$, $\chi_{11} = 0.000001$, $\chi_{21} = 0.000006$, $\chi_{22} = 0$. The *R*-square of fit is 0.9995, which proves a good fitting.

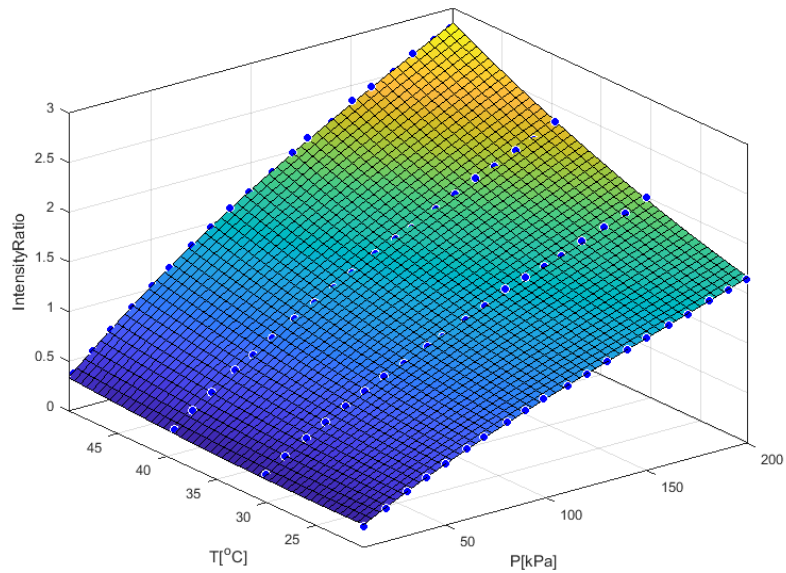


Figure 5.9 Stern-Volmer plot of in-house developed PC-PSP

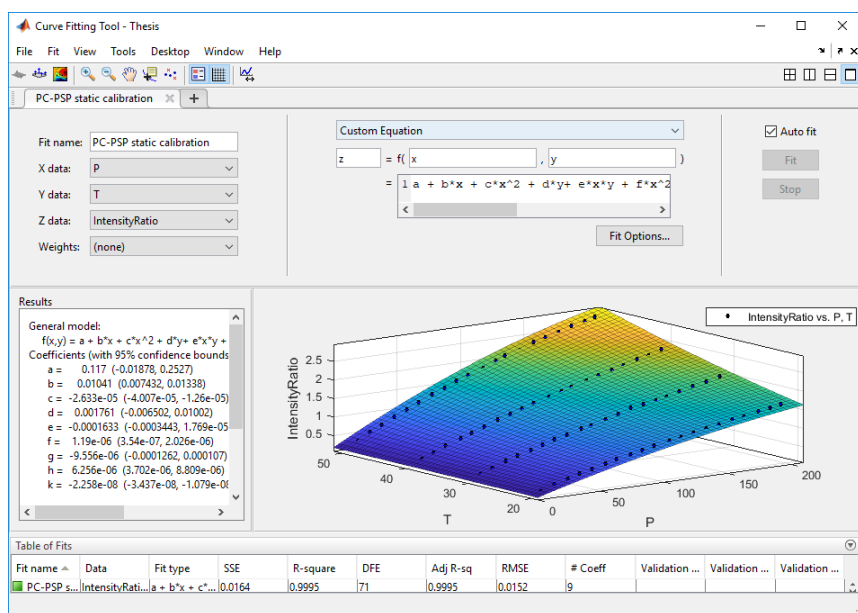


Figure 5.10 Interface for curve fitting of Stern-Volmer equation

It is worth mentioning that the error in calculating Stern-Volmer constants χ_{ij} is defined as PSP static calibration uncertainty, which is always represented by the standard deviation of Stern-Volmer constants obtained in several replication tests [188]. Since the pressure and temperature values in the calibration chamber can be well controlled, PSP static calibration error is usually small. Therefore, the PSP static calibration uncertainty is not evaluated in this research. Next, the error propagation and total uncertainty estimation model for PSP wind tunnel tests will be established based on previous studies [188], including static calibration error, camera noise, paint temperature effect, illumination variation, filter leakage and other error sources.

The pressure sensitivity defined as: $\Delta(I_{ref}/I)/\Delta P$, can be calculated from the Stern-Volmer plot. Figure 5.11 demonstrates Stern-Volmer calibration curves at different temperatures of PC-PSP sample cured at 80°C for 8 hours. As presented in Figure 5.11, the responding of the PC-PSP is nonlinear to some extent. In a smaller pressure range, the calibration curve can be dealt with as a linear function. For a wider pressure range, the nonlinearity cannot be ignored. Overall, the pressure sensitivity in high pressure region is lower than that of low pressure region, which is probably caused by the high self-quenching rate in high pressure conditions.

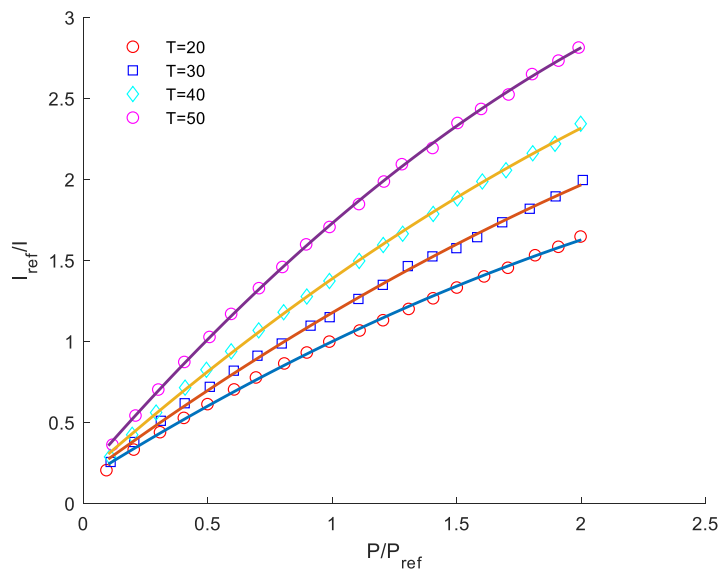


Figure 5.11 Stern–Volmer curves of PtTFPP-based PC-PSP in different temperatures

Although the nonlinearity of the calibration curves, overall pressure sensitivity is still calculated from a linear fit model in a pressure range of 10kPa-200kPa. The pressure sensitivity of the PtTFPP-based PC-PSP is 0.75% per kPa at 20°C.

Temperature sensitivity

The emission intensity of the pressure sensitive paint is not only determined by the surface pressure and is also affected by temperature. To improve the pressure measurement accuracy by PSP, its temperature sensitivity should be as low as possible. Figure 5.18 demonstrates the curve between the normalised intensity output I_{ref}/I and the temperature T of the PtTFPP-based PC-PSP used in this study.

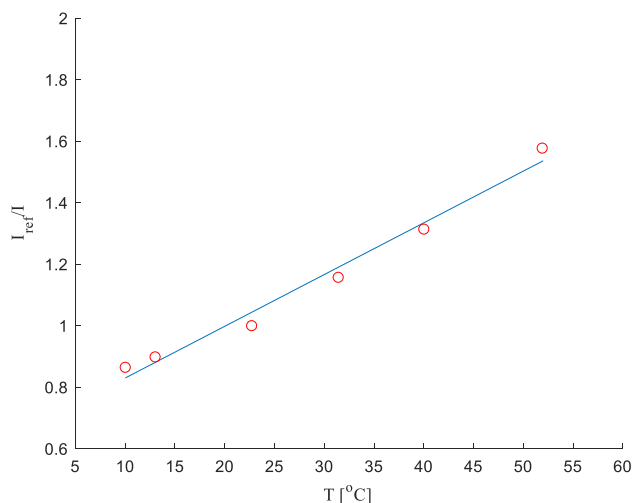


Figure 5.12 Temperature sensitivity of in-house developed PC-PSP

As shown in Figure 5.12, the normalised intensity from the PtTFPP-based PC-PSP increases linearly versus temperature and the temperature sensitivity is around 1.94%/°C. The experimental uncertainty of PSP temperature sensitivity test can be calculated by the standard deviation of temperature sensitivity constants obtained in several replication tests. Because the temperature in the PSP calibration chamber can be well controlled with a small measurement and hysteresis error, the uncertainty of the PSP temperature sensitivity experiment is not evaluated in this preliminary research. However, it will be taken into account in the total uncertainty estimation model for PSP wind tunnel tests.

Photo-Degradation

The phenomenon that the luminescent intensity of the pressure sensitive paint decreases gradually under a stable illumination is known as the photo-degradation of the paint [188, 193]. Generally speaking, the photo-degradation rate of porous unsteady PSP is much higher than that of conventional steady PSP. To investigate the photo-degradation characteristics of the PC-PSP developed in this study, the paint was illuminated under two continuous LEDs. The emission intensity was captured once per 5 minutes. Figure 5.13 shows the photo-degradation curve of the PtTFPP-based PC-PSP. It can be seen from Figure 5.13 that the luminescence intensity varies nonlinearly versus time, decreasing faster in the first place and slower thereafter. An overall photo-degradation rate is still evaluated based on a linear fit in a period of 30 minutes. The photo-degradation rate of the PtTFPP-based PC-PSP is around 0.86% per minute.

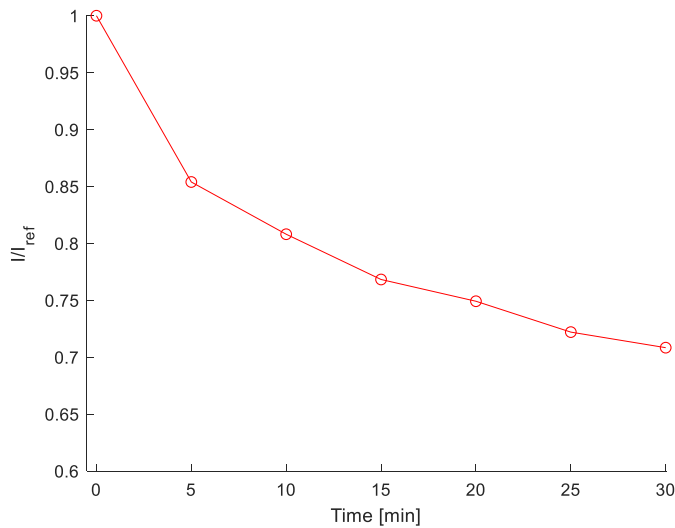


Figure 5.13 Photo-degradation rate of in-house developed PC-PSP

The comparison of properties between in-house developed PC-PSP and commercial one from ISSI is given in Table 5.1. It is obvious that the in-house developed PC-PSP has a better static performance than that of commercial one from ISSI, including higher pressure sensitivity, smaller temperature sensitivity, and lower photo-degradation rate. Currently, the shock tube facility for dynamic calibration of unsteady PSP has been fabricated. The response time of the in-house developed PC-PSP and its behaviour in wind tunnel tests will

be validated further.

Table 5.1 Comparison of properties between in-house developed PC-PSP and a commercial one from ISSI

	Property	PC-PSP from ISSI	In-house PC-PSP
1	Pressure sensitivity	0.6% per kPa	0.75% per kPa
2	Pressure range	0-kPa to 200-kPa	10-kPa to 200-kPa
3	Temperature sensitivity	3.6% per °C	1.94%/°C
4	Temperature range	0°C to 80°C	0°C to 50°C
5	Excitation	380-nm to 550-nm	380-nm to 550-nm
6	Emission	600-nm to 720-nm	600-nm to 720-nm
7	Photo-degradation rate	1% per minute	0.86% per minute

5.3 Conclusions

The unsteady background-oriented schlieren (BOS) system was preliminarily established in this work. A MATLAB program was developed to generate and optimize the background pattern through a user-controlled and fully customizable approach. The number and diameter of dots along with the size of the background (A1-A4 paper) can be set through the application. The pattern then is printed by a common ink-jet printer. The paper for printing can be a conventional white copy paper sheet, white reflective film sheet, or semi-transparent paper to improve the efficiency of the illumination.

Based on the light source and high-speed camera from the time-resolved shadowgraph, a validation BOS test was performed in the supersonic wind tunnel of the University of Glasgow to visualize the supersonic flow structure around a pitot tube in the test section. All the BOS images were processed using an open source PIV software, PIVlab. The preliminary BOS result shows that the sensitivity of the BOS system is good enough to visualize weak density variations caused by expansion waves, boundary layer, and weak oblique shock. However, shock waves visualized by the present BOS system were quite thick and blurry. The reason for this is probably the long exposure time (33μs) and the high unsteadiness of the shock waves due to the wind tunnel vibration and its inherent unsteady flow feature. Next, to improve the performance and capacity of the current BOS system, it will be optimized further including adding extra light sources to shorten the exposure time, testing new fast

cameras with better spatial resolution, and optimizing the background pattern.

Pressure-sensitive paint (PSP) is a novel optical measurement technique for global surface pressure measurements in wind tunnel testing. In University of Glasgow, there is a commercial steady PSP system from Innovative Scientific Solutions Inc. (ISSI). In this dissertation, an unsteady PSP system based on a novel PtTFPP-based PSP formulation was built up. Pt(II) meso-tetra(pentafluorophenyl) porphine (PtTFPP) from Santa Cruz Biotechnology, Inc. was selected as the pressure sensitive luminophore, which is ideally excited at 395nm. Mesostructured-silica (M-silica) purchased from Sigma-Aldrich and KE-441-T room temperature vulcanizing silicone rubber (RTV) from Shin-Etsu Chemical was chosen as incorporated particles and the polymer of the binder respectively. Toluene purchased from Sigma-Aldrich was used as the solvent. To validate the performance of the unsteady PSP system, the properties of the PtTFPP-based PC-PSP were investigated based on the PSP static calibration system. Compared with the commercial PC-PSP from ISSI, the in-house developed one has higher pressure sensitivity, smaller temperature sensitivity and lower photo-degradation rate. The response time of the in-house developed PC-PSP and its behaviour in wind tunnel tests need to be validated further.

Chapter 6

Image processing techniques for shock wave detection and tracking

Schlieren and shadowgraph have been widely applied since the early 19th century to visualize the flow features in compressible flows, such as expansion and shock waves, shear layers and vortices [167, 257, 316-325]. With only a small number of frames, there is no need to process them automatically to detect and track flow structures. Once the number of images in unsteady flow phenomena is large, even over thousands, extracting data manually becomes too time-consuming and no longer reliable. Given a large set of schlieren or shadowgraph images, image algorithms in computer vision can be used for automatic image processing. Therefore, the ability to automatically detect, extract, and track flow features from a large number of experimental or numerical shadowgraph and schlieren sequences has increased quickly in the last decades [320, 326-328].

Estruch et al. [329] proposed a method to evaluate shock wave unsteadiness, which subtracts the wind-off image from the test images, followed by Canny edge detection. Shock wave tracking was achieved by point tracking in edge images. Although the shock motion can be estimated by this method, other flow properties such as shock distortion and inclination angle

were not attainable. An approach [330] was also proposed, in which shock angles were calculated by two edge points obtained through scanning image lines. However, shock motion may pitch outside of the area being scanned in this method. Also, software for extracting flow features by automatically processing wind tunnel schlieren sequences was developed at the High Enthalpy Shock Tunnel Göttingen [331]. Hough transform and its variants were used to track the model motion and calculate the shock standoff distance from a cylinder and oblique shock angle. The comparison between results from the software and the data from conventional pressure measurements shows considerable agreement; however, the image processing in the software is not fully rule-based and needs significant user involvement. These methods without a classifier feature extraction and with significant feature subjectivity are limited to specific data sequences. Additionally, N. T. Smith et al. [320] developed a method to detect the motion of the large-scale shock wave structure by the sharp model tip and intersection point of the shock wave. Fused feature identification algorithms were adopted to track these points from a large data set of schlieren or shadowgraph images. They also proposed a scheme that uses the curvature scale space (CSS) representation to isolate shock contours.

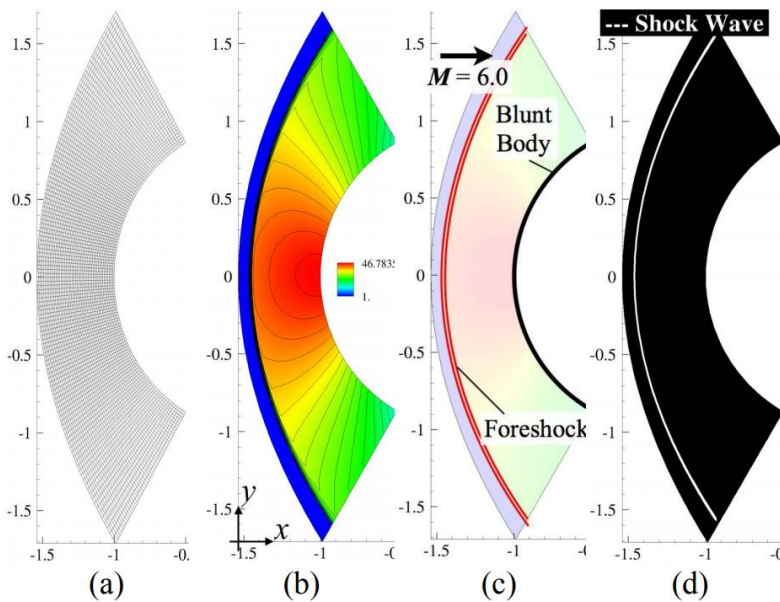


Figure 6.1 A shock wave detection method by combining Canny's edge detection and Rankine-Hugoniot relations for CFD simulation of a hypersonic flow over blunt body: (a) mesh; (b) pressure distribution; (c) schematic drawing; (d) detection result [326]

T. Fujimoto et al. [326] developed a novel method for detecting shock by combining the Canny edge detecting algorithm, which is one of the common image processing methods for detecting edges, and Rankine-Hugoniot relations. This scheme can detect shock successfully and automatically without threshold values that were required for the traditional Canny algorithm, making it both lower cost and better theoretical accuracy. Furthermore, Cui et al. [332] investigated the influence of the image edge detection algorithm such as Roberts, Prewitt, Sobel Canny, and Laplacian of Gaussian for improving the shock detection accuracy. Dehghan et al. [333] provided a two-level image processing scheme to study the effects of speed change on the airplane surface.

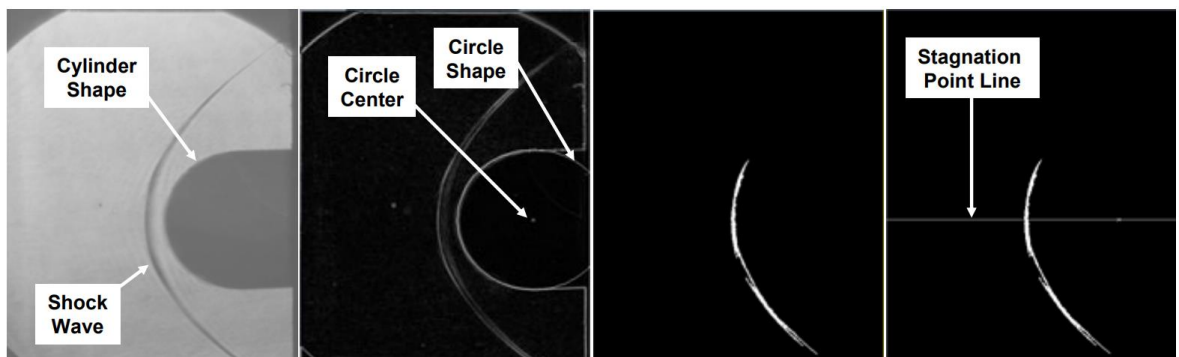


Figure 6.2 Software development for pattern recognition in high speed schlieren visualization at the high enthalpy shock tunnel Göttingen: (a) original image; (b) gradient image with the detected circle as cylinder shape; (c) partial shock wave fitting; (d) stagnation point line intersecting circle centre and shock shape [331]

Most of the above work has not kept pace with advances in imaging processing capabilities. Synthesizing up-to-date computer vision algorithms, a graphical application is developed for automatically detecting and tracking shock waves. Image processing techniques discussed in this dissertation include image segmentation algorithms to isolate and label different regions, filter methods for denoising and image enhancement, resampling algorithms to improve the resolution and edge detection accuracy, representation of flow features based on edge maps, feature recognition, extraction, and fitting. Compared with previous studies, the software in this work provides multiple algorithms for denoising, edge detection, and feature extraction, which makes it more versatile and applicable. A large shadowgraph data

set with a low signal to noise ratio (SNR) and small spatial resolution (312×260 pixels), is used to validate the software. The approach outlined in this work can be applied to analyse common flows in which expansion and shock waves, shear layers, and vortex motion are a dominant feature. Such flows can be found in shock wave reflections, shock-shock and shock-boundary layer interactions, and inlet unstart.

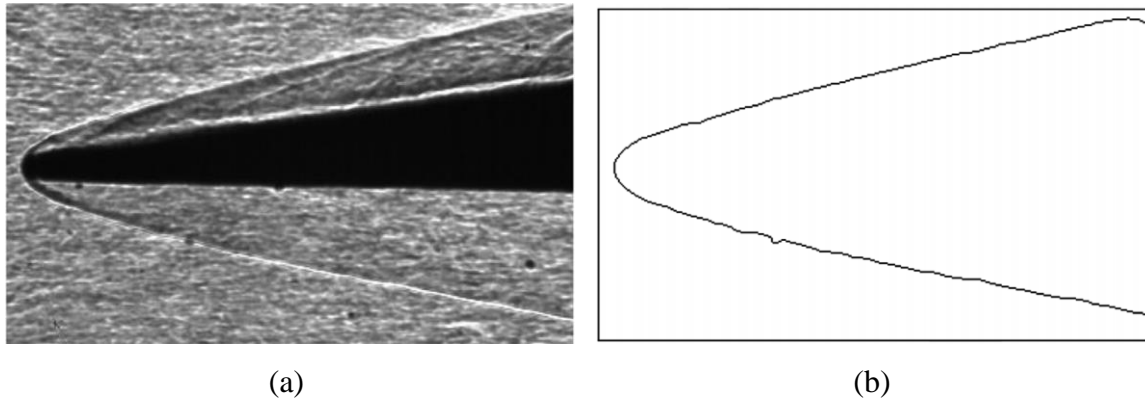


Figure 6.3 Shock detection for a three-dimensional waverider installed in AEDC Tunnel 9 with a nominal free stream Mach number of 8: (a) original schlieren image; (b) shock contour extracted after applying a bilateral filter [320, 334]

6.1 Image processing algorithms

6.1.1 Background subtraction

In schlieren or shadowgraph images, shock waves are usually distinguished as darker or lighter regions compared with the background light intensity. To display the image intensity gradient more clearly and eliminate the contaminated area, an image processing procedure involving background image (the test image without flow) subtraction and test model area restoration is applied.

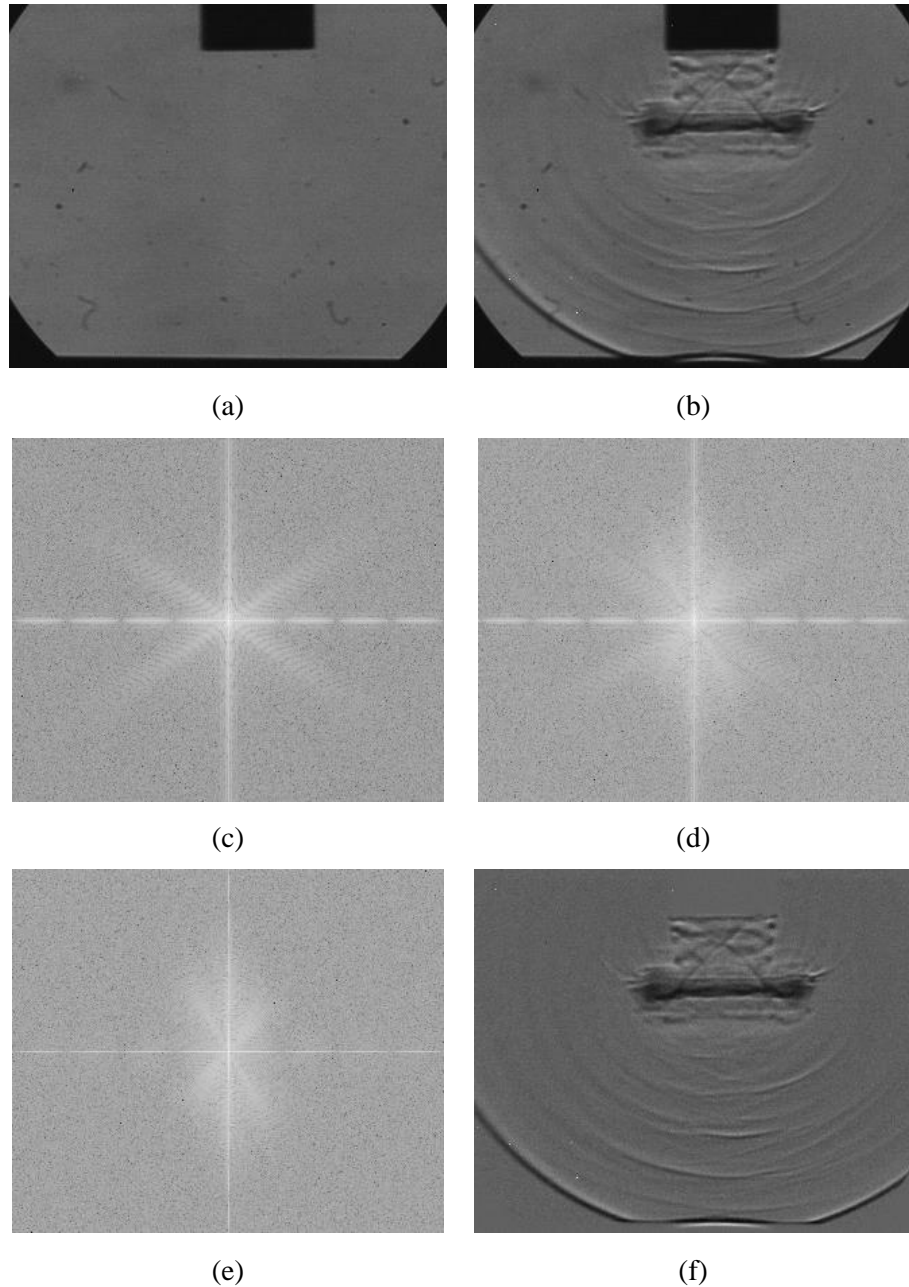


Figure 6.4 Background image subtraction in frequency domain for a shadowgraph image of the jet flow from a circular shock tube: (a) background image; (b) test image; (c) background image in frequency domain; (d) test image in frequency domain; (e) background subtracted image in frequency domain; (f) background subtracted image in spatial domain

Figure 6.4(a) presents an original shadowgraph image from the open end of the circular shock tube driven by transmission detonation tubing (see Chapter 4). Apparently, the original shadowgraph image has a lot of noise due to the contamination of the lens, mirrors, or camera sensors. This problem can be partially resolved by cleaning all the optical

components of the shadowgraph system. However, noises can be eliminated better through background image subtraction in the frequency domain.

Converting images from the spatial domain into the frequency domain is realised by the Fourier Transform, which is a common image processing tool used for decomposing an image into its sine and cosine components [335]. The outcome of the transformation stands for the image in the frequency domain, while the source image is the spatial domain equivalent. In the frequency domain image, each point represents a specific frequency contained in the spatial domain image. Mathematically, the image Fourier transform can be described by the following equation [335] is:

$$F(k, l) = \sum_{i=0}^{N-1} \sum_{j=0}^{N-1} f(i, j) e^{-i2\pi(\frac{ki}{N} + \frac{lj}{N})} \quad (6.4)$$

$$e^{ix} = \cos x + i \sin x \quad (6.5)$$

Here f and F refer to the image intensity in its spatial domain and frequency domain respectively. Complex numbers calculated from the Fourier transformation can be displayed via a magnitude and a phase image. However, only the magnitude image containing all the information of the image geometric structure is needed in this study. Figure 6.4 (c)-(e) show examples of magnitude images of a Discrete Fourier Transform (DFT). DFT has been used in a wide range of applications, such as image analysis, image filtering, image reconstruction, and image compression. In this research, it is applied to subtract the background image from the schlieren and shadowgraph test images to distinguish the flow structure itself more clearly.

The Fourier transformation converts an image in the spatial domain into the frequency domain without loss of information. By contrast, the inverse Fourier transform (IDFT) converts the image back from the frequency domain into the spatial domain [335]:

$$f(a, b) = \frac{1}{N^2} \sum_{k=0}^{N-1} \sum_{l=0}^{N-1} F(k, l) e^{2\pi(\frac{ka}{N} + \frac{lb}{N})} \quad (6.6)$$

Figure 6.4 (f) shows the background subtracted image in the spatial domain obtained through IDFT of the background subtracted image in the frequency domain (Figure 6.4 (e)). It can be seen from Figure 6.4 (f) that most of the image noises and contamination are eliminated effectively by background image subtraction in the frequency domain. In addition, the test model, the shock tube, and the region out of shadowgraph measurement are also eliminated, which makes the flow structure itself more prominent and much easier to detect the shock wave contour. In this research, all the shock wave detection is based on images after background image subtraction in the frequency domain.

However, on some occasions, the test model, the shock tube, and the region out of shadowgraph measurement need to be displayed to show the model location and the flow region.

Table 6.1 Thresholding types and operations

Seq. No	Thresholding Type	Operation
1	Binary Threshold	$dst(x, y) = \begin{cases} \text{maxVal} & \text{if } src(x, y) > \text{thresh} \\ 0 & \text{otherwise} \end{cases}$
2	Binary Threshold, Inverted	$dst(x, y) = \begin{cases} 0 & \text{if } src(x, y) > \text{thresh} \\ \text{maxVal} & \text{otherwise} \end{cases}$
3	Threshold to Zero	$dst(x, y) = \begin{cases} src(x, y) & \text{if } src(x, y) > \text{thresh} \\ 0 & \text{otherwise} \end{cases}$
4	Threshold to Zero, Inverted	$dst(x, y) = \begin{cases} 0 & \text{if } src(x, y) > \text{thresh} \\ src(x, y) & \text{otherwise} \end{cases}$
5	Truncate	$dst(x, y) = \begin{cases} \text{threshold} & \text{if } src(x, y) > \text{thresh} \\ src(x, y) & \text{otherwise} \end{cases}$

In this work, a global thresholding algorithm in which the same threshold value is applied for every pixel is adopted to separate the image foreground from its background, isolating the test model and the region out of shadowgraph measurement from shadowgraph or

schlieren images. Actually, global thresholding is a simple but effective tool for image segmentation. For a source image in which the intensity value of the pixel (x,y) is $src(x,y)$, the corresponding global thresholding operation for each thresholding type is illustrated in Table 6.1.

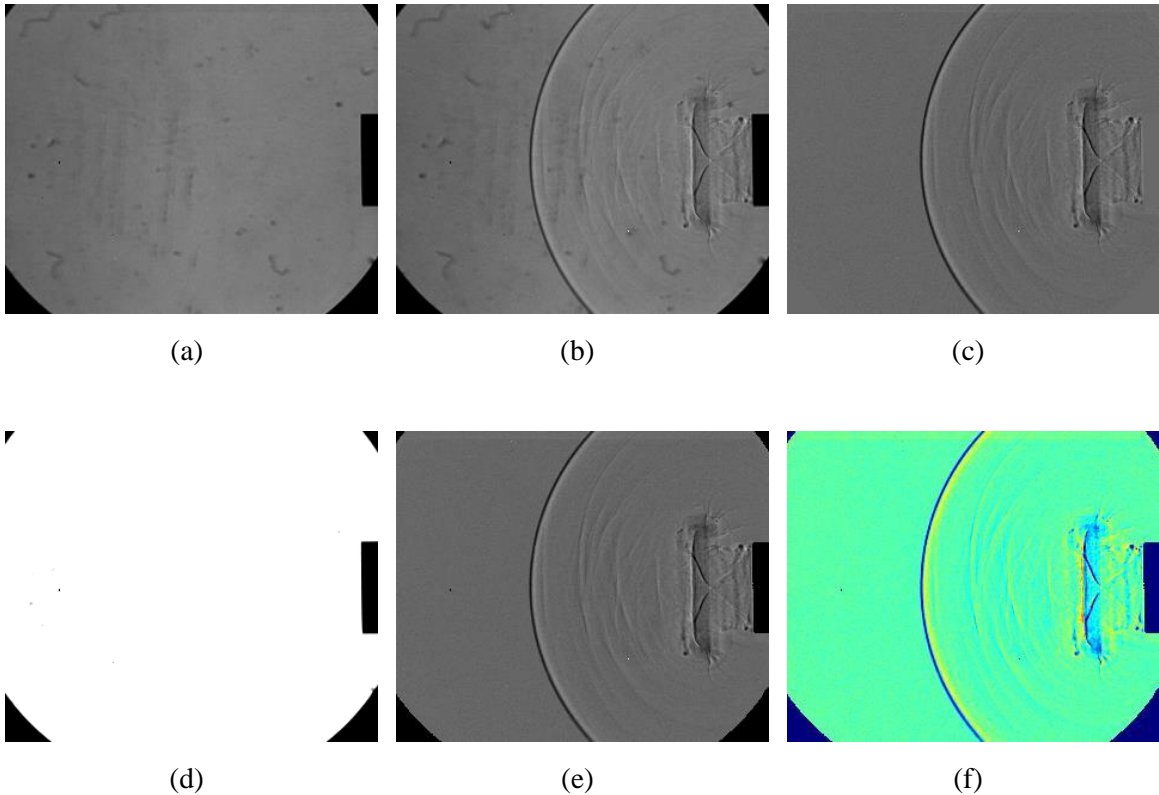


Figure 6.5 Restore the test model and the region out of measurement by global thresholding operation for a shadowgraph image from the open end of a circular shock tube: (a) background image; (b) test image; (c) background subtracted image; (d) extraction of the test model and the region out of measurement by global thresholding operation (thresholding type: Threshold Binary, threshold value: $thresh=93$); (e) background subtracted image after restoration of the test model and the region out of measurement; (f) pseudo colour image of frame (e)

In this work, the first thresholding type, “Threshold Binary”, is adopted for extracting the test model from the original shadowgraph images. Figure 6.5 demonstrates a validation case of one shadowgraph image from the open end of a circular shock tube described in chapter 4 in the case of NONEL tube length $L=500\text{mm}$. As shown in Figure 6.5 (d), the shock tube, and the region out of the shadowgraph measurement area are extracted from the background

image effectively. It is worth noting that all the shadowgraph or schlieren images are converted into 8bit grayscale images for improving the calculating efficiency, no matter what original format and depth they are. Therefore, the threshold value must be 0~255. Figure 6.5 (f) gives the pseudo colour image of Figure 6.5 (e), obtained by pseudo-colour processing that maps each of the level of a greyscale image into an assigned colour. The colour image can make the identification of image features easier for the observer. Although most of the images are displayed in a grayscale format for the consistency with the original shadowgraph and schlieren results in this work, it is computationally simple and fast to convert any of them to pseudo colour format.

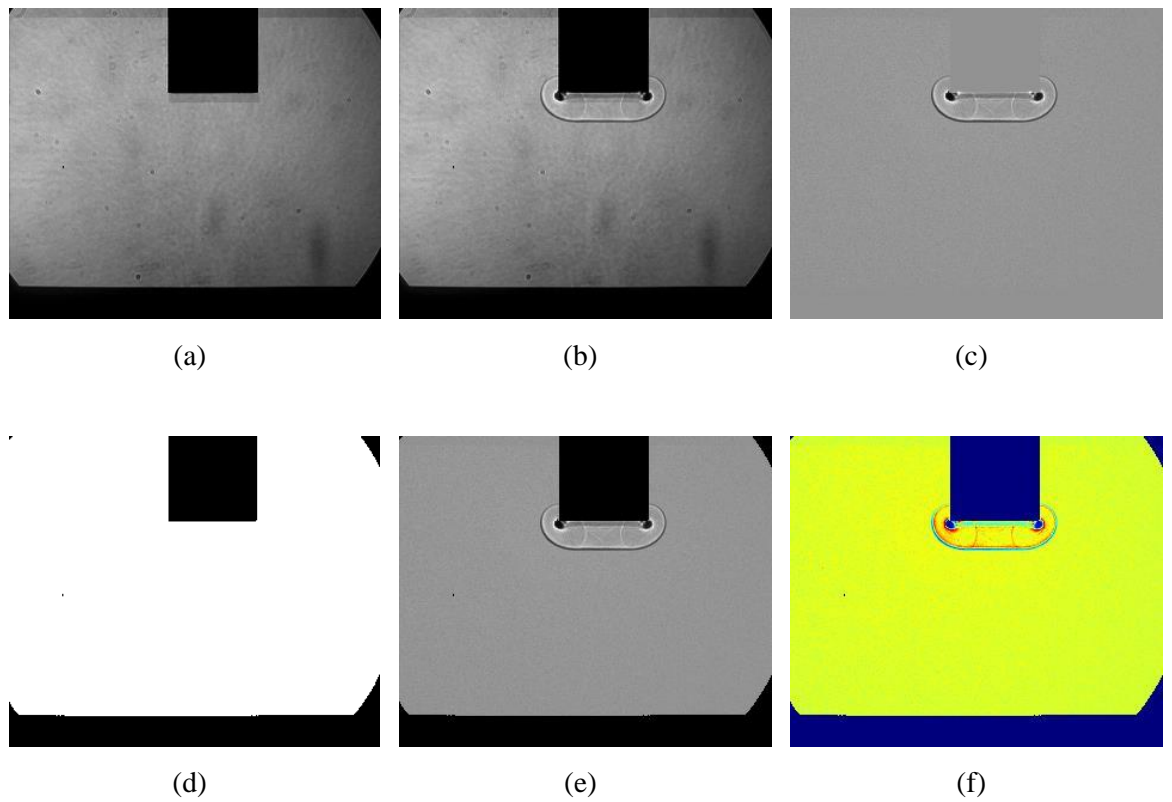


Figure 6.6 Restore the test model and the region out of measurement by global thresholding operation for a shadowgraph image from the open end of a square shock tube: (a) background image; (b) test image; (c) background subtracted image; (d) extraction of the test model and the region out of measurement by global thresholding operation (thresholding type: Threshold Binary, threshold value: $\text{thresh}=54$); (e) background subtracted image after restoration of the test model and the region out of measurement; (f) pseudo colour image of image (e)

Figure 6.6 depicts the other example of extracting and restoring the test model and region of out of measurement. This example is from the shadowgraph test of the square shock tube in the case of NONEL tube length $L=300\text{mm}$ (see chapter 4). It can be seen from Figure 6.6 that the proper threshold value for extracting the shock tube and region out of measurement is 54, different from that of in the case of Figure 6.5 because of the difference of the brightness and contrast.

In the above global thresholding, we used an arbitrary chosen value as a threshold. To process all the images more automatically, several algorithms are proposed for calculating an adaptive threshold value:

Automatic Otsu thresholding:

Otsu's method, named after Nobuyuki Otsu (Ōtsu Nobuyuki), is an image processing algorithm used to conduct automatic image thresholding [336]. In the simplest form of the Otsu's method, a single global threshold that separates pixels into two classes is returned, foreground and background. This intensity threshold is calculated by minimizing intra-class intensity variance, or equivalently, by maximizing inter-class variance. For every possible threshold intensity, the method estimates the goodness through either the heterogeneity of both classes or the homogeneity of every class. By maximizing the criterion function, the means of two classes can be separated as far as possible and the variances in both classes will be as minimal as possible.

Mathematically, the threshold value minimizing the intra-class variance, defined as a weighted sum of variances of the two classes will be searched:

$$\sigma_w^2(t) = w_0(t)\sigma_0^2(t) + w_1(t)\sigma_1^2(t) \quad (6.7)$$

Weights w_0 and w_1 are the probabilities of the two classes separated by the threshold intensity t . σ_0^2 and σ_1^2 are variances of these two classes. The class probabilities are calculated from the L bins of the histogram:

$$\begin{cases} w_0(t) = \sum_{i=0}^{t-1} p(i) \\ w_1(t) = \sum_{i=t}^{L-1} p(i) \end{cases} \quad (6.8)$$

For the case of two classes, minimizing the intra-class variance is equivalent to maximizing inter-class variance:

$$\begin{aligned} \sigma_b^2(t) &= \sigma^2 - \sigma_w^2(t) \\ &= w_0(\mu_0 - \mu_T)^2 + w_1(\mu_1 - \mu_T)^2 \\ &= w_0(t)w_1(t)[\mu_0(t) - \mu_1(t)]^2 \end{aligned} \quad (6.9)$$

which is expressed in terms of class probabilities w and class means μ , where the class means $\mu_0(t)$, $\mu_1(t)$ and μ_T are:

$$\begin{cases} \mu_0(t) = \frac{\sum_{i=0}^{t-1} ip(i)}{w_0(t)} \\ \mu_1(t) = \frac{\sum_{i=t}^{L-1} ip(i)}{w_1(t)} \\ \mu_T = \frac{\sum_{i=0}^{L-1} ip(i)}{w_0(t) + w_1(t)} \end{cases} \quad (6.10)$$

Based on equations 6.7-6.10, the following equation can be easily verified:

$$\begin{cases} w_0\mu_0 + w_1\mu_1 = \mu_T \\ w_0 + w_1 = 1 \end{cases} \quad (6.11)$$

The class probabilities w and class means μ can be calculated iteratively. Figure 6.7 demonstrates image segmentation results for cases in Figures 6.5 and 6.6 to separate the test model and the region out of measurement from the shadowgraph images through Otsu automatic thresholding algorithm. It can be seen from Figure 6.7 that the test model and the region out of measurement are extracted automatically and effectively by the Ostu

method. However, this algorithm automatically computes the threshold value of a bimodal image from its histogram. If images are not bimodal, this method probably is not accurate enough.

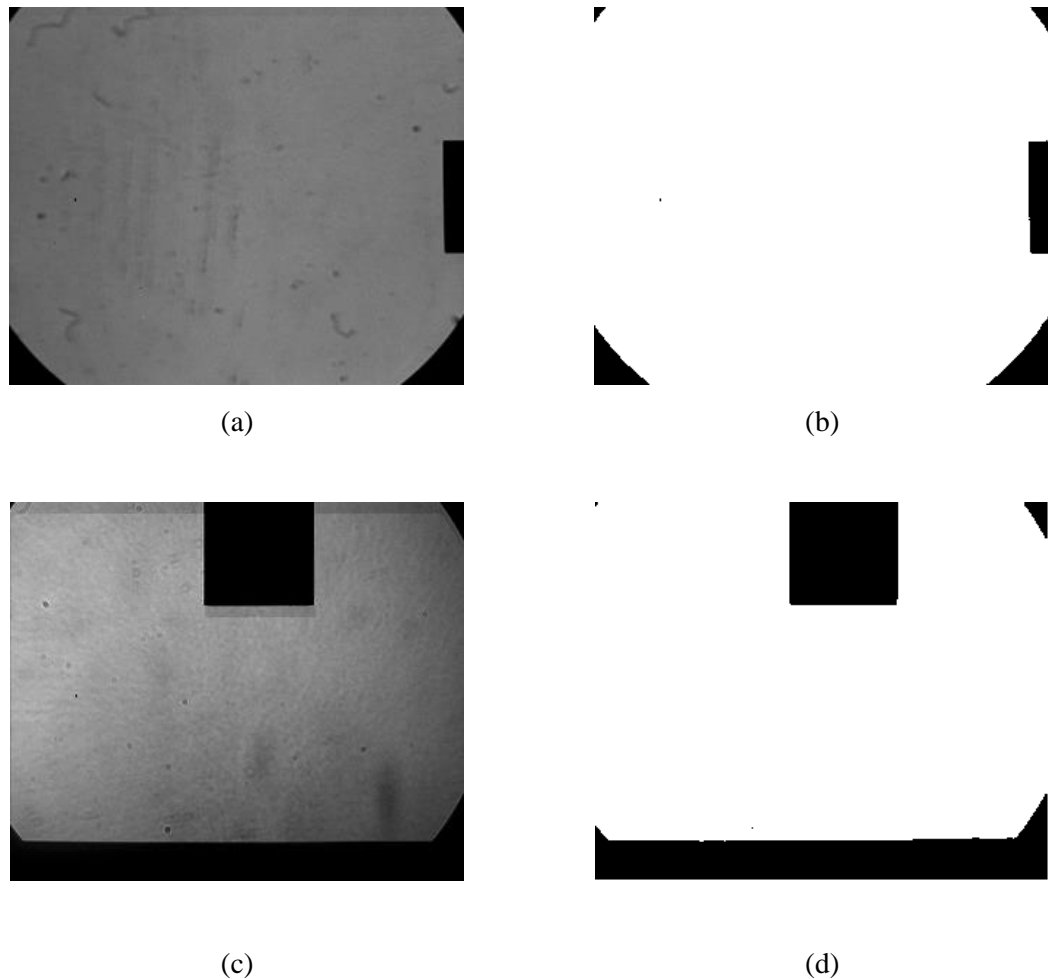


Figure 6.7 Image segmentation for separating the test model and the region out of measurement from the shadowgraph images through Otsu automatic thresholding algorithm

Automatic Triangle thresholding:

As shown in Figure 6.8, the Triangle algorithm [337] is a geometric method for automatically calculating the threshold value, assuming a maximum peak (mode) near one end of the image histogram and searches towards the other end. A line is constructed between the maximum of the image histogram at B on the grey level axis and the lowest (or highest

depending on context) value A where the intensity histogram is significantly larger than 0. The distance normal to the constructed line and between this line and the intensity histogram is calculated for all values on the grey level axis from A to B . The value where the distance is maximal is just the threshold. This algorithm is particularly effective when the foreground generates a weak peak in the histogram.

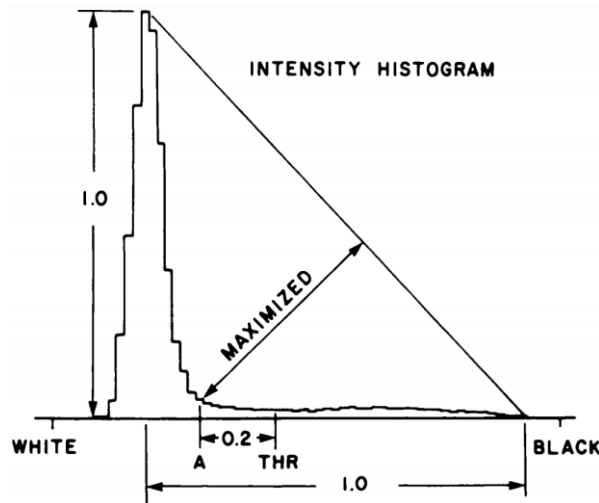


Figure 6.8 Schematic of triangle thresholding algorithm [337]

Figure 6.9 shows image segmentation results for cases in Figure Figures 6.5 and 6.6 to separate the test model and the region out of measurement from shadowgraph images through Triangle automatic thresholding algorithm. As shown in Figure 6.9, the Triangle thresholding algorithm can effectively isolate the test model and region out of measurement from shadowgraph images in different grayscale levels.

It is worth noting that there are several other popular and effective automatic thresholding algorithms such as histogram thresholding [338] and maximum entropy [339]. However, Otsu and Triangle methods have been proven effective for most of the cases in shock wave detection and tracking. Therefore, only these two automatic thresholding algorithms are adopted in this research.

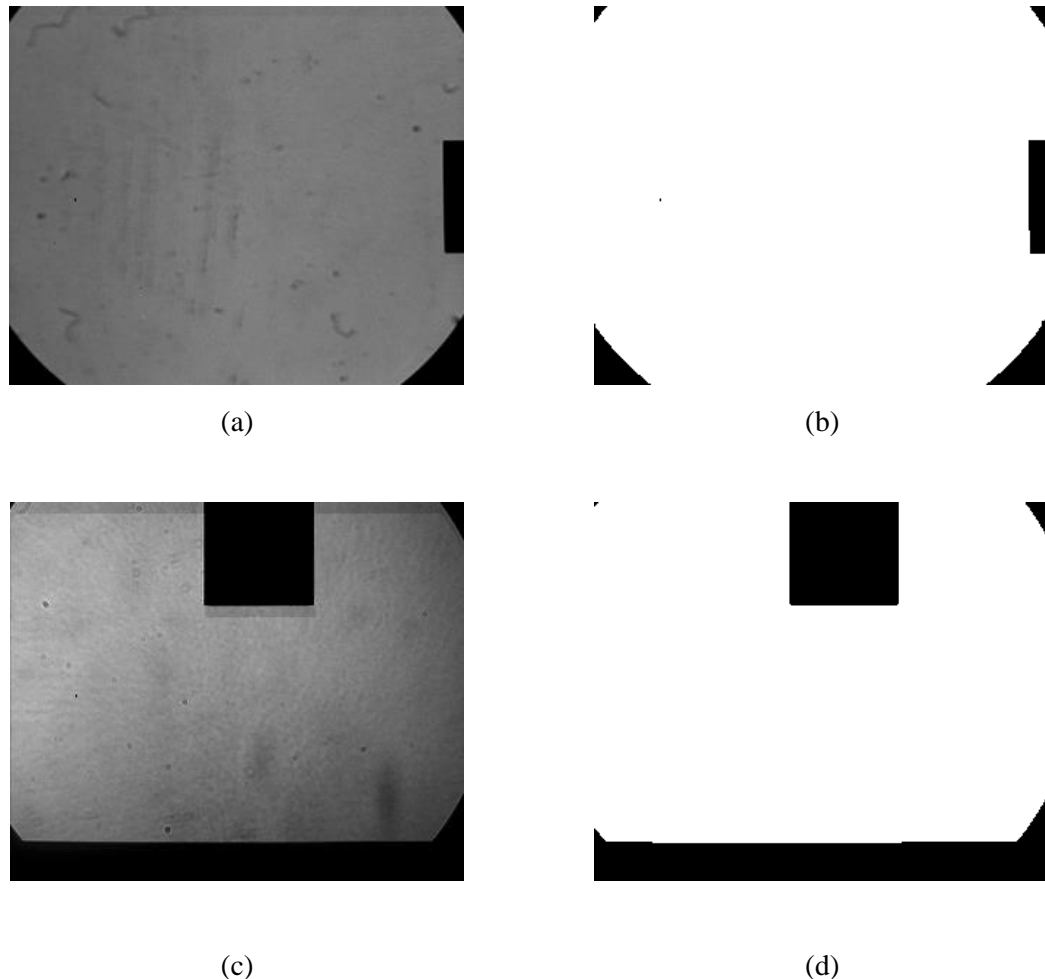


Figure 6.9 Image segmentation for separating the test model and the region out of measurement from shadowgraph images through Triangle automatic thresholding algorithm

6.1.2 Image filter

Occasionally, boundaries between the flow field and the body are not strong enough in high speed shadowgraph and schlieren images. Image preprocessing including image segmentation and image filter can be performed on noisy raw images. Image segmentation by automatic global thresholding has been introduced in the last section. A filtering method that blurs images within boundaries but not across them is desired.

Convolution:

The trick of image filtering is the operation of convolution. Consider that you have a two-

dimensional filter matrix, and a two-dimensional image. Then, for every pixel of the target image, take the sum of the greyscale values of the current pixel and its neighbour pixels, with the corresponding element of the filter matrix. The central value of the filter matrix must be multiplied with the current pixel, the other elements of the filter matrix with corresponding neighbour pixels. This operation is called convolution that has a kernel which could be any matrix smaller than the original image in height and width. The general expression of a convolution is:

$$g(x, y) = K * f(x, y) = \sum_{s=-a}^a \sum_{t=-b}^b K(s, t) f(x-s, y-t) \quad (6.12)$$

where $g(x, y)$ is the filtered image, $f(x, y)$ is the source image and K is the filter kernel. Every element of the filter kernel is considered by $-a \leq s \leq a$ and $-b \leq t \leq b$.

It is worth noting that the kernel size must be uneven to have a centre, for example, 3×3 , 5×5 and 7×7 . Furthermore, the 2D convolution operation requires a 4-double loop, so the executive speed is not extremely fast unless you use small kernels. In this work, 3×3 or 5×5 filters are usually adopted.

Mean filter:

The mean filter is one of the common filter methods for removing image noise. It involves determining the mean of the pixel values within a $n \times n$ kernel. The kernel matrix of the mean filter is denoted as follows (kernel size $d=3 \times 3$):

$$K_{mean} = \frac{1}{9} \begin{bmatrix} 1 & 1 & 1 \\ 1 & 1 & 1 \\ 1 & 1 & 1 \end{bmatrix} \quad (6.13)$$

Figure 6.10 demonstrates the mean filter results in different kernel sizes. It is apparent that the shadowgraph image after the mean filter is smoother with less noise, however, it also decreases the sharpness of the image when the kernel size is larger than 5×5 .

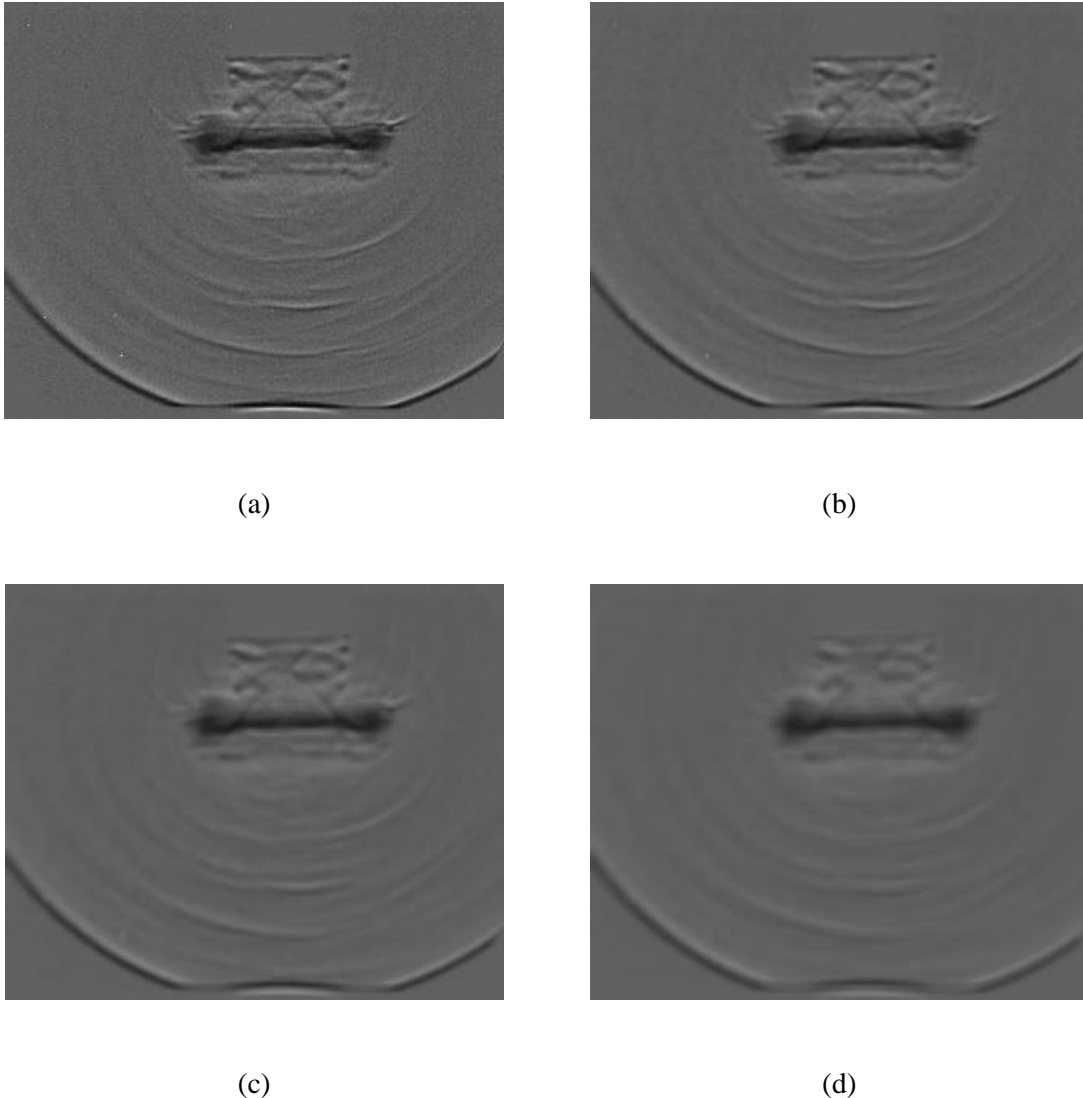


Figure 6.10 Mean filter: (a) original shadowgraph image after background subtraction; (b) image after 3×3 mean filter; (c) image after 5×5 mean filter; (d) image after 7×7 mean filter

Gaussian Filter:

The Gaussian filter is similar to the mean filter. It involves a weighted average of the neighbour pixels in the vicinity of the target pixel. The kernel of Gaussian filter refers to a discrete approximation of a Gaussian distribution. In this method, the standard deviation in the X and Y directions, sigmaX and sigmaY also need to be specified respectively. Figure 6.11 illustrates Gaussian filter results in different kernel sizes. The sigmaX is set to be equal to the sigmaY and determined by the kernel size $ksize$ as $\text{sigma} = 0.3((ksize - 1) / 2) + 0.8$. As shown in Figure 6.11, Gaussian filtering can remove image Gaussian noise effectively and

remains more sharpness than that of the mean filter when kernel size is larger than 5×5 .

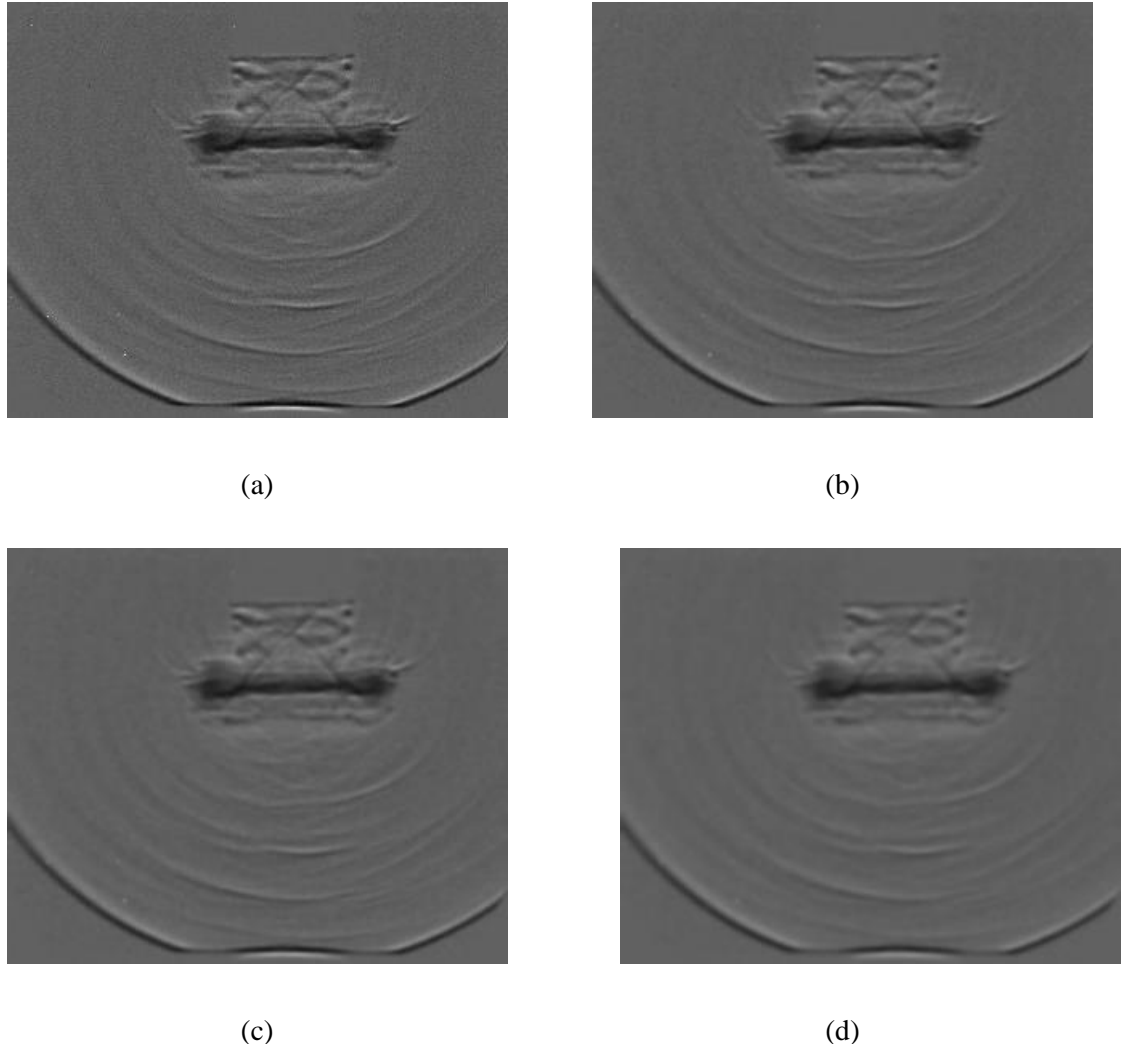
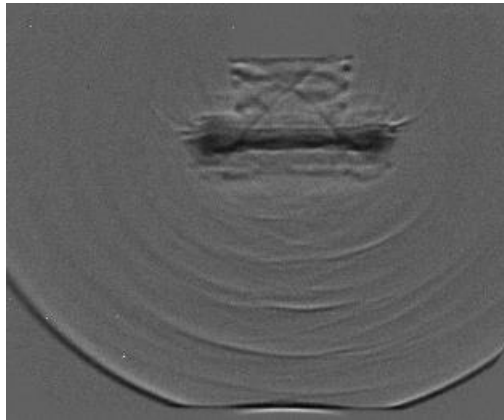


Figure 6.11 Gaussian filter: (a) original shadowgraph image after background subtraction; (b) image after 3×3 Gaussian filter; (c) image after 5×5 Gaussian filter; (d) image after 7×7 Gaussian filter

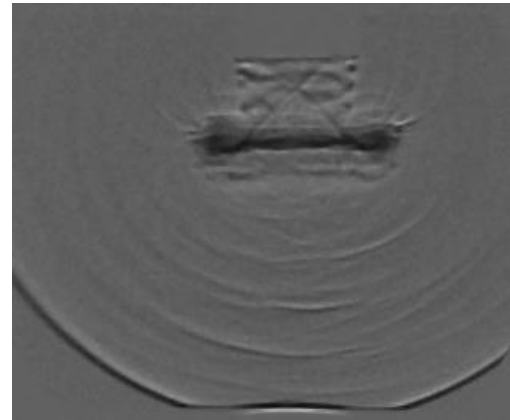
Median filter

In Median filtering, the value of the central pixel is replaced by the median value in the kernel window. This method is particularly effective in removing random peak values in the region, which can be due to noise like salt and pepper noise. Figure 6.12 (b) depicts a shadowgraph image from the open end of a circular shock tube (see Chapter 4) after a median filter (kernel size $d=3 \times 3$). By comparing Figure 6.12 (a) and Figure 6.12 (b), we can see that the white slat noise is effectively eliminated by the median filter. However, it can be seen

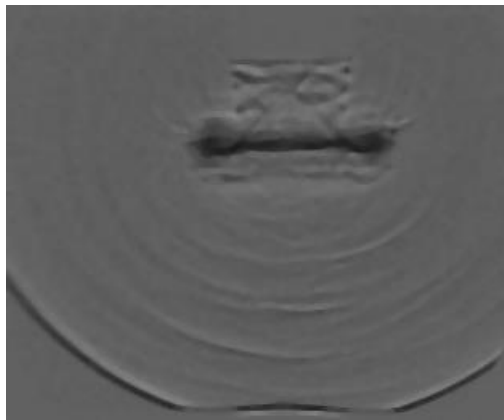
from Figure 6.12 (c) and Figure 6.12 (d) that it makes the shadowgraph image much more blur when the kernel size is too large. In this work, the kernel size of the median filter is not larger than 3×3 to get a trade-off between salt noise elimination and preserving the edges.



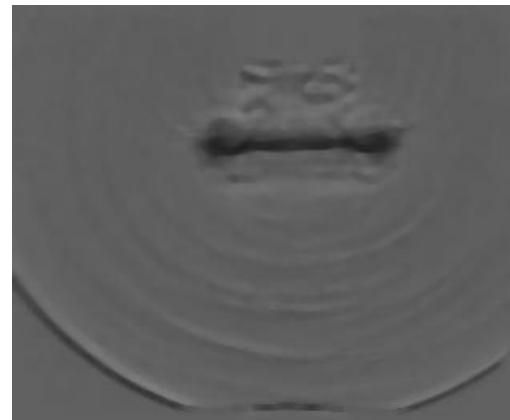
(a)



(b)



(c)



(d)

Figure 6.12 Median filter: (a) original shadowgraph image after background subtraction; (b) image after 3×3 Median filter; (c) image after 5×5 Median filter; (d) image after 7×7 Median filter

Bilateral filter:

The aforementioned filter methods tend to blur boundaries. In contrast, bilateral filter is a filter method that was defined for noise removal while keeping edges [340]. The Gaussian filter does not judge whether pixels lie on an edge or not. A Gaussian filter is used in the bilateral filter in the spatial domain. But it also takes advantage of one more Gaussian filter

component identified by pixel intensity differences, which ensures only pixels with intensities similar to that of the central pixel in the kernel window are used to calculate the filtered intensity value.

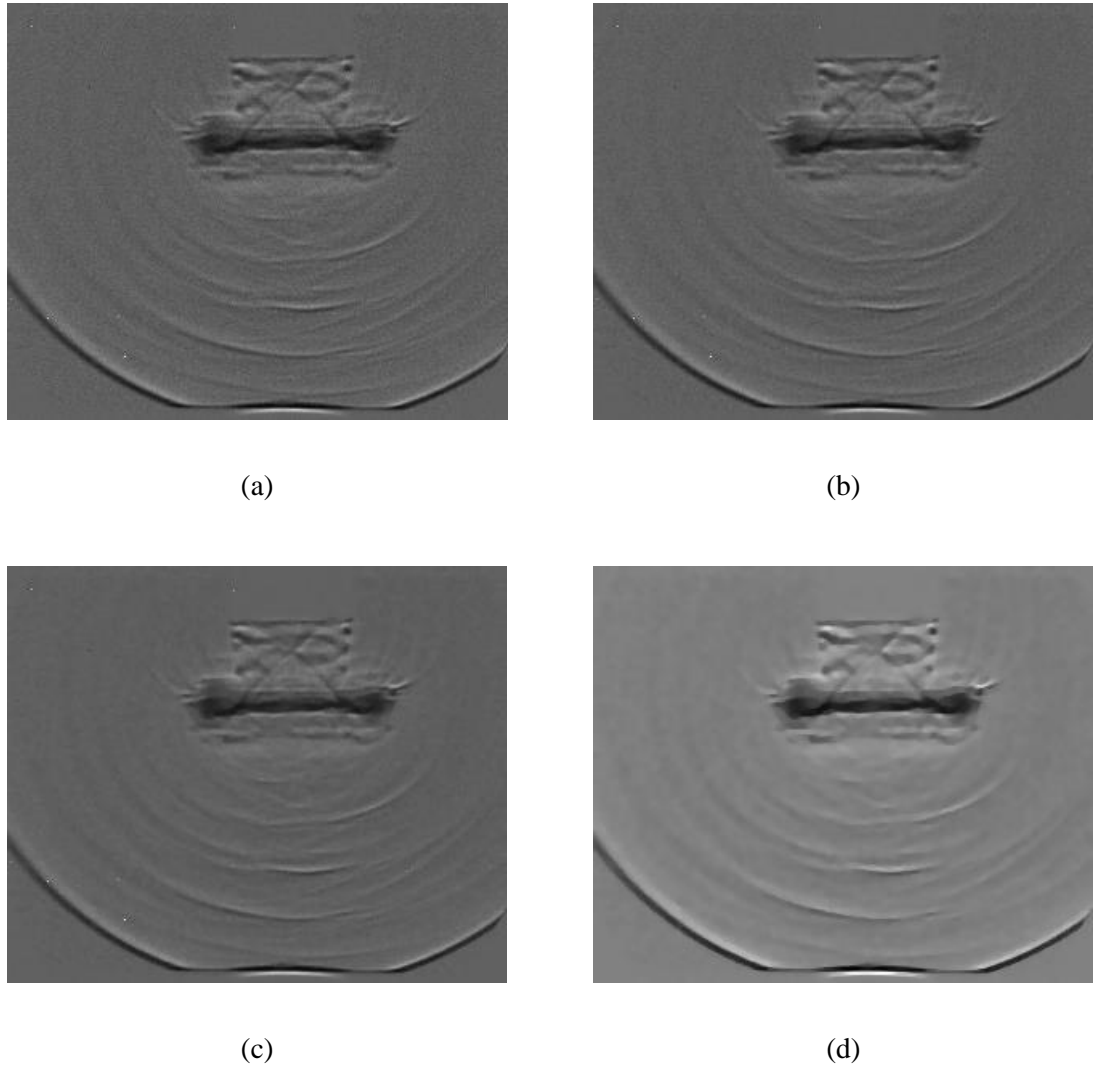


Figure 6.13 Bilateral filter: (a) original shadowgraph image after background subtraction; (b) image after 3×3 bilateral filter; (c) image after 5×5 bilateral filter; (d) image after 3×3 median filter and 3×3 bilateral filter

The bilateral filter is controlled by domain and range scale parameters: σ_s and σ_r . As the range parameter σ_r increases, the bilateral filter becomes closer to the Gaussian filter. If the spatial parameter σ_s increases, larger features are smoothed. As shown in Figure 6.13, image edges are preserved well using the bilateral filter method even if the kernel size is larger than

5×5 for a 312×360 -pixel shadowgraph image. The main drawback of the bilateral filter operation is that it is much slower compared to other filters. Therefore, kernel size $d=5$ or 3 can be used for real-time applications, and $d=9$ or a larger kernel size for offline applications if images are heavily noisy. In this research, combining 3×3 median filter and 5×5 bilateral filter is adopted for the pre-processing of high speed shadowgraph images.

Sobel filter

Sobel filter is generally used in computer vision to create image emphasising edges. In this dissertation, it is an effective tool to compute image gradients and make shock detection easier when the contrast of the shadowgraph or schlieren image is not strong enough. Sobel and Feldman presented this algorithm at a talk at SAIL in 1968 [335]. Technically, it is a discrete differentiation operator, calculating an approximation of the gradient of the image intensity function. The 3×3 kernel of the Sobel filter in the x -direction is given as follows:

$$K_{SobelX} = \frac{1}{8} \begin{bmatrix} -1 & 0 & 1 \\ -2 & 0 & 2 \\ -1 & 0 & 1 \end{bmatrix} \quad (6.14)$$

The 3×3 kernel in the y -direction is:

$$K_{SobelY} = \frac{1}{8} \begin{bmatrix} 1 & 2 & 1 \\ 0 & 0 & 0 \\ -1 & -2 & -1 \end{bmatrix} \quad (6.15)$$

Figure 6.14 (b) and Figure 6.14 (c) illustrate the Sobel filter results of a shadowgraph image after background subtraction in x and y direction respectively. It is apparent that the shock wave and jet flow features become clearer after Sobel operation. However, high-frequency variations in the background area are cruder after the Sobel gradient approximation. Figure 6.14 (d) depicts the shadowgraph image after the median filter and Sobel operation in y direction. We can see that a better result is obtained by combining different filter methods.

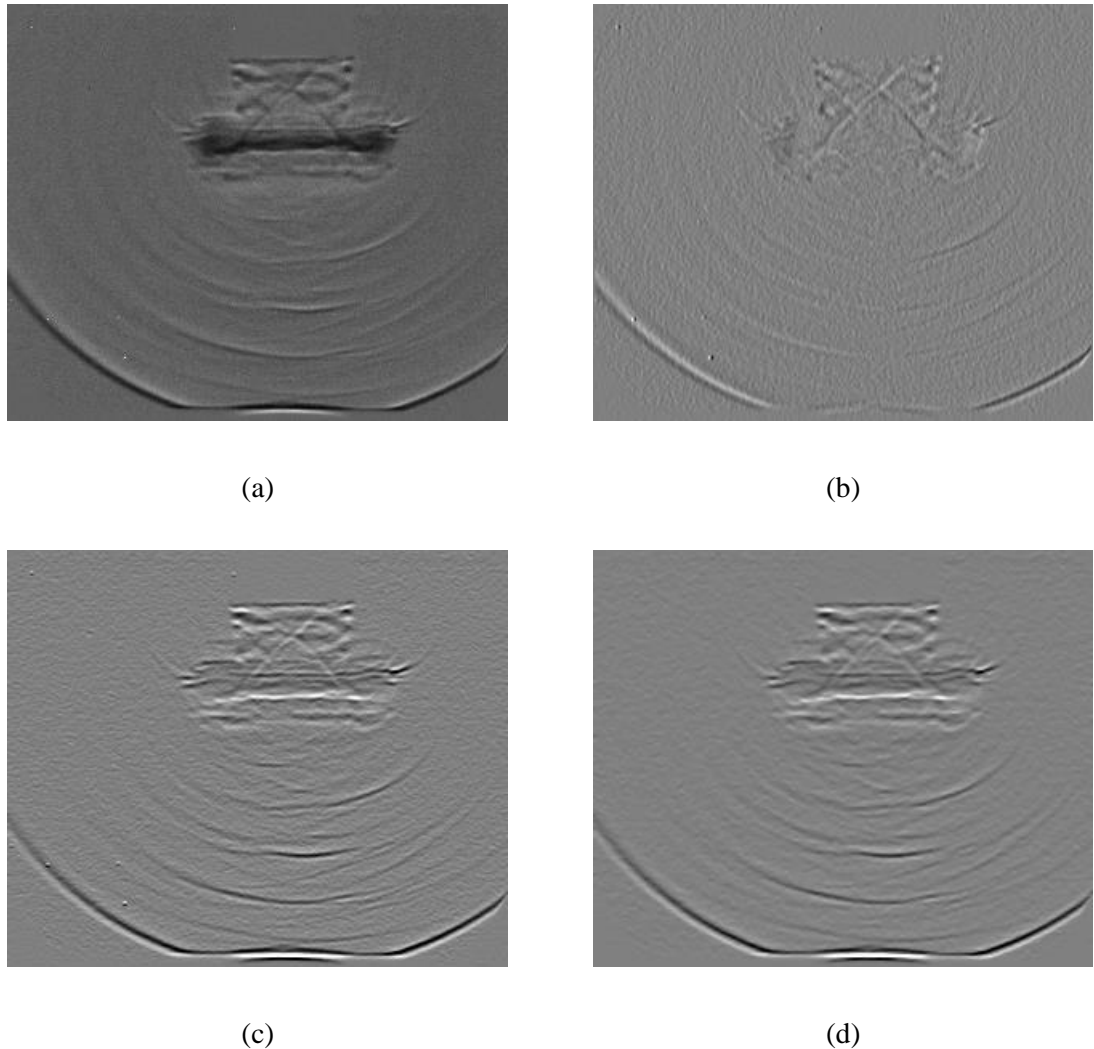


Figure 6.14 Sobel filter: (a) original shadowgraph image after background subtraction; (b) image after Sobel filter in x direction; (c) image after Sobel filter in y direction; (d) image after 3×3 median filter and Sobel filter in y direction

Laplacian filter:

A Laplacian filter is an edge detector to find areas of rapid change in an image by computing the second derivatives of the image. Laplacian filter kernels usually include negative values in a cross pattern, centred within the array. The following array is an example of a 3×3 kernel for a Laplacian filter:

$$K_{SobelY} = \frac{1}{8} \begin{bmatrix} 1 & 2 & 1 \\ 0 & 0 & 0 \\ -1 & -2 & -1 \end{bmatrix} \quad (6.16)$$

Since derivative filters are very sensitive to noise, it is common to smooth the image by a Gaussian before applying the Laplacian. This two-step process is called the Laplacian of Gaussian operation (see Figure 6.15(c)).

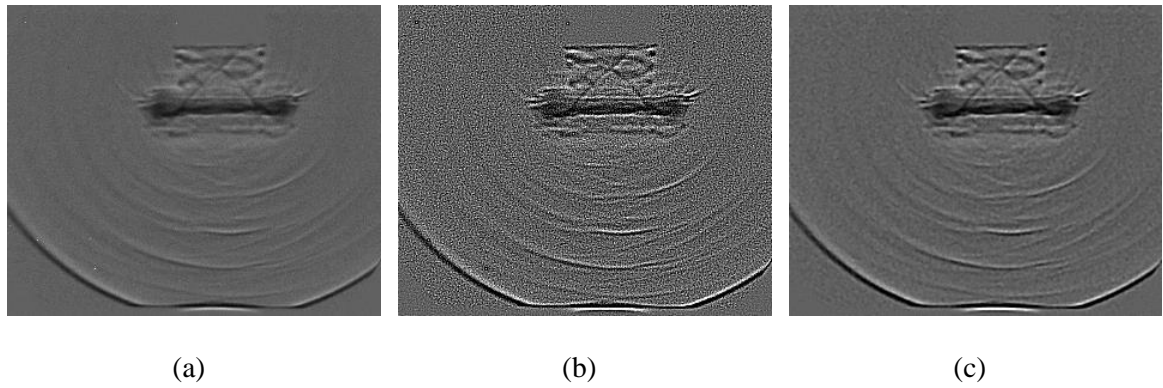


Figure 6.15 Laplacian filter: (a) original shadowgraph image after background subtraction; (b) image after Laplacian filter; (c) image after 3×3 Gaussian filter and Laplacian filter

6.1.3 Image resampling

In high speed shadowgraph and schlieren, the image spatial resolution is relatively low to get a higher frame rate. For example, the Shimazu HPV-1 high-speed camera used in the shadowgraph experiment in Chapter 4 and Chapter 7 only has a 312×260 -pixel resolution. As shown in Figure 6.16 (b), the shadowgraph image becomes apparently blur after a median filter and Gaussian filter with a minimum kernel size, which will affect the accuracy of following shock location detection. Therefore, some image resampling approaches are proposed to overcome the problem of low resolution in high speed shadowgraph and schlieren imaging.

Image resampling is the technique used to create a new version of an image with a different size [341-344]. Increasing the size of the image is called upsampling and reducing the size of an image is called downsampling. These are several common types of resampling

interpolation algorithms [341-344] used with digital images: nearest-neighbour interpolation, bilinear, bicubic, Lanczos, directional cubic convolution interpolation, Mipmap, among which Lanczos algorithm has been considered the "best compromise" involving a trade-off between efficiency, smoothness, sharpness, and speed.

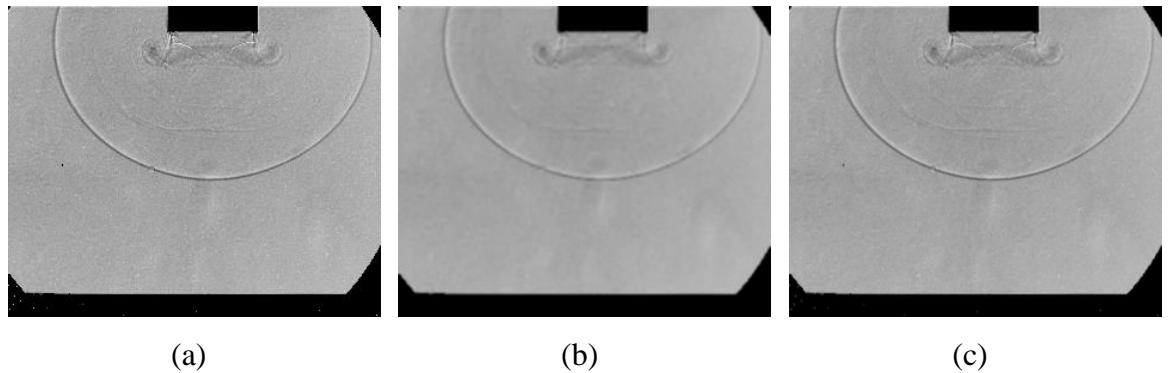


Figure 6.16 Image resampling: (a) original shadowgraph image with a 312×260-pixel resolution; (b) image after 3×3 median filter and 3×3 Gaussian filter; (c) shadowgraph image after upsampling (624×520-pixel resolution) followed by 3×3 median filter and 3×3 Gaussian filter

In this research, Lanczos algorithm is adopted to get the best shock detection results, although it is relatively time-consuming. Lanczos resampling uses a convolution kernel to interpolate the pixels of the input image to calculate the pixel values of the output image. The Lanczos convolution kernel $k(x)$ is defined as:

$$k(x) = \begin{cases} \sin(x) \sin(x/a) & \text{if } -a < x < a \\ 0 & \text{otherwise} \end{cases} \quad (6.17)$$

The parameter a is a positive integer, typically 2 or 3, which determines the size of the kernel. Each interpolated value is the weighted sum of $2a$ consecutive input samples. As shown in Figure 6.16 (c), the result upsampling the original shadowgraph image from 312×260-pixel to 624×520-pixel before filtering keeps more sharpness, which improves the accuracy of subsequent edge and contour detection.

6.1.4 Edge detection

Edge detection [345] is an image processing technique for finding the boundaries of objects

within images. In this work, edge detection is used to label and separate different regions, representation of flow features. Generally, boundaries related to flow structure are extracted by edge detection based on image gradients. Canny edge detection algorithm [330, 345, 346] is the most popular one in the computer vision community due to its low error rate and single response criterion. It was also widely used in shock wave detection in previous studies [320, 326, 329, 330, 334]. In this research, a modified Canny algorithm is proposed, which is composed of 5 steps:

(1) Noise reduction

Because the mathematics involved are mainly based on derivatives, edge detection results are highly sensitive to image noise. One way to get rid of this problem is to apply an image filter before conducting edge detection. To do so, the image convolution technique (see Section 6.1.2) is applied to reduce small-scale noise. In the conventional Canny edge algorithm, the Gaussian kernel is adopted [330, 345, 346]. However, since both edges and noises are high frequency components in the image, a simple Gaussian filter not only smoothes the noises but also the edge. To improve the accuracy of detecting the real edge, a much more smooth effect should be performed to noises. In the software developed in this work, noise reduction and following edge detection procedures are separated, which means all the filter methods described in Section 6.1.2 can be chosen. In practice, 3×3 or 5×5 bilateral filter combining with a 3×3 median filter is selected for shock wave detection and tracking in this research.

(2) Gradient calculation

The Gradient calculation step detects the edge intensity and direction by calculating the gradient of the image. Edges correspond to a rapid change of pixels' intensity. To detect edges, the easiest way is to apply filters that highlight this intensity change in both directions: horizontal G_x and vertical G_y . When the image is smoothed, the derivatives G_x and G_y are calculated by convolving with Sobel kernels (see Section 6.1.2) respectively. Then, the edge gradient and direction for each pixel can be computed by the following equation:

$$\text{Edge - Gradient } (G) = \sqrt{G_x^2 + G_y^2} \quad (6.18)$$

$$\text{Angle } (\theta) = \tan^{-1}\left(\frac{G_y}{G_x}\right) \quad (6.19)$$

(3) Non-maximum suppression

After yielding the edge gradient, pixels that do not belong to the edge are removed. For the current edge images, the thickness of all edges is not the same. To solve this problem, non-maximum suppression can be conducted to thin out the edge, which checks all the points on the gradient intensity matrix and returns the pixels with the maximum intensity value in the edge directions. In short, a binary image with “thin edges” is obtained after the non-maximum suppression of the gradient magnitude image.

(4) Double threshold

This stage determines whether edges are wanted or not. Two threshold values, a high threshold T_H , and a low threshold T_L are generally used. If the gradient of the edge pixel is higher than the high threshold value T_H , it is labelled as a strong edge pixel. Edge pixels whose gradient is smaller than T_H and larger than the low threshold value T_L , are marked as weak edge pixels. Pixels with a gradient value smaller than T_L will be suppressed.

T. Fujimoto et al. [326] proposed a theoretical method for calculating the double threshold values in Canny edge detection automatically based on Rankine-Hugoniot relations. In this research, automatic thresholding algorithms described in Section 6.1.1 are used to determine the high threshold T_H . Specifically, the threshold automatically calculated by Otsu algorithm is set to T_H and the low threshold value T_L is 1/2 of the high threshold value T_H . This method was used in the validation cases in Chapter 7 and demonstrated effective for most of the application occasions. Additionally, different automatic thresholding algorithms described in Section 6.1.1 can be switched in the software for shock wave detection and tracking developed in this research.

(5) Edge Tracking by Hysteresis

The weak edge pixels can either be detected from true edges, or noises. Canny edge detector uses Hysteresis thresholding to determine whether these weak edge pixels are true edges or not. As shown in Figure 6.17, pixels having gradient magnitude between high threshold value T_h and low threshold value T_L are checked. If they are connected to a strong edge, they will be kept. So, these two threshold values T_h and T_L have a significant effect on the final edge detection result.

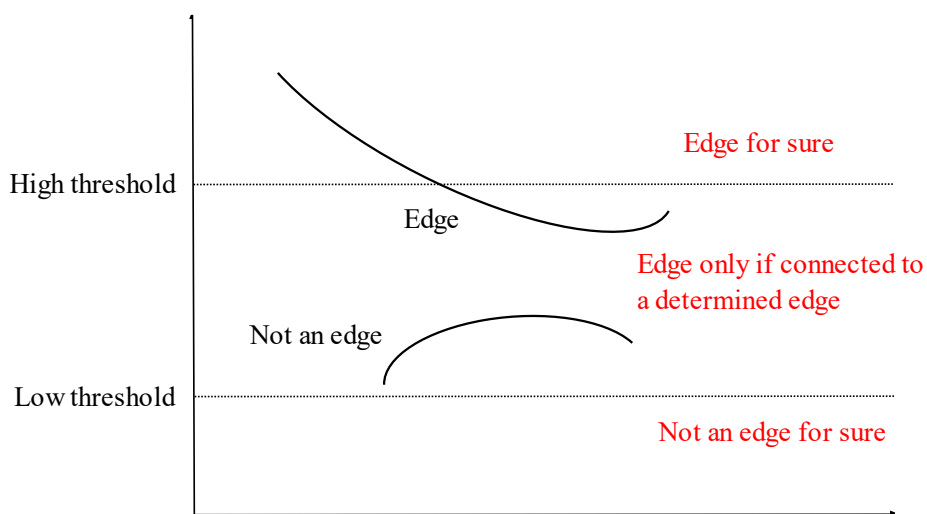


Figure 6.17 Schematic of hysteresis thresholding

Figure 6.18 demonstrates the edge detection result of a shadowgraph image by the aforementioned Canny algorithm, in which the resolution of the image is resampled from 312×260 -pixel to 624×520 -pixel, 3×3 median filter and 5×5 bilateral filter are used in sequence and Otsu algorithm is adopted to calculate the double threshold values. As shown in Figure 6.18, the initial shock wave and subsequent weak pressure waves are detected successfully. In the jet flow region out of the open end of the circular shock tube, there are a number of small edges because of the shock wave and vortex ring interaction. To isolate the embedded shock wave, feature extraction (see Section 6.1.6) can be performed further.

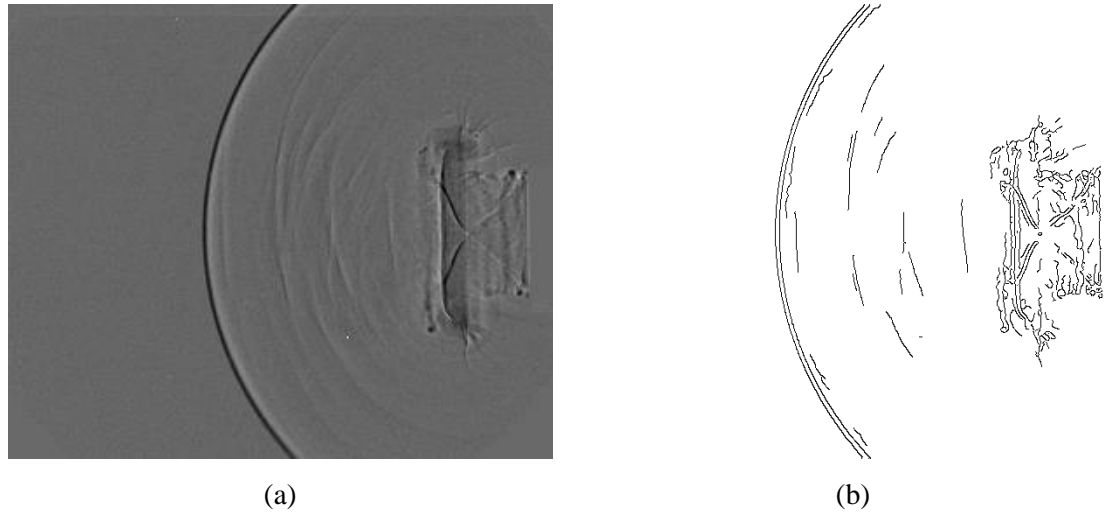


Figure 6.18 Edge detection through modified Canny algorithm: (a) original shadowgraph image; (b) edge detection result

6.1.5 Adaptive threshold

In Section 6.1.4, edge detection is performed based on the gradient magnitude and direction of grayscale shadowgraph or schlieren images. In this dissertation, we proposed the other algorithm detecting shock waves from binary shadowgraph and schlieren images based on an adaptive threshold. In Section 6.1.1, a fixed threshold value is set automatically or manually, to get a binary image from the original shadowgraph or schlieren images. For example, anything that is greater than 127 in the grayscale, can be set to 255 in the binary image and anything that is less than or equal to 127 in the grayscale image can be set to 0 in the binary image. This process is called fixed thresholding.

Unlike the fixed threshold, the threshold value in the adaptive threshold algorithm depends on the neighbouring pixel intensities, varying for each pixel. To calculate the threshold value $T(x, y)$ at a pixel location (x, y) , the following steps are performed :

- (1) A $d \times d$ region around the target pixel (x, y) is selected.
- (2) The next step is to calculate the weighted average $WA(x, y)$ of the $d \times d$ region. In this dissertation, two methods are adopted to calculate this weighted average. The first method is to calculate the mean of intensity values of all the pixels that lie in the $d \times d$ region. The

other way is the Gaussian weighted average, in which the pixel values that are near to the centre of the $d \times d$ box have a higher weight.

- (3) The next step is to compute the threshold value $T(x, y)$ by subtracting a constant parameter c from the weighted average value $WA(x, y)$:

$$T(x, y) = WA(x, y) - c \quad (6.20)$$

- (4) Compare the pixel value with this threshold. The intensity of the pixel that is larger than $T(x, y)$ is set to 255 in the binary image and set to 0 if it is less than or equal to the threshold value $T(x, y)$.

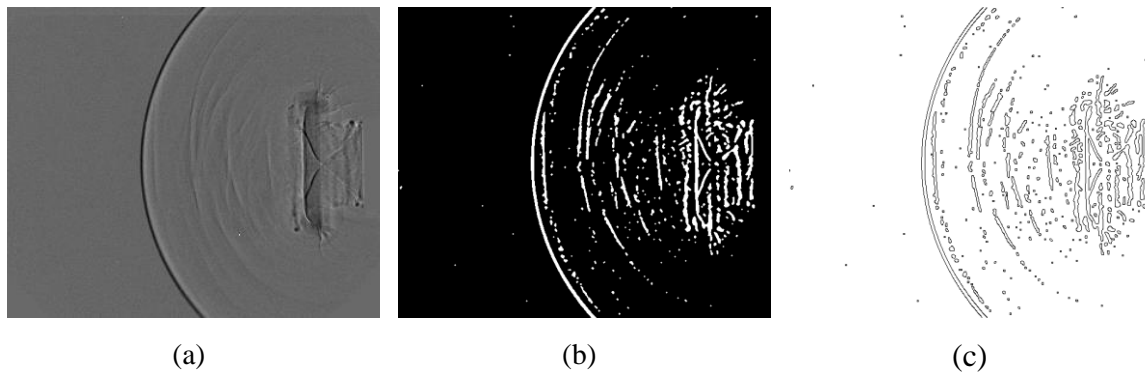


Figure 6.19 Edge detection through adaptive threshold algorithm: (a) original shadowgraph image; (b) adaptive threshold image; (c) edge detection result

Figure 6.19 depicts the edge detection result through the adaptive threshold algorithm, in which the pre-processing methods and corresponding parameters are the same as those in Figure 6.18. Compared these two figures, more details can be detected by the adaptive threshold algorithm. However, more noise exists in the final edge detection image.

The adaptive threshold overcomes the limitation of conventional threshold methods when the image background or the feature intensities are not homogeneous. Of course, with other advanced filtering methods, a cleaner feature extraction result can be obtained. But for most of the applications, this adaptive threshold algorithm is sufficient and generic to different features.

6.1.6 Contour detection and feature extraction

In the above sections, we have already got edge maps of the shadowgraph or schlieren images. However, the core part is how to define the properties of edges and extract the flow features by their property values. In this dissertation, the properties of edges are calculated based on contour detection.

Contour is a curve joining all the continuous points along the boundary that have the same intensity value. The contours are widely used for object detection and shape analysis [347-349]. To detect contours and extract features related to physical structures of interest, such as a shock wave, we perform the following steps:

(1) binary image calculation

In this work, contours are built from binary images for better accuracy, which is accomplished by the modified Canny algorithm (see Section 6.1.4) or adaptive threshold (see Section 6.1.5), although alternative methods such as level sets or snakes [335] may also be used for contour extraction. Figure 6.18 (b) demonstrates an example of calculating the binary image by the modified Canny algorithm. Figures 6.19 (b-c) are examples of binary images obtained through the adaptive threshold algorithm.

(2) contour detection

Contours are detected as a curve joining all the continuous points along the boundary, having the same intensity. Each detected contour is stored as a vector of pixel coordinates.

There are several popular contour retrieval algorithms in computer vision [350-352]: (1) external algorithm that retrieves only the extreme outer contours; (2) tree algorithm retrieving all contours and reconstructing a hierarchy of all nested contours; (3) list algorithm in which all of the contours are retrieved without any hierarchies; (4) connected component algorithm retrieving and organizing all of the contours into a two-level hierarchy. In this work, the second algorithm is used. Figure 6.20 presents contour detection results through the second contour retrieval algorithm with different procedures, in which different contours

are displayed in different colours. As shown in Figures 6.20 (*b-d*), the contour image is the same as the binary image obtained through the modified Canny algorithm or adaptive threshold algorithm. Both these two algorithms can detect the initial shock wave and other main flow features such as the secondary shock waves, the embedded shock wave, and the oblique shock structure successfully.

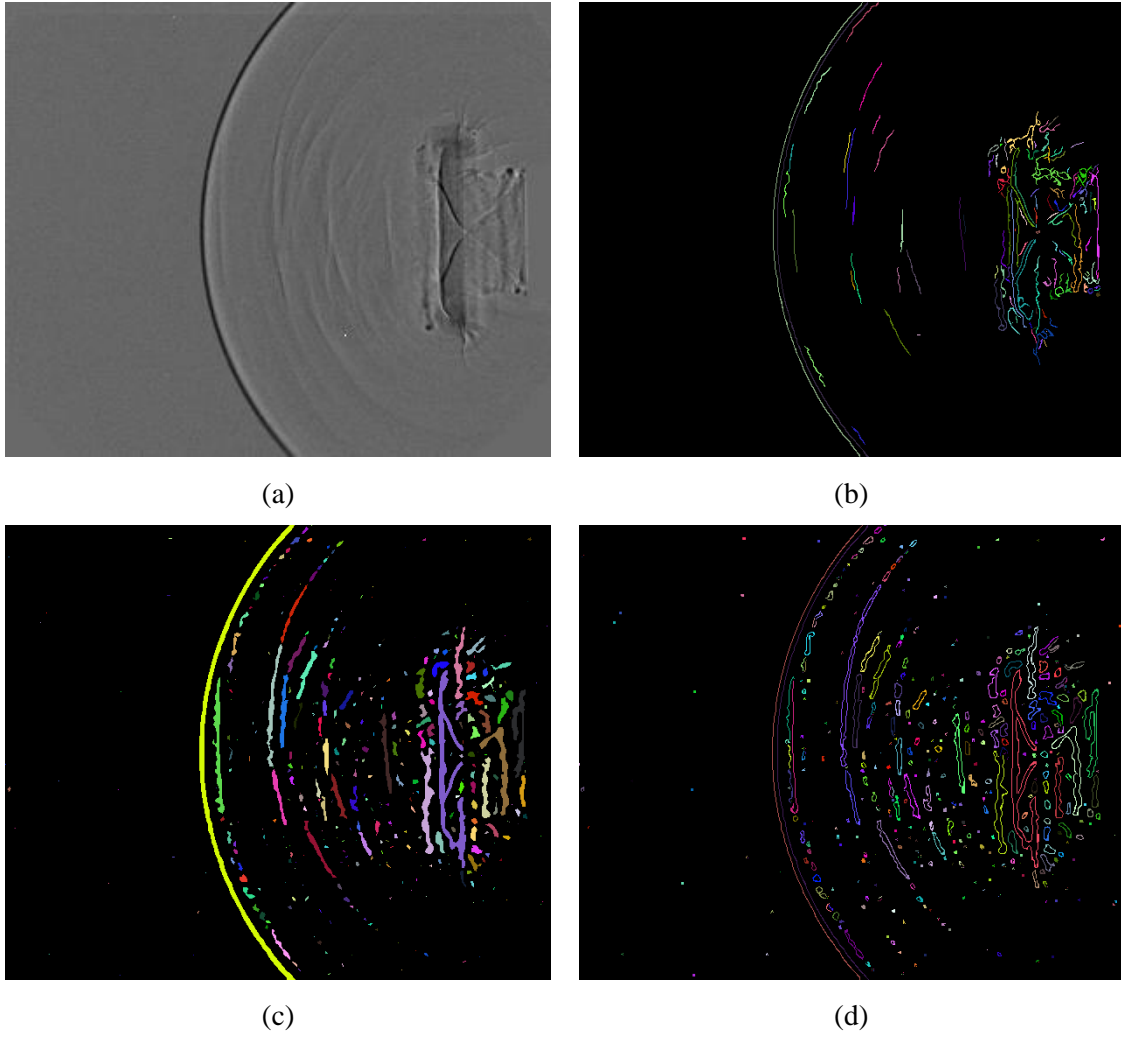


Figure 6.20 Contour detection through different algorithms: (a) original shadowgraph image; (b) contour detection by modified Canny edge detection; (c) contour detection by adaptive threshold; (d) contour detection by performing adaptive threshold and modified Canny edge detection in sequence

(3) contour properties calculation

This step calculates properties of each contour, including the hierarchy[347, 353], size, area,

perimeter [354], centroid [355-358] and bounding box [359, 360]. In addition, to improve processing efficiency, coordinates of contour points do not need to be fully stored, which is usually realized by contour approximation methods [361-363]. In this work, a simple contour approximation algorithm that leaves only end points of compressed horizontal, vertical, and diagonal segments is adopted to remove redundant contour points. Thereafter, all the aforementioned properties are calculated based on corresponding functions of MATLAB Image Processing Toolbox, combining with part of the in-house developed program.

(4) contour and feature extraction

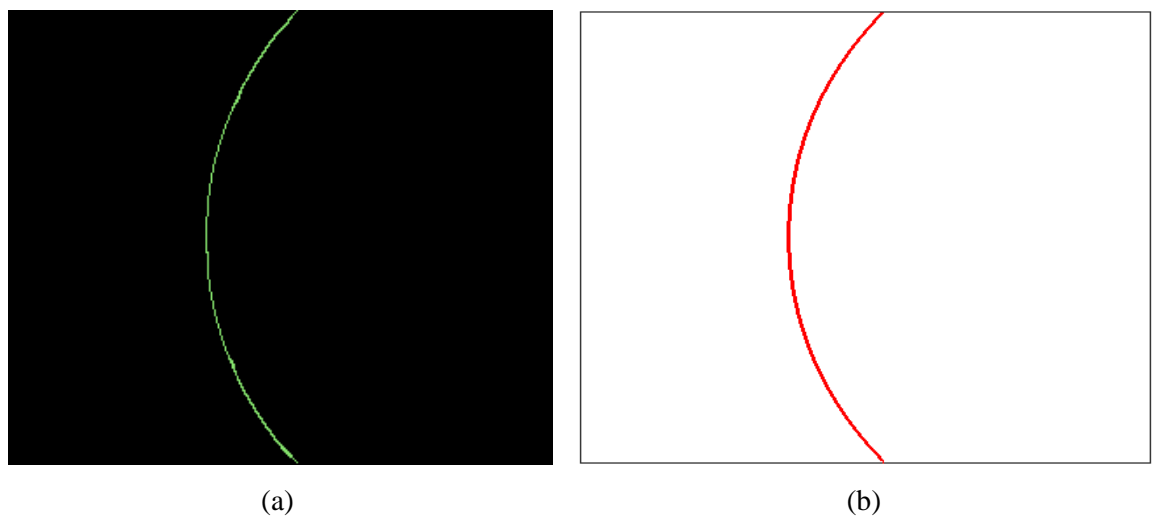


Figure 6.21 shock wave extraction and fitting: (a) shock wave extraction from the contour image; (b) shock wave fitting

The main task of this stage is to extract the contour or edge corresponding to a physical structure of interest, such as a shock wave. N. T. Smith et al. [320] used corner detection algorithms developed by He and Yung [364, 365] to label and isolate contours from edge images. Then, the contour images were scanned with three horizontal lines. If a contour is intersected with all the three rays, this contour would be kept and assumed as the outer shock. However, for this image processing scheme, short contours related true feature were removed. In this work, the contour extraction is accomplished by removing contours based on their property values. For the validating case in Figure 6.20 (b), the contour size is selected as the property for contour extraction. In this image, 133 contours are detected in total. The outer shock wave is the largest contour with a size of 552 points, followed by the

inner shock wave with 530 points. The sizes of all the other contours are smaller than 150. As shown in Figure 6.21 (a), the single contour that represents the outer shock is extracted from the contour images (see Figure 6.20) based on the property of the contour size. This method is simple but effective. At the level of pixel inspection, although the image coordinates of each pixel on the outer shock wave are extracted, the discrete curvature is a little noisy at a small scale rather than a smooth one because some points that do not belong to the shock wave are detected during the edge detection (see Figure 6.21 (a)). To solve this problem, the extracted shock wave needs to be fitted.

(5) contour fitting and post-analysis

In this dissertation, the extracted outer shock wave shown in Figure 6.21 (a) is fitted using a fourth-order polynomial. The fitting curve is given in Figure 6.21 (b). As shown in Figure 6.21 (b), the fitted shock is much smoother and points caused by the noise are removed efficiently. Contour evolution and curvature calculation can be performed as in the work of Mokhtarian, Mackworth, and Suomela [366-368]. Actually, with a reasonable representation of the isolated shock wave, the shock speed, the shock distortion, the shock thickness, and the shock angle will be capable to be estimated. Additionally, corner detection algorithms such as Curvature Scale Space (CSS) [320, 368-370], Harris [371-373] also can be performed to detect salient features as properties of the contour.

6.2 Software development for shock wave detection and tracking

Although all the algorithms in Section 6.1 have been validated and executed by text-based MATLAB codes, software with graphical user interfaces is still developed, allowing higher productivity for setting, displaying, and operation. In this research, Image Processing Toolbox and App Designer of MATLAB are adopted to develop the software [374] for shock wave detection and tracking based on the aforementioned image processing algorithms. In this section, the main interface and functions of the software are given.

6.2.1 Image processing procedure

To sum up, the shock wave detection and tracking are mainly performed by the following steps:

(1) image pre-processing

The aim of pre-processing is to improve the image data and enhance flow features for further processing. Pre-processing techniques for shock wave detection and tracking include: the background image subtraction in the frequency domain, noise elimination, image enhancement, and resampling (see Section 6.1.1-6.1.3).

(2) binary image calculation

Binary images can be performed by the modified Canny algorithm (see Section 6.1.4) or adaptive threshold (see Section 6.1.5).

(3) contour detection

Each detected contour is stored as a vector of pixel coordinates. A tree algorithm that retrieves all the contours and reconstructs a full hierarchy of nested contours is recommended among several contour retrieval algorithms.

(4) contour properties calculation

This step calculates the properties of each contour, like hierarchy, size, area, perimeter, centroid, bounding box, etc. A simple contour approximation algorithm that leaves only end points of compressed horizontal, vertical, and diagonal segments is adopted to remove redundant contour points.

(5) contour and feature extraction

The contour related to the shock wave is extracted and those not corresponding to true flow structure are removed based on their properties.

(6) contour fitting and post-analysis

The shock wave contours are fitted to give a reasonable representation of the shock configuration. Thereafter, shock speed, shock distortion, shock thickness or the shock angle will be capable to be estimated. Additionally, corner detection also can be performed to detect salient features as properties of shock waves.

The image pre-processing and contour detection are two key steps that determine the final shock detection accuracy. If image pre-processing algorithms such as filter method and kernel size for noise elimination cannot be selected properly, the shock wave boundaries will become much more blur. Similarly, only part of the shock wave or some false contours will be detected if the appropriate contour detection algorithm and corresponding parameters are not chosen. It is also worth mentioning that, although a lot of adaptive algorithms are adopted in this scheme, a specific group of settings including filter method, filter kernel size, resampling algorithm and scale, edge detection algorithm and corresponding parameters, and the type of contour property for shock extraction cannot ensure the success of detecting shock wave for every image when there is an apparent difference in image quality or shock strength between a large set of shadowgraph or schlieren frames. In such cases, images in which shock waves are not detected successfully need to be dealt with independently.

6.2.2 Software graphical interface

Figure 6.22 presents the main interface of the software, in which algorithms and parameters for filtering, resampling, automatic global thresholding, adaptive thresholding, and contour detection can be configured conveniently. More typical graphical interfaces of this software can be found in Appendix D and our previous work [374]. Once all the algorithms and parameters are set, a large set of shadowgraph or schlieren sequences can be processed automatically.

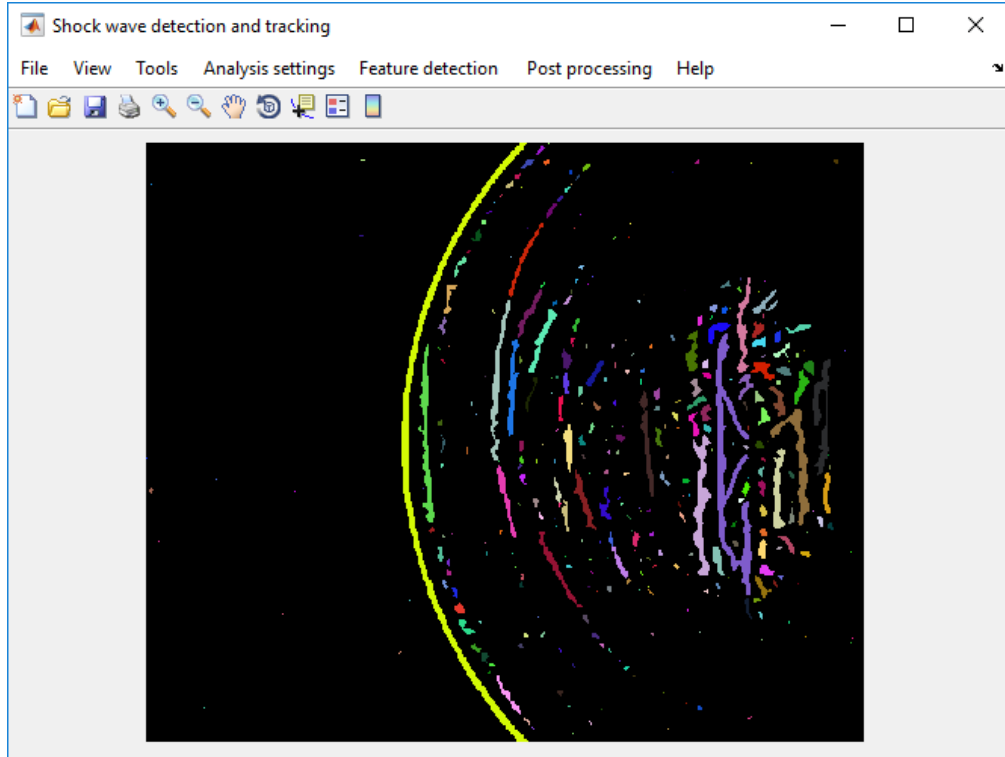


Figure 6.22 Software main interface

6.3 Conclusions

To detect, localize and track fluid features from measured or computed shadowgraph and schlieren data sets at higher frame rates automatically and effectively, an image processing scheme involving background subtraction in the frequency domain, filtering, resampling, edge detection, adaptive threshold, contour detection, extraction, and fitting is proposed and demonstrated. The conventional Canny edge detection algorithm is modified to calculate the double threshold values automatically. Additionally, the adaptive threshold algorithm is adopted as one of binary image calculation algorithms for contour detection, apart from the modified Canny edge algorithm. Also, a contour approximation algorithm is performed to remove contour redundant points to improve calculating efficiency. Although all the above algorithms have been validated and executed by text-based MATLAB codes, software with graphical user interfaces is still developed, allowing higher productivity for setting, displaying, and operation. A shadowgraph data set visualizing the jet flow from the open end of a circular shock tube is used as a test bed to validate the software. The result shows that image processing algorithms proposed in this research are reliable and effective. The

image processing scheme outlined in this work can be applied to analyse common flows in which expansion and shock waves, shear layers, and vortex motion are a dominant feature. Such flows can be found in shock wave reflections, shock-shock and shock-boundary layer interactions, and inlet unstart.

Chapter 7

Impingement of a supersonic staring jet on flexible surfaces

When a shock wave propagates along a tube and reaches the open end, an impulsive transmitting shock wave is emitted outward from the tube exit toward the surrounding area and causes an impulsive noise like a sonic boom. The understanding of transmitting shock wave discharged from the open end of a tube interaction with different geometries and flow patterns is of great importance in a wide variety of applications such as the design of supersonic jets [253, 375-378], pulse detonation engines [69, 379-382] and, more dramatically for the success in the space race with the study of re-entry flight conditions [87, 383, 384].

For the launch of space rockets, military missiles or the space travel such as the future missions involving lunar and Mars exploration with the aim at returning the capsules to Earth, there is a serious concern associated with the effectiveness of the propulsion system, either continuous or pulse-driven, due to the impact of the shock wave generated by the propellant explosion on a surrounding surface and the capsule. Thus, the prediction, evaluation, and attenuation of shock wave loading have been the subject of research in the last decades. Heimbs, Ritzer et al. [87] developed an empirical method to calculate the shock wave

loading induced during the missile launch from a military aircraft. Wang et al. [384] evaluated the damage mechanism of the jet to the structure of the rocket body and the effect of shock peak overpressure, positive pressure time, and specific impulse on the payload. Moshman, Hobson et al. [385] presented a formulation and computational solution of an optimal control problem concerning unsteady shock wave attenuation. The control solutions with physical constraints were presented for attenuating shocks travelling at Mach 1.5 and 3.5 down to 85%, 80%, and 75% of the uncontrolled wave's driving pressure.

However, so far, few results have been obtained for the interaction of unsteady transmitting shock wave from compressible starting jet with flexible surfaces. In this chapter, behaviours of the unsteady shock wave interactions over flexible surfaces are explored based on the aforementioned shock tube driven by detonation transmission tubing (Chapter 4) and the in-house developed software specialized for shock wave detection and tracking (Chapter 6).

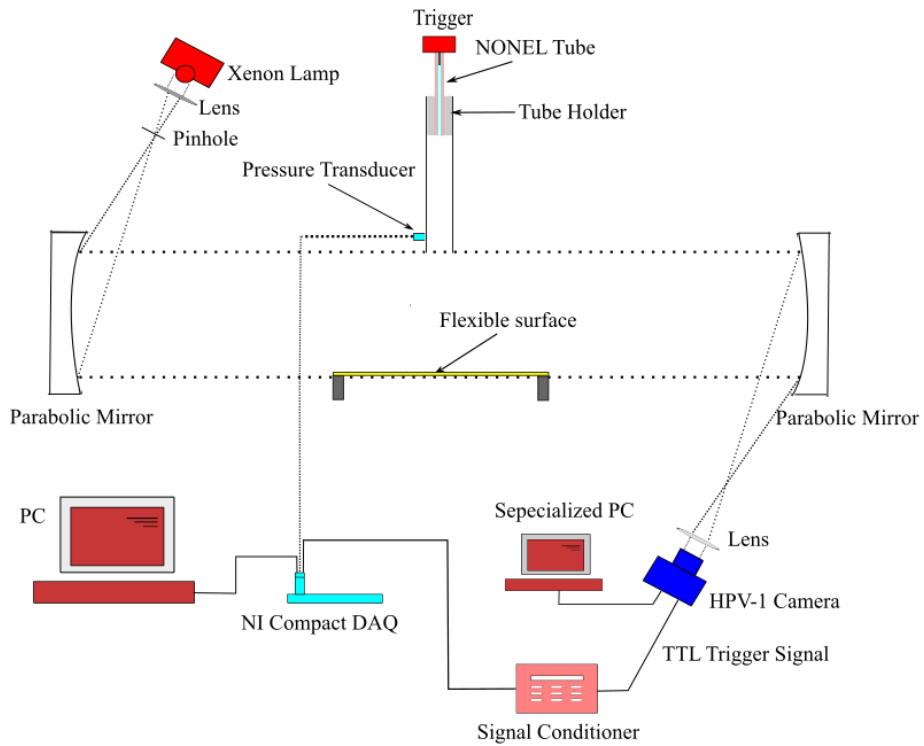


Figure 7.1 Schematic of the flexible surface design and experimental setup

The schematic diagram of the flexible surface and the experimental setup is shown in Figure 7.1. In the present study, circular aluminium alloy sheets (diameter $\phi = 210\text{mm}$, thickness $\delta = 0.1\text{-}0.3\text{mm}$) were glued on a hollow cylinder (outer diameter $\phi_1 = 210\text{mm}$, inner diameter $\phi_2 = 190\text{mm}$), acting as the flexible surfaces. Using the glue as the fixed method, the flexible

surfaces can be fixed stably on all sides. It is worth noting that the fixed end condition of flexible surfaces has a significant influence on the process of supersonic starting jet and flexible surface interaction. In this preliminary research, the clamping condition that the flexible surface is clamped on all sides was adopted. Different fixed conditions such as flexible panel clamped on two sides will be compared based on experimental techniques developed in this work in the future. The novel type of square shock tube driven by detonation transmission tubing (see Chapter 4) was employed. Meanwhile, the process of shock wave impingement and reflection over flexible surfaces was visualized using a time-resolved shadowgraph system with a typical Z-type optical arrangement. As a benchmark case, a 10mm-thick solid plate replaced the flexible surfaces to investigate the flow structure of supersonic starting jet interaction with a solid surface.

7.1 Impingement of a supersonic starting jet on a solid surface

7.1.1 Shock reflection and distortion

According to the discussion in Chapter 4, four major physical processes can be identified in the flow of supersonic starting jets. The first one is the initial shock, which is planar when releasing from the square shock tube exit but converts to a spherical shape rapidly. The secondary flow structure is the secondary shock(s) due to the rarefaction. When the pressure behind the initial shock wave drops enough to a value below the atmospheric pressure, a secondary shock wave is generated. This secondary shock wave then separates from the jet head and the abovementioned process repeats, generating additional shock waves until the jet flow becomes subsonic and no longer able to sustain the formation of secondary shock waves. The third process is the vortex loop distortion created by the shear layer originating from the tube exit. The fourth major feature is the so-called secondary oblique shock structure when the initial shock Mach number exceeds 1.43 approximately.

In this chapter, an investigation on the interaction of the initial transmitting shock wave from a square starting jet with solid and flexible surfaces is conducted. Figures 7.2-7.5 depict the initial shock reflection process on a solid plate with the distance between shock tube end and solid plate $D=55\text{mm}$ at NONEL tube length $L=200\text{mm}$, 300mm , 400mm , and 500mm respectively. The elapsed time when the initial shock wave from the square nozzle reaches

the solid plate surface is defined as $t=0$. It can be seen from Figures 7.2-7.5 that the initial shock wave is reflected less than 4 μ s after it reaches the solid plate surface in all the cases of $M_s \sim 1.28-1.53$.

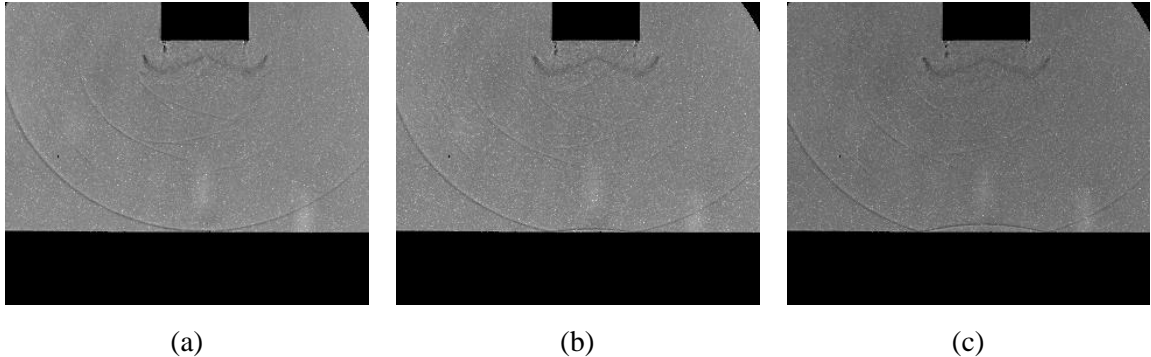


Figure 7.2 Shock reflection at $M_s \sim 1.28$, NONEL tube length $L=200\text{mm}$, the distance between shock tube end and solid plate $D=55\text{mm}$: (a) $\Delta t=0$; (b) $\Delta t=4\mu\text{s}$; (c) $\Delta t=8\mu\text{s}$

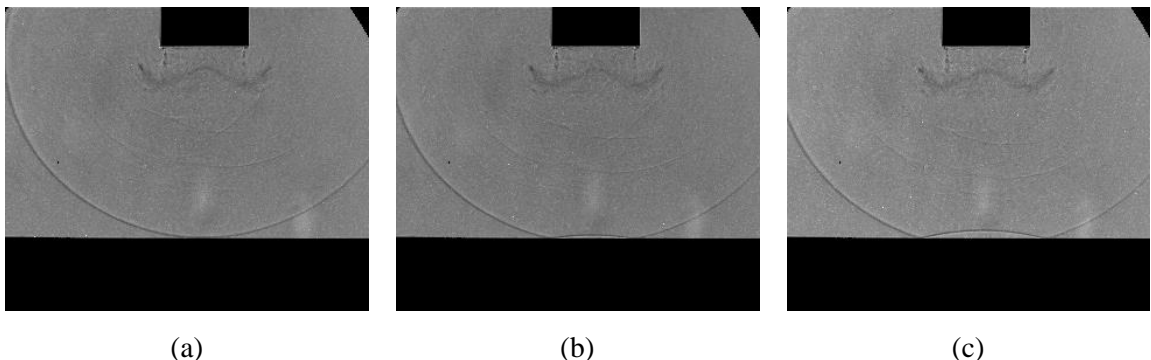


Figure 7.3 Shock reflection at $M_s \sim 1.37$, NONEL tube length $L=300\text{mm}$, the distance between shock tube end and solid plate $D=55\text{mm}$: (a) $\Delta t=0$; (b) $\Delta t=4\mu\text{s}$; (c) $\Delta t=8\mu\text{s}$

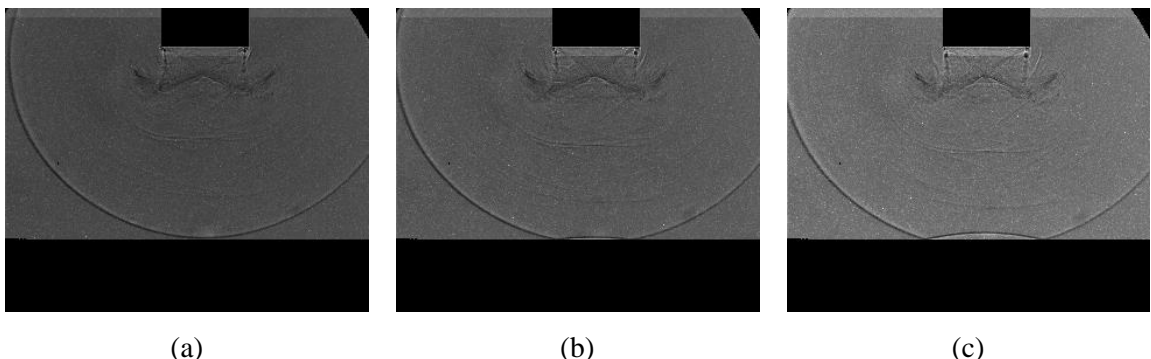


Figure 7.4 Shock reflection at $M_s \sim 1.46$, NONEL tube length $L=400\text{mm}$, the distance between shock tube end and solid plate $D=55\text{mm}$: (a) $\Delta t=0$; (b) $\Delta t=4\mu\text{s}$; (c) $\Delta t=8\mu\text{s}$

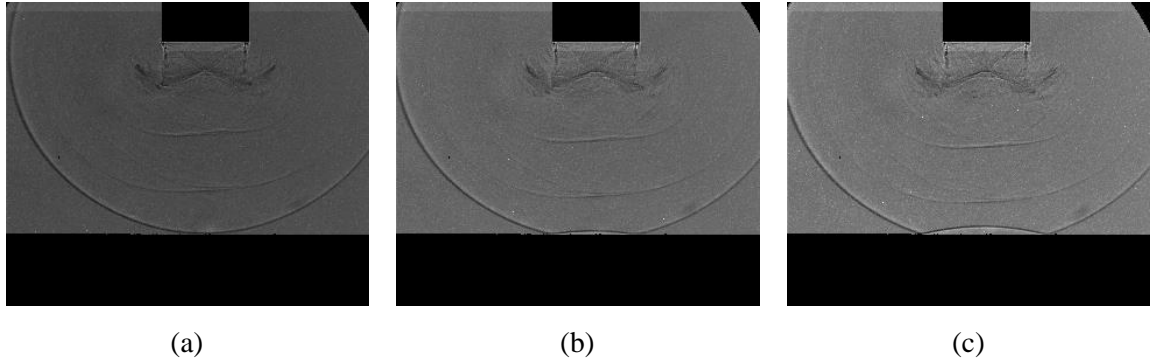


Figure 7.5 Shock reflection at $M_s \sim 1.53$, NONEL tube length $L=500\text{mm}$, the distance between shock tube end and solid plate $D=55\text{mm}$: (a) $\Delta t=0$; (b) $\Delta t=4\mu\text{s}$; (c) $\Delta t=8\mu\text{s}$

The trace line of the reflected shock wave is shown in Figure 7.6 and Figure 7.7 presents the instantaneous vertical locations of the incident initial shock wave at $M_s \sim 1.53$ and the distance between shock tube end and solid plate $D=30\text{mm}$. The elapsed time after the initial shock wave from the square nozzle reaches the solid plate surface is defined as t . We define that the elapsed time before the initial shock wave from the square nozzle arrives at the solid plate surface is negative. The software and image processing techniques developed in Chapter 6 is used to detect and track the shock wave. In this case, the pre-processing mainly involves background subtraction in the frequency domain, image upsampling by Lanczos algorithm, median and bilateral filter, and adaptive threshold. The modified automatic Canny algorithm (see Chapter 6) is adopted and the shock wave is extracted by the contour size. The calculation uncertainty in the shock wave velocity due to ± 1 pixel error estimation is 9.4m/s . The first derivative of the time evolution curve of shock wave locations in Figure 7.7 stands for the shock propagation velocity. To evaluate the shock speed variation, the reflected shock location data in Figure 7.7 is fitted using polynomial functions. As given in Figure 7.7, the incident shock location evolution can be fitted by a linear polynomial function, which means the velocity of the incident initial shock stays the same before it arrives at the plate. By contrast, the evolution of reflected shock is nonlinear and its speed decreases versus time. The opposing flow in the front of reflected shock might cause a reduction in its propagation speed. Specifically, the velocity of incident initial shock from the square shock tube is about $529.17 \pm 9.4\text{m/s}$ and remains unchanged during a period of time $20\mu\text{s}$ before it reaches the solid plate surface, whereas the velocity of reflected shock wave declines to

364.54 ± 9.4 m/s because of the energy loss during the shock wave and solid surface interaction.

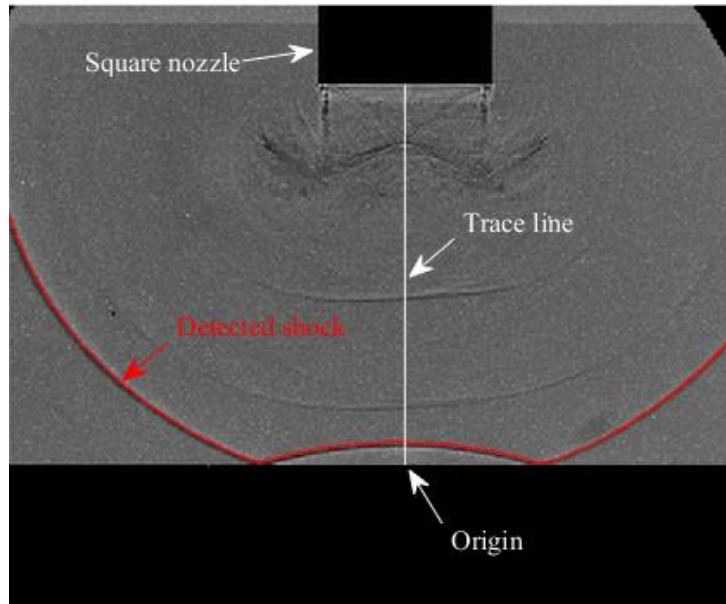


Figure 7.6 Trace line for calculating reflected shock velocity

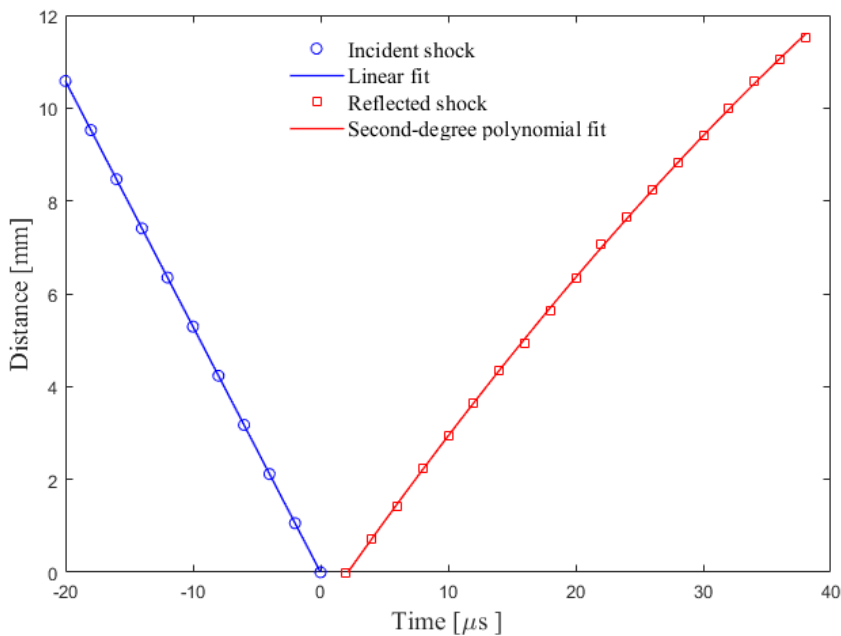


Figure 7.7 Time evolution of reflected shock wave at $M_s \sim 1.53$, NONEL tube length $L=500$ mm, the distance between shock tube end and solid plate $D=30$ mm

Figure 7.8 shows the distortion of the reflected shock wave. To demonstrate the distortion more clearly, only a portion of the incident and reflected shock wave obtained from the shock wave detection and tracking software in Chapter 6 is plotted in Figure 7.8 (b). Figure 7.8 (a) shows the definition of the image coordinate system, whereas Figure 7.8 (b) presents the incident shock configuration in the case of $\Delta t=0\mu s$ (the blue solid line) and the reflected shock configuration at $\Delta t=8\mu s$ (the red solid line) without curve fitting. To compare the shape of the reflected shock wave and incident shock wave, the incident shock wave is translated (the blue dash line) to make it overlapped with the non-reflected portion of reflected shock, whereas the reflected portion of the reflected shock is mirrored (the red dash line). It can be seen from Figure 7.8 (b) that the propagation velocity of the reflected portion of the initial shock wave is lower, which makes the reflected portion to have a smaller curvature than the incident shock. By contrast, the configuration of the non-reflected portion of the initial shock basically remains the same in a period of elapsed time $\Delta t=8\mu s$.

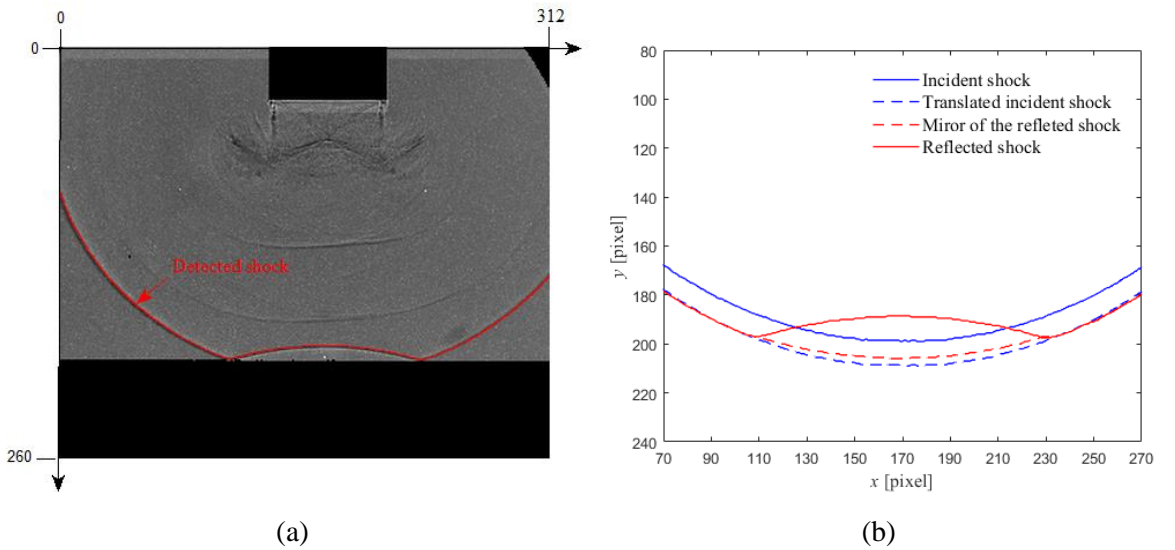


Figure 7.8 Distortion of the reflected shock wave at $M_s \sim 1.53$, NONEL tube length $L=500\text{mm}$, $\Delta t=8\mu s$ and the distance between shock tube end and solid plate $D=55\text{mm}$

7.1.2 Shock and vortex loop interaction

As the reflected shock wave propagates further, it will impinge on the opposing three-dimensional vortex loop. The shock and vortex loop interaction is a key noise source for high-speed flight vehicles [253, 386, 387]. Figure 7.9 demonstrates framing shadowgraph

framings of reflected shock and vortex loop interaction in the case of $M_s \sim 1.37$, NONEL tube length $L=300\text{mm}$ and the distance between shock tube end and solid plate $D=55\text{mm}$. Previous studies [110, 388] have proved that the shock wave and vortex ring interaction process in an axisymmetric supersonic jet has two parts: the central and the outer parts of the vortex ring. As presented in Figure 7.9, during the process of the shock wave and square vortex loop interaction, diffracted shock waves are generated at the outer and central portion of the square vortex loop. Before the reflected shock encounters the vortex loop, the central portion of the reflected shock wave is almost planar (Figure 7.9 (e)) due to the influence of the subsonic opposing flow between the initial shock and vortex loop. Thereafter, the reflected shock wave impinges on the vortex loop central portion and slows down by the relatively high-speed opposed flow generated by the vortex loop (Figure 7.9 (f)). At the vortex loop outer parts, the reflected shock wave speeds up due to the rotating vortex core, resulting in the formation of a diffracted shock wave. In the process of shock wave interacting with the circular vortex ring, the reflected planar shock wave is distorted to a concave configuration at the vortex central part [388-390], however, the reflected shock is not deformed to be concave in the present case. As shown in Figure 7.9 (h), the high-speed opposing flow from the tube exit weakens the shock wave at the vortex loop corner, resulting in shock wave distortion towards the vortex loop central portion. Afterwards, the distorted shock continues to propagate and scatters towards the outer parts due to the pulling of the vortex core outer parts. Around the vortex loop centre, the distorted shock becomes convex to some extent (Figure 7.9 (j)), and then propagates to the vortex loop outside.

The process of shock wave distortion determines the shock propagation direction and affects the shock focusing phenomena [253]. As illustrated in Figure 7.9, the vortex loop propagates from top to bottom at a relatively low speed. The reflected shock wave strength decreases gradually before the shock wave and vortex loop interaction, which can be demonstrated by the intensity gradient of the shadowgraph images. By contrast, the density gradient intensity becomes stronger during the process of the shock wave and vortex loop interaction. Moreover, shock focusing comes up because the concave shock induced at the vortex central parts converges towards the centre line (see Figure 7.9 (j-l)). The pressure increase induced by this shock focusing would generate noises [389, 390].

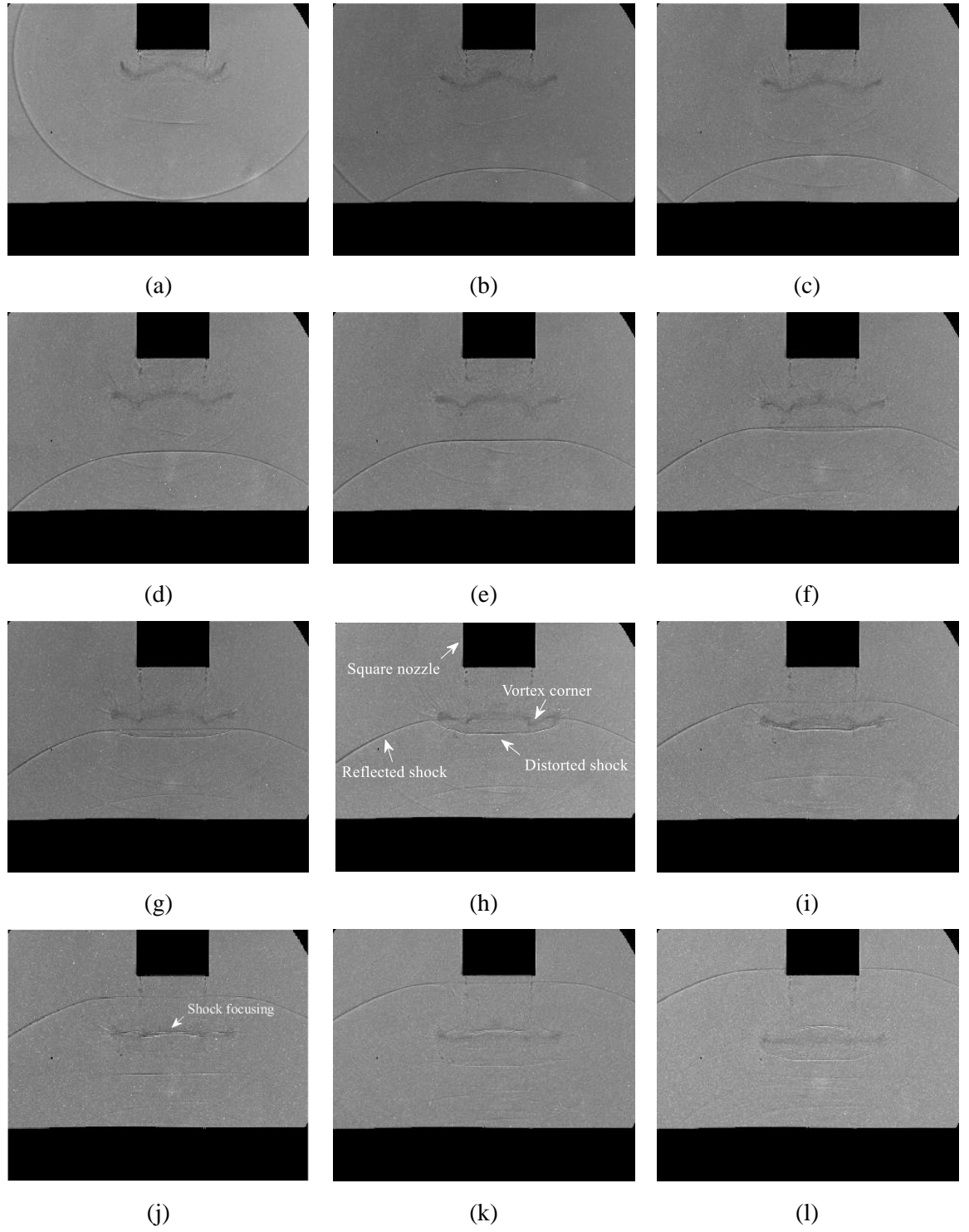


Figure 7.9 Framing shadowgraph images demonstrating reflected shock and vortex loop interaction at $M_s \sim 1.37$, NONEL tube length $L = 300\text{mm}$, the distance between shock tube end and solid plate $D = 55\text{mm}$: (a) $\Delta t = 0$; (b) $\Delta t = 58\mu\text{s}$; (c) $\Delta t = 72\mu\text{s}$; (d) $\Delta t = 86\mu\text{s}$; (e) $\Delta t = 100\mu\text{s}$; (f) $\Delta t = 114\mu\text{s}$; (g) $\Delta t = 120\mu\text{s}$; (h) $\Delta t = 128\mu\text{s}$; (i) $\Delta t = 142\mu\text{s}$; (j) $\Delta t = 156\mu\text{s}$; (k) $\Delta t = 170\mu\text{s}$; (l) $\Delta t = 184\mu\text{s}$

7.2 Effects of the surface thickness

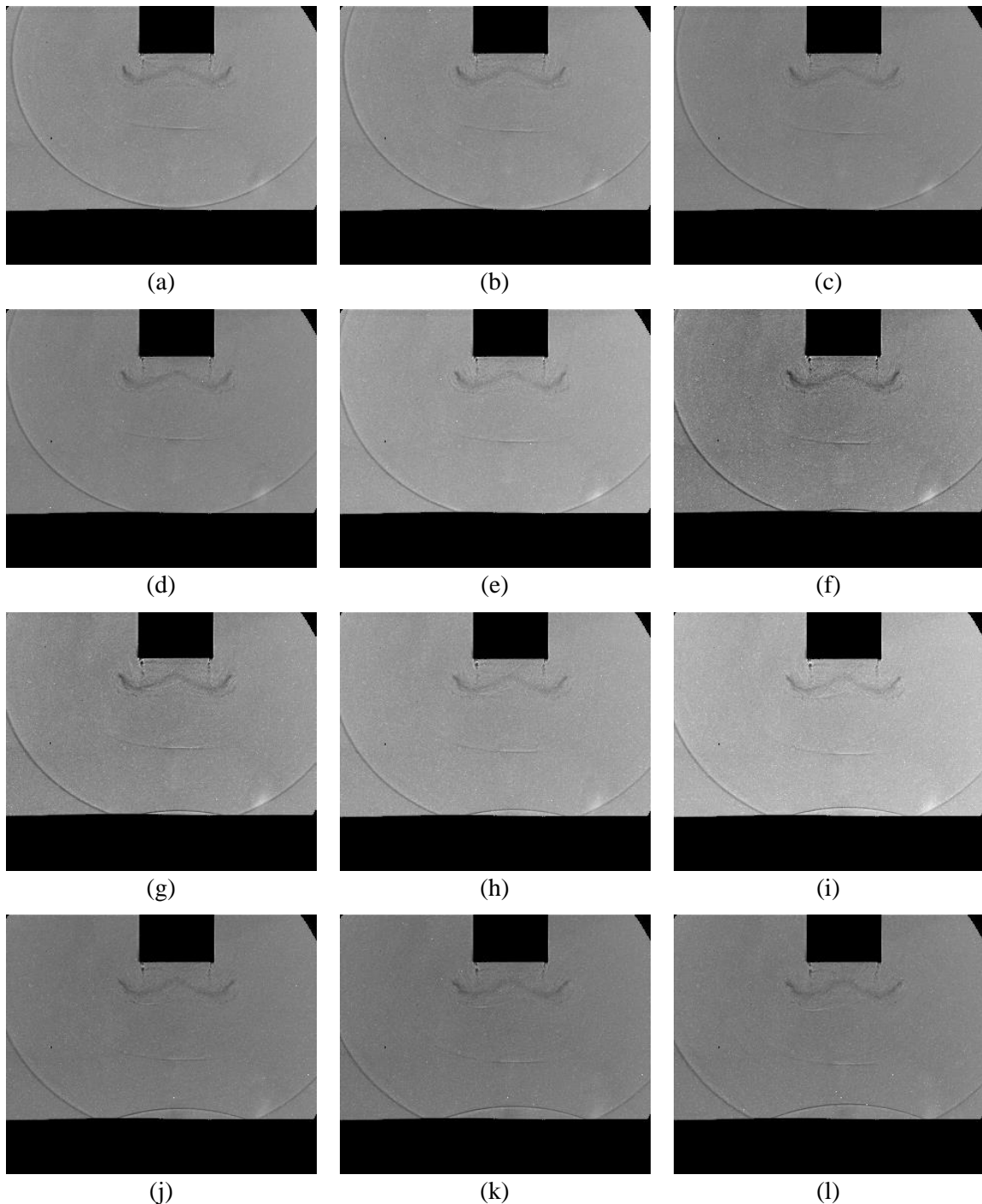


Figure 7.10 Shock reflection on a 0.1mm-thick alloy aluminium surface in the case of $M_s \sim 1.37$, NONEL tube length $L = 300\text{mm}$, the distance between shock tube end and solid plate $D = 55\text{mm}$: (a) $\Delta t = 0$; (b) $\Delta t = 2\mu s$; (c) $\Delta t = 4\mu s$; (d) $\Delta t = 6\mu s$; (e) $\Delta t = 8\mu s$; (f) $\Delta t = 10\mu s$; (g) $\Delta t = 12\mu s$; (h) $\Delta t = 14\mu s$; (i) $\Delta t = 16\mu s$; (j) $\Delta t = 18\mu s$; (k) $\Delta t = 20\mu s$; (l) $\Delta t = 22\mu s$

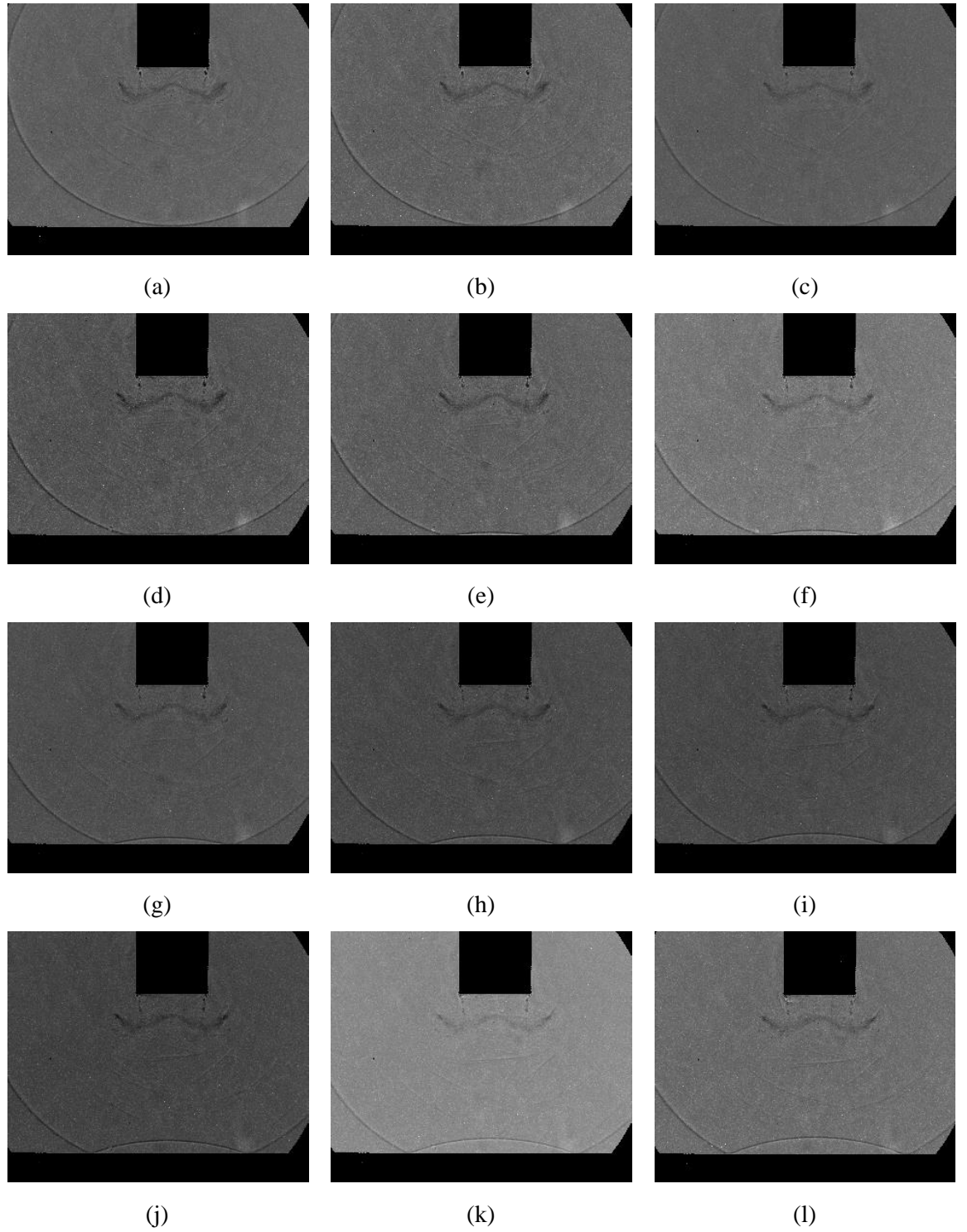


Figure 7.11 Shock reflection on a 0.3mm-thick alloy aluminium surface in the case of $M_s \sim 1.37$, NONEL tube length $L=300\text{mm}$, the distance between shock tube end and solid plate $D=55\text{mm}$: (a) $\Delta t=0$; (b) $\Delta t=2\mu\text{s}$; (c) $\Delta t=4\mu\text{s}$; (d) $\Delta t=6\mu\text{s}$; (e) $\Delta t=8\mu\text{s}$; (f) $\Delta t=10\mu\text{s}$; (g) $\Delta t=12\mu\text{s}$; (h) $\Delta t=14\mu\text{s}$; (i) $\Delta t=16\mu\text{s}$; (j) $\Delta t=18\mu\text{s}$; (k) $\Delta t=20\mu\text{s}$; (l) $\Delta t=22\mu\text{s}$

Figures 7.10 and 7.11 present the impingement and reflection process of the initial shock from the supersonic starting jet on a 0.1mm and 0.3mm thick alloy aluminium flexible surfaces respectively ($M_s \sim 1.37$, NONEL tube length $L=300\text{mm}$, the distance between shock tube end and solid plate $D=55\text{mm}$). Compared with that of the solid plate case in Figure 7.3, the initial shock wave impinges “into” the flexible surfaces due to the pressure loading induced by the initial shock, which results in an occlusion of the leading portion of the initial shock (Figure 7.10 (b-e) and Figure 7.11(b-c)). The force acting on the plates consists of the overpressure loading induced by the reflected shock wave on the top surface and the viscous force due to the spanwise flow. The overpressure loading induced by the shock wave is expected to be dominant to the structural response of the plates. In the present study, only the flow structure is visualized by shadowgraph photography. The unsteady pressure loading on the top of the plates will be measured when the fast pressure-sensitive paint system developed in Chapter 5 is fully established. Actually, the mechanism of the shock and flexible surface interaction is important for the launch of a space rocket or military missile that produces a shock wave from the nozzle exit with high pressure loading on the surroundings. In the solid plate case, there is not any deformation and the initial shock wave is reflected instantly after the impingement. By contrast, the flexible surfaces can delay this reflection process because of the flexible panel deformation generated by the pressure difference between the top and the bottom. In the present study, the pressure of the bottom side of all surfaces is the ambient pressure. There is a significant pressure rise when the shock arrives at the surfaces. It can be seen from Figure 7.10 (b-e) that the delay time is around $8\mu\text{s}$ in the case of 0.1mm thick flexible surface, whereas it declines to around $4\mu\text{s}$ in the case of 0.3mm thick flexible surface because of the lower flexibility and deformation magnitude. Herein, the behaviour of the initial shock wave during the interaction with flexible surfaces is focused. To investigate the mechanism of the shock wave and flexible surface interaction in more detail, the unsteady surface pressure loading will be measured by fast PSP in the future. Additionally, the frequency and the magnitude of the structural response will be monitored by digital image correlation technique.

Figure 7.12 shows the time evolution of the reflected shock wave in cases of the solid plate case and the 0.1mm thick flexible surface at $M_s \sim 1.53$, NONEL tube length $L=500\text{mm}$ and the distance between shock tube end and surfaces $D=30\text{mm}$. The elapsed time when the initial shock wave from the square nozzle reaches the surfaces is defined as $t=0$. The frame rate of the shadowgraph system is 500k frames/s, meaning a time resolution of $2\mu\text{s}$. As shown in Figure 7.12, there is an $8\mu\text{s}$ delay for the initial shock wave reflection. However,

it is interesting that these two curves have basically the same curvature, in which the first derivative stands for the propagation velocity of the reflected shock wave. Specifically, the reflected shock wave velocity in the solid plate case and 0.1mm-thick flexible alloy aluminium surface case is $364.5 \pm 9.4 \text{ m/s}$ and $352.8 \pm 9.4 \text{ m/s}$ respectively with the same incident shock wave $529.17 \text{ m/s} \pm 9.4 \text{ m/s}$. So, the propagation velocity of the reflected shock wave is basically the same for these two cases, which means the flexible surface doesn't reduce the strength of the reflection wave, although it delays its propagation.

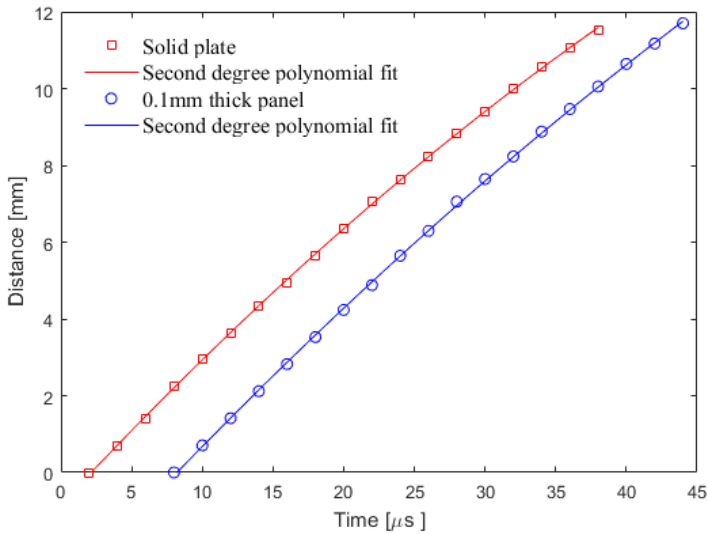


Figure 7.12 Comparison of time evolution between of the reflected shock wave locations between the solid plate and 0.1mm thick flexible surface at $M_s \sim 1.53$, NONEL tube length $L=500\text{mm}$ and the distance between shock tube end and surfaces $D=30\text{mm}$

It is worth mentioning that all the aforementioned velocities are calculated from shadowgraph images. To improve the accuracy of the shock propagation speed, the visualization area was reduced (Figure 7.13 (a)) compared with the case for demonstrating the shock flow structure (Figures 7.10-7.11). The software and image processing techniques developed in Chapter 6 are used to detect and track the shock wave. In this case, the pre-processing mainly involves background subtraction in the frequency domain, image upsampling by Lanczos algorithm, median and bilateral filter, and adaptive threshold. The modified automatic Canny algorithm (see Chapter 6) is adopted and the shock wave is extracted by the contour size. Figure 7.13 (b) depicts an example of shock detection and extraction result in the case of $\Delta t=10\mu\text{s}$, $M_s \sim 1.27$, NONEL tube length $L=200\text{mm}$, and the distance between shock tube end and surfaces $D=30\text{mm}$. As presented in Figure 7.13 (b), the shock contour extracted from the original shadowgraph image is not smooth enough

because of image noises. The polynomial function is used to fit the shock configuration based on the image coordinates of shock contour points. Figure 7.13 (c) demonstrates the shock configuration after contour fitting. Based on the fitted shock contour, the tip of this convex shock can be obtained in a subpixel accuracy.

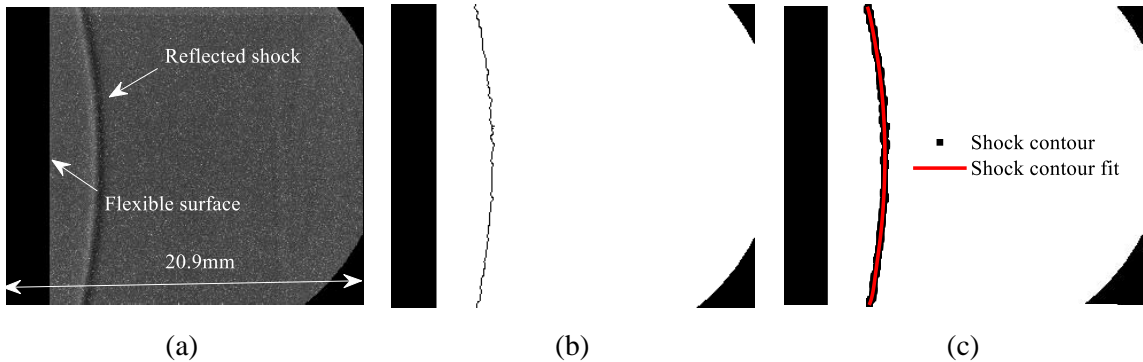


Figure 7.13 Shock detection and fit for calculating reflected shock velocity in the case of $M_s \sim 1.27$, NONEL tube length $L=200\text{mm}$ and distance between shock tube end and the surface $D=30\text{mm}$: (a) original shadowgraph image; (b) shock contour detection and extraction; (c) shock contour fitting

7.3 Effects of Mach number

Figures 7.14-7.16 present the impingement and reflection process of the initial shock from the supersonic starting jet on a 0.3mm thick alloy aluminium flexible surface at NONEL tube length $L=200\text{mm}$, 400mm, and 500mm respectively. The shadowgraph images in the case of NONEL tube length $L=300\text{mm}$ have been given in Figure 7.11. It can be seen from Figure 7.11 and 7.14 that only the two major physical processes, initial shock wave, and vortex loop, can be found when NONEL tube length L is smaller than 300mm, namely the initial shock Mach number is lower than 1.37 approximately. By contrast, in the case of $L=400\text{mm}$ and 500mm (Figures 7.15 and 7.16), the supersonic flow regions induced by the non-uniform flow expansion results in the formation of the secondary oblique shock wave structure. However, interestingly, the reflection delay time of the initial shock wave is basically the same for the initial shock Mach number $M_s \sim 1.27-1.53$, which is around 4-6 μs . It means that the difference of the pressure loading in different M_s is not big enough to generate an apparent variation in the deformation magnitude of the 0.3mm-thick alloy aluminium flexible surface.

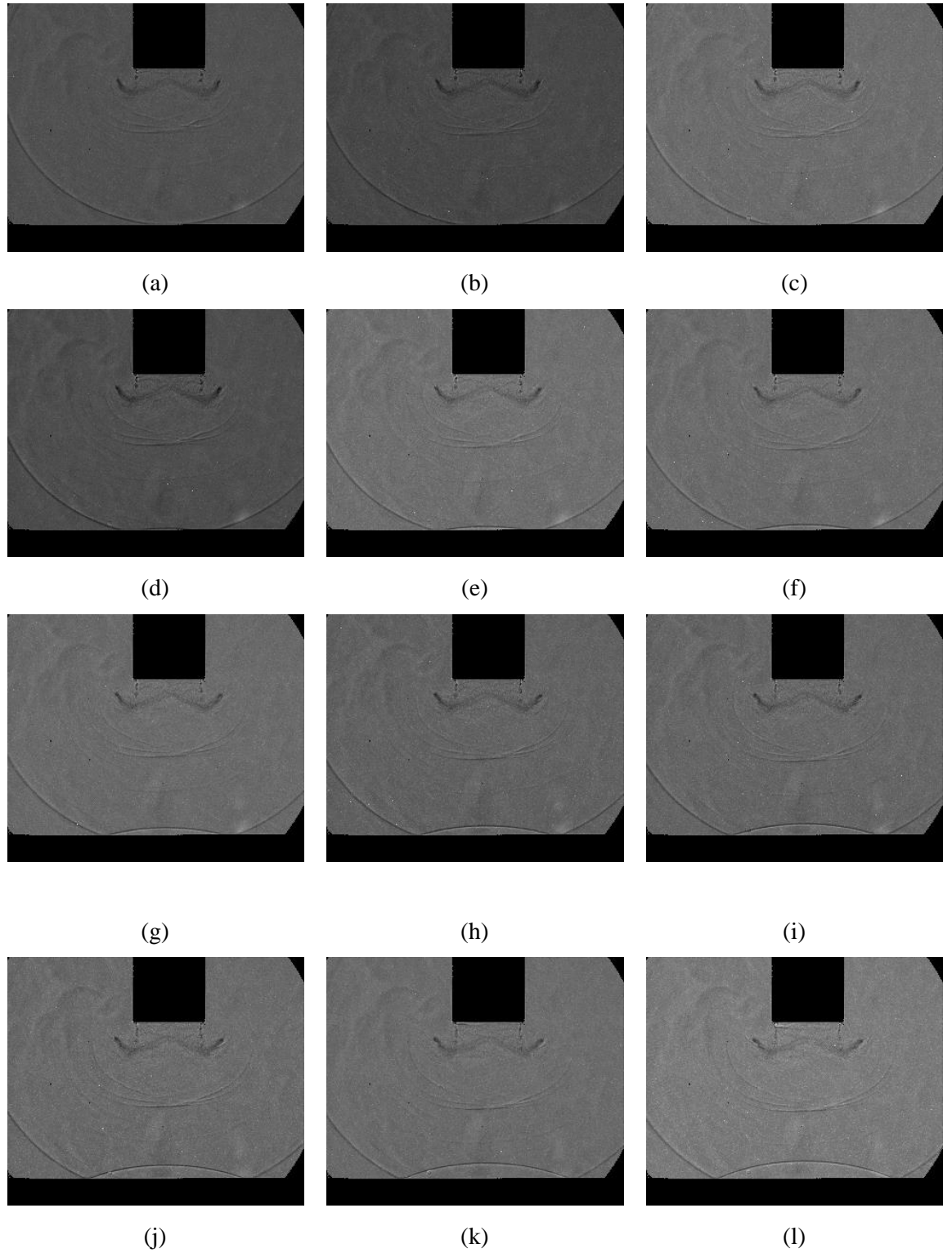


Figure 7.14 Shock reflection on a 0.3mm-thick alloy aluminium surface in the case of $M_s \sim 1.27$, NONEL tube length $L=200\text{mm}$, the distance between shock tube end and the surface $D=55\text{mm}$: (a) $\Delta t=0$; (b) $\Delta t=2\mu\text{s}$; (c) $\Delta t=4\mu\text{s}$; (d) $\Delta t=6\mu\text{s}$; (e) $\Delta t=8\mu\text{s}$; (f) $\Delta t=10\mu\text{s}$; (g) $\Delta t=12\mu\text{s}$; (h) $\Delta t=14\mu\text{s}$; (i) $\Delta t=16\mu\text{s}$; (j) $\Delta t=18\mu\text{s}$; (k) $\Delta t=20\mu\text{s}$; (l) $\Delta t=22\mu\text{s}$

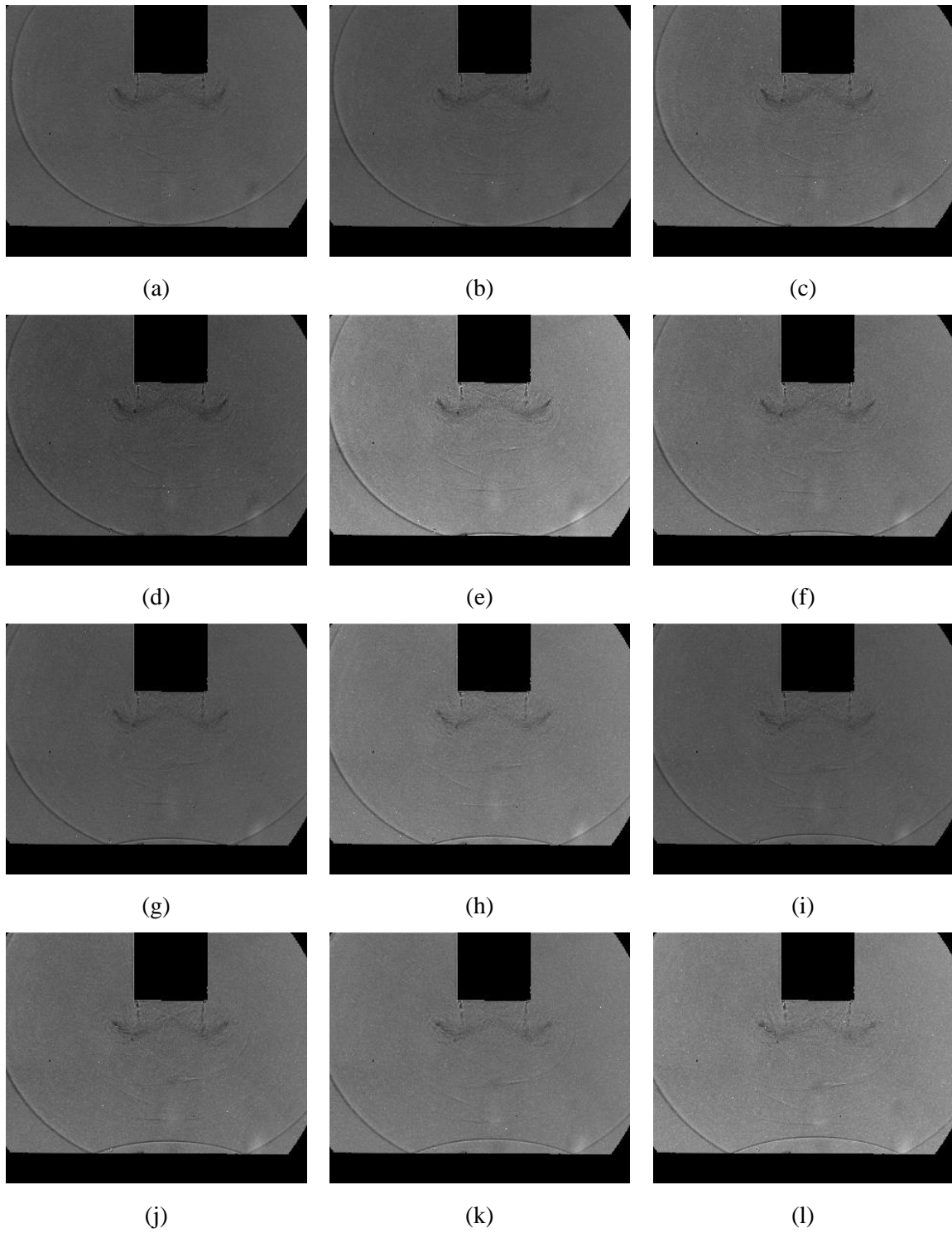


Figure 7.15 Shock reflection on a 0.3mm-thick alloy aluminium surface in the case of $M_s \sim 1.46$, NONEL tube length $L=400\text{mm}$, the distance between shock tube end and the surface $D=55\text{mm}$: (a) $\Delta t=0$; (b) $\Delta t=2\mu\text{s}$; (c) $\Delta t=4\mu\text{s}$; (d) $\Delta t=6\mu\text{s}$; (e) $\Delta t=8\mu\text{s}$; (f) $\Delta t=10\mu\text{s}$; (g) $\Delta t=12\mu\text{s}$; (h) $\Delta t=14\mu\text{s}$; (i) $\Delta t=16\mu\text{s}$; (j) $\Delta t=18\mu\text{s}$; (k) $\Delta t=20\mu\text{s}$; (l) $\Delta t=22\mu\text{s}$

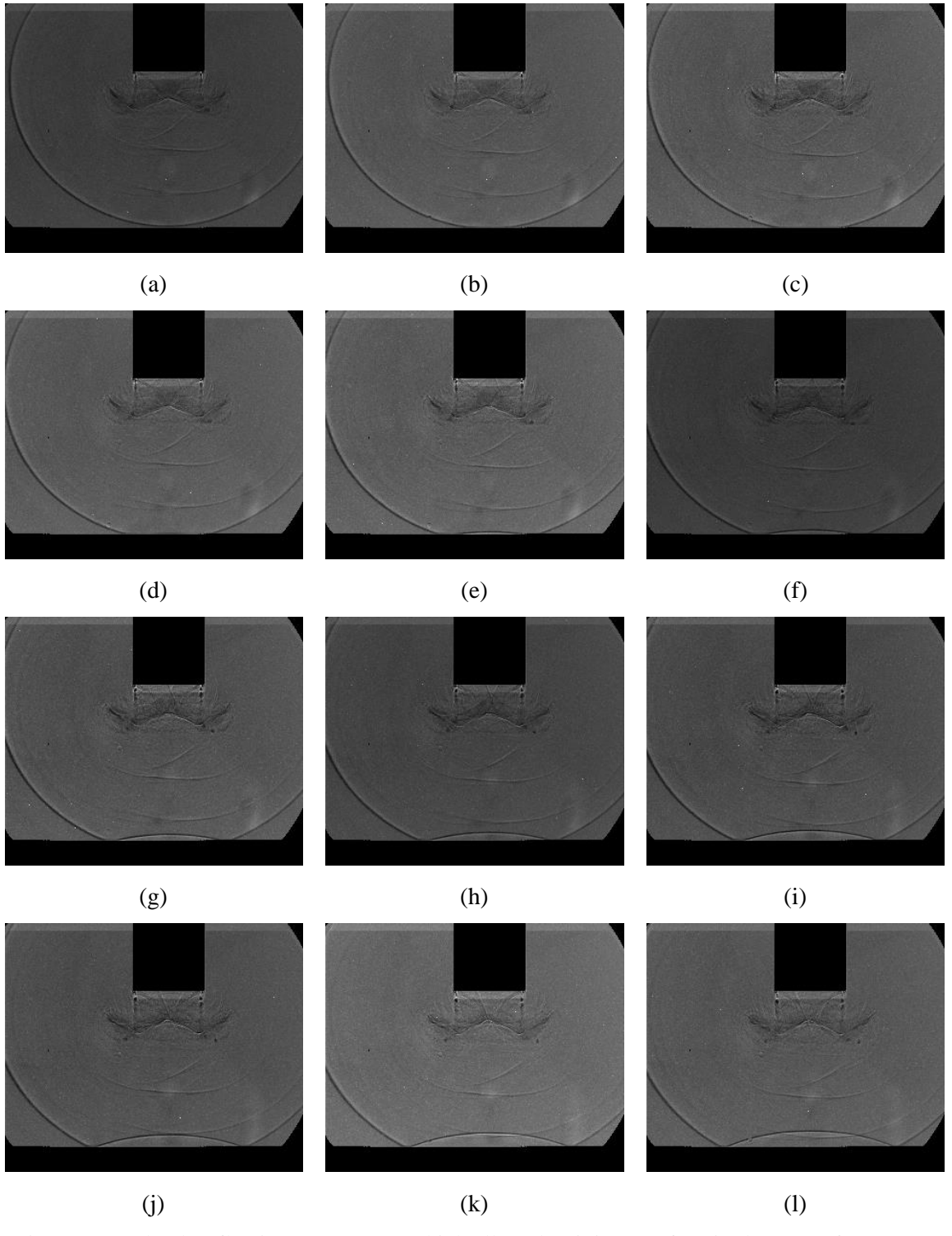


Figure 7.16 Shock reflection on a 0.3mm-thick alloy aluminium surface in the case of $M_s \sim 1.53$, NONEL tube length $L=500\text{mm}$, the distance between shock tube end and the surface $D=55\text{mm}$: (a) $\Delta t=0$; (b) $\Delta t=2\mu\text{s}$; (c) $\Delta t=4\mu\text{s}$; (d) $\Delta t=6\mu\text{s}$; (e) $\Delta t=8\mu\text{s}$; (f) $\Delta t=10\mu\text{s}$; (g) $\Delta t=12\mu\text{s}$; (h) $\Delta t=14\mu\text{s}$; (i) $\Delta t=16\mu\text{s}$; (j) $\Delta t=18\mu\text{s}$; (k) $\Delta t=20\mu\text{s}$; (l) $\Delta t=22\mu\text{s}$

Table 7.1 Velocities of incident shock and reflected shock for different NOENL tube lengths in the case of 0.1mm thick alloy aluminium flexible surface and $D=30\text{mm}$

<i>L (mm)</i>	<i>Incident shock speed (m/s)</i>	<i>Incident shock Mach number</i>	<i>Reflected shock speed</i>	<i>Speed loss</i>
200	421.24	1.22	351.03	16.6%
300	469.80	1.37	352.40	25.0%
400	499.20	1.44	349.70	30.0%
500	529.17	1.54	352.80	33.4%

To investigate the influence of incident shock Mach number on the velocity of the reflected shock, the visualization area was reduced (see Figure 7.13 (a)) compared with the case for demonstrating the shock flow structure (Figures 7.11 and 7.14-7.16). The software and image processing techniques developed in Chapter 6 are used to detect and track the shock wave. Table 7.1 presents velocities of incident shock and reflected shock for different NOENL tube lengths in the case of 0.1mm thick alloy aluminium flexible surface and $D=30\text{mm}$. Interestingly, there is not an apparent difference in the velocity of the reflected shock wave in the case of different incident shock Mach numbers. The reason probably is that the velocity of the opposing flow behind the initial shock wave is higher in the case of larger incident shock Mach number, which results in a larger speed loss of the reflected shock. Therefore, the reflected shock wave velocity is basically the same for incident shock Mach number $M_s \sim 1.22-1.54$.

7.4 Conclusions

For the launch of space rockets, military missiles or the space travel such as the future missions involving lunar and Mars exploration with the aim at returning the capsules to Earth, there is a serious concern associated with the effectiveness of the propulsion system, either continuous or pulse-driven, due to the impact of the shock wave generated by the propellant explosion on a surrounding surface and the capsule. In this chapter, the mechanism of the interaction of the initial shock wave from a supersonic starting jet with flexible surfaces is investigated preliminarily. The square shock tube driven by detonation transmitting tube proposed in Chapter 4 is used to simulate the supersonic starting jet, whereas the software and the image processing scheme in Chapter 6 are adopted to detect, track, extract and fit

shock waves visualized in a high-speed shadowgraph system. Based on the fitted shock contour, shock wave location can be obtained in a subpixel accuracy.

Compared with that of the solid plate case, the initial shock wave impinges “into” the flexible surfaces due to the pressure loading induced by the initial shock, which results in an occlusion of the leading portion of the initial shock. In the solid plate case, there is not any deformation and the initial shock wave is reflected instantly after the impingement. By contrast, the flexible surfaces can delay this reflection process because of the flexible panel deformation generated by the pressure difference between the top and the bottom. The delay time is around $8\mu\text{s}$ in the case of 0.1mm thick flexible surface, whereas it declines to around $4\mu\text{s}$ in the case of 0.3mm thick flexible surface because of the lower flexibility and deformation magnitude. The velocity of incident initial shock from the square shock tube basically remains unchanged during a period of time $20\mu\text{s}$ before it reaches the solid plate surface, whereas the velocity of the reflected shock wave declines considerably because of the energy loss during the shock impingement and the opposing flow. In the case of flexible plate thickness $\delta=0.1\text{mm}$, NONEL tube length $L=500\text{mm}$ and distance between the shock tube end and the surface $D=30\text{mm}$, the velocity of incident initial shock from the square shock tube is about 529.17m/s , whereas the velocity of reflected shock wave declines to 364.54m/s . However, interestingly, the propagation velocity of the reflected shock wave is basically the same for the solid plate and flexible panels, which means the flexible surface doesn't reduce the strength of the reflection wave, although it delays its propagation. Also, there is not an apparent difference in the velocity of the reflected shock wave in the case of different incident shock Mach numbers. The reflected shock wave velocity is basically the same (around 350m/s) for incident shock Mach number $M_s \sim 1.22-1.54$ at alloy aluminium flexible surface thickness $\delta=0.1\text{mm}$ and distance between the shock tube end and the surface $D=30\text{mm}$. The reason probably is that the velocity of the opposing flow behind the initial shock wave is higher in the case of larger incident shock Mach number, which results in a larger speed loss of the reflected shock. The preliminary results from this study are useful for validating numerical codes that are used for understanding fluid-structure interaction processes.

In this research, the behaviour of the initial shock wave during the interaction with flexible surfaces is studied. To investigate the mechanism of the shock and flexible surface

interaction in more detail, the surface pressure loading and deformation need to be monitored by pressure sensitive paint and digital image correlation techniques in the future.

Chapter 8

Conclusions and future work

8.1 Conclusions

The findings of the current investigation are summarized below:

8.1.1 Design of novel shock tubes driven by detonation transmission tubing

A novel concept to design shock tubes driven by detonation transmission tubing in a reliable, repeatable, and safe manner for laboratory scale experiments is proposed and demonstrated. Specifically, a circular and open-ended shock tube with a straight driven section (inner diameter $ID = 22$ mm, driven section length $L_d = 330$ mm) was designed and manufactured. Also, a similar square shock tube was also fabricated to simulate square supersonic starting jets. To investigate the characterization of this novel type shock tube, the pressure-time measurement in the driven section and the time-resolved shadowgraph were performed, which proved that the flow structure from the open end of shock tubes driven by detonation transmission tubing is similar with that of conventional compressed-gas driven shock tubes. The relative standard deviation of the peak overpressure magnitude in the driven section of the shock tube and the initial shock wave location from the shadowgraph frames is 1.64% and 2.82% respectively in 7 replication runs, demonstrating good repeatability of less than

3%. Moreover, the Mach number range of this novel shock tube driven by NONEL tube is 1.29 to 1.58 when the weight of the NONEL explosive mixture varies from 3.6mg to 12.6mg.

Compared with conventional compressed-gas ones, shock tubes driven by detonation transmission tubing is smaller in size, more cost-effective, and much easier to operate. It can be used in aerodynamics to investigate flows involving the shock wave, vortex loop, supersonic jets, and also applicable in medicine, biology, and other industries for various applications to replace conventional shock tubes.

8.1.2 Development of BOS and PSP systems

In this dissertation, a MATLAB program was developed to generate and optimize the background pattern through a user-controlled and fully customizable approach. The number and diameter of dots along with the size of the background (A1-A4 paper) can be set through this application and then printed by a common ink-jet printer. The paper for printing can be conventional white copy paper sheets, white reflective film sheets, or semi-transparent papers to increase the efficiency of illumination.

Based on the light source and high-speed camera from the time-resolved shadowgraph, a validation BOS test was performed in the supersonic wind tunnel in the University of Glasgow to visualize the supersonic flow structure around a pitot tube in the test section. All the BOS images were processed using PIVlab, a popular open-source PIV software. The preliminary BOS result shows that the sensitivity of the BOS system is good enough to visualize weak density variations caused by expansion waves, boundary layer, and weak oblique shock. It also presents the strong density gradient caused by the bow shock in the front of the hose tip of the pitot tube, normal shock ahead of the pitot tube root near the tunnel top wall, and the strong oblique shock system. However, shock waves visualized by the present BOS system are quite thick or blur. The reason for this is the long exposure time ($33\mu s$) and the high unsteadiness of the shock waves because of wind tunnel vibration and its inherent unsteady flow feature. Next, to improve the performance and capacity of the current BOS system, it will be optimized further including adding extra light sources to shorten the exposure time, testing new fast cameras with better spatial resolution, and optimizing the background pattern dot diameter and filled ratio.

Pressure-sensitive paint (PSP) is a novel optical measurement technique for global surface pressure measurements in wind tunnel testing. In the University of Glasgow, there is a commercial steady PSP system from Innovative Scientific Solutions Inc. (ISSI). In this dissertation, a novel PtTFPP-based unsteady PSP formulation was proposed and an unsteady PSP system was built up. Pt(II) meso-tetra(pentafluorophenyl)porphine (PtTFPP) from Santa Cruz Biotechnology, Inc. was selected as the pressure sensitive luminophore in the proposed novel unsteady PSP formulation, which is ideally excited at 395nm. Mesostructured-silica (M-silica) purchased from Sigma-Aldrich and KE-441-T room temperature vulcanizing silicone rubber (RTV) from Shin-Etsu Chemical was chosen as incorporated particles and the polymer of the binder respectively. Toluene purchased from Sigma-Aldrich was used as the solvent. To validate the performance of the unsteady PSP system, the main properties of the PtTFPP-based PC-PSP were investigated based on the paint preparation system and static calibration system. The experimental result shows that the pressure sensitivity of this novel PtTFPP-based PC-PSP is 0.75% per kPa at 20°C and a pressure range of 10 kPa-200kPa, the temperature sensitivity is 1.94%/ °C at ambient pressure and a temperature range of 10 °C-50 °C, and the overall photo-degradation rate is around 0.86% per minute under a continuous illumination in a period of 30 minutes.

Compared with the commercial PC-PSP from ISSI, the in-house developed one has better static properties, including higher pressure sensitivity, lower temperature sensitivity and photo-degradation rate. The response time of the in-house developed PC-PSP and its behaviours in the wind tunnel will be validated further.

8.1.3 Software development for shock wave detection and tracking

In order to detect, localize and track fluid features from measured or computed shadowgraph and schlieren data sets at higher frame rates automatically and effectively, an image processing scheme involving background subtraction in the frequency domain, filtering, resampling, edge detection, adaptive threshold, contour detection, extraction and fitting is proposed and demonstrated in this dissertation. In this scheme, the conventional Canny edge detection algorithm was modified to calculate the double threshold values automatically. Additionally, the adaptive threshold was proposed as one of the binary image calculation algorithms for contour detection, apart from the Canny edge algorithm. Also, the contour

approximation algorithm was performed to remove redundant points and compress the contour, thereby saving memory and improving calculating efficiency. Although all aforementioned algorithms have been validated and executed by text-based MATLAB codes, an application with graphical user interfaces was still developed, allowing higher productivity for setting, displaying, and operation. A large shadowgraph data set in Chapter 4 characterized by low signal to noise ratio (SNR) and small spatial resolution (312×260 -pixel), was used as a test bed for the software. The experimental result shows that the shock wave speed obtained based on shadowgraph images and the software agrees with that calculated by the overpressure magnitude. Also, the software was used to track the shock wave motion during the supersonic starting jet and flexible surface interaction. The shock locations detected by the software are consistent with those obtained manually, demonstrating its reliability and effectivity again. The image processing scheme outlined in this work can be applied to analyse common flows in which expansion and shock waves, shear layers, and vortex motion are a dominant feature. Such flows can be found in shock wave reflections, shock-shock and shock-boundary layer interactions, and inlet unstart.

8.1.4 Impingement of a supersonic starting jet on flexible surfaces

The mechanism of the interaction of the initial shock wave from a supersonic starting jet with flexible surfaces was investigated preliminarily in this research. The square shock tube driven by detonation transmitting tube was used to simulate the supersonic starting jet, whereas the image processing scheme in Chapter 6 was adopted to detect, track, extract and fit shock waves visualized in a high-speed shadowgraph system. Based on the fitted shock contour, shock wave location can be obtained in a subpixel accuracy.

During the process of supersonic starting jet impingement on flexible surfaces, the initial shock wave impinges “into” the flexible surfaces due to the pressure loading induced by the initial shock, which results in an occlusion of the leading portion of the initial shock. In the solid plate case, there is not any deformation and the initial shock wave is reflected instantly after the impingement. By contrast, flexible surfaces can delay this reflection process because of the flexible panel deformation generated by the pressure difference between the top and the bottom. The delay time is around $8\mu\text{s}$ in the case of 0.1mm thick flexible surface, whereas it declines to around $4\mu\text{s}$ in the case of 0.3mm thick flexible surface because of the

lower flexibility and deformation magnitude. The velocity of incident initial shock from the square shock tube basically remains unchanged during a period of time $20\mu\text{s}$ before it reaches the solid plate surface, whereas the velocity of the reflected shock wave declines considerably because of the energy loss during the shock impingement and the opposing flow. In the case of flexible plate thickness $\delta=0.1\text{mm}$, NONEL tube length $L=500\text{mm}$, and the distance between shock tube end and the surface $D=30\text{mm}$, the velocity of incident initial shock from the square shock tube is about 529.17m/s , whereas the velocity of reflected shock wave declines to 364.54m/s . However, interestingly, the propagation velocity of the reflected shock wave is basically the same for the solid plate and flexible panels, which means the flexible surface doesn't reduce the strength of the reflected shock wave, although it delays its propagation. Also, there is no apparent difference in the velocity of the reflected shock wave in the case of different incident shock Mach numbers. The reason probably is that the velocity of the opposing flow behind the initial shock wave is higher in the case of larger incident shock Mach number, which results in a larger speed loss of the reflected shock. The preliminary results from this study are useful for validating numerical codes that are used for understanding fluid-structure interaction processes.

8.2 Future work and recommendations

This section provides future work to consolidate the study presented in this dissertation. Recommendation and improvements in methodology, techniques, and instrumentation are also included.

8.2.1 Shock wave/boundary layer interaction over flexible surfaces

The influence of the strength, impingement location of the impingement shock and the aspect ratio, thickness, clamping conditions of the flexible panel on flow properties such as unsteady pressure loading, static pressure recovery, and size of the separation region needs to be investigated in the supersonic wind tunnel systematically. Currently, an experimental setup including a shock wave generator, flexible panels, and the supporting unit has been designed and fabricated for investigating oblique shock and boundary layer interaction over flexible surfaces in the supersonic wind tunnel (width, height, and length of the test section:

101.60mm \times 54.42mm \times 742.95 mm) of the University of Glasgow.

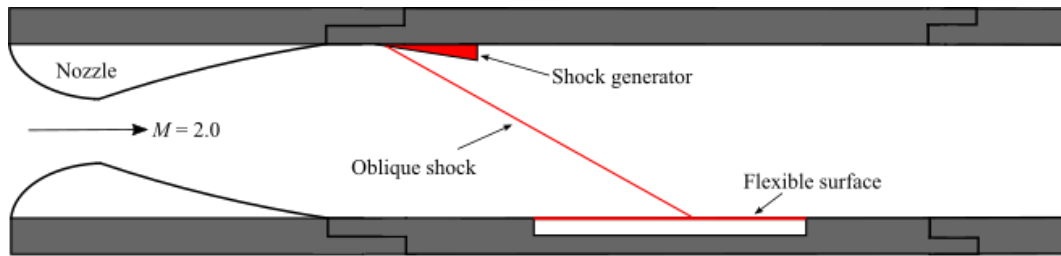


Figure 8.1 Schematic of wind tunnel test setup for oblique shock and boundary layer interaction over a flexible surface

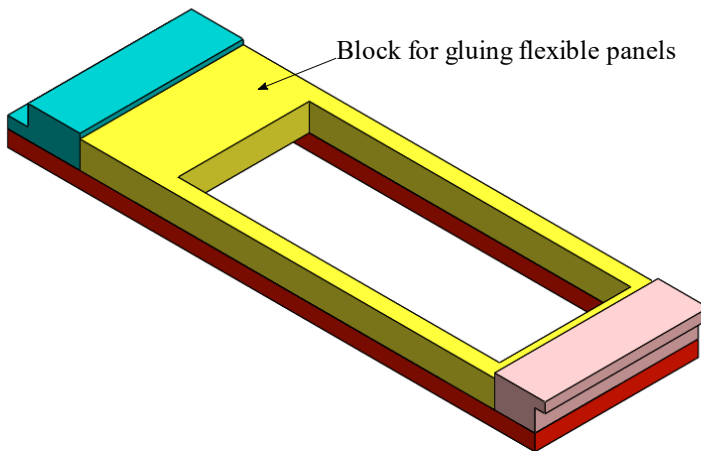


Figure 8.2 Support unit for flexible panels

Figure 8.1 presents the schematic of the wind tunnel test setup and Figure 8.2 demonstrates the design of the flexible panel support unit. The shock wave generator mounted on the top wall of the wind tunnel turns the flow 10°, and can be translated 30mm in the flow direction to adjust the shock wave impingement location. A 101.60mm (width) \times 258mm (length) stainless steel block (blue part in Figure 8.2) was machined to be inserted into the bottom wall of the test section. An 82mm \times 200mm hollow hole was fabricated on the block. Flexible panels with a dimension of 101.60mm (width) \times 258mm (length) can be glued on the top surface of the block. Two different clamping conditions need to be studied for comparison: (i) panel clamped on all sides (CCCC) and (ii) panel clamped on two sides (CCFF). It is worth mentioning that, there is a height adjustment unit on each side of the block along the flow direction to assure flexible panels with different thicknesses can be flush-mounted.

When the unsteady PSP system is fully built up, wind tunnel tests for SBLI over flexible surfaces need to be performed.

8.2.2 Enhancement of current BOS and PSP systems

Preliminary BOS wind tunnel tests showed that shock waves visualized by the present BOS system were a little thick and blur. The reason is the long exposure time ($33\mu\text{s}$) and the high unsteadiness of the shock waves due to wind tunnel vibration and its inherent unsteady flow feature. Extra light sources should be added to shorten the exposure time. Additionally, new fast cameras with better spatial resolution could be tested and the background pattern such as its dot diameter and filled ratio should be optimized further.

The square cross-sectional shock tube designed for the response time calibration of the unsteady PSP has been fabricated, which has two optical windows in the test section allowing acquiring the luminescence intensity emitted from the PSP sample mounted on the end wall of the shock tube. Next, the response time and dynamic properties of the in-house developed PC-PSP need to be validated. With this PSP dynamic calibration setup, the current paint formulation needs to be optimized further by varying its components and component ratio, and eventually used in wind tunnel tests.

8.2.3 Pressure loading and panel structure response measurements during supersonic staring jet impingement

In this dissertation, the behaviour of the initial shock wave from the supersonic staring jet during the impingement is studied. To investigate the mechanism of the shock/flexible surface interaction in more detail, the surface pressure loading and deformation will be monitored by pressure sensitive paint (PSP) and digital image correlation (DIC) techniques in the future.

Bibliography

- [1] S. Saeed and S. Salman, "Flutter Analysis of Hybrid Metal-Composite Low Aspect Ratio Trapezoidal Wings in Supersonic Flow," *Chinese Journal of Aeronautics*, vol. 30, no. 1, pp. 196-203, 2017.
- [2] M. HadžIabdić and K. Hanjalić, "Vortical Structures and Heat Transfer in a Round Impinging Jet," *Journal of Fluid Mechanics*, vol. 596, pp. 221-260, 2008.
- [3] J. L. Weightman, O. Amili, D. Honnery, J. Soria, and D. Edgington-Mitchell, "An Explanation for the Phase Lag in Supersonic Jet Impingement," *Journal of Fluid Mechanics*, vol. 815, p. R1, 2017.
- [4] A. Uzun, R. Kumar, M. Y. Hussaini, and F. S. Alvi, "Simulation of Tonal Noise Generation by Supersonic Impinging Jets," *AIAA Journal*, vol. 51, no. 7, pp. 1593-1611, 2013.
- [5] M. Akamine *et al.*, "Effect of Nozzle–Plate Distance on Acoustic Phenomena from Supersonic Impinging Jet," *AIAA Journal*, vol. 56, no. 5, pp. 1943-1952, 2018.
- [6] G. L. Brown and A. Roshko, "On Density Effects and Large Structure in Turbulent Mixing Layers," *Journal of Fluid Mechanics*, vol. 64, no. 4, pp. 775-816, 1974.
- [7] C. K. W. Tam and K. K. Ahuja, "Theoretical Model of Discrete Tone Generation by Impinging Jets," *Journal of Fluid Mechanics*, vol. 214, pp. 67-87, 1990.
- [8] B. Henderson and A. Powell, "Experiments Concerning Tones Produced by an Axisymmetric Choked Jet Impinging on Flat Plates," *Journal of Sound and Vibration*, vol. 168, no. 2, pp. 307-326, 1993.
- [9] B. Henderson, "The Connection between Sound Production and Jet Structure of the Supersonic Impinging Jet," *The Journal of the Acoustical Society of America*, vol. 111, no. 2, pp. 735-747, 2002.

- [10] B. Henderson, J. Bridges, and M. Wernet, "An Experimental Study of the Oscillatory Flow Structure of Tone-Producing Supersonic Impinging Jets," *Journal of Fluid Mechanics*, vol. 542, pp. 115-137, 2005.
- [11] G. Sinibaldi, L. Marino, and G. P. Romano, "Sound Source Mechanisms in under-Expanded Impinging Jets," *Experiments in Fluids*, vol. 56, no. 5, p. 105, 2015.
- [12] R. Gojon, C. Bogey, and O. Marsden, "Investigation of Tone Generation in Ideally Expanded Supersonic Planar Impinging Jets Using Large-Eddy Simulation," *Journal of Fluid Mechanics*, vol. 808, pp. 90-115, 2016.
- [13] C.-M. Ho and N. S. Nosseir, "Dynamics of an Impinging Jet. Part 1. The Feedback Phenomenon," *Journal of Fluid Mechanics*, vol. 105, pp. 119-142, 1981.
- [14] N. S. Nosseir and C.-M. Ho, "Dynamics of an Impinging Jet. Part 2. The Noise Generation," *Journal of fluid mechanics*, vol. 116, pp. 379-391, 1982.
- [15] T. Nonomura and K. Fujii, "Pod of Aeroacoustic Fields of a Jet Impinging on an Inclined Plate," in *16th AIAA/CEAS Aeroacoustics Conference*, 2010.
- [16] T. Nonomura and K. Fujii, "Computational Study of Effects of near-Wall Turbulent Structure on Aeroacoustic Waves from a Supersonic Jet Impinging on a Inclined Plate," in *17th AIAA/CEAS Aeroacoustics Conference* 2011.
- [17] S. Tsutsumi, T. Nonomura, K. Fujii, Y. Nakanishi, K. Okamoto, and S. Teramoto, "Analysis of Acoustic Wave from Supersonic Jets Impinging to an Inclined Flat Plate," in *7th International Conference on Computational Fluid Dynamics*, 2012.
- [18] S. Tsutsumi, R. Takaki, Y. Nakanishi, K. Okamoto, and S. Teramoto, "Numerical Study on Acoustic Radiation from a Supersonic Jet Impinging to an Inclined Plate," in *17th AIAA/CEAS aeroacoustics conference*, 2011.
- [19] C. Brehm *et al.*, "Computational Prediction of Pressure and Thermal Environments in the Flame Trench with Launch Vehicles," in *31st AIAA Applied Aerodynamics Conference*, 2013.
- [20] Y. Nakanishi, K. Okamoto, S. Teramoto, and T. Okunuki, "Acoustic Characteristics of Correctly-Expanded Supersonic Jet Impinging to an Inclined Plate," in *Asian Joint Conference on Propulsion and Power*, 2012.
- [21] M. Akamine, Y. Nakanishi, K. Okamoto, S. Teramoto, T. Okunuki, and S. Tsutsumi, "Experimental Study on Acoustic Phenomena of Supersonic Jet Impinging on Inclined Flat Plate," in *52nd Aerospace Sciences Meeting*, 2014.
- [22] T. Nonomura, Y. Goto, and K. Fujii, "Aeroacoustic Waves Generated from a Supersonic Jet Impinging on an Inclined Flat Plate," *International Journal of Aeroacoustics*, vol. 10, no. 4, pp. 401-425, 2011.
- [23] K. Eldred, "Acoustic Loads Generated by Propulsion System," *NASA-SP-8072*, 1971.
- [24] J. Haynes and R. Kenny, "Modifications to the Nasa Sp-8072 Distributed Source Method II for Ares I Lift-Off Environment Predictions," in *15th AIAA/CEAS Aeroacoustics Conference* 2009.

References

- [25] B. Skews, "Shock Wave Interaction with Porous Plates," *Experiments in Fluids*, vol. 39, no. 5, pp. 875-884, 2005.
- [26] R. Torrens, "On the Propagation of a Normal Shock Wave through a Layer of Incompressible Porous Material," *International Journal of Numerical Methods for Heat & Fluid Flow*, vol. 13, no. 2, pp. 178-198, 2003.
- [27] A. Levy, G. Ben-Dor, B. W. Skews, and S. Sorek, "Head-on Collision of Normal Shock Waves with Rigid Porous Materials," *Experiments in Fluids*, vol. 15, no. 3, pp. 183-190, 1993.
- [28] E. H. Dowell, "Panel Flutter - a Review of the Aeroelastic Stability of Plates and Shells," *AIAA Journal*, vol. 8, no. 3, pp. 385-399, 1970.
- [29] H. Babinsky, & Harvey, J., *Shock Wave-Boundary-Layer Interactions*, Cambridge: Cambridge University Press, 2011.
- [30] S. Spottswood, T. Eason, and T. Bebernick, "Influence of Shock-Boundary Layer Interactions on the Dynamic Response of a Flexible Panel," in *Proceedings of ISMA2012-USD2012*, 2012.
- [31] S. S. Davis and G. N. Malcolm, "Transonic Shock-Wave/Boundary-Layer Interactions on an Oscillating Airfoil," *AIAA Journal*, vol. 18, no. 11, pp. 1306-1312, 1980.
- [32] G. Schewe, H. Mai, and G. Dietz, "Nonlinear Effects in Transonic Flutter with Emphasis on Manifestations of Limit Cycle Oscillations," *Journal of Fluids and Structures*, vol. 1, no. 18, pp. 3-22, 2003.
- [33] D. E. Raveh and E. H. Dowell, "Frequency Lock-in Phenomenon for Oscillating Airfoils in Buffeting Flows," *Journal of Fluids and Structures*, vol. 27, no. 1, pp. 89-104, 2011.
- [34] D. E. Raveh and E. H. Dowell, "Aeroelastic Responses of Elastically Suspended Airfoil Systems in Transonic Buffeting Flows," *AIAA Journal*, vol. 52, no. 5, pp. 926-934, 2014.
- [35] A. Hartmann, M. Klaas, and W. Schröder, "Coupled Airfoil Heave/Pitch Oscillations at Buffet Flow," *AIAA Journal*, vol. 51, no. 7, pp. 1542-1552, 2013.
- [36] K. R. Brouwer, A. Gogulapati, and J. J. McNamara, "Interplay of Surface Deformation and Shock-Induced Separation in Shock/Boundary-Layer Interactions," *AIAA Journal*, vol. 55, no. 12, pp. 4258-4273, 2017.
- [37] H. T. Pham, Z. N. Gianikos, and V. Narayanaswamy, "Compression Ramp Induced Shock-Wave/Turbulent Boundary-Layer Interactions on a Compliant Material," *AIAA Journal*, vol. 56, no. 7, pp. 2925-2929, 2018.
- [38] S. S. Tan, P. J. Bruce, and M. Gramola, "Oblique Shockwave Boundary Layer Interaction on a Flexible Surface," in *AIAA Scitech 2019 Forum*, 2019.
- [39] M. Visbal, "Viscous and Inviscid Interactions of an Oblique Shock with a Flexible Panel," *Journal of Fluids and Structures*, vol. 48, pp. 27-45, 2014.
- [40] S. M. Spottswood *et al.*, "Exploring the Response of a Thin, Flexible Panel to Shock-Turbulent Boundary-Layer Interactions," *Journal of Sound and Vibration*, vol. 443, pp. 74-89, 2019.

- [41] E. R. Jinks, P. J. Bruce, and M. J. Santer, "Wind Tunnel Experiments with Flexible Plates in Transonic Flows," in *54th AIAA Aerospace Sciences Meeting*, 2016.
- [42] J. D. Anderson, *Fundamentals of Aerodynamics*, Boston: McGraw-Hill, 2004.
- [43] I. B. Zel'dovich, "Physics of Shock Waves and High-Temperature Hydrodynamic Phenomena," *Physics Today*, vol. 23, no. 2, p. 74, 1970.
- [44] R. Courant and K. O. Friedrichs, *Supersonic Flow and Shock Waves*, Beijing: World Books Publishing Corporation, 2006.
- [45] A. H. Shapiro, *The Dynamics and Thermodynamics of Compressible Fluid Flow*, Malabar, Fla.: R.E. Krieger, 1987.
- [46] B. Reinartz and M. Behr, "Computational Design Study of a 3d Hypersonic Intake for Scramjet Demonstrator Testing," in *High Performance Computing in Science and Engineering '10*, 2011.
- [47] H. Yan, F. Liu, J. Xu, and Y. Xue, "Study of Oblique Shock Wave Control by Surface Arc Discharge Plasma," *AIAA Journal*, vol. 56, no. 2, pp. 532-541, 2017.
- [48] J. M. Delery, "Shock Wave/Turbulent Boundary Layer Interaction and Its Control," *Progress in Aerospace Sciences*, vol. 22, no. 4, pp. 209-280, 1985.
- [49] T. Gan, Y. Wu, Z. Sun, D. Jin, H. Song, and M. Jia, "Shock Wave Boundary Layer Interaction Controlled by Surface Arc Plasma Actuators," *Physics of Fluids*, vol. 30, no. 5, p. 055107, 2018.
- [50] P. J. K. Bruce and S. P. Colliss, "Review of Research into Shock Control Bumps," *Shock Waves*, vol. 25, no. 5, pp. 451-471, 2015.
- [51] N. Titchener and H. Babinsky, "Shock Wave/Boundary-Layer Interaction Control Using a Combination of Vortex Generators and Bleed," *AIAA Journal*, vol. 51, no. 5, pp. 1221-1233, 2013.
- [52] W. Bo, L. Weidong, Z. Yuxin, F. Xiaoqiang, and W. Chao, "Experimental Investigation of the Micro-Ramp Based Shock Wave and Turbulent Boundary Layer Interaction Control," *Physics of Fluids*, vol. 24, no. 5, p. 055110, 2012.
- [53] R. C. Mehta, "Numerical Simulation of Base Pressure and Drag of Space Reentry Capsules at High Speed," *Hypersonic Vehicles*, 2019.
- [54] P. R. Garabedian and H. M. Lieberstein, *Examples of Detached Bow Shock Waves in Hypersonic Flow*, New York: Institute of the Aeronautical Sciences, 1958.
- [55] P. V. Marrone, *Inviscid, Nonequilibrium Flow Behind Bow and Normal Shock Waves*, Buffalo: Cornell Aeronautical Laboratory, 1964.
- [56] G. Ben-Dor, *Shock Wave Reflection Phenomena*, Berlin; Heidelberg: Springer, 2007.
- [57] M. K. Quinn, "Shock Diffraction Phenomena and Their Measurement," PhD thesis, University of Manchester, 2013.
- [58] H. Reichenbach, "Contributions of Ernst Mach to Fluid Mechanics," *Annual Review of Fluid Mechanics*, vol. 15, no. 1, pp. 1-29, 1983.

References

- [59] P. Krehl and M. van der Geest, "The Discovery of the Mach Reflection Effect and Its Demonstration in an Auditorium," *Shock Waves*, vol. 1, no. 1, pp. 3-15, 1991.
- [60] B. W. Skews, "The Perturbed Region Behind a Diffracting Shock Wave," *Journal of Fluid Mechanics*, vol. 29, no. 4, pp. 705-719, 1967.
- [61] M. Sun and K. Takayama, "A Note on Numerical Simulation of Vortical Structures in Shock Diffraction," *Shock Waves*, vol. 13, no. 1, pp. 25-32, 2003.
- [62] M. Sun and K. Takayama, "The Formation of a Secondary Shock Wave Behind a Shock Wave Diffracting at a Convex Corner," *Shock Waves*, vol. 7, no. 5, pp. 287-295, 1997.
- [63] H. Li, G. Ben-Dor, and Z. Y. Han, "Analytical Prediction of the Reflected-Diffracted Shock Wave Shape in the Interaction of a Regular Reflection with an Expansive Corner," *Fluid Dynamics Research*, vol. 14, no. 5, pp. 229-239, 1994.
- [64] J. O. Reeves and B. W. Skews, "Unsteady Three-Dimensional Compressible Vortex Flows Generated During Shock Wave Diffraction," *Shock Waves*, vol. 22, no. 2, pp. 161-172, 2012.
- [65] F. Gnani, K. H. Lo, H. Zare-Behtash, and K. Kontis, "Experimental Investigation on Shock Wave Diffraction over Sharp and Curved Splitters," *Acta Astronautica*, vol. 99, pp. 143-152, 2014.
- [66] N. A. Eliasson, *Shock Focusing Phenomena: High Energy Density Phenomena and Dynamics of Converging Shocks*: Springer, 2018.
- [67] H. Zare-Behtash, K. Kontis, N. Gongora-Orozco, and K. Takayama, "Compressible Vortex Loops: Effect of Nozzle Geometry," *International Journal of Heat and Fluid Flow*, vol. 30, no. 3, pp. 561-576, 2009.
- [68] K. Khasanov, "Visualization of Super-Compressibility in Supersonic Spiral-Twisted Jets," *Physics Letters, Section A: General, Atomic and Solid State Physics*, vol. 376, no. 5, pp. 748-752, 2012.
- [69] H. Zare-Behtash, N. Gongora-Orozco, and K. Kontis, "Effect of Primary Jet Geometry on Ejector Performance: A Cold-Flow Investigation," *International Journal of Heat and Fluid Flow*, vol. 32, no. 3, pp. 596-607, 2011.
- [70] H. Zhang, Z. Chen, X. Jiang, and H. Li, "Investigations on the Exterior Flow Field and the Efficiency of the Muzzle Brake," *Journal of Mechanical Science and Technology*, vol. 27, no. 1, pp. 95-101, 2013.
- [71] H. H. Zhang, Z. H. Chen, X. H. Sun, X. H. Jiang, and B. M. Li, "Numerical Investigations on the Thrust Augmentation Mechanisms of Ejectors Driven by Pulse Detonation Engines," *Combustion Science and Technology*, vol. 183, no. 10, pp. 1069-1082, 2011.
- [72] F. F. Grinstein, "Vortex Dynamics and Entrainment in Rectangular Free Jets," *Journal of Fluid Mechanics*, vol. 437, pp. 69-101, 2001.
- [73] B. Imine, O. Imine, M. Abidat, and A. Liazid, "Study of Non-Reactive Isothermal Turbulent Asymmetric Jet with Variable Density," *Computational Mechanics*, vol. 38, no. 2, pp. 151-162, 2006.

- [74] W. R. Quinn, "Streamwise Evolution of a Square Jet Cross Section," *AIAA Journal*, vol. 30, no. 12, pp. 2852-2857, 1992.
- [75] E. J. Gutmark and F. F. Grinstein, "Flow Control with Noncircular Jets," *Annual Review of Fluid Mechanics*, vol. 31, pp. 239-272, 1999.
- [76] X. K. Wang, S. C. M. Yu, and L. P. Chua, "Effect of Delta Tabs on Axis Switching of a Coaxial Square Jet," *Journal of Propulsion and Power*, vol. 20, no. 3, pp. 533-541, 2004.
- [77] H. Zare-Behtash, N. Gongora-Orozco, and K. Kontis, "Global Visualization and Quantification of Compressible Vortex Loops," *Journal of Visualization*, vol. 12, no. 3, pp. 233-240, 2009.
- [78] N. Chen and H. Yu, "Mechanism of Axis Switching in Low Aspect-Ratio Rectangular Jets," *Computers and Mathematics with Applications*, vol. 67, no. 2, pp. 437-444, 2014.
- [79] H. Zare-Behtash, K. Kontis, and N. Gongora-Orozco, "Experimental Investigations of Compressible Vortex Loops," *Physics of Fluids*, vol. 20, no. 12, p. 126105, 2008.
- [80] H. Zhang, Z. Chen, X. Jiang, and Z. Guo, "The Initial Flow Characteristics of Supersonic Jets with Different Geometries," *Physics Letters, Section A: General, Atomic and Solid State Physics*, vol. 379, no. 18-19, pp. 1256-1262, 2015.
- [81] K. Bremhorst and P. G. Hollis, "Velocity Field of an Axisymmetric Pulsed, Subsonic Air Jet," *AIAA Journal*, vol. 28, no. 12, pp. 2043-2049, 1990.
- [82] A. Glezer and M. Amitay, "Synthetic Jets," *Annual Review of Fluid Mechanics*, vol. 34, no. 1, pp. 503-529, 2002.
- [83] J. J. Peña Fernández and J. Sesterhenn, "Compressible Starting Jet: Pinch-Off and Vortex Ringtrailing Jet Interaction," *Journal of Fluid Mechanics*, vol. 817, pp. 560-589, 2017.
- [84] G. I. Taylor, "The Formation of a Blast Wave by a Very Intense Explosion I. Theoretical Discussion," *Mathematical and Physical Sciences*, vol. 201, no. 1065, pp. 159-174, 1950.
- [85] N. Didden, "On the Formation of Vortex Rings: Rolling-up and Production of Circulation," *Zeitschrift für angewandte Mathematik und Physik ZAMP*, vol. 30, no. 1, pp. 101-116, 1979.
- [86] W. Zhao, S. H. Frankel, and L. G. Mongeau, "Effects of Trailing Jet Instability on Vortex Ring Formation," *Physics of Fluids*, vol. 12, no. 3, pp. 589-596, 2000.
- [87] S. Heimbs, J. Ritzer, and J. Markmiller, "A Numerical Method for Blast Shock Wave Analysis of Missile Launch from Aircraft," *International Journal of Aerospace Engineering*, vol. 2015, pp. 1-8, 2015.
- [88] N.-S. Liu, "On the Comprehensive Modeling and Simulation of Combustion Systems," in *39th Aerospace Sciences Meeting and Exhibit*, 2001.
- [89] G. Kidd and M. Cloke, "Computational Modelling of Transient Blast Wave Effects," in *AIAA Paper*, 2004.
- [90] B. S. Lee, J. H. Choi, and O. J. Kwon, "Numerical Simulation of Free-Flight Rockets Air-Launched from a Helicopter," *Journal of Aircraft*, vol. 48, no. 5, pp. 1766-1775, 2011.

References

- [91] M. Gusman, J. Housman, and C. Kiris, "Best Practices for CFD Simulations of Launch Vehicle Ascent with Plumes - Overflow Perspective," *49th AIAA Aerospace Sciences Meeting including the New Horizons Forum and Aerospace Exposition*, 2011.
- [92] A. A. Alexeenko *et al.*, "Modeling of Flow and Radiation in the ATLAS Plume," *Journal of Thermophysics and Heat Transfer*, vol. 16, no. 1, pp. 50-57, 2002.
- [93] H. B. Ebrahimi, J. Levine, and A. Kawasaki, "Numerical Investigation of Twin-Nozzle Rocket Plume Phenomenology," *Journal of Propulsion and Power*, vol. 16, no. 2, pp. 178-186, 2000.
- [94] E. I. Vitkin, V. G. Karelkin, A. A. Kirillov, A. S. Suprun, and J. V. Khadyka, "A Physico-Mathematical Model of Rocket Exhaust Plumes," *International Journal of Heat and Mass Transfer*, vol. 40, no. 5, pp. 1227-1241, 1997.
- [95] Y. Wang, H. Wang, C. Cui, and B. Zhao, "Prediction Method of Blast Wave Impact on Crew Module for Liquid Rocket Explosion on Launch Pad," *Applied Sciences*, vol. 9, no. 19, 2019.
- [96] D. Vaughan, *The Challenger Launch Decision : Risky Technology, Culture, and Deviance at Nasa*: The University of Chicago Press, 2016.
- [97] R. F. Fletcher, "Characteristics of Liquid Propellant Explosions," *Annals of the New York Academy of Sciences*, vol. 152, no. 1, pp. 432-440, 1968.
- [98] C. Livermore Software Technology, *LS-DYNA Keyword User's Manual : Version 970*, Livermore, Calif: Livermore Software Technology Corp., 2003.
- [99] B. Liu, X. Wang, and H. Song, "Numerical Simulation of Explosion Shock Wave in Air with Liquid Propellant. Spacecr," *Environ. Eng*, vol. 29, pp. 129-133, 2012.
- [100] K. Sun, J. Chen, J. Zhao, and X. LUAN, "Hazard Analysis on Explosion of Cryogenic Liquid Rocket on Launch Pad," *Computer Simulation*, vol. 3, pp. 109-113, 2013.
- [101] J. Chen, S. Han, K. Sun, and X. LUAN, "Fortification Distance for Prevention of Liquid Rocket Explosion," *Fire Safety Science*, vol. 3, pp. 131-136, 2012.
- [102] J. Massoni, L. Biamino, G. Jourdan, O. Igna, and L. Houas, "Experimental and Numerical Investigation of Blast Wave Interaction with a Three Level Building," *Journal of Fluids Engineering*, vol. 139, no. 11, 2017.
- [103] R. Takemura, H. Fukuoka, S. Enoki, S. Nakamura, and K. Hiro, "Observation of Supersonic Jet Using Small Volume High-Pressure Shock Tube," in *Materials Science Forum*, 2018.
- [104] M. A. Louar *et al.*, "Explosive Driven Shock Tube Loading of Aluminium Plates: Experimental Study," *International Journal of Impact Engineering*, vol. 86, pp. 111-123, 2015.
- [105] S. R. Nagaraja, J. K. Prasad, and G. Jagadeesh, "Theoretical-Experimental Study of Shock Wave-Assisted Metal Forming Process Using a Diaphragmless Shock Tube," *Journal of Aerospace Engineering*, vol. 226, no. 12, pp. 1534-1543, 2012.
- [106] P. Kumar, J. LeBlanc, D. S. Stargel, and A. Shukla, "Effect of Plate Curvature on Blast Response of Aluminum Panels," *International Journal of Impact Engineering*, vol. 46, pp. 74-85, 2012.

- [107] G. Jagadeesh, "Industrial Applications of Shock Waves," *Journal of Aerospace Engineering*, vol. 222, no. 5, pp. 575-583, 2008.
- [108] D. M. Mitchell, D. R. Honnery, and J. Soria, "The Visualization of the Acoustic Feedback Loop in Impinging Underexpanded Supersonic Jet Flows Using Ultra-High Frame Rate Schlieren," *Journal of Visualization*, vol. 15, no. 4, pp. 333-341, 2012.
- [109] L. F. Henderson, "Experiments on the Impingement of a Supersonic Jet on a Flat Plate," *Zeitschrift für angewandte Mathematik und Physik ZAMP*, vol. 17, no. 5, pp. 553-569, 1966.
- [110] K. Kontis, R. An, H. Zare-Behtash, and D. Kounadis, "Head-on Collision of Shock Wave Induced Vortices with Solid and Perforated Walls," *Physics of Fluids*, vol. 20, no. 1, p. 016104, 2008.
- [111] D. V. Gaitonde, "Progress in Shock Wave/Boundary Layer Interactions," *Progress in Aerospace Sciences*, vol. 72, pp. 80-99, 2015.
- [112] J. E. Green, "Interactions between Shock Waves and Turbulent Boundary Layers," *Progress in Aerospace Sciences*, vol. 11, no. C, pp. 235-260, 1970.
- [113] J. D. Schmisser and P. Erbland, "Introduction: Assessment of Aerothermodynamic Flight Prediction Tools through Ground and Flight Experimentation," *Progress in Aerospace Sciences*, vol. 48-49, pp. 2-7, 2012.
- [114] C. Coe and W. Chyu, "Pressure-Fluctuation Inputs and Response of Panels Underlying Attached and Separated Supersonic Turbulent Boundary Layers," *NASA-TM-X-62189*, 1972.
- [115] L. Maestrello and T. L. J. Linden, "Measurements of the Response of a Panel Excited by Shock Boundary-Layer Interaction," *Journal of Sound and Vibration*, vol. 16, no. 3, pp. 385-388, 1971.
- [116] S. Willems, A. Gulhan, and B. Esser, "Shock Induced Fluid-Structure Interaction on a Flexible Wall in Supersonic Turbulent Flow," *Progress in Flight Physics*, vol. 5, pp. 285-308, 2013.
- [117] D. Daub, S. Willems, and A. Gülgan, "Experimental Results on Shock-Wave/Boundary-Layer Interaction Induced by a Movable Wedge," in *8th European Symposium on Aerothermodynamics*, 2015.
- [118] D. Daub, S. Willems, and A. Gülgan, "Experimental Results on Unsteady Shock-Wave/Boundary-Layer Interaction Induced by an Impinging Shock," *CEAS Space Journal*, vol. 8, no. 1, pp. 3-12, 2016.
- [119] M. Gruber and A. Nejad, "Development of a Large-Scale Supersonic Combustion Research Facility," in *32nd Aerospace Sciences Meeting and Exhibit*, 1994.
- [120] V. V. Vedeneev, "Panel Flutter at Low Supersonic Speeds," *Journal of Fluids and Structures*, vol. 29, pp. 79-96, 2012.
- [121] L.-Q. Ye and Z.-Y. Ye, "Effects of Shock Location on Aeroelastic Stability of Flexible Panel," *AIAA Journal*, vol. 56, no. 9, pp. 3732-3744, 2018.
- [122] V. Pasquariello, "Analysis and Control of Shock-Wave /Turbulent Boundary-Layer Interactions on Rigid and Flexible Walls," PhD thesis, Technische Universität München, 2018.

References

- [123] C. Mei, K. Abdel-Motagaly, and R. Chen, "Review of Nonlinear Panel Flutter at Supersonic and Hypersonic Speeds," *Applied Mechanics Reviews*, vol. 52, no. 10, pp. 321-332, 1999.
- [124] E. E. Kordes, W. J. Tuovila, and L. D. Guy, "Flutter Research on Skin Panels," *NASA-TN-D-451*, 1960.
- [125] E. H. Dowell, *Aeroelasticity of Plates and Shells*, Leyden: Noordhoff International, 1975.
- [126] E. H. Dowell and H. M. Voss, "Theoretical and Experimental Panel Flutter Studies in the Mach Number Range 1.0 to 5.0," *AIAA Journal*, vol. 3, no. 12, pp. 2292-2304, 1965.
- [127] H. Kappus, C. Lemley, and N. Zimmerman, "An Experimental Investigation of High Amplitude Panel Flutter," *NASA CR-1837*, 1971.
- [128] V. V. Vedeneev, S. V. Guvernyuk, A. F. Zubkov, and M. E. Kolotnikov, "Experimental Investigation of Single-Mode Panel Flutter in Supersonic Gas Flow," *Fluid Dynamics*, vol. 45, no. 2, pp. 312-324, 2010.
- [129] A. Shishaeva, V. Vedeneev, and A. Aksenov, "Nonlinear Single-Mode and Multi-Mode Panel Flutter Oscillations at Low Supersonic Speeds," *Journal of Fluids and Structures*, vol. 56, pp. 205-223, 2015.
- [130] A. D'Aguanno, L. C. J. M. M. , F. F. J. S. , and B. W. v. O. , "Experimental Investigation of Supersonic Panel Flutter," in *International Conference on Flight Vehicles, Aerothermodynamics and Re-entry Missions&Engineering*, 2019.
- [131] R. W. Gordon and J. J. Hollkamp, "Reduced-Order Models for Acoustic Response Prediction of a Curved Panel," in *52nd AIAA/ASME/ASCE/AHS/ASC Structures, Structural Dynamics and Materials Conference*, 2011.
- [132] S. M. Spottswood and M. P. Mignolet, "Experimental Nonlinear Response of Tapered Ceramic Matrix Composite Plates to Base Excitation," *AIAA Journal*, vol. 40, no. 8, pp. 1682-1687, 2002.
- [133] M. Morton, "Certification of the F-22 Advanced Tactical Fighter for High Cycle and Sonic Fatigue," in *48th AIAA/ASME/ASCE/AHS/ASC Structures, Structural Dynamics, and Materials Conference*, 2007.
- [134] S. L. Liguore and T. H. Beier, "Recognition and Correction of Sonic Fatigue Damage in Fighter Aircraft," in *RTO AVT Specialists' Meeting on Life Management Techniques for Ageing Air Vehicles*, 2001.
- [135] M. P. Mignolet, A. Przekop, S. A. Rizzi, and S. M. Spottswood, "A Review of Indirect/Non-Intrusive Reduced Order Modeling of Nonlinear Geometric Structures," *Journal of Sound and Vibration*, vol. 332, no. 10, pp. 2437-2460, 2013.
- [136] E. A. Thornton, "Thermal Structures - Four Decades of Progress," *Journal of Aircraft*, vol. 29, no. 3, pp. 485-498, 1992.
- [137] N. T. Clemens and V. Narayanaswamy, "Low-Frequency Unsteadiness of Shock Wave/Turbulent Boundary Layer Interactions," *Annual Review of Fluid Mechanics*, vol. 46, pp. 469-492, 2014.

- [138] D. S. Dolling, "Fifty Years of Shock-Wave/Boundary-Layer Interaction Research: What Next?," *AIAA Journal*, vol. 39, no. 8, pp. 1517-1531, 2001.
- [139] P. Pozefsky, "Identifying Sonic Fatigue Prone Structures on a Hypersonic Transatmospheric Vehicle (TAV)," in *12th Aeroacoustic Conference*, 1989.
- [140] R. D. Blevins, I. Holehouse, and K. R. Wentz, "Thermoacoustic Loads and Fatigue of Hypersonic Vehicle Skin Panels," *Journal of Aircraft*, vol. 30, no. 6, pp. 971-978, 1993.
- [141] D. A. Kontinos and G. Palmer, "Numerical Simulation of Metallic Thermal Protection System Panel Bowing," *Journal of Spacecraft and Rockets*, vol. 36, no. 6, pp. 842-849, 1999.
- [142] C. E. Glass and L. R. Hunt, "Aero thermal Tests of Spherical Dome Protuberances on a Flat Plate at a Mach Number of 6.5," *NASA-TP-2631*, 1986.
- [143] C. E. Glass and L. R. Hunt, "Aero thermal Tests of Quilted Dome Models on a Flat Plate at a Mach Number of 6.5," *NASA-TP-2804*, 1988.
- [144] A. J. Culler and J. J. McNamara, "Impact of Fluid-Thermal-Structural Coupling on Response Prediction of Hypersonic Skin Panels," *AIAA Journal*, vol. 49, no. 11, pp. 2393-2406, 2011.
- [145] S. Ramsey, *Nasa Begins Work to Build a Quieter Supersonic Passenger Jet*. <https://www.nasa.gov/press-release/nasa-begins-work-to-build-a-quieter-supersonic-passenger-jet>. 2016,
- [146] B. T. Inc, *Boom - Supersonic Passenger Airplanes*. <https://boomsupersonic.com/>. 2018,
- [147] A. Supersonic, *Aerion Supersonic - Creating a Faster Future*. <https://www.aerionsupersonic.com/>. 2018,
- [148] M. Colombo, M. di Prisco, and P. Martinelli, "A New Shock Tube Facility for Tunnel Safety," *Experimental Mechanics*, vol. 51, no. 7, pp. 1143-1154, 2010.
- [149] R. Mariani, "Compressible Vortex Rings and Their Interaction with Stationary Surfaces," PhD thesis, University of Manchester, 2012.
- [150] O. Igra, F. Seiler, and H. Grönig, *Experimental Methods of Shock Wave Research*, Cham: Springer, 2016.
- [151] H. Zare-Betash, "Experimental Studies on Compressible Vortical Flows, Phenomena and Interactions," PhD thesis, University of Manchester, 2009.
- [152] R. Brun, "Shock Tubes and Shock Tunnels: Design and Experiments," *Aix-Marseille Univ (France)*, 2009.
- [153] B. Schmidt, "GALCIT 6-Inch Shock Tube," *Technical report*, 2013.
- [154] Y.-L. Ning and Y.-G. Zhou, "Shock Tubes and Blast Injury Modeling," *Chinese Journal of Traumatology*, vol. 18, no. 4, pp. 187-193, 2015.
- [155] D. V. Reneer, R. D. Hisel, J. M. Hoffman, R. J. Kryscio, B. T. Lusk, and J. W. Geddes, "A Multi-Mode Shock Tube for Investigation of Blast-Induced Traumatic Brain Injury," *J Neurotrauma*, vol. 28, no. 1, pp. 95-104, 2011.

References

- [156] A. S. Shah Ms, B. D. Stemper Phd, and F. A. Pintar Phd, "Development and Characterization of an Open-Ended Shock Tube for the Study of Blast Mtbi," *Biomed Sci Instrum*, vol. 48, pp. 393-400, 2012.
- [157] I. Obed Samuelraj and G. Jagadeesh, "Shock Tubes: A Tool to Create Explosions without Using Explosives," in *Blast Mitigation Strategies in Marine Composite and Sandwich Structures*, Singapore: Springer, 2018.
- [158] M. S. Downey, T. J. Cloete, and A. D. B. Yates, "A Rapid Opening Sleeve Valve for a Diaphragmless Shock Tube," *Shock Waves*, vol. 21, no. 4, pp. 315-319, 2011.
- [159] D. C. Taylor, "The Characterization and Feasibility of a Low-Duty-Cycle Diaphragmless Shock Tube," Master thesis, Texas A & M University, 2012.
- [160] S. Janardhanraj and G. Jagadeesh, "Development of a Novel Miniature Detonation-Driven Shock Tube Assembly That Uses in Situ Generated Oxyhydrogen Mixture," *Rev Sci Instrum*, vol. 87, no. 8, p. 085114, 2016.
- [161] Y. Kai, W. Garen, T. Schlegel, and U. Teubner, "A Novel Shock Tube with a Laser–Plasma Driver ", *Laser and Particle Beams*, vol. 35, no. 04, pp. 610-618, 2017.
- [162] G. Li, T. Ukai, and K. Kontis, "Characterization of a Novel Open-Ended Shock Tube Facility Based on Detonation Transmission Tubing," *Aerospace Science and Technology*, vol. 94, p. 105388, 2019.
- [163] C. Lewis Research, F. Aeropropulsion, and D. Experiments, *The 10 X 10 Supersonic Wind Tunnel*, Cleveland, Ohio: National Aeronautics and Space Administration, Lewis Research Center, Aeropropulsion Facilities & Experiments Division, 1991.
- [164] F. Gnani, H. Zare-Behtash, and K. Kontis, "Indraft Supersonic Wind Tunnel for Shock Train Investigations," in *30th International Symposium on Shock Waves*, 2017.
- [165] F. Gnani, "Investigation on Supersonic High-Speed Internal Flows and the Tools to Study Their Interactions," PhD thesis, University of Glasgow, 2018.
- [166] A. Hirschberg, "Schlieren and Shadowgraph Techniques: Visualizing Phenomena in Transparent Media," *European Journal of Mechanics Series B Fluids*, vol. 21, no. 4, p. 493, 2002.
- [167] G. S. Settles and M. J. Hargather, "A Review of Recent Developments in Schlieren and Shadowgraph Techniques," *Measurement Science and Technology*, vol. 28, no. 4, 2017.
- [168] J.-M. Desse and R. Deron, "Shadow, Schlieren and Color Interferometry," *Aerospace Lab.*, vol. 1, 2009.
- [169] M. Raffel, "Background-Oriented Schlieren (BOS) Techniques," *Experiments in Fluids*, vol. 56, no. 3, p. 60, 2015.
- [170] J. Kompenhans, Raffel, M., Wereley, S. T., & Willert, C. E. , *Particle Image Velocimetry : A Practical Guide*, Berlin: Springer, 2007.

- [171] C. Reinholtz, F. Heltsley, K. Scott, and M. Rhode, "Visualization of Jettison Motor Plumes from an Orion Launch Abort Vehicle Wind Tunnel Model Using Background-Oriented Schlieren," in *U.S. Air Force T&E Days 2010*.
- [172] B. F. Bathel, S. E. Borg, E. Walker, and T. Mizukaki, "Development of Background-Oriented Schlieren for Nasa Langley Research Center Ground Test Facilities (Invited)," in *53rd AIAA Aerospace Sciences Meeting*, 2015.
- [173] F. Nicolas *et al.*, "Experimental Study of a Counter-Flow Jet in Onera's S1MA Wind Tunnel by 3D Background Oriented Schlieren," in *18th International Symposium on Flow Visualization (ISFV18)*, 2018.
- [174] N. T. Smith, J. T. Heineck, and E. T. Schairer, "Optical Flow for Flight and Wind Tunnel Background Oriented Schlieren Imaging," in *55th AIAA Aerospace Sciences Meeting*, 2017.
- [175] F. Nicolas *et al.*, "Experimental Study of a Co-Flowing Jet in ONERA's F2 Research Wind Tunnel by 3d Background Oriented Schlieren," *Measurement Science and Technology*, vol. 28, no. 8, 2017.
- [176] T. Mizukaki *et al.*, "Background-Oriented Schlieren for Large-Scale and High-Speed Aerodynamic Phenomena (Invited)," in *53rd AIAA Aerospace Sciences Meeting*, 2015.
- [177] M. Ota, K. Kurihara, H. Arimoto, K. Shida, and T. Inage, "Background Oriented Schlieren (BOS) Measurement in Supersonic Flow with 4K High-Speed Camera," in *31st International Congress on High-Speed Imaging and Photonics*, 2017.
- [178] B. F. Bathel, J. Weisberger, and S. B. Jones, "Development of Tomographic Background-Oriented Schlieren Capability at NASA Langley Research Center," in *AIAA Aviation 2019 Forum*, 2019.
- [179] F. Leopold, M. Ota, D. Klatt, and K. Maeno, "Reconstruction of the Unsteady Supersonic Flow around a Spike Using the Colored Background Oriented Schlieren Technique," *Journal of Flow Control, Measurement & Visualization*, vol. 01, no. 02, pp. 69-76, 2013.
- [180] A. Bauknecht, B. Ewers, C. Wolf, F. Leopold, J. Yin, and M. Raffel, "Three-Dimensional Reconstruction of Helicopter Blade-Tip Vortices Using a Multi-Camera BOS System," *Experiments in Fluids*, vol. 56, no. 1, 2014.
- [181] M. A. Hill and E. A. Haering, "Ground-to-Air Flow Visualization Using Solar Calcium-K Line Background-Oriented Schlieren," *Experiments in Fluids*, vol. 58, no. 1, 2016.
- [182] J. T. Heineck, D. Banks, E. T. Schairer, E. A. Haering, and P. Bean, "Background Oriented Schlieren (BOS) of a Supersonic Aircraft in Flight," in *AIAA Flight Testing Conference*, 2016.
- [183] O. K. Sommersel, D. Bjerketvedt, S. O. Christensen, O. Krest, and K. Vaagsaether, "Application of Background Oriented Schlieren for Quantitative Measurements of Shock Waves from Explosions," *Shock Waves*, vol. 18, no. 4, pp. 291-297, 2008.
- [184] M. J. Hargather, "Background-Oriented Schlieren Diagnostics for Large-Scale Explosive Testing," *Shock Waves*, vol. 23, no. 5, pp. 529-536, 2013.

References

- [185] T. Mizukaki, K. Wakabayashi, T. Matsumura, and K. Nakayama, "Background-Oriented Schlieren with Natural Background for Quantitative Visualization of Open-Air Explosions," *Shock Waves*, vol. 24, no. 1, pp. 69-78, 2014.
- [186] M. Raffel, J. T. Heineck, E. Schairer, F. Leopold, and K. Kindler, "Background-Oriented Schlieren Imaging for Full-Scale and in-Flight Testing," *Journal of the American Helicopter Society*, vol. 59, no. 1, pp. 1-9, 2014.
- [187] J. Kavandi *et al.*, "Luminescent Barometry in Wind Tunnels," *Review of Scientific Instruments Review of Scientific Instruments*, vol. 61, no. 11, pp. 3340-3347, 1990.
- [188] T. Liu, *Pressure and Temperature Sensitive Paints*: Springer, 2010.
- [189] J. Panda, "Verification of Calculation Procedure for Unsteady Aerodynamic Forces on a Launch Vehicle," *Journal of Spacecraft and Rockets*, vol. 56, no. 6, pp. 1-11, 2019.
- [190] J. Panda, T. J. Garbeff, N. J. Burnside, and J. C. Ross, "Unsteady Pressure Fluctuations Measured on a Hammerhead Space Vehicle and Comparison with Coe and Nute's 1962 Data," *International Journal of Aeroacoustics*, vol. 17, no. 1-2, pp. 70-87, 2018.
- [191] J. W. Crafton, J. W. Gregory, M. E. Sellers, and W. Ruyten, "Data Processing Tools for Dynamic Pressure-Sensitive Paint," in *55th AIAA Aerospace Sciences Meeting*, 2017.
- [192] O. D. Wong *et al.*, "Blade Tip Pressure Measurements Using Pressure-Sensitive Paint," *Journal of the American Helicopter Society*, 2018.
- [193] J. W. Gregory, K. Asai, M. Kameda, T. Liu, and J. P. Sullivan, "A Review of Pressure-Sensitive Paint for High-Speed and Unsteady Aerodynamics," *Proceedings of the Institution of Mechanical Engineers, Part G: Journal of Aerospace Engineering*, vol. 222, no. 2, pp. 249-290, 2008.
- [194] A. Pandey, M. L. Sutkowy, M. McCrink, and J. W. Gregory, "Aerodynamic Characterization of a Quad-Rotor Helicopter," in *2018 AIAA Aerospace Sciences Meeting*, 2018.
- [195] S. Fang, S. R. Long, K. J. Disotell, J. W. Gregory, F. C. Semmelmayer, and R. W. Guyton, "Comparison of Unsteady Pressure-Sensitive Paint Measurement Techniques," *AIAA Journal*, vol. 50, no. 1, pp. 109-122, 2012.
- [196] D. A. Roberts, N. P. Stokes, M. K. Quinn, J. Coppin, and T. J. Birch, "Evaluation of Dynamic Pressure-Sensitive Paint for Improved Analysis of Cavity Flows and CFD Validation," in *54th AIAA Aerospace Sciences Meeting*, 2016.
- [197] J. Panda, "Experimental Verification of Buffet Calculation Procedure Using Unsteady Pressure-Sensitive Paint," *Journal of Aircraft*, vol. 54, no. 5, pp. 1791-1801, 2017.
- [198] J. W. Gregory, H. Sakaue, T. Liu, and J. P. Sullivan, "Fast Pressure-Sensitive Paint for Flow and Acoustic Diagnostics," *Annual Review of Fluid Mechanics*, vol. 46, no. 1, pp. 303-330, 2014.
- [199] A. N. Watkins, B. D. Leighty, W. E. Lipford, K. Z. Goodman, J. Crafton, and J. W. Gregory, "Measuring Surface Pressures on Rotor Blades Using Pressure-Sensitive Paint," *AIAA Journal*, vol. 54, no. 1, pp. 206-215, 2016.

- [200] J. W. Gregory, "Resolving Vortex-Induced Pressure Fluctuations on a Cylinder in Rotor Wake Using Fast-Responding Pressure-Sensitive Paint," *Physics of Fluids*, vol. 31, no. 5, 2019.
- [201] M.-C. Merienne, V. Brion, and J.-C. Abart, "Unsteady PSP Measurements of the Shock Dynamics on a Transonic Laminar Airfoil," in *AIAA Scitech 2019 Forum*, 2019.
- [202] D. Peng, L. Jiao, and Y. Liu, "Development of a Grid PSP/TSP System for Unsteady Measurements on Rotating Surfaces," in *32nd AIAA Aerodynamic Measurement Technology and Ground Testing Conference*, 2016.
- [203] L. Yang, H. Zare-Behtash, E. Erdem, and K. Kontis, "Investigation of the Double Ramp in Hypersonic Flow Using Luminescent Measurement Systems," *Experimental Thermal and Fluid Science*, vol. 40, pp. 50-56, 2012.
- [204] L. Yang, H. Zare-Behtash, E. Erdem, and K. Kontis, "Application of AA-PSP to Hypersonic Flows: The Double Ramp Model," *Sensors and Actuators B: Chemical*, vol. 161, no. 1, pp. 100-107, 2012.
- [205] K. Nakakita, Y. Takama, K. Imagawa, and H. Kato, "Unsteady PSP Measurement of Transonic Unsteady Flow Field around a Rocket Fairing Model," in *28th Aerodynamic Measurement Technology, Ground Testing, and Flight Testing Conference*, 2012.
- [206] S. Fujii, D. Numata, H. Nagai, and K. Asai, "Development of Ultrafast-Response Anodized-Aluminum Pressure-Sensitive Paints," in *51st AIAA Aerospace Sciences Meeting including the New Horizons Forum and Aerospace Exposition*, 2013.
- [207] H. Sakaue, K. Morita, Y. Iijima, and Y. Sakamura, "Response Time Scales of Anodized-Aluminum Pressure-Sensitive Paints," *Sensors and Actuators A: Physical*, vol. 199, pp. 74-79, 2013.
- [208] A. E. Baron, J. D. S. Danielson, M. Gouterman, J. R. Wan, J. B. Callis, and B. McLachlan, "Submillisecond Response Times of Oxygen-Quenched Luminescent Coatings," *Review of Scientific Instruments*, vol. 64, no. 12, pp. 3394-3402, 1993.
- [209] R. R. Bacsa and M. Grätzel, "Rutile Formation in Hydrothermally Crystallized Nanosized Titania," *Journal of the American Ceramic Society*, vol. 79, no. 8, pp. 2185-2188, 1996.
- [210] B. D. MacCraith, C. M. McDonagh, G. O'Keeffe, A. K. McEvoy, T. Butler, and F. R. Sheridan, "Sol-Gel Coatings for Optical Chemical Sensors and Biosensors," *Sensors and Actuators B: Chemical*, vol. 29, no. 1, pp. 51-57, 1995.
- [211] K. Asai, H. Kanda, C. T. Cunningham, R. Erausquin, and J. P. Sullivan, "Surface Pressure Measurement in a Cryogenic Wind Tunnel by Using Luminescent Coating," in *ICIASF'97 Record. International Congress on Instrumentation in Aerospace Simulation Facilities*, 1997.
- [212] H. Sakaue and K. Ishii, "Optimization of Anodized-Aluminum Pressure-Sensitive Paint by Controlling Luminophore Concentration," *Sensors (Basel, Switzerland)*, vol. 10, no. 7, pp. 6836-6847, 2010.

References

- [213] A. M. Scroggin, E. B. Slamovich, J. W. Crafton, and N. Lachendro, "Porous Polymer/Ceramic Composites for Luminescence-Based Temperature and Pressure Measurement," *Materials Research Society symposia proceedings.*, vol. 560, p. 347, 1999.
- [214] H. Sakaue, "Anodized Aluminum Pressure Sensitive Paint for Unsteady Aerodynamic Applications," PhD thesis, Purdue University, 2003.
- [215] N. Gongora-Orozco, H. Zare-Behtash, and K. Kontis, "Global Unsteady Pressure-Sensitive Paint Measurements of a Moving Shock Wave Using Thin-Layer Chromatography," *Measurement*, vol. 43, no. 1, pp. 152-155, 2010.
- [216] Y. Sakamura, M. Matsumoto, and T. Suzuki, "High Frame-Rate Imaging of Surface Pressure Distribution Using a Porous Pressure-Sensitive Paint," *Measurement Science and Technology*, vol. 16, no. 3, pp. 759-765, 2005.
- [217] Y. Sakamura, T. Suzuki, M. Matsumoto, G. Masuya, and Y. Ikeda, "Optical Measurements of High-Frequency Pressure Fluctuations Using a Pressure-Sensitive Paint and Cassegrain Optics," *Measurement Science and Technology*, vol. 13, no. 10, pp. 1591-1598, 2002.
- [218] H. Sakaue, "Luminophore Application Method of Anodized Aluminum Pressure Sensitive Paint as a Fast Responding Global Pressure Sensor," *Review of Scientific Instruments*, vol. 76, no. 8, p. 084101, 2005.
- [219] H. Zare-Behtash, L. Yang, N. Gongora-Orozco, K. Kontis, and A. Jones, "Anodized Aluminium Pressure Sensitive Paint: Effect of Paint Application Technique," *Measurement*, vol. 45, no. 7, pp. 1902-1905, 2012.
- [220] J. W. Gregory, H. Sakaue, and J. P. Sullivan, "Unsteady Pressure Measurements in Turbomachinery Using Porous Pressure Sensitive Paint," in *40th AIAA Aerospace Sciences Meeting & Exhibit*, 2002.
- [221] J. Crafton, R. Forlines, S. Palluconi, K. Hsu, C. Carter, and M. Gruber, "Investigation of Transverse Jet Injection in a Supersonic Crossflow Using Fast Responding Pressure-Sensitive Paint," in *29th AIAA Applied Aerodynamics Conference*, 2011.
- [222] M. Kameda, H. Seki, T. Makoshi, Y. Amao, and K. Nakakita, "A Fast-Response Pressure Sensor Based on a Dye-Adsorbed Silica Nanoparticle Film," *Sensors and Actuators B: Chemical*, vol. 171-172, pp. 343-349, 2012.
- [223] K. Asai, K. Nakakita, M. Kameda, and K. Teduka, "Recent Topics in Fast-Responding Pressure-Sensitive Paint Technology at National Aerospace Laboratory," in *19th International Congress on Instrumentation in Aerospace Simulation Facilities* 2001.
- [224] K. Asai, Y. Amao, Y. Iijima, I. Okura, and H. Nishide, "Novel Pressure-Sensitive Paint for Cryogenic and Unsteady Wind-Tunnel Testing," *Journal of Thermophysics and Heat Transfer*, vol. 16, no. 1, pp. 109-115, 2002.
- [225] T. Masuda, E. Isobe, T. Higashimura, and K. Takada, "Poly[1-(Trimethylsilyl)-1-Propyne]: A New High Polymer Synthesized with Transition-Metal Catalysts and Characterized by Extremely

- High Gas Permeability," *Journal of the American Chemical Society*, vol. 105, no. 25, pp. 7473-7474, 1983.
- [226] Y. Amao, K. Asai, I. Okura, H. Shinohara, and H. Nishide, "Platinum Porphyrin Embedded in Poly(1-Trimethylsilyl-1-Propyne) Film as an Optical Sensor for Trace Analysis of Oxygen," *Analyst*, vol. 125, no. 11, pp. 1911-1914, 2000.
- [227] K. Nagai, T. Masuda, T. Nakagawa, B. D. Freeman, and I. Pinna, "Poly[1-(Trimethylsilyl)-1-Propyne] and Related Polymers: Synthesis, Properties and Functions," *Progress in Polymer Science*, vol. 26, no. 5, pp. 721-798, 2001.
- [228] Y. Iijima and H. Sakaue, "Platinum Porphyrin and Luminescent Polymer for Two-Color Pressure- and Temperature-Sensing Probes," *Sensors and Actuators A: Physical*, vol. 184, pp. 128-133, 2012.
- [229] M. E. Köse, B. F. Carroll, and K. S. Schanze, "Preparation and Spectroscopic Properties of Multiluminophore Luminescent Oxygen and Temperature Sensor Films," *Langmuir*, vol. 21, no. 20, pp. 9121-9129, 2005.
- [230] D. Peng *et al.*, "Temperature-Compensated Fast Pressure-Sensitive Paint," *AIAA Journal*, vol. 51, no. 10, pp. 2420-2431, 2013.
- [231] M. I. Stich, L. H. Fischer, and O. S. Wolfbeis, "Multiple Fluorescent Chemical Sensing and Imaging," *Chem Soc Rev*, vol. 39, no. 8, pp. 3102-14, 2010.
- [232] Y. Egami, Y. Sato, and S. Konishi, "Development of Polymer/Ceramic Pressure-Sensitive Paint with the Same Response Time as Anodized-Aluminum Psp," in *2018 AIAA Aerospace Sciences Meeting*, 2018.
- [233] D. Peng, J. Chen, L. Jiao, and Y. Liu, "A Fast-Responding Semi-Transparent Pressure-Sensitive Paint Based on through-Hole Anodized Aluminum Oxide Membrane," *Sensors and Actuators A: Physical*, vol. 274, pp. 10-18, 2018.
- [234] T. Hayashi and H. Sakaue, "Dynamic and Steady Characteristics of Polymer-Ceramic Pressure-Sensitive Paint with Variation in Layer Thickness," *Sensors (Basel, Switzerland)*, vol. 17, no. 5, p. 1125, 2017.
- [235] J. Gregory, H. Sakaue, and J. Sullivan, "Fluidic Oscillator as a Dynamic Calibration Tool," in *22nd AIAA Aerodynamic Measurement Technology and Ground Testing Conference*, 2002.
- [236] J. W. Gregory, J. P. Sullivan, S. S. Wanis, and N. M. Komerath, "Pressure-Sensitive Paint as a Distributed Optical Microphone Array," *J Acoust Soc Am*, vol. 119, no. 1, pp. 251-61, 2006.
- [237] T. Sugimoto, S. Kitashima, D. Numata, H. Nagai, and K. Asai, "Characterization of Frequency Response of Pressure-Sensitive Paints," in *50th AIAA Aerospace Sciences Meeting including the New Horizons Forum and Aerospace Exposition*, 2012.
- [238] C. M. McGraw, H. Shroff, G. Khalil, and J. B. Callis, "The Phosphorescence Microphone: A Device for Testing Oxygen Sensors and Films," *Review of Scientific Instruments*, vol. 74, no. 12, pp. 5260-5266, 2003.

References

- [239] C. A. Virgin, B. F. Carroll, L. N. Cattafesta, K. S. Schanze, and M. E. Kose, "Pressure Sensitive Paint for Acoustic Pressure Fluctuations," in *International Mechanical Engineering Congress and Exposition*, 2005.
- [240] R. M. McMullen, D. P. Huynh, J. Gregory, and J. W. Crafton, "Dynamic Calibrations for Fast-Response Porous Polymer/Ceramic Pressure-Sensitive Paint," in *AIAA Ground Testing Conference*, 2013.
- [241] C. Klein, W. Sachs, U. Henne, and J. Borbye, "Determination of Transfer Function of Pressure-Sensitive Paint," in *48th AIAA Aerospace Sciences Meeting Including the New Horizons Forum and Aerospace Exposition*, 2010.
- [242] H. J. Davis, H. D. Curchack, S. United, and W. D. C. Harry Diamond Laboratories, *Shock Tube Techniques and Instrumentation*, Washington, D.C.: U.S. Army Material Command, Harry Diamond Laboratories, 1969.
- [243] J. N. Bradley, "Shock Waves in Chemistry and Physics," *J. Am. Chem. Soc.*, 1962.
- [244] A. G. Gaydon and I. R. Hurle, *The Shock Tube in High-Temperature Chemical Physics*, London: Chapman and Hall, 1963.
- [245] J. H. Arakeri, D. Das, A. Krothapalli, and L. Lourenco, "Vortex Ring Formation at the Open End of a Shock Tube: A Particle Image Velocimetry Study," *Physics of Fluids*, vol. 16, no. 4, pp. 1008-1019, 2004.
- [246] A. C. Haselbacher, S. Balachandar, and S. W. Kieffer, "Open-Ended Shock Tube Flows: Influence of Pressure Ratio and Diaphragm Position," *AIAA Journal*, vol. 45, no. 8, pp. 1917-1929, 2007.
- [247] A. Kiverin and I. Yakovenko, "On the Mechanism of Flow Evolution in Shock-Tube Experiments," *Physics Letters A*, vol. 382, no. 5, pp. 309-314, 2018.
- [248] E. Y. Koroteeva, I. A. Znamenskaya, F. N. Glazyrin, and N. N. Sysoev, "Numerical and Experimental Study of Shock Waves Emanating from an Open-Ended Rectangular Tube," *Shock Waves*, vol. 26, no. 3, pp. 269-277, 2016.
- [249] R. Mariani and K. Kontis, "Experimental Studies on Coaxial Vortex Loops," *Physics of Fluids*, vol. 22, no. 12, 2010.
- [250] R. Mariani, M. K. Quinn, K. Kontis, and L. Marraffa, "Shock-Free Compressible Vortex Rings Impinging on a Stationary Surface: Effects of Surface Angle Variation," *Experimental Thermal and Fluid Science*, vol. 47, pp. 126-142, 2013.
- [251] H. D. Ng, B. B. Botros, J. Chao, J. M. Yang, N. Nikiforakis, and J. H. S. Lee, "Head-on Collision of a Detonation with a Planar Shock Wave," *Shock Waves*, vol. 15, no. 5, pp. 341-352, 2006.
- [252] M. Thangadurai and D. Das, "Characteristics of Counter-Rotating Vortex Rings Formed Ahead of a Compressible Vortex Ring," *Experiments in Fluids*, vol. 49, no. 6, pp. 1247-1261, 2010.

- [253] T. Ukai, H. Zare-Behtash, K. Kontis, and S. Obayashi, "Three-Dimensional Shock Wave Distortion in Shock-Square Vortex Loop Interaction," *Experimental Thermal and Fluid Science*, vol. 79, pp. 85-90, 2016.
- [254] H. Zare-Behtash, K. Kontis, and N. Gongora-Orozco, "Experimental Investigations of Compressible Vortex Loops," *Physics of Fluids*, vol. 20, no. 12, 2008.
- [255] E. Courtney, A. Courtney, and M. Courtney, "Shock Tube Design for High Intensity Blast Waves for Laboratory Testing of Armor and Combat Materiel," *Defence Technology*, vol. 10, no. 2, pp. 245-250, 2014.
- [256] S. Downes, A. Knott, and I. Robinson, "Towards a Shock Tube Method for the Dynamic Calibration of Pressure Sensors," *Philos Trans A Math Phys Eng Sci*, vol. 372, no. 2023, p. 20130299, 2014.
- [257] E. F. Médici and G. P. Waite, "Experimental Laboratory Study on the Formation of Multiple Shock Waves Observed During Volcanic Eruptions," *Geophysical Research Letters*, vol. 43, no. 1, pp. 85-92, 2016.
- [258] S. R. Nanda, S. Agarwal, V. Kulkarni, and N. Sahoo, "Shock Tube as an Impulsive Application Device," *International Journal of Aerospace Engineering*, vol. 2017, pp. 1-12, 2017.
- [259] H. Zare-Behtash, N. Gongora-Orozco, K. Kontis, and G. Jagadeesh, "Study of Detonation Interactions inside a Two-Dimensional Ejector Using Detonation Transmission Tubing," *Journal of Propulsion and Power*, vol. 26, no. 4, pp. 878-882, 2010.
- [260] I. O. Samuelraj, G. Jagadeesh, and K. Kontis, "Micro-Blast Waves Using Detonation Transmission Tubing," *Shock Waves*, vol. 23, no. 4, pp. 307-316, 2012.
- [261] G. Li, M. Burak Agir, K. Kontis, T. Ukai, and S. Rengarajan, "Image Processing Techniques for Shock Wave Detection and Tracking in High Speed Schlieren and Shadowgraph Systems," *Journal of Physics: Conference Series*, vol. 1215, p. 012021, 2019.
- [262] R. A. Hartunian, A. L. Russo, and P. V. Marrone, "Boundary-Layer Transition and Heat Transfer in Shock Tubes," *Journal of the Aerospace Sciences*, vol. 27, no. 8, pp. 587-594, 1960.
- [263] P. J. Musgrove and J. P. Appleton, "The Influence of Boundary Layer Growth on Shock Tube Test Times," *Applied Scientific Research*, vol. 18, no. 1, pp. 116-155, 1968.
- [264] O. Popczyk, "Investigation of the Fluid Flow Physics of Two- and Three-Dimensional Microscale Shock Wave Propagation Based on a High-Resolution Godunov-Type Finite Volume-Based in-House Code," Master Thesis, Cranfield University, 2018.
- [265] J. D. A. Walker and S. C. R. Dennis, "The Boundary Layer in a Shock Tube," *Journal of Fluid Mechanics*, vol. 56, no. 1, pp. 19-47, 1972.
- [266] C. Oommen, G. Jagadeesh, and B. N. Raghunandan, "Studies on Micro Explosive Driven Blast Wave Propagation in Confined Domains Using Nonel Tubes," in *26th International Symposium on Shock Waves*, 2009.

References

- [267] C. Wilson and H. Kleine, "The Influence of the High-Pressure Part Length on Shock Waves Exiting from an Open Tube," 2019.
- [268] W. A. Crede, "The Design and Construction of a Shock Tube Facility," Master thesis, University of Missouri at Rolla, 1965.
- [269] T. Murugan, S. De, C. L. Dora, D. Das, and P. Prem Kumar, "A Study of the Counter Rotating Vortex Rings Interacting with the Primary Vortex Ring in Shock Tube Generated Flows," *Fluid Dynamics Research*, vol. 45, no. 2, p. 025506, 2013.
- [270] C. L. Dora, D. Saravanan, K. Karunakar, and D. Das, "Characteristics of Embedded-Shock-Free Compressible Vortex Rings: A Detailed Study Using PIV," *Advances in Mechanical Engineering*, vol. 3, p. 650871, 2011.
- [271] K. Kontis, R. An, and J. A. Edwards, "Compressible Vortex-Ring Interaction Studies with a Number of Generic Body Configurations," *AIAA Journal*, vol. 44, no. 12, pp. 2962-2978, 2006.
- [272] M. Thangadurai and D. Das, "Experimental Study on a Compressible Vortex Ring in Collision with a Wall," *Journal of Visualization*, vol. 15, no. 4, pp. 321-332, 2012.
- [273] T. Minota, M. Nishida, and M. G. Lee, "Shock Formation by Compressible Vortex Ring Impinging on a Wall," *Fluid Dynamics Research*, vol. 21, no. 3, pp. 139-157, 1997.
- [274] K. Ahuja, "An Evaluation of Various Concepts of Reducing Supersonic Jet Noise," in *13th Aeroacoustics Conference*, 1990.
- [275] G. Raman, "Screech Tones from Rectangular Jets with Spanwise Oblique Shock-Cell Structures," *Journal of Fluid Mechanics*, vol. 330, pp. 141-168, 1997.
- [276] E. Gutmark, K. C. Schadow, T. P. Parr, D. M. Hanson-Parr, and K. J. Wilson, "Noncircular Jets in Combustion Systems," *Experiments in Fluids*, vol. 7, no. 4, pp. 248-258, 1989.
- [277] F. F. Grinstein, E. Gutmark, and T. Parr, "Near Field Dynamics of Subsonic Free Square Jets. A Computational and Experimental Study," *Physics of Fluids*, vol. 7, no. 6, pp. 1483-1497, 1995.
- [278] T. P. Ryan, *Sample Size Determination and Power*: John Wiley & Sons, Inc. , 2013.
- [279] S. L. Obispo, "Manufacturing and Instrumentation of an Open End Compressed Air Shock Tube," Master Thesis, California Polytechnic State University, 2017.
- [280] M. M. Biss and K. L. McNesby, "Optically Measured Explosive Impulse," *Experiments in Fluids*, vol. 55, no. 6, p. 1749, 2014.
- [281] D. C. Bowman *et al.*, "The Acoustic Signatures of Ground Acceleration, Gas Expansion, and Spall Fallback in Experimental Volcanic Explosions," *Geophysical Research Letters*, vol. 41, no. 6, pp. 1916-1922, 2014.
- [282] S. E. Widnall, D. B. Bliss, and C.-Y. Tsai, "The Instability of Short Waves on a Vortex Ring," *Journal of Fluid Mechanics*, vol. 66, no. 1, pp. 35-47, 1974.
- [283] M. Brouillette and C. Hébert, "Propagation and Interaction of Shock-Generated Vortices," *Fluid Dynamics Research*, vol. 21, no. 3, pp. 159-169, 1997.

- [284] H. Kashimura, T. Yasunobu, H. Nakayama, T. Setoguchi, and K. Matsuo, "Discharge of a Shock Wave from an Open End of a Tube," *Journal of Thermal Science*, vol. 9, no. 1, pp. 30-36, 2000.
- [285] Z. Jiang, O. Onodera, and K. Takayama, "Evolution of Shock Waves and the Primary Vortex Loop Discharged from a Square Cross-Sectional Tube," *Shock Waves*, vol. 9, no. 1, pp. 1-10, 1999.
- [286] M. Raffel, H. Richard, and G. E. A. Meier, "On the Applicability of Background Oriented Optical Tomography for Large Scale Aerodynamic Investigations," *Experiments in Fluids : Experimental Methods and their Applications to Fluid Flow*, vol. 28, no. 5, pp. 477-481, 2000.
- [287] T. Kirmse, J. Agocs, A. Schroder, M. J. Schramm, S. Karl, and K. Hannemann, "Application of Particle Image Velocimetry and the Background-Oriented Schlieren Technique in the High-Enthalpy Shock Tunnel Göttingen," *Shock Waves*, vol. 21, no. 3, pp. 233-241, 2011.
- [288] M. J. Hargather and G. S. Settles, "Background-Oriented Schlieren Visualization of Heating and Ventilation Flows: Hvac-Bos," *International Journal of Heating Ventilation Air Conditioning and Refrigerating Research*, vol. 17, no. 5, pp. 771-780, 2011.
- [289] F. Leopold, "The Application of the Colored Background Oriented Schlieren Technique (Cbos) to Free-Flight and in-Flight Measurements," in *22nd International Congress on Instrumentation in Aerospace Simulation Facilities*, 2007.
- [290] T. William and S. Eize, "PIVlab Towards User-Friendly, Affordable and Accurate Digital Particle Image Velocimetry in MATLAB," *Journal of Open Research Software*, vol. 2, no. 1, p. e30, 2014.
- [291] M. Raffel, Willert, C., Wereley, S. and Kompenhans, J, *Particle Image Velocimetry : A Practical Guide*, Berlin: Springer, 2007.
- [292] U. Shavit, R. J. Lowe, and J. V. Steinbuck, "Intensity Capping: A Simple Method to Improve Cross-Correlation PIV Results," *Exp Fluids Experiments in Fluids : Experimental Methods and their Applications to Fluid Flow*, vol. 42, no. 2, pp. 225-240, 2007.
- [293] S. M. Pizer *et al.*, "Adaptive Histogram Equalization and Its Variations," *YCVIGP Computer Vision, Graphics and Image Processing*, vol. 39, no. 3, pp. 355-368, 1987.
- [294] R. C. González, *Digital Image Processing*, Reading, Mass.: Addison-Wesley, 2001.
- [295] H. Huang, D. Dabiri, and M. Gharib, "On Errors of Digital Particle Image Velocimetry," *Measurement Science and Technology*, vol. 8, no. 12, pp. 1427-1440, 1997.
- [296] K. Okamoto, S. Nishio, T. Saga, and T. Kobayashi, "Standard Images for Particle-Image Velocimetry," *Measurement science & technology.*, vol. 11, pp. 685-691, 2000.
- [297] E. J. Stadhuis, "Basics and Principles of Particle Image Velocimetry (PIV) for Mapping Biogenic and Biologically Relevant Flows," *Aquatic Ecology*, vol. 40, no. 4, pp. 463-479, 2006.
- [298] J. Soria, "An Investigation of the near Wake of a Circular Cylinder Using a Video-Based Digital Cross-Correlation Particle Image Velocimetry Technique," *Experimental Thermal and Fluid Science*, vol. 12, no. 2, pp. 221-233, 1996.

References

- [299] R. D. Keane and R. J. Adrian, "Optimization of Particle Image Velocimeters. I. Double Pulsed Systems," *Measurement Science and Technology*, vol. 1, no. 11, pp. 1202-1215, 1990.
- [300] J. Westerweel, D. Dabiri, and M. Gharib, "The Effect of a Discrete Window Offset on the Accuracy of Cross-Correlation Analysis of Digital Piv Recordings," *Experimental in Fluids*, vol. 23, no. 1, pp. 20-28, 1997.
- [301] F. Scarano and M. L. Riethmuller, "Iterative Multigrid Approach in PIV Image Processing with Discrete Window Offset," *Experiments in Fluids*, vol. 26, no. 6, pp. 513-523, 1999.
- [302] H. T. Huang, H. E. Fiedler, and J. J. Wang, "Limitation and Improvement of Piv. Part II: Particle Image Distortion, a Novel Technique," *Experiments in Fluids*, vol. 15, no. 4/5, p. 263, 1993.
- [303] K. Jambunathan, X. Y. Ju, B. N. Dobbins, and S. Ashforth-Frost, "An Improved Cross Correlation Technique for Particle Image Velocimetry," *Measurement Science and Technology*, vol. 6, no. 5, pp. 507-514, 1995.
- [304] F. Scarano and M. L. Riethmuller, "Advances in Iterative Multigrid PIV Image Processing," *Experiments in Fluids Experiments in Fluids : Experimental Methods and their Applications to Fluid Flow*, vol. 29, no. 1, pp. S051-S060, 2000.
- [305] J. Nogueira, A. Lecuona, and P. A. Rodriguez, "Data Validation, False Vectors Correction and Derived Magnitudes Calculation on Piv Data," *Measurement science & technology.*, vol. 8, no. 12, p. 1493, 1997.
- [306] J. Westerweel and F. Scarano, "Universal Outlier Detection for Piv Data," *Exp Fluids Experiments in Fluids : Experimental Methods and their Applications to Fluid Flow*, vol. 39, no. 6, pp. 1096-1100, 2005.
- [307] J. V. E Stamhuis, "Quantitative Flow Analysis around Aquatic Animals Using Laser Sheet Particle Image Velocimetry," *Journal of Experimental Biology*, 1995.
- [308] D. Garcia, "Robust Smoothing of Gridded Data in One and Higher Dimensions with Missing Values," *Comput. Stat. Data Anal. Computational Statistics and Data Analysis*, vol. 54, no. 4, pp. 1167-1178, 2010.
- [309] Y. Egami, "1013 Effect of Solvents on Time Responsiveness of Sprayable Fast Pressure-Sensitive Paint," *The Proceedings of the Fluids engineering conference*, vol. 2015, no. 0, pp. _1013-1_-_1013-2_, 2015.
- [310] Y. Sugioka, D. Numata, K. Asai, S. Koike, K. Nakakita, and T. Nakajima, "Polymer/Ceramic Psp with Reduced Surface Roughness for Unsteady Pressure Measurement in Transonic Flow," in *54th AIAA Aerospace Sciences Meeting*, 2016.
- [311] Y. Sugioka, D. Numata, K. Asai, S. Koike, K. Nakakita, and S. Koga, "Unsteady Psp Measurement of Transonic Buffet on a Wing," in *53rd AIAA Aerospace Sciences Meeting*, 2015.
- [312] C. Klein, R. H. Engler, U. Henne, and W. E. Sachs, "Application of Pressure-Sensitive Paint for Determination of the Pressure Field and Calculation of the Forces and Moments of Models in a Wind Tunnel," *Experiments in Fluids*, vol. 39, no. 2, pp. 475-483, 2005.

- [313] B. G. McLachlan and J. H. Bell, "Pressure-Sensitive Paint in Aerodynamic Testing," *Experimental Thermal and Fluid Science*, vol. 10, no. 4, pp. 470-485, 1995.
- [314] M. E. Kose, "Multi-Luminophore Coatings for Pressure Sensitive Paint Applications," PhD Thesis, University of Florida, 2005.
- [315] J. H. Bell, E. T. Schairer, L. A. Hand, and R. D. Mehta, "Surface Pressure Measurements Using Luminescent Coatings," *Annual Review of Fluid Mechanics*, vol. 33, no. 1, pp. 155-206, 2001.
- [316] L. Nel, B. Skews, and K. Naidoo, "Schlieren Techniques for the Visualization of an Expansion Fan/Shock Wave Interaction," *Journal of Visualization*, vol. 18, no. 3, pp. 469-479, 2014.
- [317] D. Daub, S. Willems, and A. Gühan, "Experiments on the Interaction of a Fast-Moving Shock with an Elastic Panel," *AIAA Journal*, vol. 54, no. 2, pp. 670-678, 2016.
- [318] C. Desjouy, S. Ollivier, O. Marsden, M. Karzova, and P. Blanc-Benon, "Irregular Reflection of Weak Acoustic Shock Pulses on Rigid Boundaries : Schlieren Experiments and Direct Numerical Simulation Based on a Navier-Stokes Solver," *Physics of Fluids*, vol. 28, no. 2, 2016.
- [319] J. Wolfram and J. Martinez Schramm, "Pattern Recognition in High Speed Schlieren Visualization at the High Enthalpy Shock Tunnel Göttingen," in *16th STAB/DGLR Symposium Aachen*, 2010.
- [320] N. T. Smith, M. J. Lewis, and R. Chellappa, "Detection, Localization, and Tracking of Shock Contour Salient Points in Schlieren Sequences," *AIAA Journal*, vol. 52, no. 6, pp. 1249-1264, 2014.
- [321] S. Saravanan, K. Nagashetty, G. M. Hegde, G. Jagadeesh, and K. P. J. Reddy, "Schlieren Visualization of Shock Wave Phenomena over a Missile-Shaped Body at Hypersonic Mach Numbers," *Proceedings of the Institution of Mechanical Engineers, Part G: Journal of Aerospace Engineering*, vol. 225, no. 1, pp. 26-34, 2011.
- [322] L. M. Cyril Mauger, Marc Michard, Alexandre Azouzi, Stéphane Valette, "Shadowgraph, Schlieren and Interferometry in a 2D Cavitating Channel Flow," *Experiments in Fluids*, vol. 53, no. 6, pp. 1895–1913, 2012.
- [323] H. Zare-Behtash, K. Kontis, N. Gongora-Orozco, and K. Takayama, "Shock Wave-Induced Vortex Loops Emanating from Nozzles with Singular Corners," *Experiments in Fluids*, vol. 49, no. 5, pp. 1005-1019, 2010.
- [324] D. E. Mowbray, "The Use of Schlieren and Shadowgraph Techniques in the Study of Flow Patterns in Density Stratified Liquids," *Journal of Fluid Mechanics*, vol. 27, no. 03, 2006.
- [325] M. M. Clem, K. Zaman, and A. F. Fagan, "Variation of Shock-Spacing During Screech Stage-Jumps," *International Journal of Aeroacoustics*, vol. 15, no. 3, pp. 324-335, 2016.
- [326] T. Fujimoto, T. Kawasaki, and K. Kitamura, "Simpler Method of Shock Wave Detection by Using Canny Method," in *2018 Fluid Dynamics Conference*, 2018.
- [327] H. Akhlaghi, A. Daliri, and M. R. Soltani, "Shock-Wave-Detection Technique for High-Speed Rarefied-Gas Flows," *AIAA Journal*, vol. 55, no. 11, pp. 3747-3756, 2017.

References

- [328] Z. Wu, Y. Xu, W. Wang, and R. Hu, "Review of Shock Wave Detection Method in CFD Post-Processing," *Chinese Journal of Aeronautics*, vol. 26, no. 3, pp. 501-513, 2013.
- [329] D. Estruch, N. J. Lawson, D. G. MacManus, K. P. Garry, and J. L. Stollery, "Measurement of Shock Wave Unsteadiness Using a High-Speed Schlieren System and Digital Image Processing," *Review of Scientific Instruments*, vol. 79, no. 12, p. 126108, 2008.
- [330] N. T. Smith, M. J. Lewis, and R. Chellappa, "Extraction of Oblique Structures in Noisy Schlieren Sequences Using Computer Vision Techniques," *AIAA Journal*, vol. 50, no. 5, pp. 1145-1155, 2012.
- [331] J. Wolfram and J. Martinez Schramm, "Pattern Recognition in High Speed Schlieren Visualization at the High Enthalpy Shock Tunnel Göttingen (HEG)," in *New Results in Numerical and Experimental Fluid Mechanics VII*, 2010.
- [332] S. Cui, Y. Wang, X. Qian, and Z. Deng, "Image Processing Techniques in Shockwave Detection and Modeling," *Journal of Signal and Information Processing*, vol. 04, no. 03, pp. 109-113, 2013.
- [333] M. Dehghan Manshadi, H. Vahdat Nejad, M. Kazemi-Esfeh, and M. Alavi, *Speed Detection in Wind-Tunnels by Processing Schlieren Images*, 2016.
- [334] J. Norris, "Mach 8 High Reynolds Number Static Stability Capability Extension Using a Hypersonic Waverider at AEDC Tunnel 9," in *25th AIAA Aerodynamic Measurement Technology and Ground Testing Conference*, 2006.
- [335] R. Szeliski, *Computer Vision : Algorithms and Applications*, [S.l.]: Springer Nature, 2010.
- [336] N. Otsu, "Threshold Selection Method from Gray-Level Histograms," *IEEE Trans Syst Man Cybern*, vol. SMC-9, no. 1, pp. 62-66, 1979.
- [337] G. W. Zack, W. E. Rogers, and S. A. Latt, "Automatic Measurement of Sister Chromatid Exchange Frequency," *J Histochem Cytochem*, vol. 25, no. 7, pp. 741-53, 1977.
- [338] A. Mirkazemi, S. E. Alavi, and G. Akbarizadeh, "Fast Image Segmentation Based on Adaptive Histogram Thresholding," in *2015 The International Symposium on Artificial Intelligence and Signal Processing (AISP)*, 2015.
- [339] J. N. Kapur, P. K. Sahoo, and A. K. C. Wong, "A New Method for Gray-Level Picture Thresholding Using the Entropy of the Histogram," *Computer Vision, Graphics, and Image Processing*, vol. 29, no. 3, pp. 273-285, 1985.
- [340] S. Paris, P. Kornprobst, and J. Tumblin, "A Gentle Introduction to Bilateral Filtering and Its Applications," in *ACM SIGGRAPH 2007 courses*, 2007.
- [341] J. Mukhopadhyay, "Image Resizing in the Compressed Domain," in *2017 International Symposium on Signals, Circuits and Systems (ISSCS)*, 2017.
- [342] A. P. Mahmoudzadeh and N. H. Kashou, "Evaluation of Interpolation Effects on Upsampling and Accuracy of Cost Functions-Based Optimized Automatic Image Registration," *International Journal of Biomedical Imaging*, vol. 2013, p. 19, 2013.

- [343] S. Manjunatha and M. M. Patil, "Interpolation Techniques in Image Resampling," *Int. J. Eng. Technol. International Journal of Engineering and Technology(UAE)*, vol. 7, no. 3.34 Special Issue 34, pp. 567-570, 2018.
- [344] N. A. Dodgson, *Image Resampling*, Cambridge: University of Cambridge. Computer Laboratory, 1992.
- [345] S. Singh and R. Singh, "Comparison of Various Edge Detection Techniques," in *2015 2nd International Conference on Computing for Sustainable Global Development (INDIACoM)*, 2015.
- [346] J. Canny, "A Computational Approach to Edge Detection," *IEEE Transactions on Pattern Analysis and Machine Intelligence*, vol. PAMI-8, no. 6, pp. 679-698, 1986.
- [347] P. Arbeláez, M. Maire, C. Fowlkes, and J. Malik, "Contour Detection and Hierarchical Image Segmentation," *IEEE Transactions on Pattern Analysis and Machine Intelligence*, vol. 33, no. 5, pp. 898-916, 2011.
- [348] G. Papari and N. Petkov, "Edge and Line Oriented Contour Detection: State of the Art," *Image and Vision Computing*, vol. 29, no. 2, pp. 79-103, 2011.
- [349] F. Akram, M. A. Garcia, and D. Puig, "Active Contours Driven by Local and Global Fitted Image Models for Image Segmentation Robust to Intensity Inhomogeneity," *PLOS ONE*, vol. 12, no. 4, p. e0174813, 2017.
- [350] G. Bradski, "The Opencv Library," *Dr. Dobb's Journal*, vol. 25, pp. 120-126, 2000.
- [351] A. Kaehler and G. R. Bradski, *Learning OpenCV 3 : Computer Vision in C++ with the OpenCV Library*, 2017.
- [352] J. Seo, S. Chae, J. Shim, D. Kim, C. Cheong, and T.-D. Han, "Fast Contour-Tracing Algorithm Based on a Pixel-Following Method for Image Sensors," *Sensors (Basel, Switzerland)*, vol. 16, no. 3, p. 353, 2016.
- [353] P. Koomsap and N. Chansri, "Topological Hierarchy-Contour Tracing Algorithm for Nests of Interconnected Contours," *The International Journal of Advanced Manufacturing Technology*, vol. 70, no. 5, pp. 1247-1266, 2014.
- [354] C. E. Widodo and K. Adi, "Finger Edge Contour Perimeter as a Biometric Based Identification System," *Journal of Physics: Conference Series*, vol. 1217, p. 012033, 2019.
- [355] H.-G. Song and H.-S. Koo, "A Geometric Centroid Contour Distance for Scale/Rotation Robustness Using Shape Alignment and Feature Based Normalization," in *Convergence and Hybrid Information Technology*, 2012.
- [356] S. Wang, H. Kim, and H. Chen, "Contour Tracking Using Centroid Distance Signature and Dynamic Programming Method," in *2009 International Joint Conference on Computational Sciences and Optimization*, 2009.
- [357] A. Hasim, Y. Herdiyeni, and S. Douady, "Leaf Shape Recognition Using Centroid Contour Distance," *IOP Conference Series: Earth and Environmental Science*, vol. 31, p. 012002, 2016.

References

- [358] F. Fachri Yanuar Rudi and E. M. Yuniarno, "Contour to Centroid Distance Graph as Feature in Hand Gesture Recognition," *IOP Conference Series: Materials Science and Engineering*, vol. 536, p. 012150, 2019.
- [359] J.-Z. Cheng, F.-J. Chang, K.-J. Hsu, and Y.-Y. Lin, "Knowledge Leverage from Contours to Bounding Boxes: A Concise Approach to Annotation," in *Computer Vision – ACCV 2012*, 2012.
- [360] C. Lu, S. Liu, J. Jia, and C. Tang, "Contour Box: Rejecting Object Proposals without Explicit Closed Contours," in *2015 IEEE International Conference on Computer Vision (ICCV)*, 2015.
- [361] C. Teh and R. T. Chin, "On the Detection of Dominant Points on Digital Curves," *IEEE Transactions on Pattern Analysis and Machine Intelligence*, vol. 11, no. 8, pp. 859-872, 1989.
- [362] L. Liu, B. G. Schunck, and C. R. Meyer, "Optimal Contour Approximation by Deformable Piecewise Cubic Splines," in *Proceedings. 1991 IEEE Computer Society Conference on Computer Vision and Pattern Recognition*, 1991.
- [363] A. Kolesnikov and P. Fränti, "Polygonal Approximation of Closed Contours," in *Image Analysis*, 2003.
- [364] X. C. He and N. H. C. Yung, "Curvature Scale Space Corner Detector with Adaptive Threshold and Dynamic Region of Support," in *Proceedings of the 17th International Conference on Pattern Recognition, 2004. ICPR 2004.*, 2004.
- [365] X. He and N. H. C. Yung, "Corner Detector Based on Global and Local Curvature Properties," *Optical Engineering*, vol. 47, no. 5, p. 057008, 2008.
- [366] F. Mokhtarian and A. K. Mackworth, "A Theory of Multiscale, Curvature-Based Shape Representation for Planar Curves," *IEEE Transactions on Pattern Analysis and Machine Intelligence*, vol. 14, no. 8, pp. 789-805, 1992.
- [367] F. Mokhtarian and A. Mackworth, "Scale-Based Description and Recognition of Planar Curves and Two-Dimensional Shapes," *IEEE Transactions on Pattern Analysis and Machine Intelligence*, vol. 8, no. 1, pp. 34-43, 1986.
- [368] F. Mokhtarian and R. Suomela, "Robust Image Corner Detection through Curvature Scale Space," *IEEE Transactions on Pattern Analysis and Machine Intelligence*, vol. 20, no. 12, pp. 1376-1381, 1998.
- [369] B. Zhong and W. Liao, "Direct Curvature Scale Space in Corner Detection," in *Structural, Syntactic, and Statistical Pattern Recognition*, 2006.
- [370] F. Mokhtarian and M. Bober, "Robust Image Corner Detection through Curvature Scale Space," *IEEE Transactions on Pattern Analysis and Machine Intelligence*, pp. 215-242, 2003.
- [371] L. Yi-bo and L. Jun-jun, "Harris Corner Detection Algorithm Based on Improved Contourlet Transform," *Procedia Engineering*, vol. 15, pp. 2239-2243, 2011.
- [372] X. Shunqing, Z. Weihong, and X. Wei, "Optimization of Harris Corner Detection Algorithm," in *Advances in Control and Communication*, 2012.

- [373] L. Wang, Y. Zhao, P. Qin, and Y. Gao, "Harris Corner Detection Algorithm Optimization Based on Otsu," *Recent Advances in Electrical & Electronic Engineering*, vol. 11, no. 2, pp. 91-96, 2018.
- [374] G. Li, M. BurakAgir, K. Kontis, T. Ukai, and S. Rengarajan, "Image Processing Techniques for Shock Wave Detection and Tracking in High Speed Schlieren and Shadowgraph Systems," *Journal of Physics: Conference Series*, vol. 1215, 2019.
- [375] V. Zapryagaev, N. Kiselev, and D. Gubanov, "Shock-Wave Structure of Supersonic Jet Flows," *Aerospace*, vol. 5, no. 2, 2018.
- [376] T. Ukai, H. Zare-Behtash, E. Erinc, K. H. Lo, K. Kontis, and S. Obayashi, "Effectiveness of Jet Location on Mixing Characteristics inside a Cavity in Supersonic Flow," *Experimental Thermal and Fluid Science*, vol. 52, pp. 59-67, 2014.
- [377] M. Lappa, D. Drikakis, and I. Kokkinakis, "On the Propagation and Multiple Reflections of a Blast Wave Travelling through a Dusty Gas in a Closed Box," *Physics of Fluids*, vol. 29, no. 3, 2017.
- [378] V. V. Golub, "Development of Shock Wave and Vortex Structures in Unsteady Jets," *Shock Waves*, vol. 3, no. 4, pp. 279-285, 1994.
- [379] K. M. Pandey and P. Debnath, "Review on Recent Advances in Pulse Detonation Engines," *Journal of Combustion*, vol. 2016, pp. 1-16, 2016.
- [380] F. Ma, J.-Y. Choi, and V. Yang, "Thrust Chamber Dynamics and Propulsive Performance of Single-Tube Pulse Detonation Engines," *Journal of Propulsion and Power*, vol. 21, no. 3, pp. 512-526, 2005.
- [381] K. Kailasanath, "Recent Developments in the Research on Pulse Detonation Engines," *AIAA Journal*, vol. 41, no. 2, pp. 145-159, 2003.
- [382] A. J. Glaser, N. Caldwell, E. Gutmark, J. Hoke, R. Bradley, and F. Schauer, "Study on the Operation of Pulse-Detonation Engine-Driven Ejectors," *Journal of Propulsion and Power*, vol. 24, no. 6, pp. 1324-1331, 2008.
- [383] A. Tyas, "Experimental Measurement of Pressure Loading from near-Field Blast Events: Techniques, Findings and Future Challenges," *Proceedings*, vol. 2, no. 8, 2018.
- [384] Y. Wang, H. Wang, C. Cui, B. Zhao, and T. Xin, "Damage Analysis of Explosion Blast Wave to Rocket Structure and Payload," *IOP Conference Series: Earth and Environmental Science*, vol. 237, 2019.
- [385] N. D. Moshman, G. V. Hobson, and S. S. Sritharan, "Method for Optimally Controlling Unsteady Shock Strength in One Dimension," *AIAA Journal*, vol. 51, no. 3, pp. 606-614, 2013.
- [386] T. Shimizu, Y. Watanabe, and T. Kambe, "Scattered Waves Generated by Shock Wave and Vortex Ring Interaction," *Fluid Dynamics Research*, vol. 27, no. 2, pp. 65-90, 2000.
- [387] O. Inoue and Y. Takahashi, "Successive Generation of Sound by Shock-Strong Vortex Interaction," *Physics of Fluids*, vol. 12, no. 12, pp. 3229-3234, 2000.

References

- [388] T. Minota, "Interaction of a Shock Wave with a High-Speed Vortex Ring," *Fluid Dynamics Research*, vol. 12, no. 6, pp. 335-342, 1993.
- [389] F. Takayama, Y. Ishii, A. Sakurai, and T. Kambe, "Self-Intensification in Shock Wave and Vortex Interaction," *Fluid Dynamics Research*, vol. 12, no. 6, pp. 343-348, 1993.
- [390] Z. Ding, M. Y. Hussaini, G. Erlebacher, and A. Krothapalli, "Computational Study of Shock Interaction with a Vortex Ring," *Physics of Fluids*, vol. 13, no. 10, pp. 3033-3048, 2001.

Appendices

Appendix A

Design of shock tube

This section provides the design of shock tubes driven by detonation transmission tubing used in this work.

A.1 Design of the axisymmetric shock tube

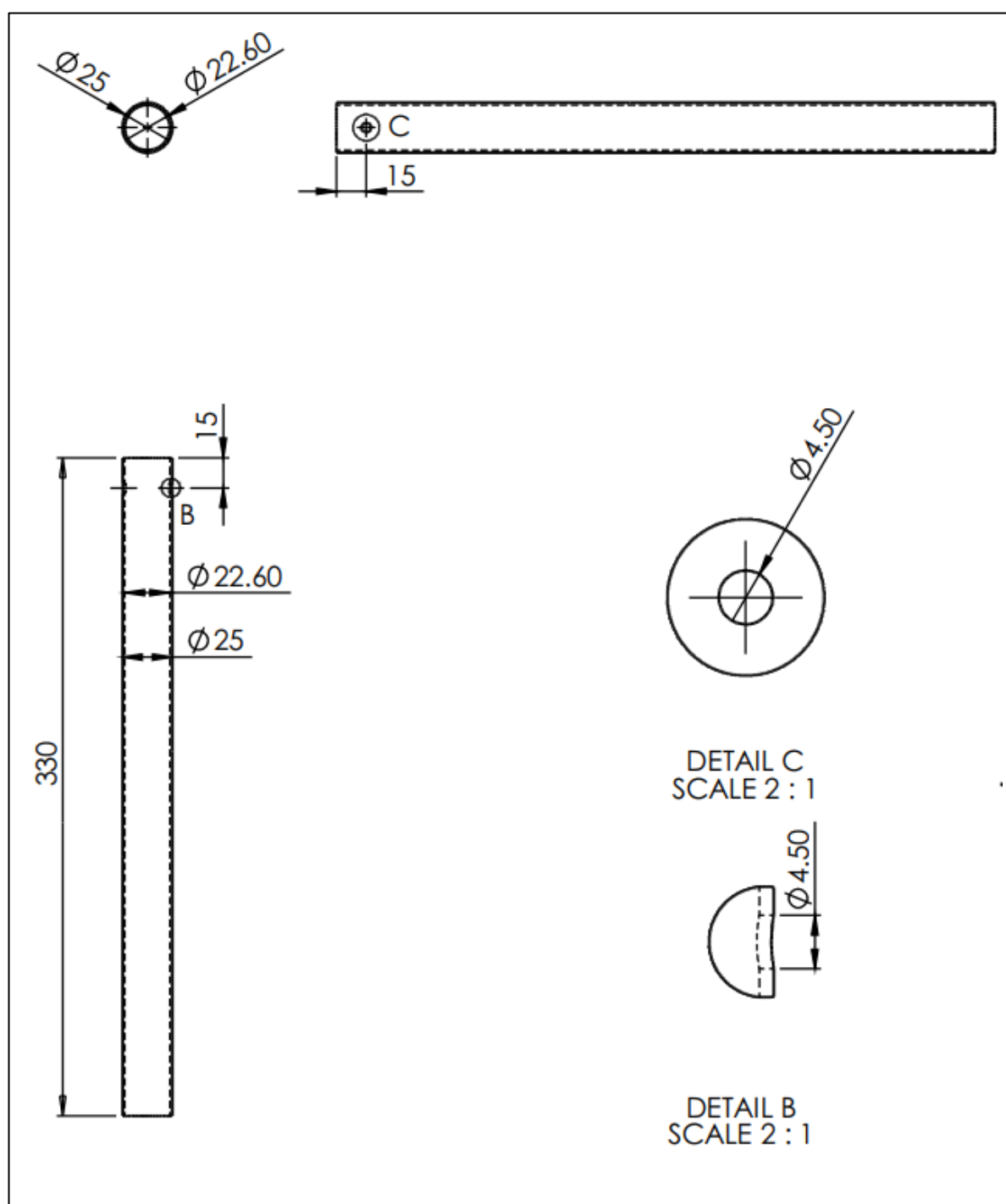


Figure A.1 Design and dimensions of the driven section of the axisymmetric shock tube

Appendix

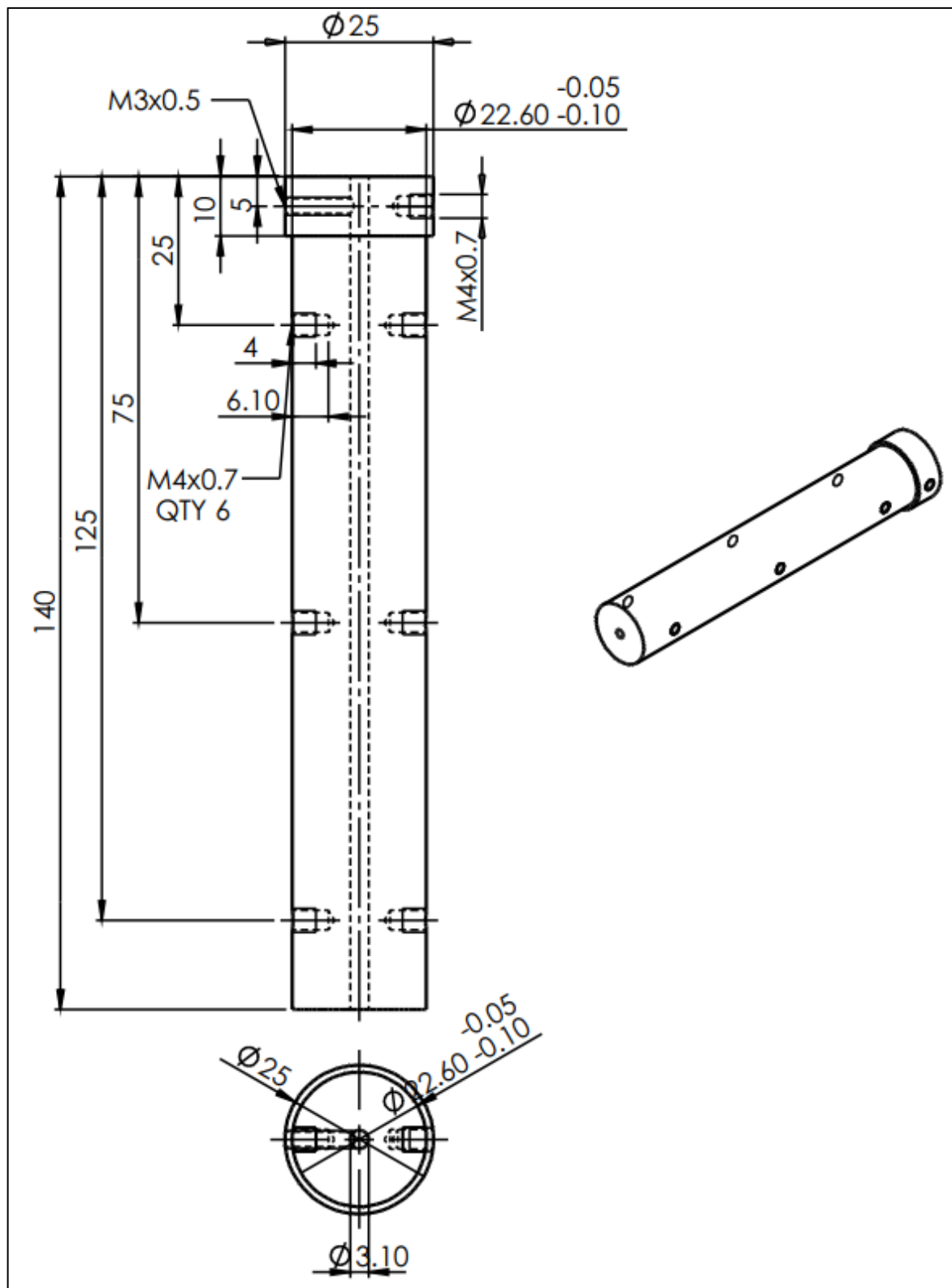


Figure A.2 Design and dimensions of NONEL tube holder of the axisymmetric shock tube

A.2 Design of the square shock tube

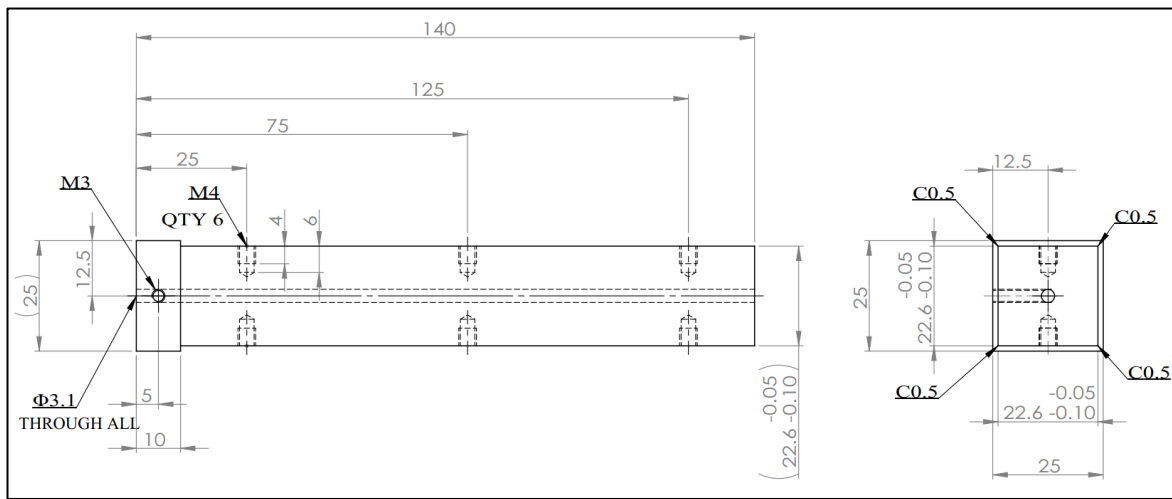


Figure A.3 Design and dimensions of NONEL tube holder of the square shock tube

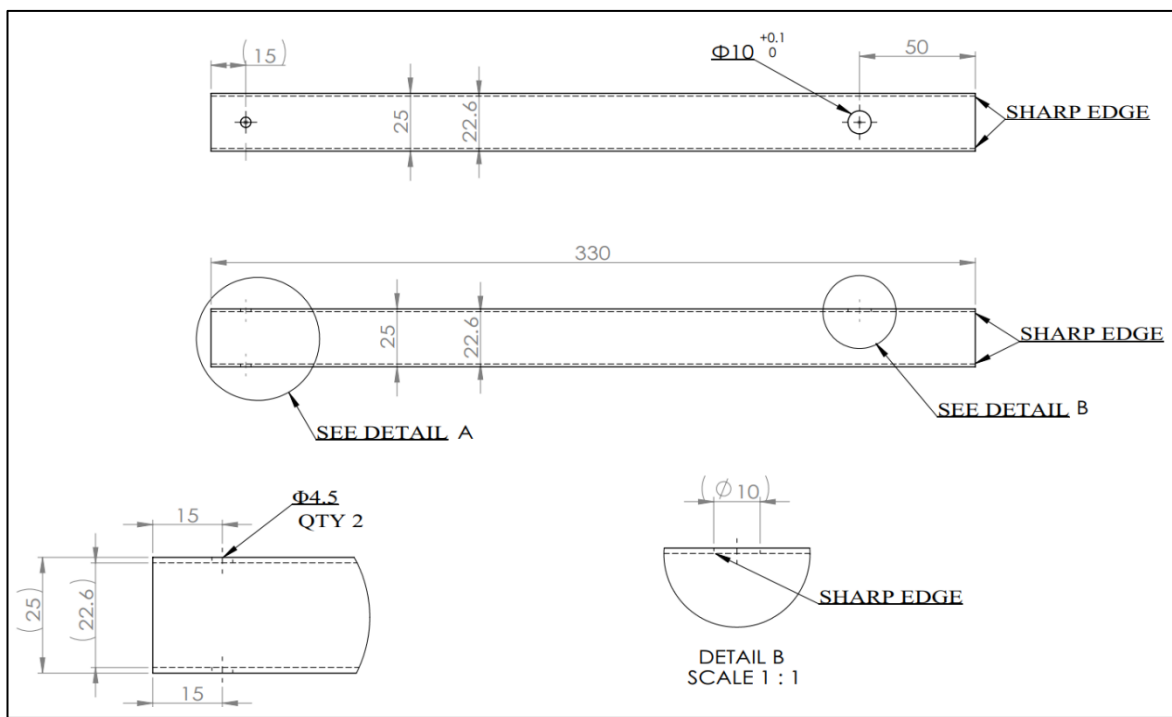


Figure A.4 Design and dimensions of the driven section of the square shock tube

A.3 Design of the shock tube for PSP dynamic calibration

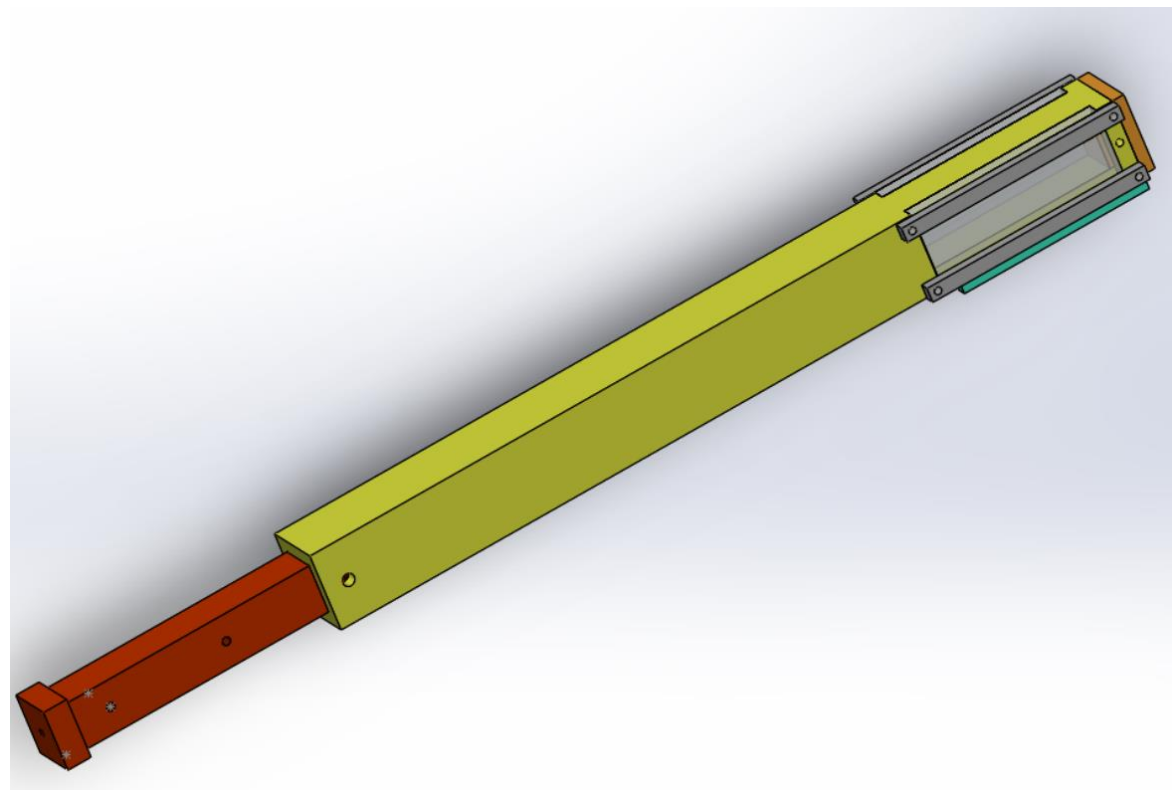


Figure A.5 Assembly of the square shock tube for PSP dynamic calibration. (The red part is the NONEL tube holder, the blue part is the driven section with two optical windows on its two sides and the orange part at the end of the driven section was designed for mounting Kulite pressure transducer).

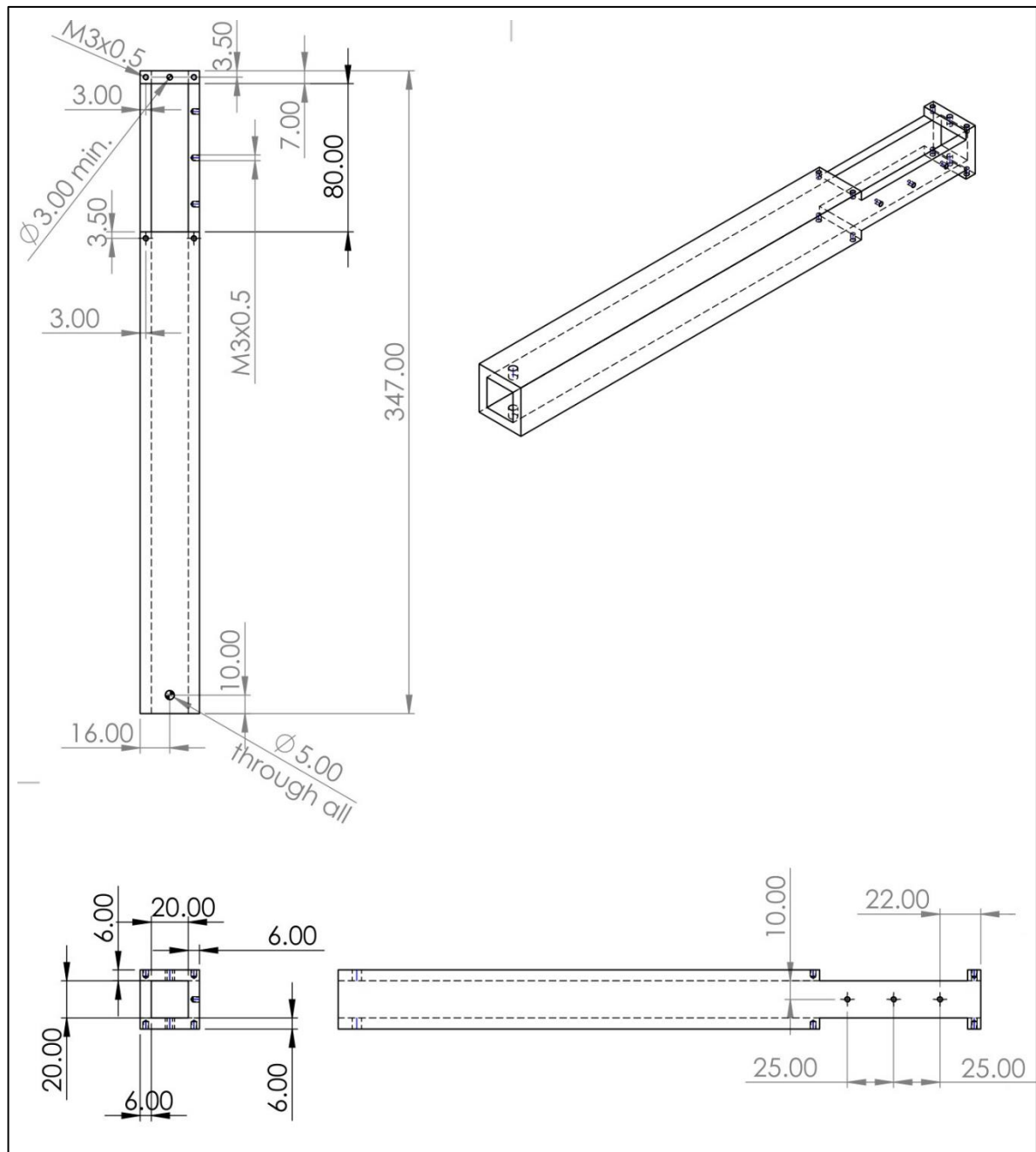


Figure A.6 Design and dimensions of the driven section of the shock tube for PSP dynamic calibration

Appendix

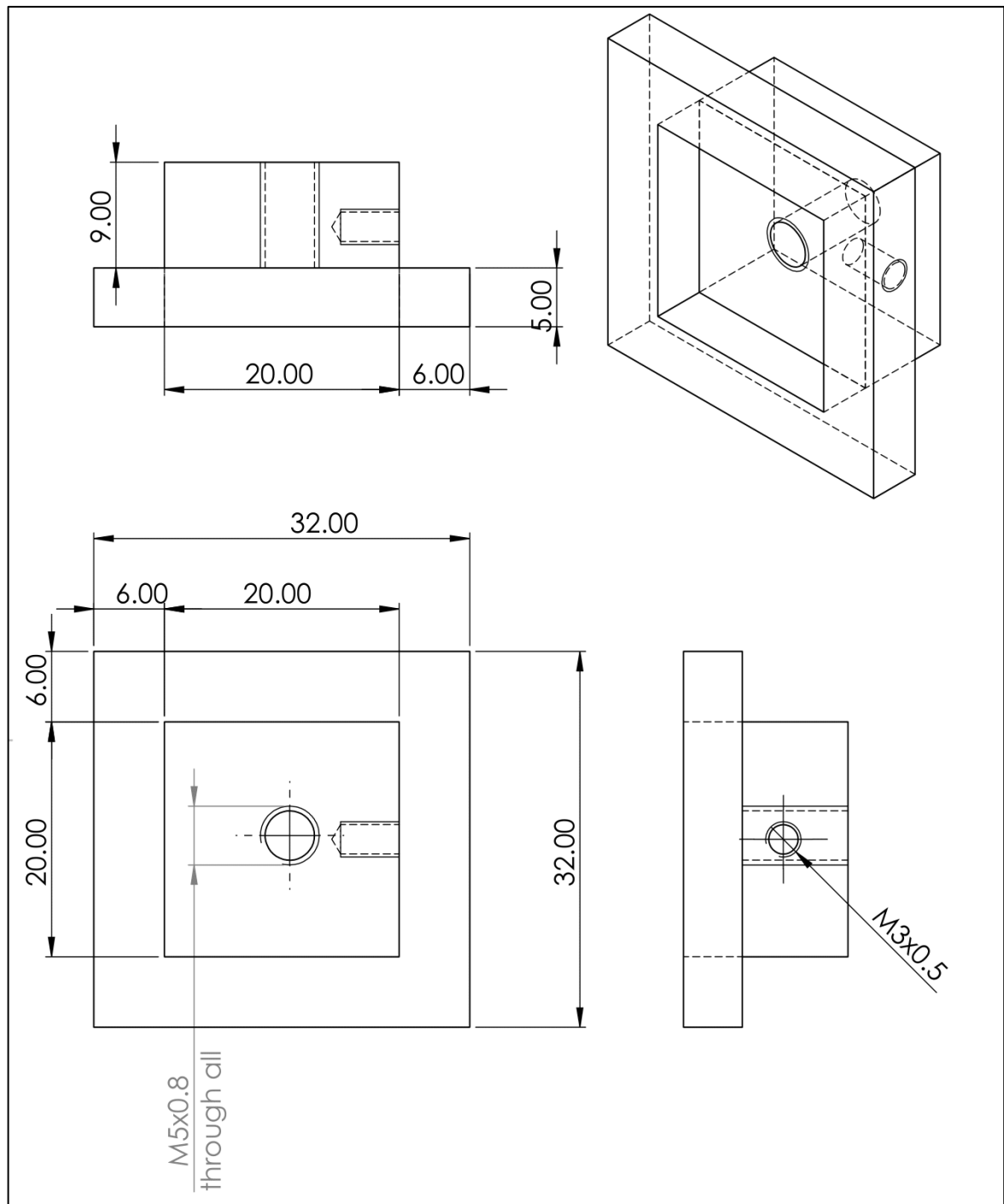


Figure A.7 Design and dimensions of shock tube end for mounting Kulite pressure transducer

Appendix B

Design of flexible panels in supersonic wind tunnel

Experimental setup including a shock wave generator, flexible panels, and the supporting unit has been designed and fabricated for investigating oblique shock and boundary layer interaction over flexible surfaces in the supersonic wind tunnel (width, height, and length of the test section: 101.60mm × 54.42mm × 742.95 mm) of the University of Glasgow. Figures B.1-B.5 present the design of the flexible panel support unit. Flexible panels with a dimension of 101.60mm (width) × 258mm (length) and variable thicknesses can be glued on the top surface of the flexible panel support (Figure B.3). The height of the flexible panels can be adjusted through a connector (Figure B.4) to ensure that the flexible panels are flush-mounted. Figure B.7 gives the design of a solid panel, which replaces the flexible panel and its support, acting as a benchmark case to be compared with the results of flexible panel cases.

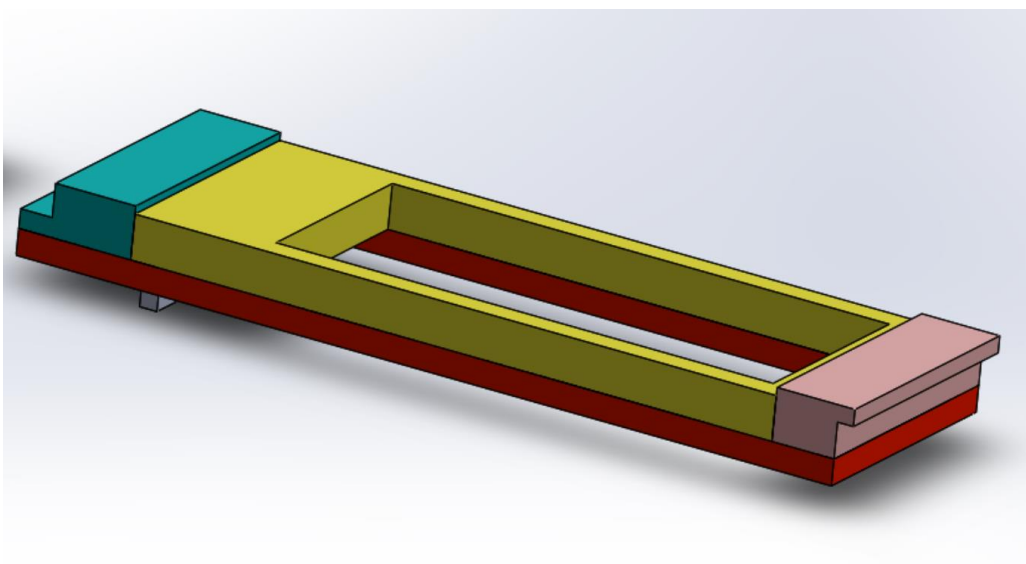


Figure B.1 Assembly of flexible panel support unit in the supersonic wind tunnel (The red part is the bottom support connecting with wind tunnel, the yellow part is the flexible panel support, the small grey part underneath the bottom support is a connector to adjust the height of the flexible panel, the green part with a step is the upstream connector and the right rosypink part is the downstream connector).

Appendix

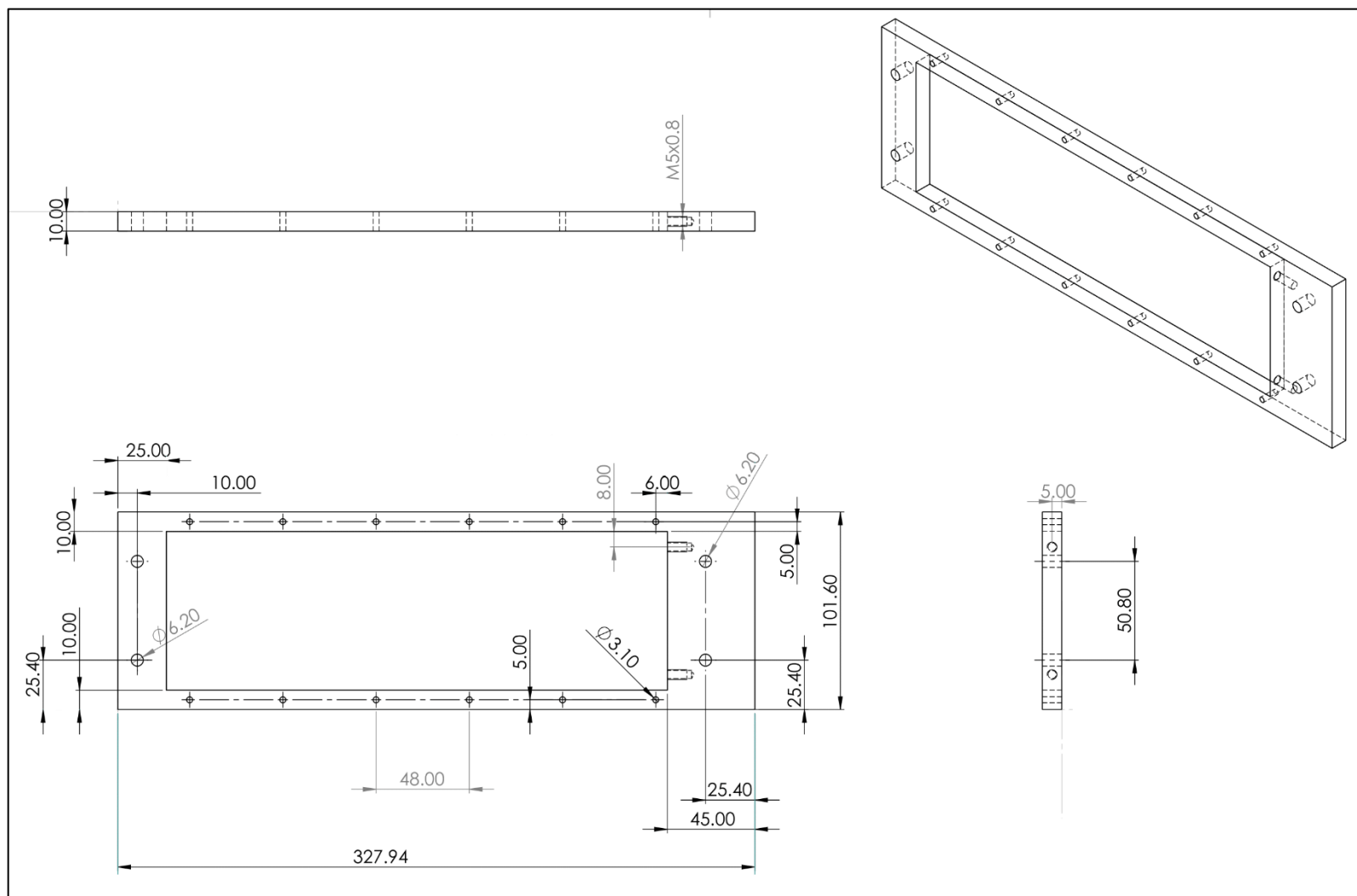


Figure B.2 Design and dimensions of the bottom support

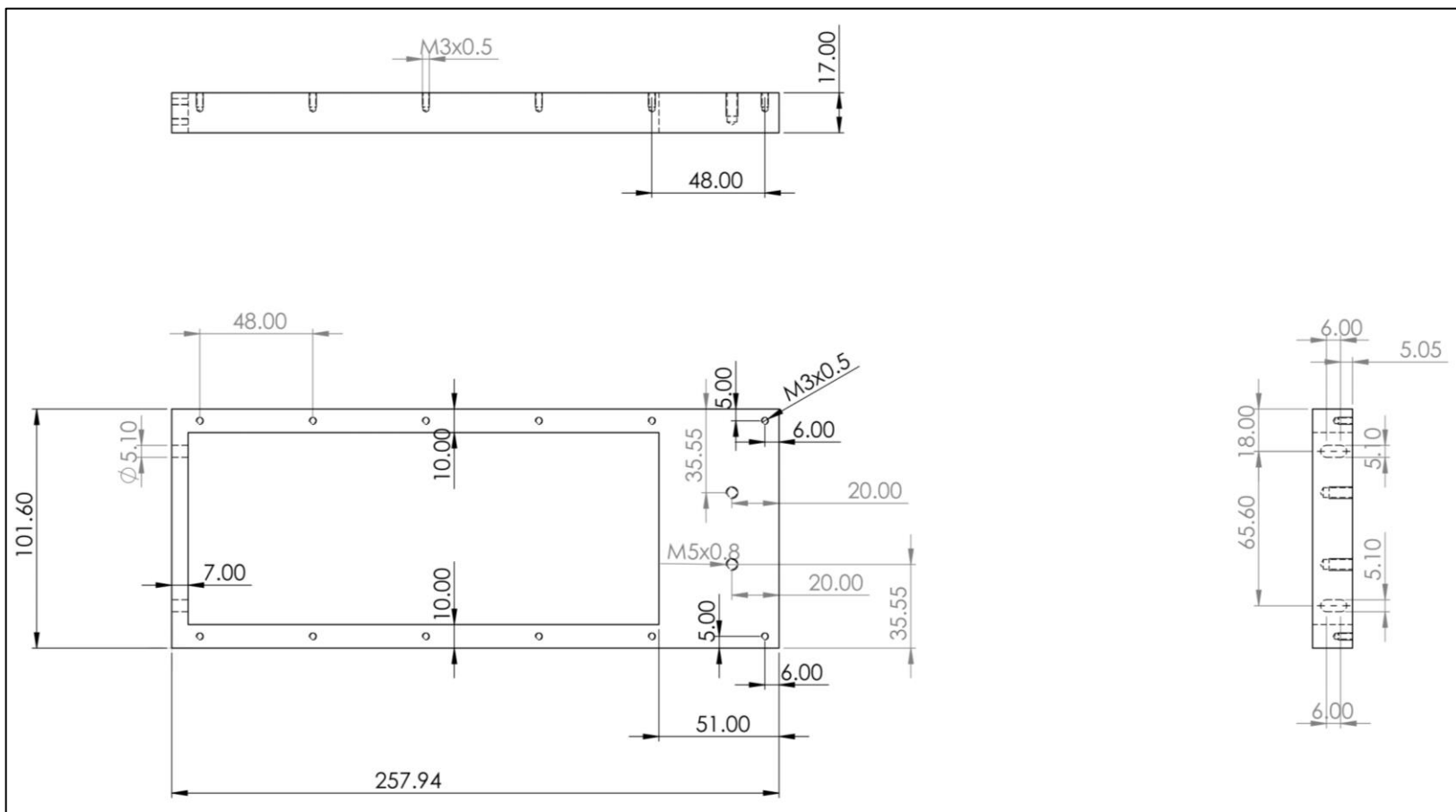


Figure B.3 Design and dimensions of the flexible panel support

Appendix

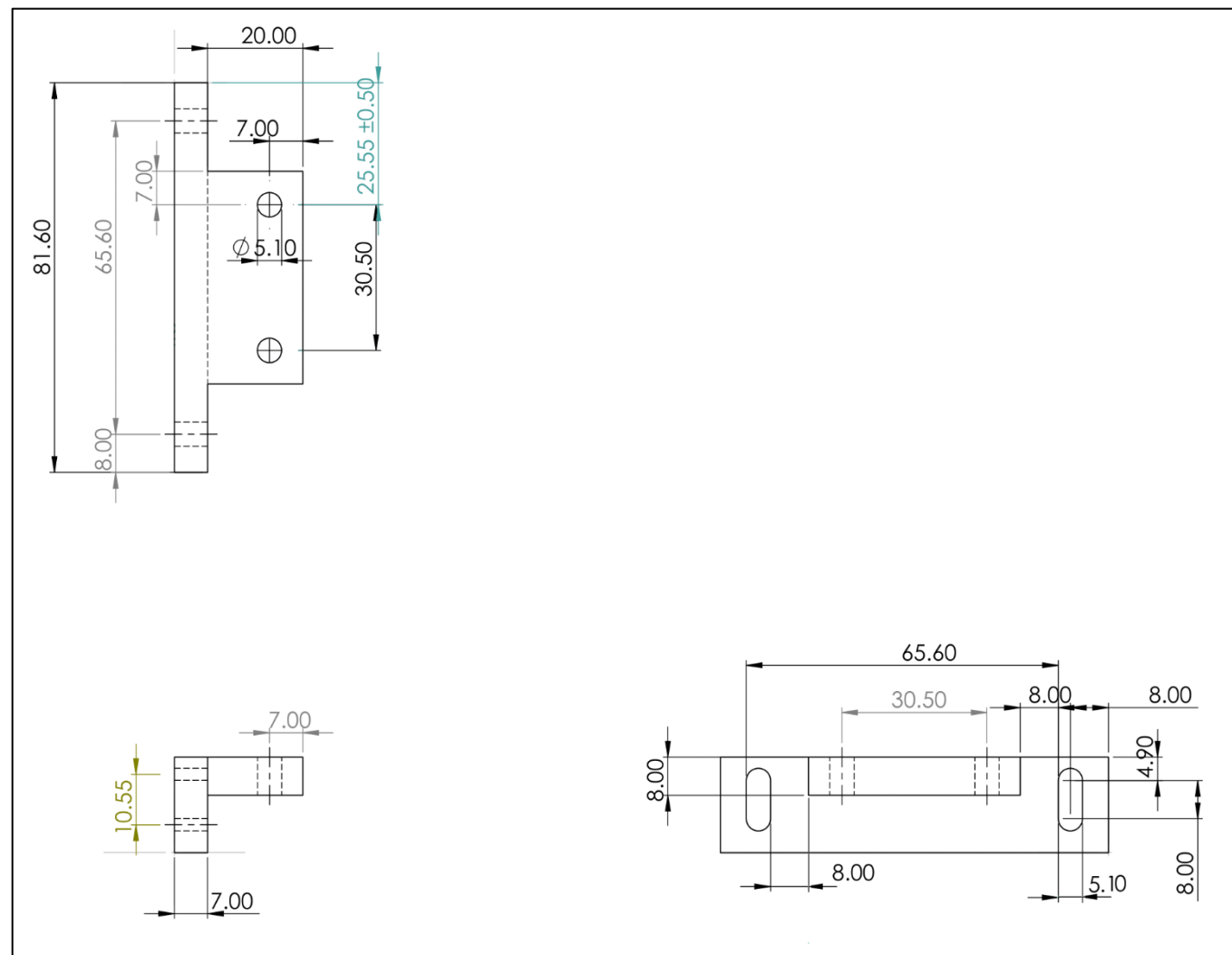


Figure B.4 Design and dimensions of the connector for flexible panel support and bottom support

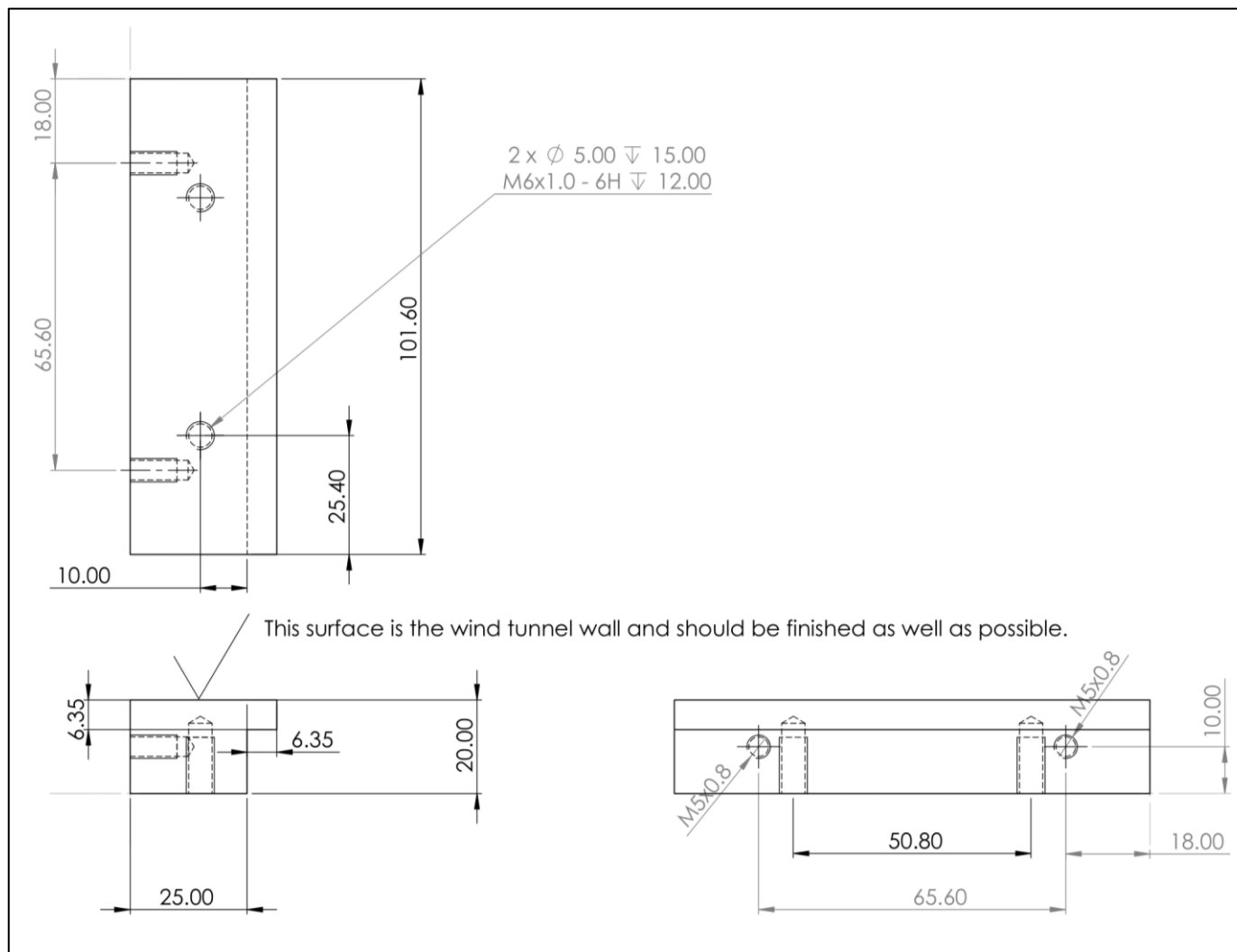


Figure B.5 Design and dimensions of the downstream connector

Appendix

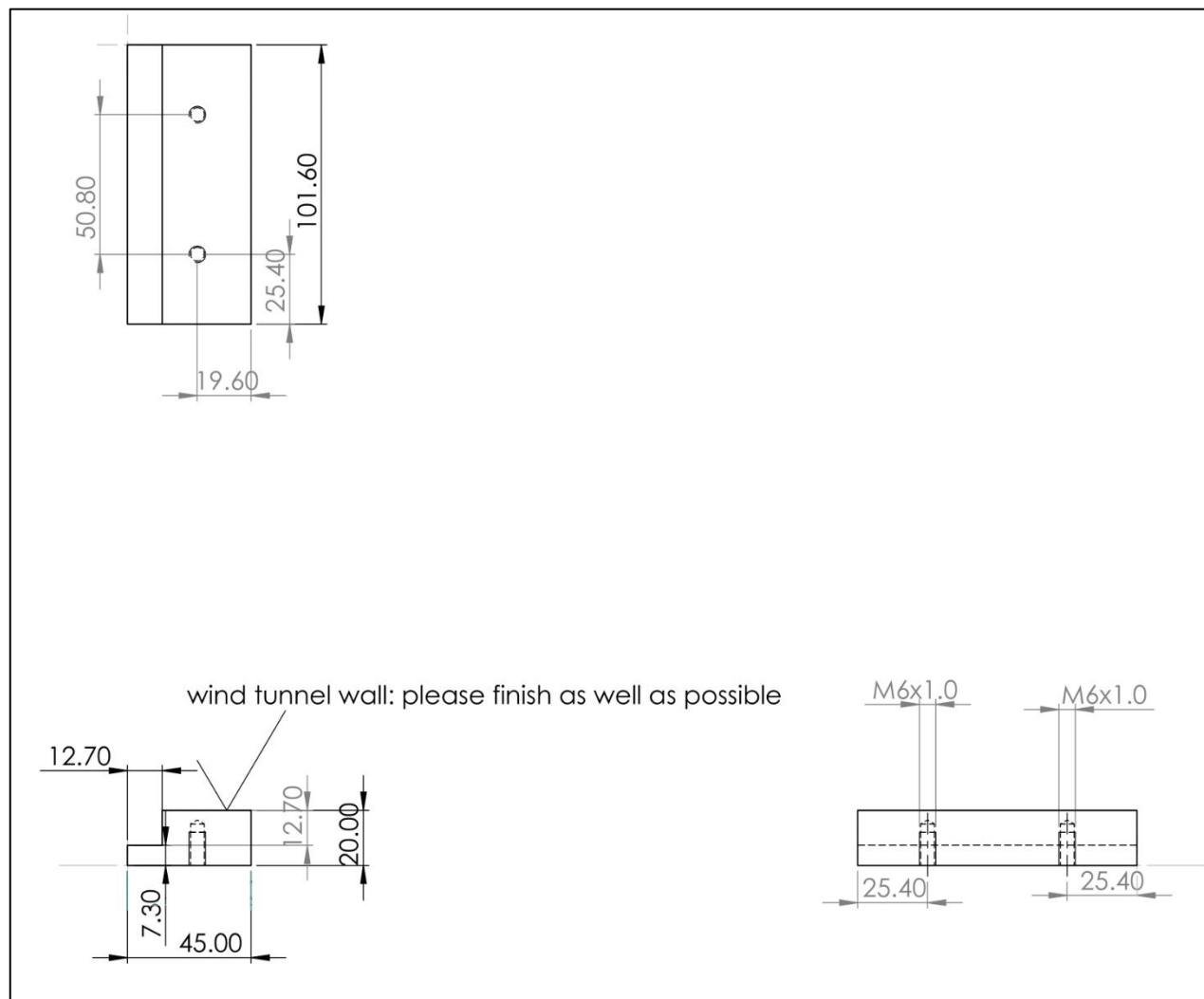


Figure B.6 Design and dimensions of the upstream connector

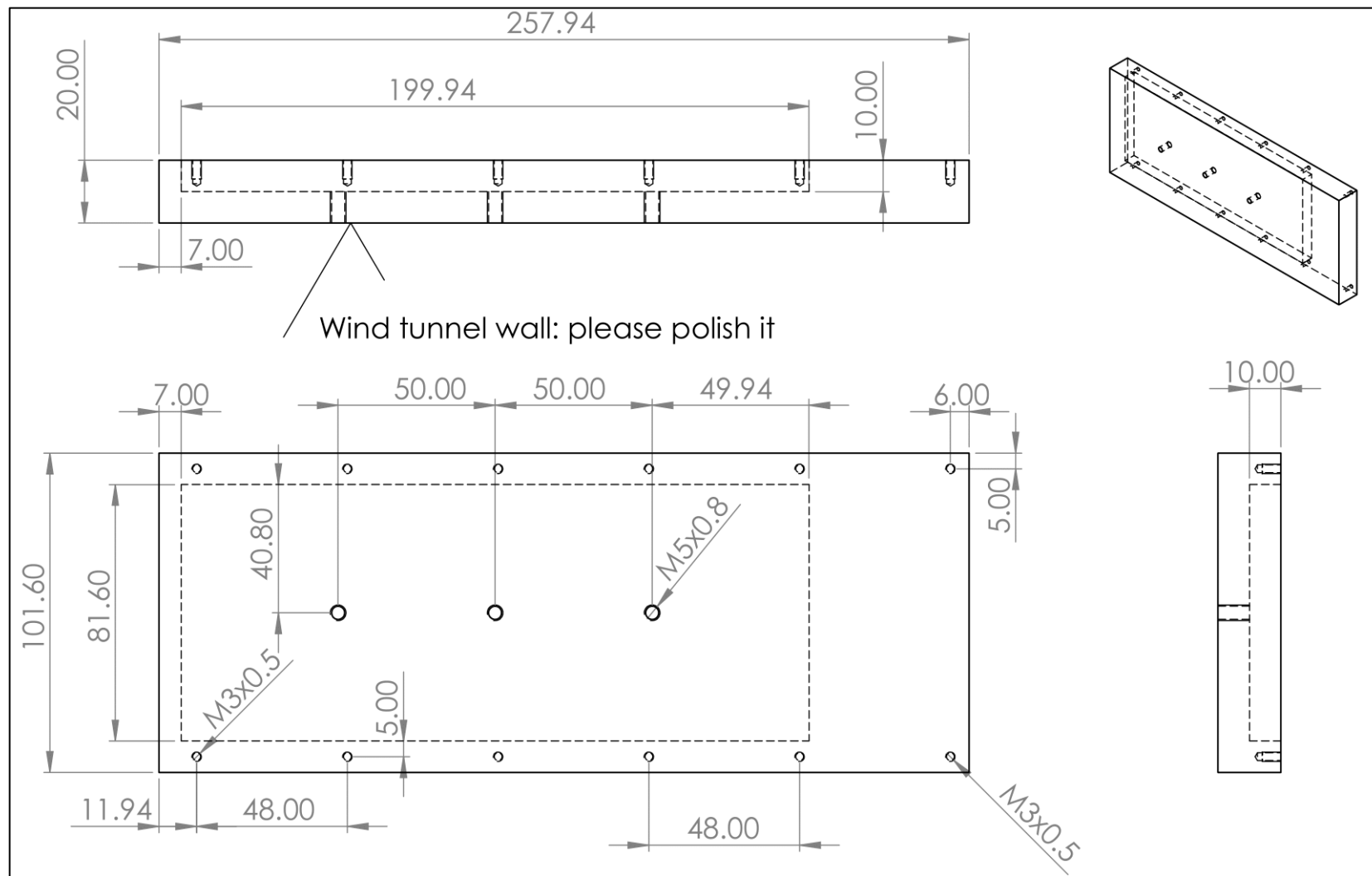


Figure B.7 Design and dimensions of the solid panel

Appendix

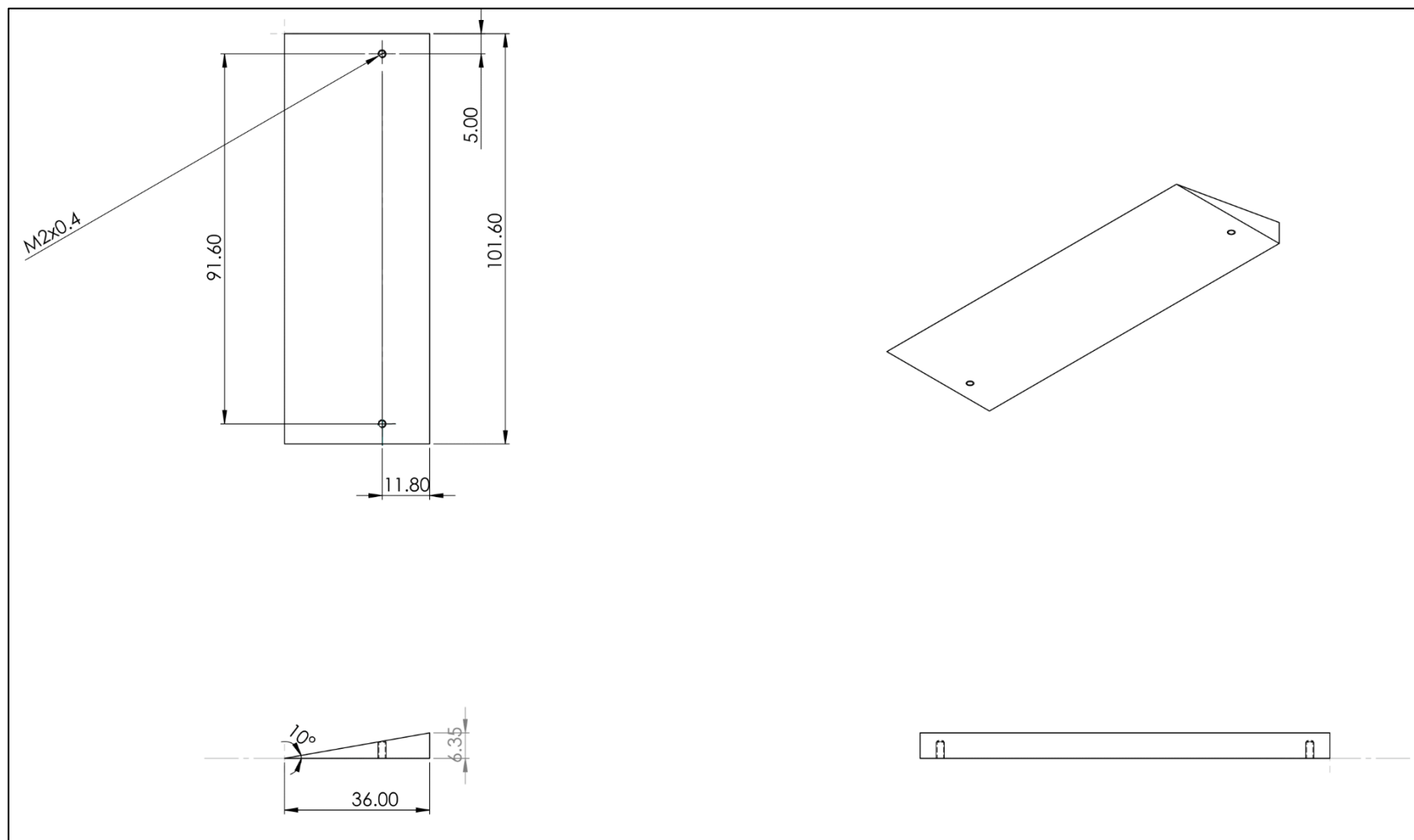


Figure B.8 Design and dimensions of the shock wave generator

Appendix C

Design of Pitot rake

To calibrate the velocity profile of the supersonic wind tunnel in the University of Glasgow, a Pitot rake was designed by Dr. Francesca Gnani. The design and dimensions of the Pitot rake are shown in Figure C.1. Figure C.2 illustrates the axial coordinate of the pressure taps for static pressure measurements and the installation of the Pitot rake for velocity measurement in the supersonic wind tunnel. As demonstrated in Figure C.2, the Pitot rake can be adjusted along y direction.

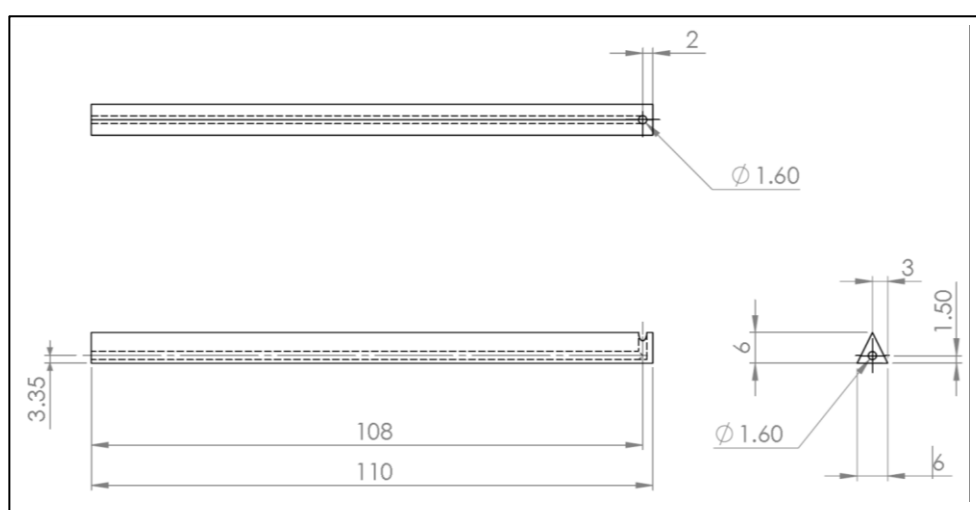


Figure C.1 Geometry of the Pitot rake (all dimensions in mm).

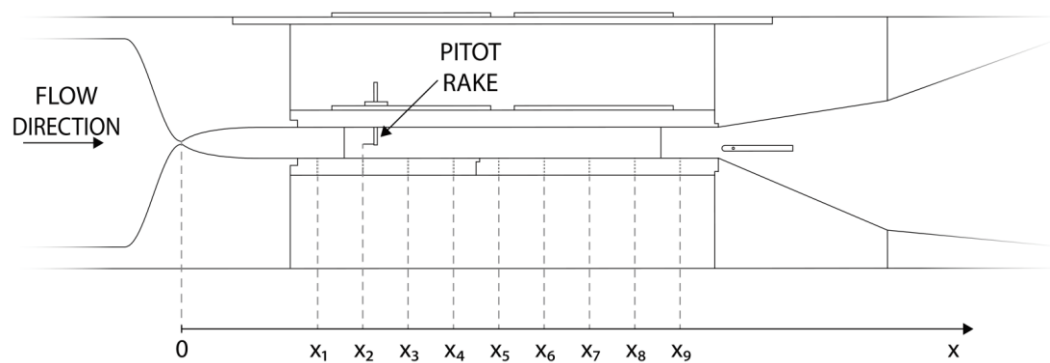


Figure C.2 Schematic of Pitot rake installation in the supersonic wind tunnel with pressure taps locations.

Appendix D

Interfaces of the software for shock wave detection and tracking

This section presents typical graphical interfaces of the software for shock wave detection and tracking.

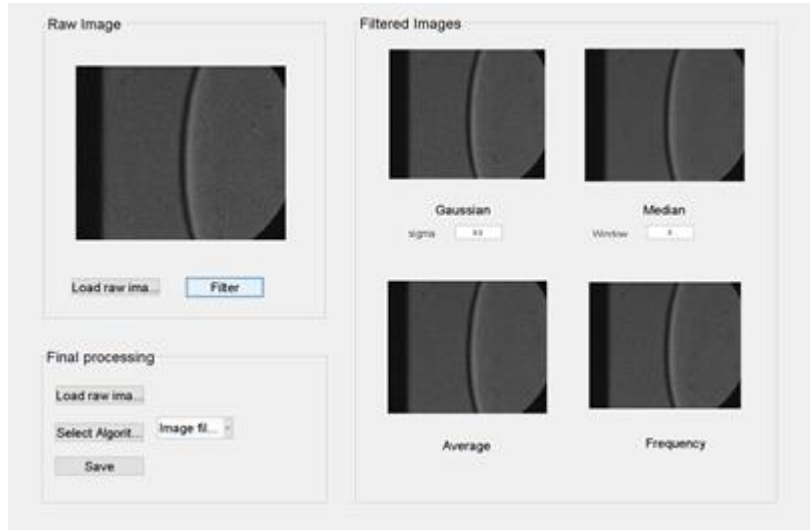


Figure D.1 The graphical interface for image filter setting



Figure D.2 The graphical interface for background image subtraction

Appendix

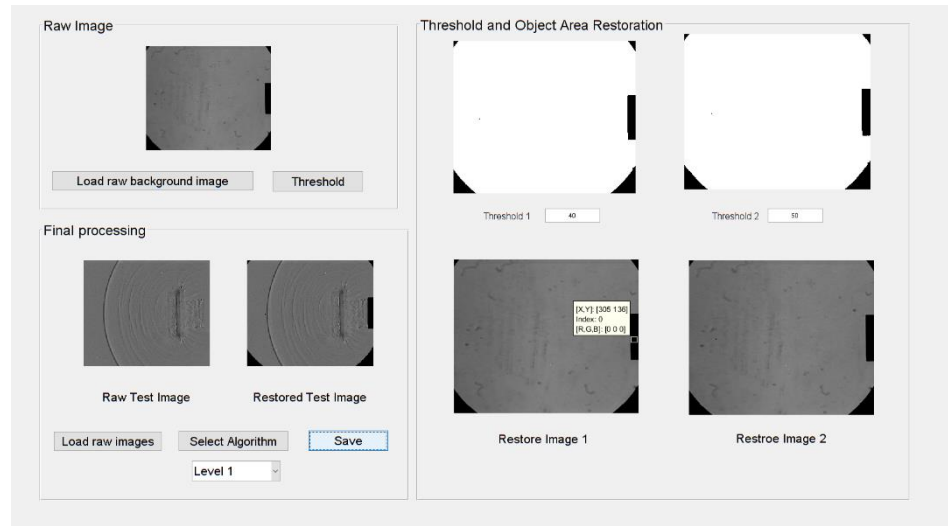


Figure D.3 The graphical interface for restoring the test model and the region out of measurement

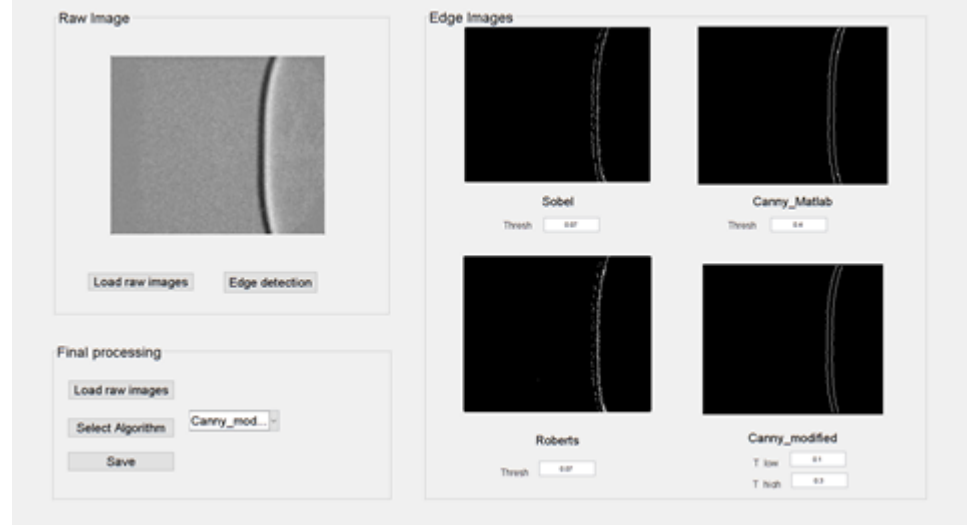


Figure D.4 The graphical interface for edge detection

Appendix E

Program code examples of the software for shock wave detection

E.1 Background image subtraction in frequency domain

```
% Key part of the callback function of the pushbutton for background image subtraction
% Programming Language: MATLAB
function BckImgSub_pushbutton_Callback(hObject, eventdata, handles)
clc
bckImg=handles.bckImg; %load the background image
bckImg=imread(bckImg);

TestImgs=handles.TestImgs; %load the background image
N=length(TestImgs);
path=handles.path;
file_TestImgs =handles.file;
```

```

for i=1:N % subtract the background image from the test images
    I=imread (TestImgs{i});
    FFTbakImg = fft (bckImg);
    FFTtestImg = fft (I);
    IFFT = ifft (FFTtestImg - FFTbakImg);
    IFFT= mat2gray(IFT);
    imwrite (IFFT,fullfile( path, strcat ('bckImgSubtracted_', file_ TestImgs {i})));

```

E.2 Contour detection and extraction

// Key part of program codes for contour detection and extraction

// Programming Language: C++

//1. load test images

```

double fscale=2; // resampling factor
String strs; // load test images
Mat dst;
StringList file_list, output_name;
StringList str_path_list = FileDialog::getOpenFileNames(this, tr("Open images"), tr("/"),
tr("Images (*.tif *.jpg)"));

```

for (int i = 0; i < str_path_list.size(); i++) //shock detection, extraction and fitting

{

```

String str_path = str_path_list[i];
String fileName, Img_name, file_path, file_suffix, ImgSaveName, fileBaseName ;
FileInfo fileinfo;
fileName=str_path;
fileinfo = FileInfo(fileName);
file_path = fileinfo.absolutePath(); //absolute path
fileBaseName=fileinfo.baseName(); //image file name
file_suffix = fileinfo.suffix(); //image format
ImgSaveName=file_path+"/"+ "ShockDetection_" +fileBaseName+"."+file_suffix;

```

Appendix

```
Mat src= imread (fileName.toStdString(), 0);
Mat gray=convertTo8UC1(src);

// 2. Image resampling to improve accuracy
Resize (gray, gray, Size(), fscale, fscale,INTER_LANCZOS4 );

// 3. blur the image
int FilterSize= 3 + (fscale-1) * 2;
int isMedianBlur= 0;
int isGaussianBlur= 1;
int isBilateralBlur= 1;
if (isMedianBlur)
    {medianBlur (gray, gray,3);}
if (isGaussianBlur)
    {GaussianBlur(gray, gray, Size(FilterSize, FilterSize),0.0,0.0);}
if(isBilateralBlur)
{
    Mat gray2;
    gray2=convertTo8UC1(gray);
    filterBilateral (gray2, gray, -1, 6, 6, BORDER_DEFAULT);
}

// 4. adaptive threshold
int isAdaptiveThreshold=1;
if (isAdaptiveThreshold)
{
    const int maxVal = 255;
    int IsThickFeature=0;
    if (IsThickFeature)
    {
        int blockSize = 15; //the value should be an odd integer
```

```

        int constValue = 8;
        int adaptiveMethod = 0;
        int thresholdType = 1;
        adaptiveThreshold(gray, gray, maxVal, adaptiveMethod, thresholdType,
blockSize, constValue);
    }
else
{
    int blockSize = 25;
    int constValue = 5; // The constant subtracted from the mean or weighted sum of
the neighbourhood pixels
    int adaptiveMethod = ADAPTIVE_THRESH_MEAN_C;
    int thresholdType = 1;
    adaptiveThreshold(gray, gray, maxVal, adaptiveMethod, thresholdType,
blockSize, constValue);
}
}

```

// 5. Automatic threshold calculation for Canny

```

double lowThreshold, highThreshold;
calcOstuThreshold (gray, lowThreshold, highThreshold);

```

// 6. edge detection by modified Canny algorithm

```
Canny (gray, gray, lowThreshold*0.5, highThreshold*0.5);
```

// 7. Contour detection, properties calculation, and erase small contours

```

vector<vector<Point>> contours;
vector<Vec4i> hierarchy;
findContours( gray, contours, hierarchy, RETR_TREE, CHAIN_APPROX_SIMPLE,
Point(0, 0) );
double largest_size=0; // find the largest contour
int largest_contour_index;

```

Appendix

```
for (int i = 0; i< contours.size(); i++) // iterate through each contour.  
{  
    double a = contours[i].size(); // calculate the size of contour  
    if (a>largest_size)  
    {  
        largest_size = a;  
        largest_contour_index = i; //save the index of largest contour  
    }  
}  
  
double SencondLargestSize=0; //find the second largest contour  
int SecondLargestContuorIndex;  
for (int i = 0; i< contours.size(); i++) // iterate through each contour.  
{  
    double a = contours[i].size();  
    if (a>SencondLargestSize && a<largest_size)  
    {  
        SencondLargestSize = a;  
        SecondLargestContuorIndex = i; //save the index of largest contour  
    }  
}  
  
// 8. Display shock detection result  
int isContourFilter=1;  
int isDrawContourOnSrcImg=0;  
Mat clone;  
Resize (src, clone, Size(), fscale, fscale, INTER_CUBIC);  
Mat dst = Mat::zeros(clone.rows, clone.cols, 8UC3);  
if (isContourFilter)  
{  
    // iterate through all the top-level contours and draw each connected component with  
    // its own random colour  
    int idx = 0;
```

```

for( ; idx >= 0; idx = hierarchy [idx][0] )
{
    if ( contours[idx].size() > SencondLargestSize)
    {
        Scalar color( rand()&255, rand()&255, rand()&255 );
        if (isDrawContourOnSrcImg)
            { drawContours( clone, contours, idx, Scalar(0,0,0), FILLED, 8, hierarchy); }
        else
            { drawContours( dst, contours, idx, color, FILLED, 8, hierarchy); }
    }
}
else
{
    int idx = 0;
    for ( ; idx >= 0; idx = hierarchy[idx][0] )
    {
        Scalar color( rand()&255, rand()&255, rand()&255 );
        if (!isDrawContourOnSrcImg)
            { drawContours (dst, contours, idx, color, FILLED, 8, hierarchy); }
        else
            { drawContours (clone, contours, idx, Scalar(0,0,0), FILLED, 8, hierarchy); }
    }
}

```

// 9. save the result images

```

int isConvertGray=1;
int isInvertBinary=1;
if (isDrawContourOnSrcImg)
{
    if (isConvertGray)
        {clone=convertTo8UC1(clone);}

```

Appendix

```
if (isInvertBinary)
{ BasicThreshold(clone, clone, 10, 255, 1);}
imwrite(ImgSaveName.toStdString(), clone);
}
else
{
if (isConvertGray)
{dst=convertTo8UC1(dst);}
if (isInvertBinary)
{ BasicThreshold(dst, dst, 10, 255, 1);}
Imwrite (ImgSaveName.toStdString(), dst);
}
}
}
```